SYMPLECTIC APPROXIMATION OF HAMILTONIAN FLOWS AND ACCURATE SIMULATION OF FRINGE FIELD EFFECTS

By

Béla Erdélyi

AN ABSTRACT OF A DISSERTATION

Submitted to
Michigan State University
in partial fulfillment of the requirements
for the degree of

DOCTOR OF PHILOSOPHY

Department of Physics and Astronomy

2001

Professor Martin Berz

ABSTRACT

SYMPLECTIC APPROXIMATION OF HAMILTONIAN FLOWS
AND ACCURATE SIMULATION OF FRINGE FIELD EFFECTS

By

Béla Erdélyi

In the field of accelerator physics, the motion of particles in the electromagnetic fields of periodic accelerators is usually approximated by the iteration of a symplectic map, which represents the system over short time, such as one turn around the accelerator. Unfortunately, due to the complexity of the systems, in practice only some approximation of the one-turn map can be computed, as, for example, the truncated Taylor series. To this end, simulation of the nonlinear dynamics consists, in general, of the following three steps: 1) Computation of the truncated Taylor approximation of the one-turn map, 2) Symplectification of the Taylor map, and 3) Iteration of the resulting exactly symplectic map. This dissertation addresses all three components of the process, with the emphasis being on developing new methods that allow long-term tracking as accurately and efficiently as possible.

Specifically, the contributions to the first step concern the fringe field effects. The truncated Taylor map should include every relevant effect, so that it is an accurate representation of the system over one turn. While it is straightforward to compute the truncated maps over the regions where the fields are independent of the longitudinal variable, it is not so anymore at the ends of the magnets, the so-called fringe field regions. We study fringe fields generically, to show their importance, and develop a

method that allows "exact" fringe field map computation of superconducting magnets, for which the coils and the iron parts are represented by current wires. The theory is illustrated by a detailed study of fringe field effects on the nonlinear dynamics of the Large Hadron Collider at collision energy.

Many contributions are established to the second step. It is well known that the theory of generating functions of canonical transformations provides a possible symplectification method. It is shown that, by transforming the dynamical problem into a problem in symplectic geometry, a general theory can be developed, which leads to a set of infinitely many new types of generating functions. It follows that it is possible to use this extended set to produce symplectic maps, and to reduce the whole set of generators to classes that give the same symplectified map. Moreover, the effects of factorization of the linear parts on the outcome of symplectification were studied. A variety of examples show the performance of various generator types, from which it can be concluded that it is not only important to symplectify, but also to symplectify "the right way". The precise meaning of the last statement is the subject of the optimal symplectification theory, which can be formulated using methods of symplectic topology. In particular, Hofer's metric allows the formulation of the optimality condition in a very general setting, and the solution leads to a generating function type (EXPO) that, in general, gives optimal results. In the proof, an interesting one-to-one correspondence between fixed points of symplectic maps and critical points of generating functions is developed, and a generalized Hamilton-Jacobi equation is derived.

Finally, as contribution to the third step, it is pointed out that the numerical method used to solve the implicit equations arising in the iteration of the symplectic maps makes a difference in the final results, and, in general, a fixed point iteration is more robust than the widely used Newton method.

SYMPLECTIC APPROXIMATION OF HAMILTONIAN FLOWS AND ACCURATE SIMULATION OF FRINGE FIELD EFFECTS

By

Béla Erdélyi

A DISSERTATION

Submitted to
Michigan State University
in partial fulfillment of the requirements
for the degree of

DOCTOR OF PHILOSOPHY

Department of Physics and Astronomy

2001

ABSTRACT

SYMPLECTIC APPROXIMATION OF HAMILTONIAN FLOWS
AND ACCURATE SIMULATION OF FRINGE FIELD EFFECTS

By

Béla Erdélyi

In the field of accelerator physics, the motion of particles in the electromagnetic fields of periodic accelerators is usually approximated by the iteration of a symplectic map, which represents the system over short time, such as one turn around the accelerator. Unfortunately, due to the complexity of the systems, in practice only some approximation of the one-turn map can be computed, as, for example, the truncated Taylor series. To this end, simulation of the nonlinear dynamics consists, in general, of the following three steps: 1) Computation of the truncated Taylor approximation of the one-turn map, 2) Symplectification of the Taylor map, and 3) Iteration of the resulting exactly symplectic map. This dissertation addresses all three components of the process, with the emphasis being on developing new methods that allow long-term tracking as accurately and efficiently as possible.

Specifically, the contributions to the first step concern the fringe field effects. The truncated Taylor map should include every relevant effect, so that it is an accurate representation of the system over one turn. While it is straightforward to compute the truncated maps over the regions where the fields are independent of the longitudinal variable, it is not so anymore at the ends of the magnets, the so-called fringe field regions. We study fringe fields generically, to show their importance, and develop a

method that allows "exact" fringe field map computation of superconducting magnets, for which the coils and the iron parts are represented by current wires. The theory is illustrated by a detailed study of fringe field effects on the nonlinear dynamics of the Large Hadron Collider at collision energy.

Many contributions are established to the second step. It is well known that the theory of generating functions of canonical transformations provides a possible symplectification method. It is shown that, by transforming the dynamical problem into a problem in symplectic geometry, a general theory can be developed, which leads to a set of infinitely many new types of generating functions. It follows that it is possible to use this extended set to produce symplectic maps, and to reduce the whole set of generators to classes that give the same symplectified map. Moreover, the effects of factorization of the linear parts on the outcome of symplectification were studied. A variety of examples show the performance of various generator types, from which it can be concluded that it is not only important to symplectify, but also to symplectify "the right way". The precise meaning of the last statement is the subject of the optimal symplectification theory, which can be formulated using methods of symplectic topology. In particular, Hofer's metric allows the formulation of the optimality condition in a very general setting, and the solution leads to a generating function type (EXPO) that, in general, gives optimal results. In the proof, an interesting one-to-one correspondence between fixed points of symplectic maps and critical points of generating functions is developed, and a generalized Hamilton-Jacobi equation is derived.

Finally, as contribution to the third step, it is pointed out that the numerical method used to solve the implicit equations arising in the iteration of the symplectic maps makes a difference in the final results, and, in general, a fixed point iteration is more robust than the widely used Newton method.

To my family

ACKNOWLEDGMENTS

I gratefully acknowledge the support of many for their help and encouragement. I hope that every person who has helped me can take pride in the completion of this dissertation.

I thank my advisor, Martin Berz, for providing all the support and resources necessary from start to finishing the thesis. His combination of direction and freedom provided an excellent training in scientific research, and contributed enormously to my professional growth. I learned a lot from him, and his enthusiasm, insight and commitment to science in general has been a great source of encouragement. I am also grateful for his investment in sending me to conferences.

Many thanks for my guidance committee members: Jerry Nolen, Brad Sherrill, Bhanu Mahanti, and Dan Stump. Also, I would like to thank the physics graduate secretaries for the prompt and friendly help.

I have benefited greatly from discussions with many other scientists: Carol Johnstone, Weishi Wan, Francois Meot, Frank Zimmermann, Bill Ng, Jim Holt, Teddy Draghici, Frederick Siburg, and others.

It has been a pleasure to work with the other members of the Beam Theory and Dynamical Systems group, who were at MSU over various periods of time between 1996-2001: Vladimir Balandin, Lars Diening, Michael Lindemann, Jens von

Bergmann, Khodr Shamseddine, Kyoko Makino, Jens Hoefkens, and Shashikant Manikonda. Jens Hoefkens deserves special thanks for many computer related help.

Finally, I thank my family for their unconditional support, and especially my wife, daughter, mother, and sister whose love is a huge source of strength and great joy.

Contents

LIST OF TABLES xi

LIST OF FIGURES xiii

I Symplectic Approximation of Hamiltonian Flows 1

1 Introduction 2

2 General Theory of Generating Functions of Canonical Transformations 8

2.1 The Local Theory 9

2.2 The Global Theory 17

2.2.1 Fundamentals of Symplectic Geometry 18

2.2.2 Primitive Function vs. Generating Function 23

2.2.3 Symplectic Maps as Lagrangian Submanifolds 25

2.2.4 Functions as Lagrangian Submanifolds 27

2.2.5 Existence of Infinitely Many Generating Functions 31

2.3 Generating Functions from the Computational Point of View 35

2.4 Computation of Symplectic Maps from Generating Functions 40

3 The Symplectic Approximation Process 42

3.1 Symplectification of Taylor Maps and Symplectic Tracking by the Generating Function Method 43

3.2 Transformation Properties of Generating Functions 46

3.3 Equivalence Classes of Generating Functions 50

3.3.1 Application to the Conventional Generating Function Types . 59

3.4 Equivalence of Symplectification with and without Linear Part 62

3.4.1 Equivalence in the Case of Symplectic Maps Conjugated by Linear Symplectic Maps 68

3.5 Implementation 69

4 Examples **73**
4.1 Maps Generated from Random Hamiltonians 74
4.2 An Anharmonic Oscillator 81
4.3 An Exactly Symplectic Quadratic Map 91
4.4 Muon Accelerators 96
4.4.1 A Neutrino Factory Lattice 96
4.4.2 The FNAL Proton Driver 100
4.5 The Large Hadron Collider (LHC) 100

5 Optimal Symplectification **106**
5.1 Formulation of the Problem 107
5.2 Hofer's Metric and the Optimality Condition 108
5.2.1 Hofer's Metric 109
5.2.2 Connectedness of the Group of Hamiltonian Symplectic Maps 112
5.2.3 The Optimality Condition 114
5.3 Link to the Extended Generating Function Theory 115
5.3.1 The Fixed Point-Critical Point Relationship 117
5.3.2 The Generalized Hamilton-Jacobi Equation and Applications . 121
5.3.3 Siburg's Theorem 126
5.3.4 Proof of the Main Theorem 128
5.4 The Best Generating Function Type 131
5.5 Some Further Remarks 136

6 Summary of Part I **143**

II Accurate Simulation of Fringe Field Effects **146**

7 Introduction and Theoretical Background **147**

8 Generic Effects **153**
8.1 Aperture Dependent Effects on Linear Tunes and Chromaticities . . . 154
8.2 The Sharp Cutoff Limit 156
8.3 Shape Dependent Effects 165
8.4 Nonlinear Effects Due to Pseudo-Multipoles 176
8.5 Symplectification 178

8.6 Summary 179

9 Multipole Decomposition of Magnets Represented by Wire-Currents 183

9.1 Biot-Savart Law and Field Computation 184
9.2 Multipole Extraction Algorithms 190
9.2.1 The Direct Method 190
9.2.2 Multipole Extraction by Analytical Fourier Transform 192
9.3 Enforcing Maxwell's Equations 194
9.3.1 Local Maxwellification 194
9.3.2 Global Maxwellification 198
9.4 Structure of B_r and B_ϕ for Non-Maxwellian Fields 200
9.5 Examples of Exact Multipole Decompositions 204
9.6 Computation of Fringe Field Maps 208

10 Fringe Field Effects on the Nonlinear Dynamics of the LHC 216

10.1 Methods of Analysis 217
10.2 Cases Studied 219
10.3 Results and Discussion 221
10.4 Map Transformations Under Orientation Flips 246

11 Summary of Part II 253

BIBLIOGRAPHY 256

List of Tables

3.1 Number of iterations needed for convergence in solving (3.175) for several examples, using the generator type associated with $S = 0$. The orbits of the particles of small, medium, and large amplitude, respectively, have been followed for 100 turns, and the number of iterations needed is enclosed in the intervals appearing in the table. 71

3.2 Number of iterations needed for convergence in solving (3.175) for several examples, using the conventional generator type F_1. The orbits of the particles of small, medium, and large amplitude, respectively, have been followed for 100 turns, and the number of iterations needed is enclosed in the intervals appearing in the table. In the table, n.c. stands for no convergence in 100 iterations, and "not stable" means that the respective particle is predicted by the algorithm to be unstable. 71

8.1 Enge coefficients of the default fringe field falloff used in COSY INFINITY for dipoles, quadrupoles, and sextupoles, respectively. 155

8.2 Enge function with only two parameters, computed by slightly modifying the second default Enge coefficient (a_2), such that the corresponding Enge function has the same integral as the default six parameter one. 170

8.3 Enge coefficients fitted for the LHC HGQ lead and return ends, respectively. 171

8.4 A few amplitude dependent tune shifts for the 25 mm aperture case. All 6 studied fringe field falloff shapes are included. 172

8.5 A few amplitude dependent tune shifts for the 50 mm aperture case. All 6 studied fringe field falloff shapes are included. 172

8.6 A few amplitude dependent tune shifts for the 75 mm aperture case. All 6 studied fringe field falloff shapes are included. 172

8.7 A few amplitude dependent tune shifts for the 100 mm aperture case. All 6 studied fringe field falloff shapes are included. 173

9.1 Results of transforming the analytic derivatives of the Biot-Savart law, computed with Mathematica, to Fortran code. 185

9.2 Computation time of the Taylor expansion of the y-component of the magnetic field in DA at various orders. 186

9.3 Taylor expansion of the magnetic field components B_x and B_y. The columns represent the expansion coefficients, the order in the expansion and the exponents of (x, s, y), respectively. 189

9.4 Comparison of the s component of the curl, up to order 3, computed by two different implementations of the Biot-Savart law ((9.11) and (9.6), respectively). 190

9.5 The s component of the curl, up to order 12, after Maxwellification of the field in Table 9.3. 198

9.6 Opening aberrations, $(x|a^n)$, for the return and lead ends' exit focusing maps. 215

10.1 The various LHC realization cases studied. 222

List of Figures

4.1 1000 turn tracking of a random two dimensional symplectic map with the 19th order Taylor map (considered to be essentially the exact result). 75

4.2 1000 turn tracking of the random two dimensional symplectic map obtained from the 19th order Taylor map, by symplectifying it with the generator type associated with the $S = 0$ symmetric matrix. . . . 76

4.3 1000 turn tracking of the random two dimensional symplectic map with the $3, 7$, and 11th order Taylor maps, and $S = 0$ symplectified map, respectively. 77

4.4 1000 turn tracking of the random two dimensional symplectic map with the symplectified maps utilizing the F_1, F_2, F_3, F_4 generating function types for the full 11th order Taylor map, and F_2 and F_3 for the nonlinear part of the 11th order Taylor map respectively. 78

4.5 1000 turn tracking of another random two dimensional symplectic map with the 19th order Taylor map (considered to be essentially the exact result). 79

4.6 1000 turn tracking of the second random two dimensional symplectic map with the $3, 7, 11$, and 19th order $S = 0$ symplectified maps respectively. 79

4.7 1000 turn tracking of the second random two dimensional symplectic map with the symplectified maps using the conventional generator types F_1, F_2, F_3, and F_4 respectively. 80

4.8 1000 turn tracking of a anharmonic oscillator with the 19th (considered to be essentially the exact result) and 7th order Taylor maps. 82

4.9 1000 turn tracking of an anharmonic oscillator with the $3, 7$, and 11th order $S = 0$ symplectified maps respectively. 82

4.10 1000 turn tracking of an anharmonic oscillator with the symplectified maps from the 7th order Taylor map, using the conventional generator types F_1, F_2, F_3, and F_4 respectively. 83

4.11 1000 turn tracking of an anharmonic oscillator, with two random generating function types associated with symmetric matrices with entries in $[-1, 1]$ and $[-10, 10]$ respectively. 84

4.12 1000 turn tracking of an anharmonic oscillator, with the generating function type associated with the symmetric matrix S_b, which was fitted to give the best results. 85

4.13 2000 turn tracking of an anharmonic oscillator, with the generating function type associated with the symmetric matrix $S = 0$, using the 11th order 1/2 time Taylor map. 86

4.14 Corrections introduced by the symplectification to particles of small amplitude, which are predicted by symplectic tracking with generating function type associated with the symmetric matrix $S = 0$ to be on a invariant curve (a stable particle). The figure shows the correction with respect to the 7th order Taylor map of the symplectifications using the convential (the magnification factor is 10^3) as well as the $S = 0$ (the magnification factor is 10^6) generator types. 88

4.15 Corrections introduced by the symplectification to particles of medium amplitude, which are predicted by symplectic tracking with generating function type associated with the symmetric matrix $S = 0$ to be on a invariant curve (a stable particle). The figure shows the correction with respect to the 7th order Taylor map of the symplectifications using the convential (the magnification factor is 1) as well as the $S = 0$ (the magnification factor is 10^2) generator types. 89

4.16 Corrections introduced by the symplectification to particles of large amplitude, which are predicted by symplectic tracking with generating function type associated with the symmetric matrix $S = 0$ to be on a invariant curve (a stable particle). The figure shows the correction with respect to the 7th order Taylor map of the symplectifications using the convential (the magnification factor is 1) as well as the $S = 0$ (the magnification factor is 10) generator types. 90

4.17 Global error propagation in the case of nonsymplectic versus symplectic tracking of a particle for 1000 turns of the anharmonic oscillator's time one map. For the tracking, the order 7 Taylor map was used for nonsymplectic tracking, and generator of type associated with $S = 0$ for the symplectic tracking. After a short transient period, the nonsymplectic method gives large errors, while the symplectic method's error stays small. 92

4.18 The global error propagation in a log-log scale of the case shown in Figure 4.17. After a short transient period, the nonsymplectic method's slope is two, and the symplectic method's slope is one. The dotted lines have exact slopes one and two, respectively. 92

4.19 1000 turn tracking of a quadratic symplectic map with the 3rd order Taylor map (the exact result), and the 3rd order $S = 0$ symplectified map (which also gives the exact result). 93

4.20 Symplectic tracking with the four conventional generator types (F_1 through F_4), for the exactly symplectic quadratic map, using fixed point iterations to solve the implicit equations. 94

4.21 Symplectic tracking with the four conventional generator types (F_1 through F_4), for the exactly symplectic quadratic map, using Newton's method to solve the implicit equations. 95

4.22 1000 turn tracking of the case 1 of a lattice of the proposed Neutrino Factory with the 8th order Taylor map, and the corresponding $S = 0$ symplectified map. 97

4.23 1000 turn tracking of the case 2 of a lattice of the proposed Neutrino Factory with the 8th order Taylor map, and the corresponding $S = 0$ symplectified map. 97

4.24 1000 turn symplectic tracking of the case 2 of a lattice of the proposed Neutrino Factory with the conventional generating functions (F_1 through F_4). 98

4.25 1000 turn tracking of the case 3 of a lattice of the proposed Neutrino Factory with the 8th order Taylor map, and the corresponding $S = 0$ symplectified map. 98

4.26 1000 turn tracking of the case 4 of a lattice of the proposed Neutrino Factory with the 8th order Taylor map, and the corresponding $S = 0$ symplectified map. 99

4.27 1000 turn tracking of the FNAL Proton Driver with the 15th order Taylor map, and the corresponding $S = 0$ symplectified map. 101

4.28 1000 turn $(x-a)$ tracking of the FNAL Proton Driver with the element-by-element numerical integration. 102

4.29 10^5 turn tracking of the LHC with the 8th order Taylor map, and the corresponding various symplectified maps, without fringe fields taken into account. 103

4.30 10^5 turn tracking of the LHC with the 8th order Taylor map, and the corresponding various symplectified maps, with detailed fringe fields taken into account. 104

4.31 10^5 turn tracking of the LHC with the F_2 and F_3 symplectified nonlinear parts of the 8th order Taylor map, without fringe fields taken into account. 105

4.32 10^5 turn tracking of the LHC with the F_2 and F_3 symplectified nonlinear parts of the 8th order Taylor map, with detailed fringe fields taken into account. 105

5.1 Plot of Hofer's distance between the exact and the symplectified maps over the region enclosing the dynamic aperture of the anharmonic oscillator studied in section 4.2. 141

8.1 Center tunes as a function of aperture. The fringe field shape is given by the default Enge coefficients. 156

8.2 Traces of the $x - a$ and $y - b$ submatrices versus aperture. The fringe field shape is given by the default Enge coefficients. 157

8.3 First and second order x chromaticities as a function of aperture. The fringe field shape is given by the default Enge coefficients. 158

8.4 First and second order y chromaticities as a function of aperture. The fringe field shape is given by the default Enge coefficients. 159

8.5 Same as Fig. 8.1 (top), and Fig. 8.2 (bottom), but without the matching section, where most of the fringe field effects are concentrated. . . 160

8.6 Same as Fig. 8.3 (top), and Fig. 8.4 (bottom), but without the matching section, where most of the fringe field effects are concentrated. . . 161

8.7 Convergence to a constant of the second order (top) and blow-up of the fourth order (bottom) amplitude dependent tune shifts in the x tune. The fringe field shape is given by the default Enge coefficients. 166

8.8 Blow-up of the second (top) and fourth (bottom) order amplitude dependent tune shifts in the y tune. The fringe field shape is given by the default Enge coefficients. 167

8.9 Second order amplitude dependent tune shifts as a function of aperture in log-log scale. x tune shifts are on the top, and y tune shifts are on the bottom. The maximum slope is around 1. 168

8.10 Fourth order amplitude dependent tune shifts as a function of aperture in log-log scale. x tune shifts are on the top, and y tune shifts are on the bottom. The maximum slope is around 3. 169

8.11 Tracking pictures of on-energy particles launched along the x-axis with vanishing transversal momenta, magnet aperture of 75 mm, for all six types of fringe fields. From left to right and from top to bottom the following fringe field types are depicted: default dipole, default quadrupole, default sextupole, LHC HGQ lead end, two parameter Enge function, and GSI QD spectrograph. 174

8.12 Resonance strengths of on-energy particles along the diagonal in action space, at a distance from the origin that corresponds to the approximate dynamic aperture, magnet aperture of 75 mm, for all six types of fringe fields. From left to right and from top to bottom the following fringe field types are depicted: default dipole, default quadrupole, default sextupole, LHC HGQ lead end, two parameter Enge function, and GSI QD spectrograph. 175

8.13 Tracking pictures of the Neutrino Factory, with the potential truncated in the pseudo- potential part at orders: 4 for (a), 6 for (b), and 8 for (c).177

8.14 Symplectic tracking picture (map and potential expansion at full order) of the Neutrino Factory for the same initial conditions as in Figure 8.13.177

8.15 Symplectic tracking pictures of the Proton Driver, for -4% momentum offset, (a) with full potential, and (b) with 6th order potential truncation.178

8.16 Tracking pictures of the Proton Driver without and with default fringe fields, and momentum offsets of 0 and $\pm 4\%$, respectively. 181

8.17 Tracking of the Neutrino Factory without and with default fringe fields. 182

9.1 Lead End of the High Gradient Quadrupoles of the Large Hadron Collider. 206

9.2 Return End of the High Gradient Quadrupoles of the Large Hadron Collider. 206

9.3 Multipole strengths of the lead end as functions of s. 207

9.4 Normal multipole strengths of the return end as functions of s: $b_2(s)$, $b_6(s)$, $b_{10}(s)$, and $b_{14}(s)$. 208

9.5 The even order s-derivatives of the lead end's $b_2(s)$. Shown are ${b_2}^{(2)}(s)$, ${b_2}^{(4)}(s)$, ${b_2}^{(6)}(s)$, ${b_2}^{(8)}(s)$, ${b_2}^{(10)}(s)$, and ${b_2}^{(12)}(s)$. 209

9.6 The even order s-derivatives of the lead end's $b_6(s)$. Shown are ${b_6}^{(2)}(s)$, ${b_6}^{(4)}(s)$, ${b_6}^{(6)}(s)$, and ${b_6}^{(8)}(s)$. 210

9.7 The even order s-derivatives of the lead end's $b_{10}(s)$. Shown are ${b_{10}}^{(2)}(s)$ and ${b_{10}}^{(4)}(s)$. 210

9.8 The even order s-derivatives of the lead end's $a_2(s)$. Shown are ${a_2}^{(2)}(s)$, ${a_2}^{(4)}(s)$, ${a_2}^{(6)}(s)$, ${a_2}^{(8)}(s)$, ${a_2}^{(10)}(s)$, and ${a_2}^{(12)}(s)$. 211

9.9 The even order s-derivatives of the lead end's $a_6(s)$. Shown are ${a_6}^{(2)}(s)$, ${a_6}^{(4)}(s)$, ${a_6}^{(6)}(s)$, and ${a_6}^{(8)}(s)$. 212

9.10 The even order s-derivatives of the lead end's $a_{10}(s)$. Shown are ${a_{10}}^{(2)}(s)$ and ${a_{10}}^{(4)}(s)$. 212

9.11 The even order s-derivatives of the return end's $b_2(s)$. Shown are ${b_2}^{(2)}(s)$, ${b_2}^{(4)}(s)$, ${b_2}^{(6)}(s)$, ${b_2}^{(8)}(s)$, ${b_2}^{(10)}(s)$, and ${b_2}^{(12)}(s)$. 213

9.12 The even order s-derivatives of the return end's $b_6(s)$. Shown are ${b_6}^{(2)}(s)$, ${b_6}^{(4)}(s)$, ${b_6}^{(6)}(s)$, and ${b_6}^{(8)}(s)$. 214

9.13 The even order s-derivatives of the return end's $b_{10}(s)$. Shown are ${b_{10}}^{(2)}(s)$ and ${b_{10}}^{(4)}(s)$. 214

9.14 The lead end's normal quadrupole strength, and its first and second s-derivatives, extracted from Maxwellian and non-Maxwellian fields, respectively, and superimposed on the same pictures. 214

10.1 Tune footprints for the LHC case 1. 224

10.2 Tune shifts for the LHC case 1. 224

10.3 Resonance strengths for the LHC case 1. 225

10.4 Tune footprints for the LHC case 2. 226

10.5 Tune shifts for the LHC case 2. 226

10.6 Resonance strengths for the LHC case 2. 227

10.7 Tune footprints for the LHC case 3. 228

10.8 Tune shifts for the LHC case 3. 228

10.9 Resonance strengths for the LHC case 3. 229

10.10 Tune footprints for the LHC case 4. 230

10.11Tune shifts for the LHC case 4. 230
10.12Resonance strengths for the LHC case 4. 231
10.13Tune footprints for the LHC case 5. 232
10.14Tune shifts for the LHC case 5. 232
10.15Resonance strengths for the LHC case 5. 233
10.16Resonance web for the LHC case 5, for $d = 0$. 233
10.17Tune footprints for the LHC case 6. 234
10.18Tune shifts for the LHC case 6. 234
10.19Resonance strengths for the LHC case 6. 235
10.20Tune footprints for the LHC case 7. 236
10.21Tune shifts for the LHC case 7. 236
10.22Resonance strengths for the LHC case 7. 237
10.23Tune footprints for the LHC case 8. 238
10.24Tune shifts for the LHC case 8. 238
10.25Resonance strengths for the LHC case 8. 239
10.26Tune footprints for the LHC case 9. 240
10.27Tune shifts for the LHC case 9. 240
10.28Resonance strengths for the LHC case 9. 241
10.29Resonance web for the LHC case 9, for $d = 0$. 241
10.30Tune footprints for the LHC case 10. 242
10.31Tune shifts for the LHC case 10. 242
10.32Resonance strengths for the LHC case 10. 243
10.33Resonance web for the LHC case 10, for $d = -2.5s_E$ and $d = 0$. . . . 244
10.34Dominating resonances for the LHC cases 9 and 10. 245

Part I

Symplectic Approximation of Hamiltonian Flows

Chapter 1

Introduction

A symplectic integration method is an integration method that preserves the symplectic structure ($\omega = d\vec{q} \wedge d\vec{p}$, for more details see subsection 2.2.1) at every time step. It is well known that symplectic integration methods have favorable qualitative properties compared to non-symplectic ones, when used for long term integration. The good long term behavior has been explained by favorable global error propagation (which is usually linear in the symplectic case, compared to generically quadratic in the non-symplectic case, and at least in certain cases stays bounded in the radial direction [1]), and the fact that the methods introduce only Hamiltonian perturbations of the original system; if the perturbations are small enough, according to the KAM theorem, most invariant tori, and hence most of the geometric structure, survive [2]. Also, symplectic methods have very good energy conservation properties. Although it is known that in general the symplectic structure and the energy cannot be conserved simultaneously by a numerical method for a Hamiltonian system [3], the Hamiltonian is preserved by a symplectic integration scheme up to a function of the accuracy of the integrator, up to exponentially long times [4]. Sometimes (as a function of time step and initial condition) quasi-periodic and bounded energy errors are observed that seemingly last forever. There are various implementations of symplectic integrators in the fields of molecular dynamics [5], celestial mechanics [6],

non-equilibrium statistical mechanics [7, 8], beam physics, etc.

However, it is not clear geometrically what is the exact meaning of symplecticity. This is even more true for symplectic tracking with maps, as applied in the case of beam physics. On the one hand, the element by element symplectic integration usually is implemented in the thin lens (kick) approximation. While it is exactly symplectic, it is also slow, only accurate to first or second order in the time step, and not applicable in the case of general, nonseparable Hamiltonians, i.e. Hamiltonians that can be written as a sum of functions, which have flows that can be computed exactly. On the other hand, to assess the long-term stability of particles in a periodic accelerator structure in a reasonable amount of time, it is customary to compute an approximation of the one turn map, and then track with the map. Unfortunately, by approximating the originally symplectic map, for example by truncation of the Taylor series of the true map, its symplecticity is lost. Tracking large numbers of turns with truncated Taylor maps thus can potentially give inaccurate results. The best we can hope is that by recovering the exact symplecticity "artificially" from the truncated map, the long term tracking with the map will restore the properties of the original system, and will speed up considerably the estimation of the dynamic aperture. As we shall see, in the Differential Algebraic framework [9, 10] this can be done to very high orders.

Therefore, tracking symplectically with high order maps is symplectic integration taken in its usual sense, but because of the use of integrators of very high order [10], it is usually more accurate in the time step and faster. It is also true that the speed is achieved at the expense of increasing the time step; here the time step is in fact one turn around the accelerator (using the arclength along the reference orbit as the independent variable). Sometimes it might be necessary to balance the length of the part of the system represented by a map with the required accuracy. This

can be done by splitting the whole system into several pieces and representing each lump by a transfer map. Also, the map approach allows the important advantage of incorporating effects in the map that are otherwise very time consuming to compute, as, for example, fringe fields [11, 12, 13].

The main step in tracking symplectically with maps is the symplectification of the truncated, order n symplectic, Taylor maps. Several methods have been developed to achieve the symplectification of maps. There are two main streams: one is based on factorization methods, and consist of Cremona symplectification [14], integrable polynomial factorization [15] and monomial factorization [16]; the other one is based on mixed variable generating function methods [17]. All methods provide valid symplectification schemes. However, the symplectified map depends on the specific method used. It was realized that the particular schemes applied often make considerable differences in the final results. This realization triggered the studies of optimal symplectification. For details concerning optimal Cremona symplectification see [14]. In part I of this dissertation we extend the method of generating function symplectification to an exceedingly large class of generators, study the optimality of generating function symplectification expressed in terms of Hofer's metric [18], and solve it by choosing the type of generating function that comes closest to satisfy the optimality condition in general.

The first mention of the possibility of symplectic integration using generating functions dates back to 1956 [19]. Later it was rediscovered by others; see for example [20, 21]. Specifically, in beam physics, symplectic tracking with maps based on generating functions was proposed in [17, 16, 22]. In particular, it has been shown that in the Differential Algebraic framework it is straightforward to compute the order $n+1$ truncation of the generating function from the order n truncation of the one turn map to any order n [17, 10]. Symplectic tracking to order three was first implemented in

the code MARYLIE [23], and to arbitrary order it was first implemented in COSY INFINITY [24]. The possibility to estimate the SSC dynamic aperture with generating functions-based symplectic tracking with one turn maps has been considered in [25]. Another approach to generating functions and maps is based on fitted maps [26].

All these methods use only the conventional $F_1, ..., F_4$ (in Goldstein's notation) types of generating functions [27]. Recently, a symplectic integration scheme has been developed that is based on generating functions, and it has been shown that actually there are infinitely many generating functions associated to a symplectic map [28, 29]. The methods of [28] are based on [30], which is basically a linear algebra problem, and its local generalizations to the nonlinear case. On the other hand, the rigorous mathematical foundation on manifolds of the classical global generating function theory has been laid in the 1970s [31, 32, 33, 34]. We combine the two, and give the general theory of generating functions of canonical transformations, with an eye on usefulness for computation in the Differential Algebraic framework [10] used in COSY INFINITY [24].

To be able to say which generating function is the best one first requires a characterization of the various types. This provides the motivation to develop the general theory of generating functions in chapter 2. First, it is shown that locally there is an isomorphism between symplectic and gradient maps, and this leads to infinitely many generating function types for every symplectic map. Then, the global theory is developed, which is based on transformation of the problem into a problem in symplectic geometry. This approach gives insight into various problems of locality versus globality of the generating functions, and emphasizes the generality of the approach. We mention that following Weinstein's work, the geometric approach to generating functions in the physics literature appeared at various degrees of completeness, as, for example, in [35, 36, 37, 38].

Chapter 3 contains results related to the symplectification of truncated symplectic Taylor maps. Specifically, it is shown that the general theory of generating functions can be used to produce exactly symplectic maps. In fact, infinitely many can be produced, each map being associated to a different generator type. It is shown that not every generator type produces distinct symplectified maps, and a certain subset of generators can be reduced to equivalence classes. Two types of generating functions are said to be equivalent if they produce exactly the same symplectified map, when applied to a given order n symplectic Taylor map. In this endeavor some transformation properties of the generating functions are derived, which are interesting also in their own right. Also, there is a brief presentation of how the conventional generators fit into this framework.

Sometimes it is preferred to factor out the linear part of the map to be symplectified, and apply the symplectification procedure to the nonlinear part only (in fact this part will have identity as linear part). It is proved that there is nothing to be gained by this approach if the appropriate types of generating functions are utilized. The implications of linear symplectic variable changes for the outcome of the symplectification process are also analyzed. The last section of the chapter gives some details about the implementation of the method in the code COSY INFINITY.

Chapter 4 is devoted to a variety of examples. The tracking pictures obtained for standard test cases and accelerator lattices of practical interest are studied, and several generator symplectifications are compared. For a few cases, the local corrections introduced by the symplectification process to the Taylor maps are shown to exhibit unusual patterns.

The examples of chapter 4 point out the necessity for optimal symplectification studies. In chapter 5 the problem is approached from the perspective of symplectic

topology in general, and Hofer's metric for compactly supported Hamiltonian symplectic maps in particular. In a very general way, the chapter gives a precise meaning to "the right way" to symplectify, and obtains a partial answer by singling out the generator type that is closest to satisfy the optimality condition in general. As by-products, a generalized Hamilton-Jacobi equation is found, which describes the time evolution of any generator type, and an interesting duality is developed between fixed points of symplectic maps and critical points of generating functions.

Chapter 2

General Theory of Generating Functions of Canonical Transformations

In the classical mechanics literature, traditionally only the 4 Goldstein type of generating functions are well known. However, it is easy to show that, for example, the identity transformation cannot be generated by the type 1 and 4 generating functions. On the other hand, this set can be easily extended to 2^n, or 4^n, generating functions. It can be showed that for any symplectic map, at least one generating function from this set exists locally [10]. The common factor for this set is that they all depend on mixed coordinates, more specifically on n initial coordinates and momenta, and n final coordinates and momenta.

The first sign that in fact there are more generating functions dates back to Poincaré, who used a different type of generating function, which not only is a mixed variable function in the sense discussed above, but also mixes (linearly) initial and final conditions in all the $2n$ variables [39]. Later this generating function reappeared in [40] and [28], where also a unifying approach to the theory of generating functions has been presented, from which it resulted that there are infinitely many generating functions.

However, while the approach of [28] gives important computational insight, the general mathematical foundation of the theory is contained in the series of papers [31, 32, 33, 40]. On the other hand, the general theory lacks exactly the computational aspect. Our purpose is to give a rigorous account of the mathematical basis, and to cast the theory into a convenient computational tool within the framework of Differential Algebraic methods. We start with the local theory, since it already contains the main ideas, and it is easier to understand the underlying principles. The detailed account of the global theory follows in the next section, where light is shed on the somewhat obscure aspects of the local theory.

2.1 The Local Theory

The theory is developed in Euclidean space, and all definitions and statements refer to this case. It will be generalized to arbitrary symplectic manifolds in the next section. First we introduce a few notations. Every map is regarded as a column vector. Let

$$\alpha = \begin{pmatrix} \alpha_1 \\ \alpha_2 \end{pmatrix} \tag{2.1}$$

be a diffeomorphism of a subset of $\mathbb{R}^{4n}$ onto its image, and let

$$\alpha^{-1} = \begin{pmatrix} \alpha^1 \\ \alpha^2 \end{pmatrix} \tag{2.2}$$

be its inverse. Notice that α_i and α^i, $i = 1, 2$, are the first $2n$ and second $2n$ components of α and α^{-1} respectively. This entails that $\alpha_i : U \subset \mathbb{R}^{4n} \to V_i \subset \mathbb{R}^{2n}$, and analogously for α^i. It is worthwhile to note that there is a geometric significance to the use of $\mathbb{R}^{4n}$. Both symplectic maps and functions under certain conditions can be given a geometric interpretation in the form of Lagrangian submanifolds of $\mathbb{R}^{4n}$. (Lagrangian submanifolds are $2n$ dimensional submanifolds of $4n$ dimensional symplectic

manifolds on which the symplectic forms vanish identically.) Let

$$\mathrm{Jac}\,(\alpha) = \begin{pmatrix} A & B \\ C & D \end{pmatrix} \tag{2.3}$$

be the $4n \times 4n$ Jacobian of α, split into $2n \times 2n$ blocks. Let

$$\tilde{J}_{4n} = \begin{pmatrix} J_{2n} & 0_{2n} \\ 0_{2n} & -J_{2n} \end{pmatrix}, \tag{2.4}$$

where

$$J_{2n} = \begin{pmatrix} 0_n & I_n \\ -I_n & 0_n \end{pmatrix}, \tag{2.5}$$

and I_n is the unit matrix of appropriate dimension. A map α is called conformal symplectic if

$$(\mathrm{Jac}\,(\alpha))^T J_{4n}\,\mathrm{Jac}\,(\alpha) = \mu \tilde{J}_{4n}, \tag{2.6}$$

where μ is a non-zero real constant [41]. Also, we denote by $\mathcal{I}$ the identity map of appropriate dimension. A map $\mathcal{M}$ is called symplectic if its Jacobian M satisfies the symplectic condition [42], that is

$$M^T J M = J. \tag{2.7}$$

Also, (2.7) can be written is several different forms [10]. We always assume that the symplectic maps are origin preserving. We call a map a gradient map if it has symmetric Jacobian N. It is well known that, at least over simply connected domains, gradient maps can be written as the gradient of a function (hence the name) [10], that is

$$N = \mathrm{Jac}\,(\nabla F)^T. \tag{2.8}$$

(∇F is regarded as a row vector [43].) The function F is called the potential of the map.

The best way to formulate the main result of this section is a theorem.

Theorem 1 *Let $\mathcal{M}$ be a symplectic map. Then, for every point z there is a neighborhood of z such that $\mathcal{M}$ can be represented by functions F via the relation*

$$(\nabla F)^T = \left(\alpha_1 \circ \begin{pmatrix} \mathcal{M} \\ \mathcal{I} \end{pmatrix}\right) \circ \left(\alpha_2 \circ \begin{pmatrix} \mathcal{M} \\ \mathcal{I} \end{pmatrix}\right)^{-1}, \tag{2.9}$$

where α is any conformal symplectic map such that

$$\det\left(C\left(\mathcal{M}\left(z\right), z\right) \cdot Mz + D\left(\mathcal{M}\left(z\right), z\right)\right) \neq 0. \tag{2.10}$$

Conversely, let F be a twice continuously differentiable function with gradient $\mathcal{N}$, where $\mathcal{N} = \mathrm{Jac}\left(\nabla F\right)^T$. Then, the map $\mathcal{M}$ defined by

$$M = \left(NC - A\right)^{-1}\left(B - ND\right) \tag{2.11}$$

is symplectic.

Definition 1 *The function F is called the generating function of type α of $\mathcal{M}$, and denoted by $F_{\alpha,\mathcal{M}}$.*

The theorem says that, once the generator type is fixed, locally there is a one-to-one correspondence between symplectic maps and scalar functions, which are unique up to an additive constant. The constant can be normalized to zero without loss of generality. Due to the fact that there exist uncountably many maps of the form (2.6), we can conclude that for each symplectic map one can construct infinitely many generating function types.

A question that naturally arises is about the locality of the description of symplectic maps by generating functions, i.e. what is the size of the region where the generating functions are defined? A rigorous lower bound can be computed by combining the theory of this section with high-order Taylor model based verified methods. The results, using several examples of practical interest, suggest that at least certain

carefully chosen generating function types' domain of definition enclose the region of interest in simulations (for example the dynamic aperture) [44].

Proof. We notice that, by the implicit function theorem, the proof can be reduced to the linear case. In particular, the linearization of (2.9) at some point reads

$$N = (AM + B)(CM + D)^{-1}. \tag{2.12}$$

Here all the entries in the equation are matrices. Therefore, by the implicit function theorem, if (2.9) is well defined at some point, i.e. $\det(CM + D) \neq 0$, then it also holds in a neighborhood of that point. Therefore, the proof is complete if we prove the following lemma. ■

Lemma 2 *Let $A, B, C, D \in \mathbb{R}^{2n\times 2n}$, and*

$$\alpha = \begin{pmatrix} A & B \\ C & D \end{pmatrix}. \tag{2.13}$$

Let $M \in \mathbb{R}^{2n\times 2n}$ be given. If A, B, C, D is chosen such that

$$\det(CM + D) \neq 0, \tag{2.14}$$

and if $N \in \mathbb{R}^{2n\times 2n}$ is defined as

$$N = (AM + B)(CM + D)^{-1}, \tag{2.15}$$

which is equivalent to

$$M = (NC - A)^{-1}(B - ND), \tag{2.16}$$

then any two of the following statements imply the third one:

1) *M is symplectic, i.e. $M^T J M = J$,*

2) *N is symmetric, i.e. $N^T = N$,*

3) *α is conformal symplectic, i.e. $\alpha^T J_{4n} \alpha = \mu \tilde{J}_{4n}$.*

The proof is split into three part. First, it is shown that 1) and 2) implies 3), then that 2) and 3) implies 1), and finally that 1) and 3) implies 2). In the proof of the lemma we need the following proposition.

Proposition 3 *Let* $\det(CM+D) \neq 0$ *and* N *defined as in (2.15). Then*

$$\det(NC - A) \neq 0. \tag{2.17}$$

Proof. Taking determinants on both sides of (2.6) if follows that $\det(\alpha) \neq 0$. Thus, denote its inverse by

$$\alpha^{-1} = \begin{pmatrix} \bar{A} & \bar{B} \\ \bar{C} & \bar{D} \end{pmatrix}. \tag{2.18}$$

Then, if we expand the relations $\alpha \cdot \alpha^{-1} = \alpha^{-1} \cdot \alpha = I$, we obtain

$$A\bar{A} + B\bar{C} = \bar{A}A + \bar{B}C = I,\ C\bar{B} + D\bar{D} = \bar{C}B + \bar{D}D = I, \tag{2.19}$$

$$A\bar{B} + B\bar{D} = \bar{A}B + \bar{B}D = 0,\ C\bar{A} + D\bar{C} = \bar{C}A + \bar{D}C = 0. \tag{2.20}$$

First we compute

$$\begin{aligned} \left(\bar{C}N + \bar{D}\right)(CM+D) &= \left[\bar{C}(AM+B)(CM+D)^{-1} + \bar{D}\right](CM+D) && (2.21)\\ &= \bar{C}(AM+B) + \bar{D}(CM+D) && (2.22)\\ &= \left(\bar{C}A + \bar{D}C\right)M + \left(\bar{C}B + \bar{D}D\right) && (2.23)\\ &= I. && (2.24) \end{aligned}$$

Taking determinants on both sides we obtain that

$$\det(CM+D) \neq 0 \Rightarrow \det\left(\bar{C}N + \bar{D}\right) \neq 0. \tag{2.25}$$

Next consider the identity

$$\begin{pmatrix} I & 0 \\ \bar{C} & I \end{pmatrix}\begin{pmatrix} I & -N \\ 0 & \bar{C}N + \bar{D} \end{pmatrix}\begin{pmatrix} A & B \\ C & D \end{pmatrix} = \begin{pmatrix} A - NC & B - ND \\ 0 & I \end{pmatrix} \tag{2.26}$$

Taking determinants on both sides yet again, we obtain that

$$\det\left(\bar{C}N+\bar{D}\right)\cdot\det\left(\alpha\right)=\det\left(A-NC\right). \tag{2.27}$$

But $\det\left(\alpha\right)\neq 0$, hence

$$\det\left(\bar{C}N+\bar{D}\right)\neq 0\Rightarrow\det\left(A-NC\right)\neq 0. \tag{2.28}$$

Combining (2.25) and (2.28) we arrive at

$$\det\left(CM+D\right)\neq 0\Rightarrow\det\left(NC-A\right)\neq 0, \tag{2.29}$$

and the proposition is proved. ■

We can proceed to prove the lemma.

Proof. The first step is to prove that $1)+2)\Rightarrow 3)$. We rewrite (2.12) to give

$$N\left(CM+D\right)=\left(AM+B\right). \tag{2.30}$$

Knowing that N is symmetric, transposition gives

$$\left(M^TC^T+D^T\right)N=\left(M^TA^T+B^T\right). \tag{2.31}$$

Combining (2.30) and (2.31) results that

$$\begin{aligned}\left(M^TC^T+D^T\right)\left(AM+B\right)\left(CM+D\right)^{-1} &= \left(M^TA^T+B^T\right) \qquad (2.32)\\ \left(M^TC^T+D^T\right)\left(AM+B\right) &= \left(M^TA^T+B^T\right)\left(CM+D\right).\end{aligned}$$

Therefore we obtain that

$$M^T\left(C^TA-A^TC\right)M+\left(D^TB-B^TD\right)+ \tag{2.33}$$

$$M^T\left(C^TB-A^TD\right)+\left(D^TA-B^TC\right)M=0. \tag{2.34}$$

The only way for this to hold for any symplectic M is by requiring that

$$\begin{aligned}M^T\left(C^TA-A^TC\right)M+\left(D^TB-B^TD\right) &= 0, \qquad (2.35)\\ M^T\left(C^TB-A^TD\right) &= 0, \qquad (2.36)\\ \left(D^TA-B^TC\right)M &= 0, \qquad (2.37)\end{aligned}$$

for any symplectic M. This is true because the symplectic condition is a condition that involves quadratic relations among the entries of M, and these relations give as their results constants. From the first equation we conclude that it holds if and only if

$$C^T A - A^T C = \mu J, \tag{2.38}$$

$$D^T B - B^T D = -\mu J, \tag{2.39}$$

for any real number μ different from zero, and the second and third equations hold simultaneously if and only if

$$D^T A - B^T C = 0. \tag{2.40}$$

These relations can be cast into a convenient matrix form, namely

$$\begin{pmatrix} A & B \\ C & D \end{pmatrix}^T \begin{pmatrix} 0 & I \\ -I & 0 \end{pmatrix} \begin{pmatrix} A & B \\ C & D \end{pmatrix} = \mu \begin{pmatrix} J & 0 \\ 0 & -J \end{pmatrix}, \tag{2.41}$$

where $\mu \in \mathbb{R}^{\times}$. Hence, we can conclude that for any symmetric N and symplectic M there can be found nonsingular matrices A, B, C, and D such that (2.6) holds. Therefore, α is a conformal symplectic map.

The second step is to show that $2) + 3) \Rightarrow 1)$. From (2.15) we can deduce that

$$N^T = (CM + D)^{-T} (AM + B)^T. \tag{2.42}$$

Using the assumption that $N^T = N$, we get that

$$(CM + D)^{-T} (AM + B)^T = (AM + B) (CM + D)^{-1}. \tag{2.43}$$

To remove the inverses, the above equation can be rewritten as

$$\left(M^T C^T + D^T\right) (AM + B) = \left(M^T A^T + B^T\right) (CM + D). \tag{2.44}$$

Performing the operations and regrouping of terms gives

$$M^T \left(C^T A - A^T C\right) M + M^T \left(C^T B - A^T D\right) + \tag{2.45}$$

$$\left(D^T A - B^t C\right) M + \left(D^T B - B^T D\right) = 0. \tag{2.46}$$

From the expansion of (2.6) it follows that

$$A^T C - C^T A = \mu J,\ B^T D - D^T B = -\mu J, \tag{2.47}$$

$$A^T C - C^T A = 0,\ B^T C - D^T C = 0. \tag{2.48}$$

This entails that (2.45) reduces to

$$M^T J M = J, \tag{2.49}$$

showing that M is symplectic.

To complete the proof now we need to show that $1) + 3) \Rightarrow 2)$. First we notice that, according to the above lemma, (2.15) always can be solved for M to give

$$M = (NC - A)^{-1} (B - ND). \tag{2.50}$$

Therefore,

$$M^T = (B - ND)^T (NC - A)^{-T}, \tag{2.51}$$

$$M^{-1} = (B - ND)^{-1} (NC - A). \tag{2.52}$$

Also, from the symplectic condition $M^T J M = J$ it follows that $J M^T = M^{-1} J$. Inserting (2.51) and (2.52) in this equation, gives

$$J (B - ND)^T (NC - A)^{-T} = (B - ND)^{-1} (NC - A) J, \tag{2.53}$$

which can be expressed as

$$(B - ND) J \left(B^T - D^T N^T\right) = (NC - A) J \left(C^T N^T - A^T\right). \tag{2.54}$$

Rearrangement of terms gives

$$N\left(CJC^T - DJD^T\right)N^T - N\left(CJA^T - DJB^T\right) - \tag{2.55}$$

$$\left(AJC^T - BJD^T\right)N^T + \left(AJA^T - BJB^T\right) = 0. \tag{2.56}$$

Next, we need to manipulate (2.6), which is equivalent to $\alpha^T J = \mu\alpha^{-1}\tilde{J}$. Transposition gives $J\alpha = \mu\alpha^{-T}\tilde{J}$, where we used that $J^T = -J$ and $\tilde{J}^T = -\tilde{J}$. Also, from $J^{-1} = -J$ and $\tilde{J}^{-1} = -\tilde{J}$ it finally follows that

$$\alpha\tilde{J}\alpha^T = \mu J. \tag{2.57}$$

Expanding this relation yields

$$AJA^T - BJB^T = 0,\ CJC^T - DJD^T = 0, \tag{2.58}$$

$$AJC^T - BJD^T = \mu I,\ CJA^T - DJB^T = -\mu I. \tag{2.59}$$

As the last step, inserting these in (2.55) results in

$$N^T = N. \tag{2.60}$$

This completes the proof. ■

Theorem 1 has a simple, intuitive interpretation. It provides a way to construct infinitely many generating function types for any given symplectic map. The various types are parametrized by the group of conformal symplectic maps. For the existence of a certain type of generator, $\det(CM + D) \neq 0$ must hold. Conversely, given any function and a conformal symplectic map, theorem 1 provides a method for generation of symplectic maps.

2.2 The Global Theory

The local theory is sufficient in most situations, as the cases of interest to us are weakly nonlinear Taylor maps around fixed points. Therefore, the treatment of practically

relevant systems is inherently local. However, there are important aspects that the local theory does not answer. For example, how can the theory be extended to symplectic manifolds? Moreover, the definition of N in (2.15) seems to be taken from thin air. Is there a deeper reason behind this definition? Or, is there a more general definition that provides even more generator types? Finally, what can be said about the domain of definition of the generators? Can a global generating function be defined for any symplectic map? In this section we try to answer these questions.

The local theory shows that around any point local generators can be found. The question is whether the various local generators can be glued smoothly to form a global generator. Apparently, this cannot be done in general by generators of type linear α. However, the existence of nonlinear conformal symplectic maps is not a priori obvious. Moreover, even if a global generator exists for a given symplectic map, does the same type of generator exist globally for other symplectic maps? The solution of these questions requires the "geometrization" of the problem, that is, reformulation of the problem into a problem in symplectic geometry. We begin with a brief introduction to symplectic geometry, the language used for the mathematical basis of the theory. More details can be found in [45, 46].

2.2.1 Fundamentals of Symplectic Geometry

Symplectic geometry is the natural mathematical language of classical mechanics, specifically Hamiltonian dynamics, as any variational principle can be given a symplectic interpretation. To begin, some fundamental concepts are introduced. Let P be a smooth manifold, and ω a differential 2-form defined on it. If ω is closed and non-degenerate, it is called a symplectic form, and the pair (P, ω) is called a symplectic manifold. A form is called closed if its exterior differential vanishes, $d\omega = 0$. Closedness is a geometric constraint, which is equivalent to the Jacobi identity. On the other

hand, non-degeneracy is an algebraic condition. It means that at each point $p \in P$ the skew-symmetric bilinear form $\omega_p : T_pP \times T_pP \to \mathbb{R}$ which acts on tangent vectors, is non-degenerate. In terms of the associated linear map $\tilde{\omega}_p(v)(u) = \omega_p(v,u)$, we have that, if $\tilde{\omega}_p(v)(u) = 0$ for each $v \in T_pP$, then $u = 0$. Hence $\tilde{\omega}_p : T_pP \to T_p^*P$ is an isomorphism. This means that, relative to some local coordinate system around each point, the matrix of $\tilde{\omega}$, and equivalently the matrix of ω has nonzero determinant. This in turn implies that any symplectic manifold is necessarily even dimensional, due to the fact that the determinant of any odd dimensional skew-symmetric matrix vanishes.

A fundamental category of symplectic manifolds are the cotangent bundles of configuration manifolds, which are the phase spaces of dynamical systems. These manifolds carry a symplectic structure that is a generalization of the canonical symplectic structure of $\mathbb{R}^{2n}$. On the Euclidean space itself, by identifying $\mathbb{R}^{2n}$ with $T^*\mathbb{R}^n$, we have a special coordinate system in which the symplectic form takes the simple form $\omega_0 = d\vec{q} \wedge d\vec{p}$. The coordinates $(\vec{q}, \vec{p})$ are called canonical. This coordinate system is the symplectic counterpart of the orthonormal coordinate system of Euclidean geometry. The matrix of ω_0 is denoted by J and has the form

$$J = \begin{pmatrix} 0 & I \\ -I & 0 \end{pmatrix}, \tag{2.61}$$

where each entry represents a $n \times n$ block matrix, I being the appropriate unit matrix. We also note that the standard symplectic form can be defined in a coordinate-free way by $\omega_0 = -d\lambda$, where λ is called the canonical one-form, and takes the coordinate representation $\lambda = \vec{p} \cdot d\vec{q}$. Darboux's theorem states that on any symplectic manifold such a coordinate system can be found in a neighborhood of any point, hence any symplectic manifold is locally equivalent (symplectomorphic) to the Euclidean space with its standard symplectic structure ω_0. We call a symplectic form translationally

invariant if its matrix has the same form at any point on the manifold.

Now we turn to symplectic transformations between symplectic manifolds. We will use hereafter interchangeably the notions of symplectic transformations, symplectic maps, canonical transformations, symplectic diffeomorphisms and symplectomorphisms. By definition, a diffeomorphism $\mathcal{M} : P_1 \to P_2$ between two symplectic manifolds (P_1, ω_1) and (P_2, ω_2) of the same dimension is called a symplectomorphism if it preserves the symplectic forms, that is

$$\mathcal{M}^* \omega_2 = \omega_1, \tag{2.62}$$

where * denotes the pull-back, which is defined as

$$\left(\mathcal{M}^* \omega\right)_z (v_1, v_2) = \omega_{\mathcal{M}(z)} \left(T_z \mathcal{M} \cdot v_1, T_z \mathcal{M} \cdot v_2\right), \tag{2.63}$$

where $z \in P_1$ and $v_1, v_2 \in T_m P_1$. In this case P_1 and P_2 are said to be symplectomorphic. In canonical coordinates this definition takes the following form for a symplectic map of the Euclidean space with its standard symplectic structure ω_0

$$\left(\mathrm{Jac}(\mathcal{M})\right)^T J \left(\mathrm{Jac}(\mathcal{M})\right) = J. \tag{2.64}$$

Here Jac denotes the Jacobian and ^{T} the matrix transpose. The above definition can be extended to include conformal symplectic maps by the following relation

$$\mathcal{M}^* \omega_2 = r\left(\mathcal{M}\right) \omega_1, \tag{2.65}$$

with $r\left(\mathcal{M}\right) \in \mathbb{R}^{\times}$. To see the significance of r, take a scaling map defined by $\phi^* \omega_1 = \mu^2 \omega_1$, $\mu \in \mathbb{R}^{\times}$, and apply it to both sides of (2.65). By choosing $\mu = 1/\sqrt{|r|}$, we obtain $\left(\mathcal{M} \circ \phi\right)^* \omega_2 = \mathrm{sgn}\left(r\left(\mathcal{M}\right)\right) \omega_1$. Hence, if $r > 0$, then $\mathcal{M} \circ \phi$ is symplectic. If $r < 0$, then $\mathcal{M} \circ \phi$ is called antisymplectic. Essentially, it means that $\mathcal{M} \circ \phi$ is orientation reversing. Actually, this is strictly true only if n is odd, otherwise, for n even, the Cartesian product $\left(\mathcal{M} \circ \phi\right) \times \mathcal{I}$ is orientation reversing; $\mathcal{I}$ being the identity map. This

follows from the definition of the symplectic map. Specifically, any symplectic map of a manifold into itself preserves the symplectic form, so it also preserves the volume form $\omega^n = \omega \wedge ... \wedge \omega$ (n times). This is a never vanishing $2n$-form on a $2n$ dimensional manifold, so the vector space it forms is 1 dimensional. Direct calculation shows that it integrates to a constant times the Euclidean volume. It follows that any symplectic manifold is oriented by the volume form, symplectic maps preserve orientation, and if global coordinates are available the determinant of the Jacobian of any symplectic map is equal to 1 at any point.

Now we turn our attention to Hamiltonian systems, as the single particle dynamics in accelerators of interest to us can be described to a very good level of approximation by a Hamiltonian dynamical system. First we establish a few notations. Obviously, the symplectic maps of a symplectic manifold form an infinite dimensional Lie group under composition, denoted by $\mathrm{Symp}(P, \omega) \equiv \mathrm{Symp}(P)$, if it is clear which symplectic form is considered. Also its Lie algebra of symplectic vector fields will be denoted by $\mathcal{X}(P)$. In the view of non-degeneracy of symplectic forms, there is a one-to-one correspondence between vector fields and 1-forms via

$$\mathcal{X}(P) \to \Omega^1(P) : X \to \imath(X)\,\omega, \tag{2.66}$$

where we used $\imath$ for the interior product. A vector field X is called symplectic if $\imath(X)\,\omega$ is closed, that is $d(\imath(X)\,\omega) = 0$. By the Poincaré lemma, on connected manifolds every closed 1-form is locally exact, so $\imath(X)\,\omega$ can be written locally as the differential of a function $\imath(X)\,\omega = dH$. In this case the vector field is called locally Hamiltonian. If dH exists globally (for example if the manifold is simply connected), X is called Hamiltonian, and H the Hamiltonian function. Conversely, for any function $H : P \to \mathbb{R}$, the vector field $X_H : P \to TP$ determined by the identity $\imath(X_H)\,\omega = dH$ is called the Hamiltonian vector field associated to the Hamiltonian function H. A

Hamiltonian dynamical system is the triple (P, ω, H). Hamiltonian vector fields form a Lie subalgebra of the Lie algebra of symplectic vector fields. The map $X_H \to H$ is a homomorphism. However, if we restrict ourselves to compactly supported Hamiltonians, then the map becomes an isomorphism, and it can be viewed as a normalization condition, by specifying the arbitrary constant in H. With this normalization different Hamiltonians generate different flows. This will be important later in the definition of the Hofer metric on the space of compactly supported Hamiltonian symplectomorphisms. Specifically, compact support means that the Hamiltonian and hence the associated vector field vanishes outside a compact subset. Recall that vanishing Hamiltonians generate the identity map. Hence, the support of a symplectic map is defined as the closure of the set where it is different from identity.

To define Hamiltonian symplectomorphisms we need first the notion of isotopy. The time-dependent vector field X_{H_t}, associated to the time-dependent Hamiltonian H_t at every t, generates a smooth 1-parameter group of diffeomorphisms $\phi^t_{H_t}$ satisfying

$$\frac{d}{dt}\phi^t_{H_t} = X_{H_t} \circ \phi^t_{H_t} \quad , \quad \phi^0_{H_t} = \mathcal{I}. \tag{2.67}$$

$\phi^t_{H_t}$ is called the Hamiltonian flow associated to H_t, or the Hamiltonian isotopy. A symplectomorphism $\phi \in \mathrm{Symp}\,(P)$ is called Hamiltonian if there exists a Hamiltonian isotopy $\phi_t \in \mathrm{Symp}\,(P)$ from $\phi_0 = \mathcal{I}$ to $\phi_1 = \phi$. We denote the space of Hamiltonian symplectic maps by $\mathrm{Ham}\,(P, \omega)$, or simply $\mathrm{Ham}\,(P)$. It turns out that $\mathrm{Ham}\,(P)$ is a normal subgroup of $\mathrm{Symp}\,(P)$, and its Lie algebra is the Lie algebra of Hamiltonian vector fields. On simply connected manifolds $\mathrm{Ham}\,(P)$ is the identity component of $\mathrm{Symp}\,(P)$, that is any symplectic isotopy is Hamiltonian [41]. The group of Hamiltonian symplectomorphisms is path connected. Also, any path in the space of Hamiltonian maps is Hamiltonian. If a symplectic map is generated by compactly supported Hamiltonians, the symplectic map is also compactly supported, which means that it

is the identity map outside a compact subset.

To prove that the flows of Hamiltonian systems are symplectic we need the following two formulae [47]: the Lie derivative formula

$$\frac{d}{dt}\phi_t^*\omega = \phi_t^*\mathcal{L}_{X_t}\omega, \tag{2.68}$$

and Cartan's magic formula

$$\mathcal{L}_{X_t}\omega = \imath\left(X_t\right)d\omega + d\left(\imath\left(X_t\right)\omega\right). \tag{2.69}$$

Now it is straightforward to see that if $d\omega = 0$ and $\left(\imath\left(X_t\right)\omega\right) = dH_t$, then $\frac{d}{dt}\phi_t^*\omega = 0$, that is constant in time and equal to its value at $t = 0$. Hence we obtain $\phi_t^*\omega = \omega$, for any t. The argument works also backwards, implying that if the flow of a dynamical system is symplectic then it is generated by Hamiltonian dynamical systems.

2.2.2 Primitive Function vs. Generating Function

In this subsection it is shown that the main ideas of mixed variable generating functions are already built in in the symplectic condition. Consider symplectic transformations, $\mathcal{M}$, of a symplectic manifold (T^*X, ω). Let us assume that the manifold is simply connected, or in other words is an exact symplectic manifold. Then, every closed form is also exact. We can write $\omega = -d\lambda$. The symplectic condition takes the form

$$d\left(\lambda - \mathcal{M}^*\lambda\right) = 0, \tag{2.70}$$

from which follows the existence of a function F, such that

$$\lambda - \mathcal{M}^*\lambda = dF. \tag{2.71}$$

The function F is called the primitive function of $\mathcal{M}$. However, there is no one-to-one correspondence between symplectic maps and primitive functions. Actually, the

symplectic map is determined up to a left action (composition with $\mathcal{M}$ from the left) of an actionmorphism, i.e. a symplectic map that preserves the 1-form λ. This can be easily seen by replacing $\mathcal{M}$ with another symplectic map, $\mathcal{N} \circ \mathcal{M}$, where $\mathcal{N}$ an actionmorphism. Therefore, we obtain

$$\begin{aligned} \lambda - (\mathcal{N} \circ \mathcal{M})^* \lambda &= \lambda - \mathcal{M}^* (\mathcal{N}^* \lambda) && (2.72) \\ &= \lambda - \mathcal{M}^* \lambda && (2.73) \\ &= dF. && (2.74) \end{aligned}$$

Hence, $\mathcal{M}$ and $\mathcal{N} \circ \mathcal{M}$ have the same primitive function. All the $\mathcal{N}$s with this property arise as lifts of diffeomorphisms on the base manifold [47]. Therefore, the primitive function determines the symplectic maps up to cotangent lifts. This is a manifestation of the coordinate independence of the symplectic condition, specifically λ. It also implies that for one-to-one correspondence between $\mathcal{M}$ and F, F cannot be defined on the phase space.

If we think of $(\vec{q}, \vec{p})$ as independent canonical coordinates, and $\mathcal{M}(\vec{q}, \vec{p}) = \left(\vec{Q}, \vec{P}\right)$, it follows from (2.71) that

$$\vec{p} \cdot d\vec{q} - \vec{P} \cdot d\vec{Q} = dF(\vec{q}, \vec{p}). \tag{2.75}$$

Now, if the equation $\vec{Q} = \vec{Q}(\vec{q}, \vec{p})$ can be solved for $\vec{p}$ to give a function $F_1\left(\vec{q}, \vec{Q}\right) = F\left(\vec{q}, \vec{p}\left(\vec{q}, \vec{Q}\right)\right)$, with $\left(\vec{q}, \vec{Q}\right)$ as independent variables, we obtain

$$\frac{\partial F_1\left(\vec{q}, \vec{Q}\right)}{\partial \vec{q}} = \vec{p} \quad , \quad \frac{\partial F_1\left(\vec{q}, \vec{Q}\right)}{\partial \vec{Q}} = -\vec{P}, \tag{2.76}$$

and we recognize it as the F_1 (Goldstein type 1) generating function. The symplectic maps with this property are called twist maps.

Now it is apparent that, in order to uniquely determine the symplectic map, a function must employ mixed variables, and this follows from the symplectic condition

itself. The method used in this section could be used to derive other types of generating functions. However, there are many λs such that $\omega = -d\lambda$, as for example $\lambda = -\vec{q} \cdot d\vec{p}$ or $\lambda = \frac{1}{2}(\vec{p} \cdot d\vec{q} - \vec{q} \cdot d\vec{p})$, etc. Moreover, different λs can be chosen on the source and target manifold, and guessing is necessary for the variable changes. Therefore, it is not clear how much freedom is possible for construction of new generating functions, and in general it is not convenient to work in this setting. We choose to work in another setting, which has been introduced by Weinstein.

2.2.3 Symplectic Maps as Lagrangian Submanifolds

Initially, we have symplectic maps of a manifold in one hand, and functions on another manifold on the other hand. The local representative of the symplectic maps are vector functions of an even number of components. Our generating function is a scalar function. A priori, the most general method to connect the two in a one-to-one manner is not clear. In the early '80s Weinstein formulated a "symplectic creed" with the motto "in symplectic geometry everything is a Lagrangian submanifold" (see definition below). Indeed, in symplectic geometry Lagrangian submanifolds are the most important objects beside the symplectic manifolds themselves. These Lagrangian submanifolds provide the most general link between symplectic maps and generating functions. Both symplectic maps, and functions under certain conditions, can be put in one-to-one correspondence with Lagrangian submanifolds of appropriate symplectic manifolds. Once this correspondence is established, instead of working at the level of symplectic maps and functions we can work with Lagrangian submanifolds. At this point, the link we are looking for will be given by the most general type of diffeomorphisms that map these Lagrangian submanifolds into each other, or in other words the diffeomorphisms of identification of the two Lagrangian submanifolds.

We will consider only submanifolds of symplectic manifolds that are properly

embedded and which inherit their topology from the ambient manifold. Also, we will need to work with injections of graphs of maps. It can be proved that the graph of a smooth map $f : P_1 \to P_2$,

$$\Gamma_f = \{(f(p), p) \mid p \in P_1,\ f(p) \in P_2\} \subset P_1 \times P_2 \tag{2.77}$$

is a smooth submanifold of $P_1 \times P_2$ of dimension $\dim(P_1)$ [47]. Moreover, if f is a diffeomorphism, then the projections $\pi_i : \Gamma_f \to P_i$, $i = 1, 2$ are diffeomorphisms [47, 32].

Lagrangian submanifolds are defined in terms of tangent spaces on which the symplectic form vanishes.

Definition 2 *Let (P, ω) be a $2n$ dimensional symplectic manifold and let L be a submanifold of P. L is called a Lagrangian submanifold if, at each $p \in L$, T_pL is a Lagrangian subspace of T_pP, i.e. $\omega_p|_{T_pL} \equiv 0$ and $\dim T_pL = \frac{1}{2}\dim T_pP$. Equivalently, if $i : L \hookrightarrow P$ is the inclusion map, then L is Lagrangian if and only if $i^*\omega = 0$ and $\dim L = \frac{1}{2}\dim P$.*

First we prove that any symplectic map $\mathcal{M} : (P_1, \omega_1) \to (P_2, \omega_2)$, $\mathcal{M}^*\omega_2 = \omega_1$, can be interpreted as a Lagrangian submanifold in the Cartesian product space $P_2 \times P_1$ with the symplectic structure $\mu(\pi_2^*\omega_1 - \pi_1^*\omega_2)$, where $\pi_i : P_2 \times P_1 \to P_i$, $i = 1, 2$, are the canonical projections and $\mu \in \mathbb{R}^\times$. The graph of the symplectic map is the $2n$-dimensional submanifold of $P_2 \times P_1$

$$\Gamma_{\mathcal{M}} = \{(\mathcal{M}(z), z) \mid z \in P_1\}. \tag{2.78}$$

Denote $P = P_2 \times P_1$ and $\omega = \mu(\pi_2^*\omega_1 - \pi_1^*\omega_2)$; then we have the following:

Theorem 4 *$\mathcal{M}$ is a symplectomorphism if and only if $\Gamma_{\mathcal{M}}$ is a Lagrangian submanifold of (P, ω).*

Proof. $\Gamma_{\mathcal{M}}$ is Lagrangian iff relative to the inclusion map $i : \Gamma_{\mathcal{M}} \hookrightarrow P$, $i^*\omega = 0$.

$$\begin{aligned} i^*\omega &= \mu\left(i^*\pi_2^*\omega_1 - i^*\pi_1^*\omega_2\right) && (2.79)\\ &= \mu\left((\pi_2 \circ i)^*\,\omega_1 - (\pi_1 \circ i)^*\,\omega_2\right) && (2.80)\\ &= \mu\left(\mathcal{I}^*\omega_1 - \mathcal{M}^*\omega_2\right) && (2.81)\\ &= \mu\left(\omega_1 - \mathcal{M}^*\omega_2\right) = 0. && (2.82) \end{aligned}$$

Hence, because $\mu \neq 0$, it follows that $\mathcal{M}^*\omega_2 = \omega_1$. ■

Arbitrary Lagrangian submanifolds of (P, ω) are called canonical relations, and can be considered as generalizations of symplectic maps. For practical applications we will be interested in the case $P_1 = P_2 = \mathbb{R}^{2n}$, and $\omega_1 = \omega_2 = \omega_0$ being the standard symplectic structure of $\mathbb{R}^{2n}$. Thus, in this case, any symplectic map $\mathcal{M} : \mathbb{R}^{2n} \to \mathbb{R}^{2n}$ is a Lagrangian submanifold in $\left(\mathbb{R}^{4n}, \mu\tilde{J}\right)$, with symplectic structure ω that has the matrix

$$\mu\tilde{J} = \mu \begin{pmatrix} J_{2n} & 0_{2n} \\ 0_{2n} & -J_{2n} \end{pmatrix}. \tag{2.83}$$

One particular Lagrangian submanifold of this kind that will be useful later is the diagonal, which by definition is the graph of the identity map

$$\Delta = \{(z, z) \mid z \in P_1\}. \tag{2.84}$$

2.2.4 Functions as Lagrangian Submanifolds

Next, we turn our attention to the one-to-one correspondence that can be set up between closed one-forms and Lagrangian submanifolds of cotangent bundles that project diffeomorphically onto the base manifold. Consider a smooth manifold X and a 1-form defined on it. Regard it as a map from X to T^*X. Then the following holds:

Proposition 5 *The canonical one-form $\lambda \in \Omega^1(T^*X)$ is uniquely characterized by the property that*

$$\sigma^*\lambda = \sigma, \tag{2.85}$$

for every one-form $\sigma : X \to T^*X$.

Proof. The σ on the left hand side is considered as a map, and on the right hand side as a one-form. Denote the coordinates of T^*X by $(\vec{q}, \vec{p})$. Then σ regarded as a map in these coordinates can be written as $\sigma = \left(\vec{q}, \vec{f}(\vec{q})\right)$ for some functions f_i. Recall that the canonical one-form has the expression $\lambda = \vec{p} \cdot d\vec{q}$. Thus, using the definition of the pull-back we obtain

$$\begin{aligned} (\sigma^*\lambda)_{\vec{q}} &= \lambda_{\sigma(\vec{q})} \cdot d_{\vec{q}}\sigma & (2.86)\\ &= \begin{pmatrix} \sigma_{\vec{q}} \\ 0 \end{pmatrix}^T \begin{pmatrix} I \\ d_{\vec{q}}\vec{f}(\vec{q}) \end{pmatrix} & (2.87)\\ &= \sigma_{\vec{q}}. & (2.88) \end{aligned}$$

where we used that $\lambda_{\sigma(\vec{q})} = \left(\vec{p} \circ \vec{f}(\vec{q})\right) \cdot d\left(\vec{q} \circ \vec{q}\right) = \vec{f}(\vec{q}) \cdot d\vec{q} = \sigma_{\vec{q}}$, $(\vec{q}, \vec{p})$ being regarded as components of the identity map. ■

Now we demonstrate that when σ is closed, its image $\sigma(X)$ (σ regarded as a map) is a Lagrangian submanifold of T^*X with the standard symplectic structure. Note that the graph Γ_σ of the one-form σ is defined as

$$\Gamma_\sigma = \{(\sigma(w), w) \mid w \in X, \sigma(w) \in T^*_w X\}. \tag{2.89}$$

Its image by the inclusion $i : \Gamma_\sigma \to T^*X$ is Lagrangian. Relative to the projection $\pi : \Gamma_\sigma \to X$, Γ_σ is uniquely determined by the one-form σ if and only if π is a diffeomorphism. This can be seen from the fact that $i = \sigma \circ \pi$. Hence, Γ_σ is Lagrangian iff $i^*\omega_0 = 0$. Thus we get

$$\begin{aligned} (\sigma \circ \pi)^* \omega_0 &= (\sigma \circ \pi)^* (-d\lambda) = -\pi^* (d(\sigma^*\lambda)) & (2.90)\\ &= -\pi^* d\sigma = 0, & (2.91) \end{aligned}$$

where we used $\omega_0 = -d\lambda$, the fact that the pull-back commutes with the exterior differential and the result of the above proposition. Therefore, there is a one-to-one correspondence between Lagrangian submanifolds of $(T^*X, \nu\omega_0)$ of the form (2.89) which project diffeomorphically onto X, and closed one-forms σ on X; here $\nu \in \mathbb{R}^\times$.

In general, there are two ways to ensure that π is a diffeomorphism; if the embedding is C_1 close enough (i.e. close enough in norm to the function values as well as the values of the first derivatives) to the canonical embedding of the zero section into the cotangent bundle, or σ (as the differential of a function) is a diffeomorphism. In the first case the projection mapping will be C_1 close enough to identity to be a diffeomorphism. Indeed, it can be showed [45] that if

$$\| df - \mathcal{I} \| \leq \frac{1}{2}, \tag{2.92}$$

then f is a diffeomorphism. Hence, in this case π can be guaranteed to be a diffeomorphism if σ is C_1 close enough to 0.

For example, the zero section of T^*X, defined by

$$Z = \{(\xi, w) \mid \xi = 0, w \in X, \xi \in T^*_w X\} = \{0\} \times X \tag{2.93}$$

is such a Lagrangian submanifold. This obviously follows from the fact that $\xi = 0$, so $\lambda|_Z = 0$.

Other examples of Lagrangian submanifolds are the fibers of cotangent bundles ("delta functions" at a fixed point in the base manifold), any smooth curve on a 2 dimensional symplectic manifold, invariant tori (KAM tori) of Hamiltonian systems, etc.

The next step is to make the connection between functions on X and the Lagrangian submanifolds of the form (2.89) of T^*X. This is possible if the one-form σ is exact, that is can be written as the differential of a function. The condition when

this is possible can be described by the first Betti number. First we define the de Rham cohomology groups $H^k(X,\mathbb{R})$ by

$$H^k(X,\mathbb{R}) = \frac{\ker\left(d:\Omega^k(X)\to\Omega^{k+1}(X)\right)}{\operatorname{range}\left(d:\Omega^{k-1}(X)\to\Omega^k(X)\right)}. \tag{2.94}$$

The elements of $H^k(X,\mathbb{R})$ form a vector space, and its dimension is called the k-th Betti number

$$b_k = \dim H^k(X,\mathbb{R}), \tag{2.95}$$

which measures the failure of closed forms to be globally exact. On the other hand, if X is connected, by the Poincaré lemma every closed form is locally exact. If $b_1 = 0$, it follows that every closed one-form is globally the differential of a function. In this case the closed one-form σ can be written as dF for a function F that is unique up an additive arbitrary constant. The function $F \in \mathcal{F}(C^\infty(X))$ is called the generating function of the Lagrangian submanifold Γ_σ. Hence, if $b_1 = 0$ we can think of Lagrangian submanifolds Γ_σ as generalized functions on X. We note the well-known fact that for $\mathbb{R}^{2n}$, $b_0 = 1$ and $b_i = 0$ for $i \geq 1$. In the case relevant for our applications, in Euclidean space, every function "generates" a Lagrangian submanifold, and conversely, given a Lagrangian submanifold of the form (2.89), which projects diffeomorphically onto the base manifold, its generating function can be computed by mere integration along an arbitrary path. Also, this function will be called the generating function of the canonical transformation. However, it is still necessary to link the Lagrangian submanifolds (2.78) and (2.89) with suitable diffeomorphisms. We do that in the next subsection.

We mention that the projection π is actually a fiber translation, and Γ_σ intersects each fiber at most in only one point. The fact that Γ_σ might not project diffeomorphically is a hint that some generating functions do not exist for certain symplectic maps. In the case that the projection is not a global diffeomorphism, we certainly

cannot have a global generating function, but still it might be possible to define a local generating function, if the origin has a neighborhood that projects diffeomorphically. While, for special cases of symplectic maps and types of generating functions it might be possible to ensure that the projection is a global diffeomorphism (see for example twist maps and Goldstein type 1 generating functions), in general the projection can be guaranteed to be a global diffeomorphism only if Γ_σ is close enough to the zero section. In this case, the projection map is C^1-close enough to identity to be a diffeomorphism. Hence, every C^2-small enough function is in one-to-one correspondence with such a Lagrangian submanifold. At this point it is not clear how much freedom we have to map Lagrangian submanifolds into each other, but it is a basic requirement of the theory to try to map as close to the zero section as possible. As we will see, this condition also plays a crucial role in the optimal symplectification.

2.2.5 Existence of Infinitely Many Generating Functions

Now we are ready to link symplectic maps with their generating functions. The most natural and general way is to require the Lagrangian submanifold determined by a function to be diffeomorphic to the Lagrangian submanifold determined by the symplectic map, if such a map exists. A well-known theorem [31] states that a neighborhood of any Lagrangian submanifold can be identified by a local symplectomorphism with a neighborhood of the zero section in the cotangent bundle of the submanifold. In general there are two difficulties with this approach. If the manifolds are not simply connected, the generating functions in general cannot be defined globally, and from the computational point of view, it is difficult to deal with the complicated cotangent bundles of the Lagrangian submanifolds determined by the symplectic maps. That is why in general this approach is best suited for symplectic maps close to identity. Also, the theorem states the existence of a local symplectomorphism that identifies

the appropriate Lagrangian submanifolds, but is not a priori clear that this is the most general way to do that. Fortunately, for our purpose it is enough to consider only the case of Euclidean space, for which more results can be obtained.

If we limiting ourselves to simply connected manifolds, and if it happens that P_i, $i = 1, 2$, is diffeomorphic to X, then we have the following commutative diagram:

$$\begin{array}{ccc} \Gamma_{\mathcal{M}} & \xrightarrow{\alpha} & \Gamma_{dF} \\ \pi_i \downarrow & & \downarrow \pi \\ P_i & \xrightarrow{\varphi_i} & X \end{array} \tag{2.96}$$

$\mathcal{M}$ being a symplectomorphism, the projections π_i are diffeomorphisms. Moreover, it is assumed that π is a diffeomorphism, and there exist a diffeomorphism $\varphi_i : P_i \to X$. Thus, in this case there exists a diffeomorphism $\alpha : \Gamma_{\mathcal{M}} \to \Gamma_{dF}$, for any pair of Lagrangian submanifolds of this form, satisfying the above conditions. The following theorem [48, 49] shows that α extends to a local symplectomorphism. It can be thought of as a generalization of the main theorem of [31].

Theorem 6 *Let L_i be two Lagrangian submanifolds of the symplectic manifolds (P_i, ω_i), $i = 1, 2$. Then **any** diffeomorphism $\alpha : L_1 \to L_2$ extends to a conformal symplectomorphism $\beta : U_1 \to U_2$ of some neighborhoods U_i of L_i in P_i, such that $\beta|_{L_1} \equiv \alpha$.*

Consider the following diagram:

$$\begin{array}{ccccccc} & & (P, \omega) & \xrightarrow{\qquad\beta\qquad} & (T^*X, \nu\omega_0) & & \\ & & i_{\mathcal{M}} \uparrow & & \uparrow i_{dF} & & \\ & & \Gamma_{\mathcal{M}} & \xrightarrow{\qquad\alpha\qquad} & \Gamma_{dF} & & \\ \pi_2 \circ i_{\mathcal{M}} \swarrow & & & \searrow \pi_1 \circ i_{\mathcal{M}} & & \pi \swarrow \quad \nwarrow i & \\ z & \xrightarrow{\mathcal{M}} & \mathcal{M}(z) & \qquad w & \xrightarrow{dF} & dF(w) & \end{array}$$

where $z \in P_1$ and $w \in X$ are arbitrary points of the respective manifolds.

We pointed out that the local classification, around a point, of symplectic structures is completely solved by Darboux's theorem. Here we have another concept of locality, namely local around a submanifold, of which one can think of as germs of the symplectic manifolds. Marle's theorem is an example of such a tubular theorem, first proved to exist by Weinstein. It says that Lagrangian submanifolds do not have geometric invariants in order to distinguish each other. In general there are no global theorems similar to the tubular ones. This is true even in the $\mathbb{R}^{2n}$ case, due to the existence of exotic symplectic structures proved by Gromov [50].

The importance of the above theorem consists of two main aspects: it gives the most general way to represent symplectic maps globally by scalar functions, and implies that once a symplectomorphism β exists for a symplectic map $\mathcal{M}$ and a function F, it is automatically valid for all nearby symplectic maps. It follows that the freedom for selecting generating function types is given by the set of conformal symplectic maps of the form $\beta^*\omega_0 = \omega/\nu$. A generating function of type α, which exists for a given $\mathcal{M}$, exists for all nearby symplectic maps. In case the assumptions of the theorem are satisfied, any Lagrangian submanifold $\Gamma_{\mathcal{M}}$ can be identified with any Lagrangian submanifold Γ_{dF}; therefore, in principle the scalar function F can always be chosen in such a way that π is a diffeomorphism, guaranteeing global generating function types for any symplectic map. Clearly, once α is fixed, there is a one-to-one correspondence between symplectic maps and functions, hence they are called the generating functions of the symplectic maps. Interestingly enough, the diagram shows that, when the theorem's conditions hold, to any pair $(\mathcal{M}, F)$ can be found an α (which is not unique) such that F becomes the generating function of type α of $\mathcal{M}$. Also, generating functions can be defined on any simply connected manifold X diffeomorphic to P_i, and as mentioned above, β cannot in general be extended to a global conformal symplectic map.

Now we specialize these result to the case of Euclidean spaces. Notice that for our practical cases in beam dynamics $\mathcal{M} : \mathbb{R}^{2n} \to \mathbb{R}^{2n}$, and it is computationally convenient to define the generating functions also on $\mathbb{R}^{2n}$. Hence $P_1 = P_2 = X = \mathbb{R}^{2n}$, and $\omega_1 = \omega_2 = \omega_0$. As long as π is a diffeomorphism, the theorem applies and the existence of the diffeomorphism α, which can be extended to a local symplectomorphism β follows. Global canonical coordinates are available, in which the symplectic structures ω and $\nu\omega_0$ are translationally invariant with matrices, $\mu\tilde{J}$ and νJ respectively. Therefore, there is an α which can be used to identify any Lagrangian submanifold of $\left(\mathbb{R}^{4n}, \mu\tilde{J}\right)$ of the form (2.78) with any Lagrangian submanifold of $(\mathbb{R}^{4n}, \nu J)$ of the form (2.89). According to the theorem, the most general form of β is a conformal symplectic map. Since α is the restriction of β to the Lagrangian submanifolds, we conclude that the most general form of the diffeomorphism α that links the symplectic maps to their generating functions is

$$\alpha^* \omega_0 = \frac{1}{\nu}\omega. \tag{2.97}$$

The coordinate expression of this equation is (2.6). In fact, this was expected from the local theory. Using elementary methods, it has been shown in section 2.1 that if (2.15) holds, the most general map that gives the generator type is a conformal symplectic matrix. The global theory just states that instead of matrices nonlinear maps can be used, and the local maps around each point can be glued together along germs of Lagrangian submanifolds, which entail the existence of global generating function types.

In conclusion, we have the following fundamental results in the case of Euclidean space: there is a one-to-one correspondence between any small function (in the C^2 sense) $F \in \mathcal{F}\left(C^\infty\left(\mathbb{R}^{2n}\right)\right)$ and symplectic map $\mathcal{M} : \mathbb{R}^{2n} \to \mathbb{R}^{2n}$, realized through a

diffeomorphism $\alpha : \Gamma_{\mathcal{M}} \to \Gamma_{dF}$ such that

$$\Gamma_{dF} = \alpha\left(\Gamma_{\mathcal{M}}\right), \tag{2.98}$$

$$\alpha^* \omega_0 = \frac{1}{\nu}\omega. \tag{2.99}$$

For a fixed α, the function F that satisfies the above equations is called the generating function of type α of the canonical transformation represented by $\mathcal{M}$. The same type of generator exists for all symplectic maps close enough to each other (in the C^1 topology). Obviously, from these equations it follows that to every symplectic map infinitely many generating functions can be constructed, due to the fact that the Lie group of diffeomorphisms of the form (2.99) contains infinitely many elements.

This completes the global theory of generating functions. It is worthwhile to note that the theory is global in the sense that guarantees the existence of global generating functions for any symplectic map. However, it is local in the sense that it proves that one fixed type of generator cannot exist for all symplectic maps, not even locally around a point.

2.3 Generating Functions from the Computational Point of View

This section presents a computationally convenient method to obtain generating functions of given symplectic maps. First, it is necessary to rewrite (2.98-2.99) in a form that is convenient computationally. The vector function associated to the one-form dF by the standard Euclidean scalar product is the gradient, ∇F. We write $\mathcal{N} = (\nabla F)^T$ for the map, regarded as a column vector, represented by ∇F. "$d\mathcal{N} = 0$" means that

$$\frac{\partial \mathcal{N}_i}{\partial w_j} = \frac{\partial \mathcal{N}_j}{\partial w_i}, \quad i, j = 1, ..., 2n. \tag{2.100}$$

These are the well-known necessary and sufficient conditions for the existence of a scalar potential [10]. The generating function is the potential of the closed one-form that determines the Lagrangian submanifold.

Denote some canonical coordinates by $z = (\vec{q}, \vec{p})$, and denote the coordinates of the space where the generating function is defined by w. Introduce $\hat{z}$ and $\hat{w}$ by $\hat{z} = \mathcal{M}(z)$ and $\hat{w} = \mathcal{N}(w)$. Then (2.98) can be expressed as

$$\begin{pmatrix} \hat{w} \\ w \end{pmatrix} = \alpha \begin{pmatrix} \hat{z} \\ z \end{pmatrix}, \tag{2.101}$$

$$\begin{pmatrix} \mathcal{N}(w) \\ w \end{pmatrix} = \alpha \begin{pmatrix} \mathcal{M}(z) \\ z \end{pmatrix}. \tag{2.102}$$

Splitting α into the first $2n$ and last $2n$ components, we obtain

$$\alpha = \begin{pmatrix} \alpha_1 \\ \alpha_2 \end{pmatrix}. \tag{2.103}$$

Similarly, for its inverse α^{-1} we write

$$\alpha^{-1} = \begin{pmatrix} \alpha^1 \\ \alpha^2 \end{pmatrix}. \tag{2.104}$$

From (2.102) it follows that

$$w = \alpha_2 \circ \begin{pmatrix} \mathcal{M} \\ \mathcal{I} \end{pmatrix}(z), \tag{2.105}$$

$$\mathcal{N}(w) = \alpha_1 \circ \begin{pmatrix} \mathcal{M} \\ \mathcal{I} \end{pmatrix}(z). \tag{2.106}$$

Combining the two equations we obtain that

$$\mathcal{N} \circ \alpha_2 \circ \begin{pmatrix} \mathcal{M} \\ \mathcal{I} \end{pmatrix}(z) = \alpha_1 \circ \begin{pmatrix} \mathcal{M} \\ \mathcal{I} \end{pmatrix}(z). \tag{2.107}$$

Requiring $\alpha_2 \circ \begin{pmatrix} \mathcal{M} \\ \mathcal{I} \end{pmatrix}$ to be invertible, in terms of maps we obtain the following formula, useful for the actual computation of the generating function:

$$(\nabla F)^T = \left(\alpha_1 \circ \begin{pmatrix} \mathcal{M} \\ \mathcal{I} \end{pmatrix}\right) \circ \left(\alpha_2 \circ \begin{pmatrix} \mathcal{M} \\ \mathcal{I} \end{pmatrix}\right)^{-1}. \tag{2.108}$$

Therefore, the formula (2.9) that has been defined in section 2.1, without apparent deep logic behind it, is recovered, and the general condition that requires π to be a diffeomorphism appears in computations as the above mentioned invertibility condition. If the respective map does not have a global inverse, clearly there is no global generating function. Obviously, the symplectic map $\mathcal{M}$ needs to be defined globally. If (2.105) fails to be a global diffeomorphism, there is still a chance to be defined locally, producing local generators. The invertibility condition sometimes is called the transversality condition. Locally, around the origin, this is satisfied whenever

$$\det\left(\mathrm{Jac}\left(\alpha_2 \circ \begin{pmatrix} \mathcal{M} \\ \mathcal{I} \end{pmatrix}(z)|_{z=0}\right)\right) \neq 0. \tag{2.109}$$

Denote the Jacobian of α by $\alpha_{\#} = \mathrm{Jac}\,(\alpha)$. $\alpha_{\#}$ can be written as

$$\alpha_{\#} = \begin{pmatrix} A & B \\ C & D \end{pmatrix}, \tag{2.110}$$

A, B, C, D being $2n \times 2n$ block matrices. Hence, assuming that the symplectic maps are origin preserving, i.e. $\mathcal{M}\,(0) = 0$, the local transversality condition around the origin is

$$\det\left(C\,(0,0) \cdot M\,(0) + D\,(0,0)\right) \neq 0, \tag{2.111}$$

where $M = \mathrm{Jac}\,(\mathcal{M})$. If this necessary condition is satisfied, then the generating function is defined in a neighborhood of the origin, and can be calculated from (2.108) by mere integration along an arbitrary path. The arbitrariness of the path is assured by Stokes' theorem. This has been known also from the local theory of section 2.1.

We note that in fact the computation of F according to (2.108), and subsequent integration, gives F, which is the primitive function rather than the generating function. To get the generating function itself, one has to keep in mind to which α it is associated, and compute F in the w coordinates,

$$F \longmapsto F \circ \left(\alpha_2 \circ \begin{pmatrix} \mathcal{M} \\ \mathcal{I} \end{pmatrix}\right). \tag{2.112}$$

There is a nice geometric interpretation of the global existence of the generating functions. As has been seen, any Lagrangian submanifold in unique correspondence with $\mathcal{M}$ can be sent diffeomorphically onto the Lagrangian submanifold determined by F. If, for some choice of α, this is achieved in such a way that Γ_{dF} is close enough to the zero section to project diffeomorphically onto the base, the generating function of type α exists globally. Recall that the group of diffeomorphisms is open in the set of smooth maps in the C^1 topology. Therefore, any smooth map close enough to the identity is a global diffeomorphism [41]. The reflection of this fact is that $\alpha_2\left(\hat{z}, z\right)$ has a global inverse. However, it might not be possible in practice to find an α satisfying this condition, especially for very nonlinear symplectic maps, and we need to consider local generating functions. If the projection diffeomorphisms are local, defined in a neighborhood of the origin, then we have local generating functions. In this case, one can think intuitively that fixing the type of generating function, as the nonlinearities of the symplectic map increase, the singularities move closer to the origin, limiting the domain of validity of the generating function. However, we always assume that the dynamics is taking place in a finite region of the phase space, so there is no loss of generality in assuming that the symplectic maps are compactly supported, and requiring only that the generating function to be defined in the region of interest. If the symplectic maps are too "big" for the generating functions to cover the region of interest, the problem can always be alleviated by taking roots of the symplectic map.

Next, we are interested in the constraints imposed by α. Equation (2.99) written in coordinates is

$$\alpha_{\#}^{T} J_{4n} \alpha_{\#} = \frac{\mu}{\nu} \tilde{J}_{4n}. \tag{2.113}$$

By abuse of notation, for μ/ν we write $\mu \in \mathbb{R}^{\times}$. More explicitly (2.113) reads

$$\begin{pmatrix} A^T & C^T \\ B^T & D^T \end{pmatrix} \begin{pmatrix} 0_{2n} & I_{2n} \\ -I_{2n} & 0_{2n} \end{pmatrix} \begin{pmatrix} A & B \\ C & D \end{pmatrix} = \mu \begin{pmatrix} J_{2n} & 0_{2n} \\ 0_{2n} & -J_{2n} \end{pmatrix}, \tag{2.114}$$

which gives the constraints

$$A^T C - C^T A = \mu J_{2n}, \tag{2.115}$$

$$B^T D - D^T B = -\mu J_{2n}, \tag{2.116}$$

$$A^T D - C^T B = 0. \tag{2.117}$$

Knowing that α is a diffeomorphisms, obviously $\alpha_\#$ is invertible. It is easy to see that $\det(J_{4n}) = 1$ and $\det\left(\tilde{J}_{4n}\right) = \det(J_{2n}) \cdot \det(-J_{2n}) = 1$, and hence $(\det(\alpha_\#))^2 = \mu^{4n} \neq 0$. Then equivalently, (2.113) can be written as follows:

$$\alpha_\#^T J_{4n} = \mu \tilde{J}_{4n} \alpha_\#^{-1}. \tag{2.118}$$

Transposition gives

$$J_{4n} \alpha_\# = \mu \alpha_\#^{-T} \tilde{J}_{4n}, \tag{2.119}$$

where we used $J_{4n}^T = -J_{4n}$ and $\tilde{J}_{4n}^T = -\tilde{J}_{4n}$. Obviously, $J_{4n}^{-1} = -J_{4n}$ and $\tilde{J}_{4n}^{-1} = -\tilde{J}_{4n}$, so it results that

$$J_{4n} \alpha_\# \tilde{J}_{4n} = -\mu \alpha_\#^{-T}, \tag{2.120}$$

$$J_{4n} \alpha_\# \tilde{J}_{4n} \alpha_\#^T = -\mu, \tag{2.121}$$

$$\alpha_\# \tilde{J}_{4n} \alpha_\#^T = \mu J_{4n}, \tag{2.122}$$

which gives the equivalent set of constraints, but better suited for further analysis:

$$A J_{2n} A^T - B J_{2n} B^T = 0, \tag{2.123}$$

$$C J_{2n} C^T - D J_{2n} D^T = 0, \tag{2.124}$$

$$D J_{2n} B^T - C J_{2n} A^T = \mu I_{2n}. \tag{2.125}$$

The constraints show that (A, B) and (C, D) must be symplectic pencils, and there is an additional condition that links the two pencils. An important observation is that in

the process of construction of the generating function from a symplectic map (2.123-2.125) have to be satisfied exactly, not only up to order n. In the Differential Algebraic framework, where we are working with Taylor expansions, it means that we need to construct αs that are exact, at most order n, polynomial conformal symplectic maps. To our knowledge, their classification is not known. It follows that we are inherently constrained to consider linear maps α, which can be constructed and represented exactly on a computer. In this case α can be represented by a $4n \times 4n$ constant matrix. If A is invertible, it follows that $A^{-1}B$ is a symplectic matrix. The same argument holds for the case when C is invertible, resulting that $C^{-1}D$ is a symplectic matrix. Of course, even in the linear case, there are still infinitely many αs to choose from.

2.4 Computation of Symplectic Maps from Generating Functions

In this section, the inverse problem is addressed. That is, given a generating function of type α, what is the symplectic map it generates? In other words, is there a "reversion" of (2.108) that gives $\mathcal{M}$ in terms of F and α? In section 2.1 this has been shown to be possible. However, it involves a somewhat awkward definition in terms of Jacobians. Here another method is presented, without involving the Jacobians.

Introduce a transformation defined by

$$T_\alpha(\mathcal{M}) = \left(\alpha_1 \circ \begin{pmatrix} \mathcal{M} \\ \mathcal{I} \end{pmatrix}\right) \circ \left(\alpha_2 \circ \begin{pmatrix} \mathcal{M} \\ \mathcal{I} \end{pmatrix}\right)^{-1}, \tag{2.126}$$

where $\mathrm{Jac}(\alpha) \in Gl(4n)$, and suppose that the transversality condition is satisfied. Therefore, $T_\alpha(\mathcal{M}) = \mathcal{N}$ if and only if

$$(\mathcal{N} \circ \alpha_2 - \alpha_1) \circ \begin{pmatrix} \mathcal{M} \\ \mathcal{I} \end{pmatrix} = 0. \tag{2.127}$$

Now suppose that $\mathcal{M}$ is given by another transformation $T_\beta(\mathcal{K}) = \mathcal{M}$, where $\beta = (\beta_1, \beta_2)^T$, $\mathrm{Jac}(\beta) \in Gl(4n)$, with the appropriate transversality condition satisfied. Inserting it in the above equation gives

$$(\mathcal{N} \circ \alpha_2 - \alpha_1) \circ \left(\begin{array}{c} \left(\beta_1 \circ \begin{pmatrix} \mathcal{K} \\ \mathcal{I} \end{pmatrix}\right) \circ \left(\beta_2 \circ \begin{pmatrix} \mathcal{K} \\ \mathcal{I} \end{pmatrix}\right)^{-1} \\ \mathcal{I} \end{array} \right) = 0. \tag{2.128}$$

Because $\left(\beta_2 \circ (\mathcal{K}, \mathcal{I})^T\right)$ is invertible, this is equivalent to

$$(\mathcal{N} \circ \alpha_2 - \alpha_1) \circ \left(\begin{array}{c} \left(\beta_1 \circ \begin{pmatrix} \mathcal{K} \\ \mathcal{I} \end{pmatrix}\right) \\ \left(\beta_2 \circ \begin{pmatrix} \mathcal{K} \\ \mathcal{I} \end{pmatrix}\right) \end{array} \right) = 0, \tag{2.129}$$

$$(\mathcal{N} \circ (\alpha_2 \circ \beta) - (\alpha_1 \circ \beta)) \circ \begin{pmatrix} \mathcal{K} \\ \mathcal{I} \end{pmatrix} = 0, \tag{2.130}$$

which in terms of T can be written as

$$T_\alpha \circ T_\beta(\mathcal{K}) = T_{\alpha \circ \beta}(\mathcal{K}), \tag{2.131}$$

for any $\mathcal{K}$. If we choose $\beta = \alpha^{-1}$, it follows that

$$T_\alpha \circ T_{\alpha^{-1}} = T_{\mathcal{I}} = \mathcal{I}, \tag{2.132}$$

that is

$$T_{\alpha^{-1}} = (T_\alpha)^{-1}. \tag{2.133}$$

This equation entails that whenever $T_\alpha(\mathcal{M}) = \mathcal{N}$ is well defined, the inverse is automatically well defined, and gives $\mathcal{M} = T_{\alpha^{-1}}(\mathcal{N})$. Explicitly, this means that

$$\mathcal{M} = \left(\alpha^1 \circ \begin{pmatrix} \mathcal{N} \\ \mathcal{I} \end{pmatrix}\right) \circ \left(\alpha^2 \circ \begin{pmatrix} \mathcal{N} \\ \mathcal{I} \end{pmatrix}\right)^{-1}. \tag{2.134}$$

Applied to the situation where $\mathcal{N}$ is the gradient of the generating function and α is conformal symplectic, it gives a symplectic $\mathcal{M}$. Thus, (2.134) is the counterpart of (2.9). Together, they provide a convenient computational method to pass from F to $\mathcal{M}$ and back.

Chapter 3

The Symplectic Approximation Process

Chapter 2 developed the general theory of generating functions and put the results into computationally convenient forms. It has been shown that, as long as the mathematics can be performed exactly, the passing from symplectic maps to generating functions and back is easy to achieve. Moreover, this can be done utilizing any of the infinite set of generator types. Unfortunately, in practice this is not the case. Specifically, the mathematical operations can be readily performed on a computer only with the truncation of the Taylor series of the maps at some order n. Since there is a need to represent the accelerator systems by exactly symplectic maps for long term tracking purposes, procedures to recover the exact symplecticity of the truncated Taylor maps are needed. The symplectification can be achieved utilizing the generating function theory. This chapter studies various problems related to generating function symplectification.

3.1 Symplectification of Taylor Maps and Symplectic Tracking by the Generating Function Method

Symplectic integrators became famous for their long-term properties. Their accuracy is not necessarily their best feature, and very high order symplectic integrators are often not efficient enough. The overall conclusion is that, for short term integration, the methods of choice should be integration methods with the smallest possible local error. For details see Sanz-Serna [1]. One turn around an accelerator can be considered short term, and a good algorithm should give symplecticity close to machine precision over the region of interest. In the Differential Algebraic (DA) approach the integration of the reference particle also gives the truncated Taylor series of the one turn map, which is also close to machine precision order n symplecticity. The problems arise with the $10^8 - 10^9$ iteration of the maps required for evaluation of the region of stable orbits, the so-called dynamic aperture. The errors potentially build up during large number of iterations, overshadowing completely the symplectic nature of the motion if sufficient time passes. Although, as it will be seen, recovering the symplectic nature of the motion is not a complete cure, there is reasonable hope that symplectic tracking captures the most important features of the original system over a sufficiently long time and sufficiently large region of phase space to be useful for applications.

The symplectification process is the following. Using a given integration method, compute the truncated Taylor series of the map, $\mathcal{M}_n$. It is assumed that $\mathcal{M}_n$ is order n symplectic. Fix an α that satisfies the constraints and the transversality condition. Use (2.108) to compute $\mathcal{N}_n$, the truncation at order n of $\mathcal{N}$. In COSY INFINITY all the necessary operations of truncated symplectic map generation, order n

composition and inversion of maps, and integration are readily available. Now, there is a fundamental difference between $\mathcal{M}_n$ and $\mathcal{N}_n$. While in general $\mathcal{M}$ is loosing its symplectic property by truncation, because its elements are related by quadratic relations, $\mathcal{N}_n$ still satisfies conditions (2.100) if $\mathcal{N}$ satisfies them, because they represent linear relations. Hence, a function which agrees with the true generating function's Taylor expansion up to order n can be easily computed by integration of $\mathcal{N}_n$ along an arbitrary path. Therefore, if the true generating function is F, only F_n can be computed. On the other hand, F_n is a valid generating function in its own right, and can be used to generate an exactly symplectic map. The Taylor expansion of the new symplectic map agrees up to order n with the original truncated symplectic map.

Separating $\mathcal{N}_n$ and α in linear and non-linear parts, we obtain

$$\mathcal{N}_n = \mathcal{N}_n^L + \mathcal{N}_n^N, \tag{3.1}$$

$$\alpha = \begin{pmatrix} \alpha_1 \\ \alpha_2 \end{pmatrix} = \begin{pmatrix} \alpha_1^L + \alpha_1^N \\ \alpha_2^L + \alpha_2^N \end{pmatrix}. \tag{3.2}$$

Therefore, denoting by $\bar{\mathcal{M}}$, the exactly symplectic map generated by $\mathcal{N}_n$ (or F_n), and $\tilde{z} = \bar{\mathcal{M}}(z)$, (2.107) can be used to get

$$\left(\mathcal{N}_n^L + \mathcal{N}_n^N\right) \circ \left(\alpha_2^L(\tilde{z}, z) + \alpha_2^N(\tilde{z}, z)\right) = \alpha_1^L(\tilde{z}, z) + \alpha_1^N(\tilde{z}, z). \tag{3.3}$$

The linear parts α_i^L can be written as matrices

$$\alpha_1^L(\tilde{z}, z) = A\tilde{z} + Bz, \tag{3.4}$$

$$\alpha_2^L(\tilde{z}, z) = C\tilde{z} + Dz. \tag{3.5}$$

Isolating the linear part in $\tilde{z}$ we obtain

$$\left(\mathcal{N}_n^L \circ C - A\right)\tilde{z} = \alpha_1^N(\tilde{z}, z) - \mathcal{N}_n^N \circ \left(C\tilde{z} + Dz + \alpha_2^N(\tilde{z}, z)\right) \tag{3.6}$$

$$-\mathcal{N}_n^L \circ \left(Dz + \alpha_2^N(\tilde{z}, z)\right) + Bz. \tag{3.7}$$

It already has been proved in section 2.1 that $\left(\mathcal{N}_n^L \circ C - A\right)$ is always invertible; thus

$$\tilde{z} = \left(\mathcal{N}_n^L \circ C - A\right)^{-1} \circ \begin{bmatrix} \alpha_1^N\left(\tilde{z}, z\right) - \mathcal{N}_n^N \circ \left(C\tilde{z} + Dz + \alpha_2^N\left(\tilde{z}, z\right)\right) \\ -\mathcal{N}_n^L \circ \left(Dz + \alpha_2^N\left(\tilde{z}, z\right)\right) + Bz \end{bmatrix}. \tag{3.8}$$

If the right hand side is contracting, it can be solved for $\tilde{z}$ by iteration. Using as initial value $\hat{z}_n = \mathcal{M}_n\left(z\right) = \bar{\mathcal{M}}_n\left(z\right) = \tilde{z}_n$, if n is sufficiently high, it is hoped that (3.8) is contracting, and it can be interpreted as a symplectic tracking scheme. The $(k+1)$-th iterate of the map takes the form

$$z^{k+1} = \left(\mathcal{N}_n^L \circ C - A\right)^{-1} \circ \begin{bmatrix} \alpha_1^N\left(z^{k+1}, z^k\right) - \mathcal{N}_n^N \circ \left(Cz^{k+1} + Dz^k + \alpha_2^N\left(z^{k+1}, z^k\right)\right) \\ -\mathcal{N}_n^L \circ \left(Dz^k + \alpha_2^N\left(z^{k+1}, z^k\right)\right) + Bz^k \end{bmatrix}. \tag{3.9}$$

Of course, at each $(k+1)$-th iteration, it has to be solved for z^{k+1} as a function of z^k by a fixed point iteration. With only linear maps α, (3.8) simplifies somewhat:

$$\tilde{z} = \left(\mathcal{N}_n^L \circ C - A\right)^{-1} \circ \left[\left(B - \mathcal{N}_n^L \circ D\right) z - \mathcal{N}_n^N \circ \left(C\tilde{z} + Dz\right)\right]. \tag{3.10}$$

Notice that $\left(\mathcal{N}_n^L \circ C - A\right)$ is in fact a matrix. Denote $N = \mathrm{Jac}\left(\mathcal{N}_n^L\right)$. It is actually the Jacobian of $\mathcal{N}_n$ at the origin. From (2.100) follows that N is symmetric. Interestingly, the first term appearing in (3.10) is the linear part of the symplectic map. Hence, assuming that the linear part of the solution can be computed always to machine precision, (3.10) takes the following form for the non-linear part of the solution $\tilde{z}^N$

$$\tilde{z}^N = -\left(\mathcal{N}_n^L \circ C - A\right)^{-1} \circ \mathcal{N}_n^N \circ \left(C\tilde{z} + Dz\right). \tag{3.11}$$

To this end, in principle the symplectification of maps and the symplectic tracking utilizing the generating function method is solved. We conclude the section with an interesting question. One of the reasons for tracking with maps is to speed up the simulation of accelerators. It seems that always implicit equations must be solved

for tracking symplectically. If the fixed point iterations could be replaced by some explicit relations, probably the tracking would be much faster. This problem is equivalent to the question whether the generating functions must be of mixed variables? Unfortunately, in general the answer is yes. For any α, denote $\mathrm{Jac}\,(\alpha_2) = (C \quad D)$. If any generating function was non-mixed, it would mean that $C = 0$. But then it would follow that

$$\det\left(\mathrm{Jac}\,(\alpha)\right) = \det\begin{pmatrix} A & B \\ 0 & D \end{pmatrix} = \det(A) \cdot \det(D) \tag{3.12}$$

From the constraints (2.123-2.125) results that in this case $\left(\det(D)\right)^2 = \left(\det(C)\right)^2 = 0$, giving $\det\left(\mathrm{Jac}\,(\alpha)\right) = 0$, which contradicts the condition compatible with the constraints: $\left(\det\left(\mathrm{Jac}\,(\alpha)\right)\right)^2 = \mu^{4n} \neq 0$. The same argument is valid for any block entry in $\mathrm{Jac}\,(\alpha)$; hence $A, B, C, D \neq 0$.

In subsequent sections we will show that the complexity of the problem can be reduced by considering equivalence classes of generating functions. However, the results of this section, taken together with subsection (3.3.1), is a recipe for transforming any code that uses the Goldstein generating function symplectic tracking to a form which uses fixed point iterations for solving the implicit equations, instead of the more traditional Newton method. In section (3.5) it will be pointed out that the fixed point iteration has certain advantages over the Newton method.

3.2 Transformation Properties of Generating Functions

By looking at how the generating functions transform under modifications of α and/or $\mathcal{M}$, a set of rules is obtained, which are called transformation properties. These properties are based on the fact that if α is a conformal symplectic map such that

$$\left(\mathrm{Jac}\,(\alpha)\right)^T J_{4n}\,\mathrm{Jac}\,(\alpha) = \mu \tilde{J}_{4n}, \tag{3.13}$$

then for any β and γ such that

$$\left(\mathrm{Jac}\left(\beta\right)\right)^T J_{4n}\,\mathrm{Jac}\left(\beta\right) = J_{4n}, \tag{3.14}$$

$$\left(\mathrm{Jac}\left(\gamma\right)\right)^T \tilde{J}_{4n}\,\mathrm{Jac}\left(\gamma\right) = \tilde{J}_{4n}, \tag{3.15}$$

the map $\beta \circ \alpha \circ \gamma$ is also a valid conformal symplectic map. Indeed, it follows from (3.14) and (3.15) and repeated application of the chain rule that $\beta \circ \alpha \circ \gamma$ satisfies (3.13). Therefore, it gives another type of generating function. In invariant form, if $\alpha^*\omega_0 = \mu\omega$, $\beta^*\omega_0 = \omega_0$, and $\gamma^*\omega = \omega$, then

$$\left(\beta \circ \alpha \circ \gamma\right)^* \omega_0 = \gamma^*\left(\alpha^*\left(\beta^*\omega_0\right)\right) = \gamma^*\left(\alpha^*\omega_0\right) = \gamma^*\left(\mu\omega\right) = \mu\omega. \tag{3.16}$$

These rules are interesting in their own right in symplectic geometry, and some of them can be found in [29]. More importantly, the rules are used in the next sections for equivalence class reduction of the set of generating functions.

We begin with studying what happens to the generating function $F_{\alpha,\mathcal{M}}$ under the transformation $\alpha_1 \mapsto \lambda\alpha_1$, for some non-zero real λ. This affects only the conformality factor μ of α, which becomes $\lambda\mu$. Slight rearrangement of (2.9) gives

$$\left(\left(\nabla F_{\alpha,\mathcal{M}}\right)^T \circ \alpha_2 - \alpha_1\right) \circ \begin{pmatrix} \mathcal{M} \\ \mathcal{I} \end{pmatrix} = 0. \tag{3.17}$$

Then, we also have

$$\left(\left(\nabla F_{\binom{\lambda\alpha_1}{\alpha_2},\mathcal{M}}\right)^T \circ \alpha_2 - \lambda \cdot \alpha_1\right) \circ \begin{pmatrix} \mathcal{M} \\ \mathcal{I} \end{pmatrix} = 0, \tag{3.18}$$

which is equivalent to

$$\left(\left(\nabla\left(\lambda^{-1} \cdot F_{\binom{\lambda\alpha_1}{\alpha_2},\mathcal{M}}\right)\right)^T \circ \alpha_2 - \alpha_1\right) \circ \begin{pmatrix} \mathcal{M} \\ \mathcal{I} \end{pmatrix} = 0. \tag{3.19}$$

Comparing (3.17) with (3.19) we see that

$$\nabla F_{\alpha,\mathcal{M}} = \nabla \left(\lambda^{-1} \cdot F_{\binom{\lambda\alpha_1}{\alpha_2},\mathcal{M}} \right), \tag{3.20}$$

that is

$$F_{\binom{\lambda\alpha_1}{\alpha_2},\mathcal{M}} = \lambda \cdot F_{\alpha,\mathcal{M}} + c, \tag{3.21}$$

for some arbitrary constant c.

In the same way, the transformation $\alpha_2 \mapsto \lambda\alpha_2$ has the following effect:

$$\left(\left(\nabla F_{\binom{\alpha_1}{\lambda\alpha_2},\mathcal{M}} \right)^T \circ (\lambda \cdot \alpha_2) - \alpha_1 \right) \circ \begin{pmatrix} \mathcal{M} \\ \mathcal{I} \end{pmatrix} = 0, \tag{3.22}$$

$$\left(\left(\left(\nabla F_{\binom{\alpha_1}{\lambda\alpha_2},\mathcal{M}} \right)^T \circ \lambda\mathcal{I} \right) \circ \alpha_2 - \alpha_1 \right) \circ \begin{pmatrix} \mathcal{M} \\ \mathcal{I} \end{pmatrix} = 0, \tag{3.23}$$

$$\left(\lambda^{-1} \cdot \left(\nabla \left(F_{\binom{\alpha_1}{\lambda\alpha_2},\mathcal{M}} \circ \lambda\mathcal{I} \right) \right)^T \circ \alpha_2 - \alpha_1 \right) \circ \begin{pmatrix} \mathcal{M} \\ \mathcal{I} \end{pmatrix} = 0, \tag{3.24}$$

$$\left(\left(\nabla \left(\lambda^{-1} \cdot \left(F_{\binom{\alpha_1}{\lambda\alpha_2},\mathcal{M}} \circ \lambda\mathcal{I} \right) \right) \right)^T \circ \alpha_2 - \alpha_1 \right) \circ \begin{pmatrix} \mathcal{M} \\ \mathcal{I} \end{pmatrix} = 0. \tag{3.25}$$

Again, comparison of (3.17) and (3.132) gives

$$\nabla \left(\lambda^{-1} \cdot \left(F_{\binom{\alpha_1}{\lambda\alpha_2},\mathcal{M}} \circ \lambda\mathcal{I} \right) \right) = \nabla F_{\alpha,\mathcal{M}}, \tag{3.26}$$

that is

$$F_{\binom{\alpha_1}{\lambda\alpha_2},\mathcal{M}} = \lambda \cdot F_{\alpha,\mathcal{M}} \circ \lambda^{-1}\mathcal{I} + c. \tag{3.27}$$

Also, from these two transformation properties it is easy to see the effect of the two transformations combined.

Next, we study what happens if we change the symplectic map, for example, by

$\mathcal{M} \mapsto \mathcal{M} \circ \mathcal{A}$, for some symplectic map $\mathcal{A}$. From (2.9) we have

$$\left(\left(\nabla F_{\alpha,\mathcal{M}\circ\mathcal{A}}\right)^T \circ \alpha_2 - \alpha_1\right) \circ \begin{pmatrix} \mathcal{M}\circ\mathcal{A} \\ \mathcal{I} \end{pmatrix} = 0 \tag{3.28}$$

$$\left(\left(\nabla F_{\alpha,\mathcal{M}\circ\mathcal{A}}\right)^T \circ \alpha_2 - \alpha_1\right) \circ \begin{pmatrix} \mathcal{M} \\ \mathcal{A}^{-1} \end{pmatrix} = 0 \tag{3.29}$$

$$\left(\left(\nabla F_{\alpha,\mathcal{M}\circ\mathcal{A}}\right)^T \circ (\alpha_2 \circ T_{\mathcal{A}}) - (\alpha_1 \circ T_{\mathcal{A}})\right) \circ \begin{pmatrix} \mathcal{M} \\ \mathcal{I} \end{pmatrix} = 0, \tag{3.30}$$

where $T_{\mathcal{A}}$ is defined by $T_{\mathcal{A}}(\hat{z}, z) = (\hat{z}, \mathcal{A}^{-1}(z))$. Equation (3.30) can be written also as

$$\left(\left(\nabla F_{\alpha\circ T_{\mathcal{A}},\mathcal{M}}\right)^T \circ (\alpha_2 \circ T_{\mathcal{A}}) - (\alpha_1 \circ T_{\mathcal{A}})\right) \circ \begin{pmatrix} \mathcal{M} \\ \mathcal{I} \end{pmatrix} = 0, \tag{3.31}$$

from where we conclude

$$F_{\alpha,\mathcal{M}\circ\mathcal{A}} = F_{\alpha\circ T_{\mathcal{A}},\mathcal{M}} + c. \tag{3.32}$$

In the same manner, the left action of another symplectomorphism on the map, i.e. $\mathcal{M} \mapsto \mathcal{K} \circ \mathcal{M}$ leads to

$$\left(\left(\nabla F_{\alpha,\mathcal{K}\circ\mathcal{M}}\right)^T \circ \alpha_2 - \alpha_1\right) \circ \begin{pmatrix} \mathcal{K}\circ\mathcal{M} \\ \mathcal{I} \end{pmatrix} = 0. \tag{3.33}$$

Define $T_{\mathcal{K}}(\hat{z}, z) = (\mathcal{K}(\hat{z}), z)$. Then,

$$F_{\alpha,\mathcal{K}\circ\mathcal{M}} = F_{\alpha\circ T_{\mathcal{K}},\mathcal{M}} + c. \tag{3.34}$$

We are also interested what happens when we change the coordinates in the generating function, $F \mapsto F \circ \mathcal{L}$, by a diffeomorphism $\mathcal{L}$ (here not necessarily a symplectomorphism); we have

$$\left(\left(\nabla (F \circ \mathcal{L})\right)^T \circ \alpha_2 - \alpha_1\right) \circ \begin{pmatrix} \mathcal{M} \\ \mathcal{I} \end{pmatrix} = 0 \tag{3.35}$$

$$\left(\mathrm{Jac}\,(\mathcal{L})\right)^T \cdot \left(\nabla F\right)^T \circ \mathcal{L} \circ \alpha_2 - \alpha_1\right) \circ \begin{pmatrix} \mathcal{M} \\ \mathcal{I} \end{pmatrix} = 0 \tag{3.36}$$

$$\left(\nabla F_{T_{\mathcal{L}}\circ\alpha,\mathcal{M}}\right)^T \circ (\mathcal{L} \circ \alpha_2) - \left(\left(\mathrm{Jac}\,(\mathcal{L})\right)^{-T} \cdot \alpha_1\right)\right) \circ \begin{pmatrix} \mathcal{M} \\ \mathcal{I} \end{pmatrix} = 0, \tag{3.37}$$

where we defined $T_{\mathcal{L}}(\hat{z}, z) = \Big(\left(\mathrm{Jac}\left(\mathcal{L}\right)\right)^{-T} \cdot \hat{z}, \mathcal{L}(z) \Big)$. Hence,

$$\nabla \left(F_{T_{\mathcal{L}} \circ \alpha, \mathcal{M}} \circ \mathcal{L} \right) = \nabla F_{\alpha, \mathcal{M}}, \tag{3.38}$$

that is

$$F_{T_{\mathcal{L}} \circ \alpha, \mathcal{M}} = F_{\alpha, \mathcal{M}} \circ \mathcal{L}^{-1} + c. \tag{3.39}$$

Finally, if we replace $\mathcal{M}$ with $\mathcal{M}^{-1}$, we arrive to

$$\Big(\left(\nabla F_{\alpha, \mathcal{M}^{-1}}\right)^T \circ \alpha_2 - \alpha_1 \Big) \circ \begin{pmatrix} \mathcal{M}^{-1} \\ \mathcal{I} \end{pmatrix} = 0. \tag{3.40}$$

Applying $\mathcal{M}$ from the right we get

$$\Big(\left(\nabla F_{\alpha, \mathcal{M}^{-1}}\right)^T \circ \alpha_2 - \alpha_1 \Big) \circ \begin{pmatrix} \mathcal{I} \\ \mathcal{M} \end{pmatrix} = 0. \tag{3.41}$$

This is equivalent to say that, if in both α_1 and α_2 we interchange the first $2n$ variables with the second $2n$, we get back $F_{\mathcal{M}}$ with this changed α. In terms of the Jacobian $\alpha_{\#}$, or in case of linear αs, this can be written as the transformation

$$\begin{pmatrix} A & B \\ C & D \end{pmatrix} \mapsto \begin{pmatrix} B & A \\ D & C \end{pmatrix}, \tag{3.42}$$

so we can conclude that

$$F_{\left(\begin{smallmatrix} A & B \\ C & D \end{smallmatrix}\right), \mathcal{M}^{-1}} = F_{\left(\begin{smallmatrix} B & A \\ D & C \end{smallmatrix}\right), \mathcal{M}} + c. \tag{3.43}$$

3.3 Equivalence Classes of Generating Functions

We call two types of generating function equivalent if both types generate exactly the same symplectified map when applied to a truncated, order n symplectic, Taylor map. As we showed, the different types are parametrized by conformal symplectic maps. In this section we show that all the types generated by linear αs, and which

exist at least locally for a given symplectic map, can be organized into equivalence classes characterized by symmetric matrices.

Assume that for a given symplectic map $\mathcal{M}$ there exists a generating function of type α given by

$$(\nabla F)^T = \left(\alpha_1 \circ \begin{pmatrix} \mathcal{M} \\ \mathcal{I} \end{pmatrix}\right) \circ \left(\alpha_2 \circ \begin{pmatrix} \mathcal{M} \\ \mathcal{I} \end{pmatrix}\right)^{-1}, \tag{3.44}$$

and

$$\mathrm{Jac}\,(\alpha) = \begin{pmatrix} A & B \\ C & D \end{pmatrix}. \tag{3.45}$$

From (2.6) it readily follows that

$$(\mathrm{Jac}\,(\alpha))^{-1} = \begin{pmatrix} JC^T & -JA^T \\ -JD^T & JB^T \end{pmatrix}. \tag{3.46}$$

First of all, it is straightforward to see that one can always change the conformality factor to $\mu = 1$ using the transformation rule (3.21), by choosing $\lambda = \mu^{-1}$. From (2.134) and (3.46) it easily follows that we get the same symplectified map in both cases. Therefore, the conformality factor does not introduce any flexibility into the symplectification process. Hence we can always assume that $\mu = 1$, which is the most convenient value from the numerical implementation point of view.

Denote the linear part of $\mathcal{M}$ by M. Then the generating function of the same type that generates the linear part M is given by

$$(\nabla F_0)^T = \left(\alpha_1 \circ \begin{pmatrix} M \\ \mathcal{I} \end{pmatrix}\right) \circ \left(\alpha_2 \circ \begin{pmatrix} M \\ \mathcal{I} \end{pmatrix}\right)^{-1}. \tag{3.47}$$

Subtraction of (3.47) from (3.44) gives

$$(\nabla\,(F - F_0))^T = \left[\left(\alpha_1 - (\nabla F_0)^T \circ \alpha_2\right) \circ \begin{pmatrix} \mathcal{M} \\ \mathcal{I} \end{pmatrix}\right] \circ \left(\alpha_2 \circ \begin{pmatrix} \mathcal{M} \\ \mathcal{I} \end{pmatrix}\right)^{-1} \tag{3.48}$$

$$= \left(\bar{\alpha}_1 \circ \begin{pmatrix} \mathcal{M} \\ \mathcal{I} \end{pmatrix}\right) \circ \left(\alpha_2 \circ \begin{pmatrix} \mathcal{M} \\ \mathcal{I} \end{pmatrix}\right)^{-1} = (\nabla G)^T, \tag{3.49}$$

where we used the notations $G = F - F_0$ and $\bar{\alpha}_1 = \alpha_1 - (\nabla F_0)^T \circ \alpha_2$. Define

$$\beta(\hat{w}, w) = \begin{pmatrix} \hat{w} - (\nabla F_0)^T(w) \\ w \end{pmatrix}. \tag{3.50}$$

Obviously, being a kick, i.e. changing only one component, β is a symplectic map for any function F_0. Clearly, with $\bar{\alpha}_2 = \alpha_2$ we have $\bar{\alpha} = \beta \circ \alpha$. Therefore, according to the transformation properties of the previous section, G is a valid generating function of type $\bar{\alpha}$. If we denote $N = \mathrm{Jac}(\nabla F_0)^T = (AM + B)(CM + D)^{-1}$, the Jacobian of $\bar{\alpha}$ is given by

$$\mathrm{Jac}(\bar{\alpha}) = \begin{pmatrix} A - NC & B - ND \\ C & D \end{pmatrix}, \tag{3.51}$$

and its inverse by

$$(\mathrm{Jac}(\bar{\alpha}))^{-1} = \begin{pmatrix} JC^T & -J\left(A^T - C^T N\right) \\ -JD^T & J\left(B^T - D^T N\right) \end{pmatrix}. \tag{3.52}$$

Notice that N is actually the Hessian of a function, and hence symmetric, i.e. $N^T = N$.

Here we have to make an important observation. The symplectification procedure consists of starting with $\mathcal{M}_n$ and an a priori fixed α, and computing F_n using (2.9). Then (2.134) gives an exactly symplectic map, which we call the symplectified map. Unfortunately, on a computer (2.9) has to be represented by implicit equations and solved by fixed point iterations, but formally the Taylor expansion of the symplectified map (2.134) will be $\mathcal{M}_n$ up to order n. The point to be emphasized is that one needs an a priori fixed α that is exactly symplectic (not only up to order n) for the procedure to work. However, in general it is not easy to construct useful exactly symplectic polynomial maps of degree at most n. Even in the case that one constructs such a map, in general there is no reason to believe that $(\nabla F_0)^T$ as given by (3.47) will be a polynomial map of degree at most n. Thus, in this case the exact symplecticity of $\bar{\alpha}$ will be spoiled. Therefore, we are constrained to consider equivalence classes of

the types of generating functions associated with the subgroup of linear conformal symplectic maps.

To this end, we can compare the two symplectified maps, that is the map obtained from F_n and α, and the map obtained from G_n and $\bar{\alpha}$. Notice that if α is linear, $(\nabla F_0)^T$ and hence $\bar{\alpha}$ are also linear. Then for the Jacobians of the symplectified maps we obtain from (2.134)

$$\begin{aligned}
\mathrm{Jac}\left(\mathcal{M}_{F_n,\alpha}\right) &= \left[\begin{pmatrix} JC^T & -JA^T \end{pmatrix}\begin{pmatrix} \mathrm{Jac}\left(\nabla F_n\right)^T \\ I \end{pmatrix}\right]\cdot && (3.53)\\
&\quad \left[\begin{pmatrix} -JD^T & JB^T \end{pmatrix}\begin{pmatrix} \mathrm{Jac}\left(\nabla F_n\right)^T \\ I \end{pmatrix}\right]^{-1} && (3.54)\\
&= \left(JC^T\cdot \mathrm{Jac}\left(\nabla F_n\right)^T - JA^T\right)\cdot && (3.55)\\
&\quad \left(-JD^T\cdot \mathrm{Jac}\left(\nabla F_n\right)^T + JB^T\right)^{-1}, && (3.56)
\end{aligned}$$

$$\begin{aligned}
\mathrm{Jac}\left(\mathcal{M}_{G_n,\bar{\alpha}}\right) &= \left[\begin{pmatrix} JC^T & -J\left(A^T - C^TN\right) \end{pmatrix}\begin{pmatrix} \mathrm{Jac}\left(\nabla F_n\right)^T - N \\ I \end{pmatrix}\right]\cdot && (3.57)\\
&\quad \left[\begin{pmatrix} -JD^T & J\left(B^T - D^TN\right) \end{pmatrix}\begin{pmatrix} \mathrm{Jac}\left(\nabla F_n\right)^T - N \\ I \end{pmatrix}\right]^{-1} && (3.58)\\
&= \left(JC^T\cdot \mathrm{Jac}\left(\nabla F_n\right)^T - JC^TN - JA^T + JC^TN\right)\cdot && (3.59)\\
&\quad \left(-JD^T\cdot \mathrm{Jac}\left(\nabla F_n\right)^T + JD^TN + JB^T - JD^TN\right)^{-1} && (3.60)\\
&= \left(JC^T\cdot \mathrm{Jac}\left(\nabla F_n\right)^T - JA^T\right)\cdot && (3.61)\\
&\quad \left(-JD^T\cdot \mathrm{Jac}\left(\nabla F_n\right)^T + JB^T\right)^{-1}. && (3.62)
\end{aligned}$$

Since the maps are assumed to be origin preserving, we can conclude that

$$\mathcal{M}_{F_n,\alpha} = \mathcal{M}_{G_n,\bar{\alpha}}. \tag{3.63}$$

Thus we get the same symplectified map regardless of using F_n of type α, or G_n of type $\bar{\alpha}$. So why is G_n interesting? It is interesting because of the following property:

if we denote the Jacobian of $\bar{\alpha}$ by

$$\begin{pmatrix} \bar{A} & \bar{B} \\ C & D \end{pmatrix}, \tag{3.64}$$

from (3.51) we observe that

$$\begin{aligned} \bar{A}M + \bar{B} &= (A - NC)\, M + (B - ND) && (3.65)\\ &= (AM + B) - N\,(CM + D) && (3.66)\\ &= (AM + B) - (AM + B)\,(CM + D)^{-1}\,(CM + D) && (3.67)\\ &= 0. && (3.68) \end{aligned}$$

Therefore we need to consider only the types that satisfy $\bar{A}M + \bar{B} = 0$, in addition to the usual constraints imposed by (2.6).

However, it is possible to further reduce the equivalence classes. We will use the transformation rule (3.39) with linear $\mathcal{L}$. Denoting $\mathrm{Jac}\,(\mathcal{L}) = L$ and $\tilde{\alpha} = T_{\mathcal{L}} \circ \bar{\alpha}$ we obtain

$$\mathrm{Jac}\,(\tilde{\alpha}) = \begin{pmatrix} (L^{-1})^T \bar{A} & (L^{-1})^T \bar{B} \\ LC & LD \end{pmatrix}. \tag{3.69}$$

We choose $L = (CM + D)^{-1}$. After writing out explicitly the constraints contained in (2.6), a straightforward calculation shows that

$$\begin{aligned} (CM + D)^{-1} &= -M^{-1} J \bar{A}^T, && (3.70)\\ (CM + D)^T &= -M^T J \bar{A}^{-1}. && (3.71) \end{aligned}$$

This entails that

$$\mathrm{Jac}\,(\tilde{\alpha}) = \begin{pmatrix} -M^T J & J \\ -M^{-1} J \bar{A}^T C & -M^{-1} J \bar{A}^T D \end{pmatrix}, \tag{3.72}$$

and

$$(\mathrm{Jac}\,(\tilde{\alpha}))^{-1} = \begin{pmatrix} J C^T \bar{A} M J & M \\ -J D^T \bar{A} M J & I \end{pmatrix}. \tag{3.73}$$

As mentioned above, from (3.39) we obtain that $G_{\bar{\alpha},\mathcal{M}} = F_{\tilde{\alpha},\mathcal{M}} \circ \mathcal{L}$. We drop the subscript, as there is no danger of confusion. Since $\mathcal{L}$ is linear, we also infer that

$$G_n = F_n \circ \mathcal{L}, \tag{3.74}$$

and as a consequence $(\nabla G_n)^T = L^T \cdot (\nabla F_n)^T \circ \mathcal{L}$, or

$$(\nabla F_n)^T = \left(L^{-1}\right)^T \cdot (\nabla G_n)^T \circ \mathcal{L}^{-1}. \tag{3.75}$$

We are now in position to compare the Jacobians of the two symplectified maps, and obtain

$$\begin{aligned}
\mathrm{Jac}\left(\mathcal{M}_{G_n,\bar{\alpha}}\right) &= \left[\begin{pmatrix} JC^T & -J\bar{A}^T \end{pmatrix} \begin{pmatrix} \mathrm{Jac}\left(\nabla G_n\right)^T \\ I \end{pmatrix}\right] \cdot && (3.76)\\
&\quad \left[\begin{pmatrix} -JD^T & -JM^T\bar{A}^T \end{pmatrix} \begin{pmatrix} \mathrm{Jac}\left(\nabla G_n\right)^T \\ I \end{pmatrix}\right]^{-1} && (3.77)\\
&= \left(JC^T \cdot \mathrm{Jac}\left(\nabla G_n\right)^T - J\bar{A}^T\right) \cdot && (3.78)\\
&\quad \left(-JD^T \cdot \mathrm{Jac}\left(\nabla G_n\right)^T - JM^T\bar{A}^T\right)^{-1}, && (3.79)
\end{aligned}$$

where we used $\bar{B} = -\bar{A}M$ in the second line. Another calculation shows that

$$\begin{aligned}
\mathrm{Jac}\left(\mathcal{M}_{F_n,\tilde{\alpha}}\right) &= \left[\begin{pmatrix} JC^T\bar{A}J\left(M^T\right)^{-1} & M \end{pmatrix} \begin{pmatrix} \left(L^{-1}\right)^T \cdot \mathrm{Jac}\left(\nabla G_n\right)^T \cdot L^{-1} \\ I \end{pmatrix}\right] \cdot \\
&\quad \left[\begin{pmatrix} -JD^T\bar{A}MJ & I \end{pmatrix} \begin{pmatrix} \left(L^{-1}\right)^T \cdot \mathrm{Jac}\left(\nabla G_n\right)^T \cdot L^{-1} \\ I \end{pmatrix}\right]^{-1} && (3.80)\\
&= \left(JC^TAJ\left(M^T\right)^{-1}M^TJ\bar{A}^{-1} \cdot \mathrm{Jac}\left(\nabla G_n\right)^T - MM^{-1}J\bar{A}^T\right) \cdot && (3.81)\\
&\quad \left(JD^TAMJM^TJ\bar{A}^{-1} \cdot \mathrm{Jac}\left(\nabla G_n\right)^T - M^{-1}J\bar{A}^T\right)^{-1} && (3.82)\\
&= \left(JC^T \cdot \mathrm{Jac}\left(\nabla G_n\right)^T - J\bar{A}^T\right) \cdot && (3.83)\\
&\quad \left(-JD^T \cdot \mathrm{Jac}\left(\nabla G_n\right)^T - JM^T\bar{A}^T\right)^{-1}, && (3.84)
\end{aligned}$$

where we used $MJM^T = J$. Hence, we obtained again that

$$\mathcal{M}_{G_n,\bar{\alpha}} = \mathcal{M}_{F_n,\tilde{\alpha}}, \tag{3.85}$$

and after combining (3.63) and (3.85) we finally arrive at

$$\mathcal{M}_{F_n,\alpha} = \mathcal{M}_{F_n,\tilde{\alpha}}. \tag{3.86}$$

Thus, the symplectified map obtained from a truncated generating function of type (linear) α agrees with the symplectified map obtained from type $\tilde{\alpha}$. Denote

$$\text{Jac}\,(\tilde{\alpha}) = \begin{pmatrix} \tilde{A} & \tilde{B} \\ \tilde{C} & \tilde{D} \end{pmatrix}. \tag{3.87}$$

Notice that the property from the first step of the reduction, that is

$$\begin{aligned} \tilde{A}M + \tilde{B} &= -M^T JM + J & (3.88) \\ &= -J + J = 0 & (3.89) \end{aligned}$$

is preserved, and in addition it has another very nice property, namely

$$\begin{aligned} \tilde{C}M + \tilde{D} &= -M^{-1}J\bar{A}^T\left(CM + D\right) & (3.90) \\ &= -M^{-1}J\bar{A}^T\left(\bar{A}^T\right)^{-1}JM = I, & (3.91) \end{aligned}$$

where we used (3.70) in the second line.

Therefore, every generating function type associated with linear maps, which exists at least locally for a given symplectic map, is equivalent for symplectification purposes with another type associated with

$$\begin{pmatrix} A & B \\ C & D \end{pmatrix}, \tag{3.92}$$

such that the following relations hold:

$$\begin{aligned} AM + B &= 0, & (3.93) \\ CM + D &= I. & (3.94) \end{aligned}$$

Equations (3.93) and (3.94) have to be imposed in addition to the usual constraints derived from (2.6), that is

$$AJA^T - BJB^T = 0,\ CJC^T - DJD^T = 0,\ DJB^T - CJA^T = I. \tag{3.95}$$

These five conditions restrict very much the pool of independent generator types. From (3.93) and (3.94) we obtain $B = -AM$ and $D = I - CM$ respectively, which inserted in (3.95) gives

$$A = -JM^{-1}, \tag{3.96}$$

and re-inserted in (3.93) gives

$$B = -AM = -\left(-JM^{-1}\right) M = J. \tag{3.97}$$

The first condition in (3.95) is automatically satisfied if we impose (3.93) and (3.94). Inserting $D = I - CM$ in the second relation of (3.95) we obtain

$$CMJ - (CMJ)^T = J. \tag{3.98}$$

We make the ansatz

$$CM = \frac{1}{2}\left(I + JS\right). \tag{3.99}$$

This is always possible for some matrix S. Insertion of (3.99) in (3.98) gives that S must be symmetric, i.e.

$$S^T = S, \tag{3.100}$$

but can otherwise be arbitrary. Thus we obtained

$$C = \frac{1}{2}\left(I + JS\right)M^{-1}, \tag{3.101}$$

$$D = \frac{1}{2}\left(I - JS\right). \tag{3.102}$$

Therefore, every generator type belongs to an equivalence class $[S]$ associated with

$$\begin{pmatrix} -JM^{-1} & J \\ \frac{1}{2}(I+JS)M^{-1} & \frac{1}{2}(I-JS) \end{pmatrix}, \tag{3.103}$$

and represented by the symmetric matrix S.

Given an arbitrary type of generating function, how do we know which equivalence class it belongs to? We saw that

$$\tilde{C} = (CM+D)^{-1} C,\ \tilde{D} = (CM+D)^{-1} D, \tag{3.104}$$

and similarly

$$\tilde{C} = \frac{1}{2}(I+JS)M^{-1},\ \tilde{D} = \frac{1}{2}(I-JS). \tag{3.105}$$

We can express $\tilde{C}M - \tilde{D}$ from the first two and second two relations respectively, obtaining

$$(CM+D)^{-1}(CM-D) = JS, \tag{3.106}$$

or equivalently

$$S = -J(CM+D)^{-1}(CM-D). \tag{3.107}$$

To remind ourselves, equivalence means that generating functions from the same equivalence class will produce indistinguishable results if used to symplectify a given order n symplectic map. Thus we just proved the following theorem.

Theorem 7 *Every generating function type associated with a linear conformal symplectic map that exists at least locally for a given symplectic map belongs to an equivalence class represented by a symmetric matrix. An arbitrary type of generator, associated with a linear α satisfying conditions (3.95) and (2.111), belongs to a class associated with (3.103), and characterized by the symmetric matrix given by (3.107).*

3.3.1 Application to the Conventional Generating Function Types

To exemplify the process, we show how the general theory contains the traditional, Goldstein type, generating functions. Because of (3.107), without loss of generality we can assume that the symplectic maps have identity as linear part. More explicitly, fixing the linear part does not affect the calculation of the matrices A, B, C, and D, but it does influence the calculation of S. However, for a different linear part, use of (3.107) will give the appropriate matrix S in each case. Here we arbitrarily fix the linear part to identity to exemplify the calculation process. In canonical coordinates $(\vec{q}, \vec{p})$, an origin preserving symplectic map acts as

$$\mathcal{M} \begin{pmatrix} \vec{q} \\ \vec{p} \end{pmatrix} = \begin{pmatrix} \vec{Q} \\ \vec{P} \end{pmatrix}. \tag{3.108}$$

The type F_1 is the solution of the implicit relations

$$(\nabla F_1)^T \begin{pmatrix} \vec{q} \\ \vec{Q} \end{pmatrix} = \begin{pmatrix} \vec{p} \\ -\vec{P} \end{pmatrix}. \tag{3.109}$$

Clearly, in this case α can be chosen as a linear map, so in view of (2.107) we have

$$(\nabla F)^T \left(C \begin{pmatrix} \vec{Q} \\ \vec{P} \end{pmatrix} + D \begin{pmatrix} \vec{q} \\ \vec{p} \end{pmatrix} \right) = A \begin{pmatrix} \vec{Q} \\ \vec{P} \end{pmatrix} + B \begin{pmatrix} \vec{q} \\ \vec{p} \end{pmatrix}. \tag{3.110}$$

We choose

$$A = \begin{pmatrix} 0_n & 0_n \\ 0_n & -I_n \end{pmatrix}, \qquad B = \begin{pmatrix} 0_n & I_n \\ 0_n & 0_n \end{pmatrix}, \tag{3.111}$$

$$C = \begin{pmatrix} 0_n & 0_n \\ I_n & 0_n \end{pmatrix}, \qquad D = \begin{pmatrix} I_n & 0_n \\ 0_n & 0_n \end{pmatrix}. \tag{3.112}$$

These matrices satisfy the constraints (2.123-2.125) and clearly substitution into (3.110) gives (3.109). We say that the F_1 type of generating function is associated to

$$\mathrm{Jac}\,(\alpha_1) = \begin{pmatrix} 0_n & 0_n & 0_n & I_n \\ 0_n & -I_n & 0_n & 0_n \\ 0_n & 0_n & I_n & 0_n \\ I_n & 0_n & 0_n & 0_n \end{pmatrix}, \tag{3.113}$$

or that F_1 is of type α_1.

Similarly, the Goldstein type 2 generating function F_2, given by

$$(\nabla F_2)^T \begin{pmatrix} \vec{q} \\ \vec{P} \end{pmatrix} = \begin{pmatrix} \vec{p} \\ \vec{Q} \end{pmatrix}, \tag{3.114}$$

is associated with

$$\mathrm{Jac}\,(\alpha_2) = \begin{pmatrix} 0_n & 0_n & 0_n & I_n \\ I_n & 0_n & 0_n & 0_n \\ 0_n & 0_n & I_n & 0_n \\ 0_n & I_n & 0_n & 0_n \end{pmatrix}. \tag{3.115}$$

It can be easily checked from (3.107) that it belongs to the class represented by

$$S_2 = -\begin{pmatrix} 0 & I \\ I & 0 \end{pmatrix}. \tag{3.116}$$

The conventional type three (F_3), determined by

$$(\nabla F_3)^T \begin{pmatrix} \vec{p} \\ \vec{Q} \end{pmatrix} = \begin{pmatrix} -\vec{q} \\ -\vec{P} \end{pmatrix}, \tag{3.117}$$

is associated with

$$\mathrm{Jac}\,(\alpha_3) = \begin{pmatrix} 0 & 0 & -I & 0 \\ 0 & -I & 0 & 0 \\ 0 & 0 & 0 & I \\ I & 0 & 0 & 0 \end{pmatrix}, \tag{3.118}$$

and belongs to the class

$$S_3 = \begin{pmatrix} 0 & I \\ I & 0 \end{pmatrix}, \tag{3.119}$$

differing only by a sign from the type F_2

$$S_3 = -S_2. \tag{3.120}$$

Finally, the conventional type four (F_4) is determined by

$$(\nabla F_4)^T \begin{pmatrix} \vec{p} \\ \vec{P} \end{pmatrix} = \begin{pmatrix} -\vec{q} \\ \vec{Q} \end{pmatrix}, \tag{3.121}$$

and is associated with

$$\text{Jac}\,(\alpha_4) = \begin{pmatrix} 0 & 0 & -I & 0 \\ I & 0 & 0 & 0 \\ 0 & 0 & 0 & I \\ 0 & I & 0 & 0 \end{pmatrix}. \tag{3.122}$$

It is well-known that the type F_1 cannot be used in the case when $\mathcal{M} = \mathcal{I}$. This naturally follows from the general theory, due to the fact that the transversality condition is not satisfied. That is,

$$\det\,(C \cdot I + D) = \det \begin{pmatrix} I_n & 0_n \\ I_n & 0_n \end{pmatrix} = 0. \tag{3.123}$$

Therefore, it does not belong to any equivalence class for symplectic maps having identity as linear part. The transversality condition is also violated in the case of the F_4. On the other hand, in the case of the F_2 the transversality condition is satisfied for the identity map, as expected

$$\det\,(C \cdot I + D) = \det \begin{pmatrix} I_n & 0_n \\ 0_n & I_n \end{pmatrix} = 1. \tag{3.124}$$

An analogous result is found for F_3 too.

Thus, we recovered from the general theory the well known facts that F_1 and F_4 cannot, while F_2 and F_3 can be used to represent at least locally symplectic maps having identity as linear part. Also, we identified the equivalence classes which F_2 and F_3 belong to. The only difference if the symplectic maps do not have identity as linear part is that we obtain different symmetric matrices, and hence classes, which also can be computed using (3.107).

3.4 Equivalence of Symplectification with and without Linear Part

Symplectification can be performed on the nonlinear part only by first factoring out the linear part, or on the whole map. The next question that arises naturally is whether there is something to be gained if one first factors out the linear part of the symplectic map to be symplectified. This section answers the question in the negative. Moreover, combining results of this section, we show in subsection 3.4.1 that not even a linear symplectic change of variables can provide additional freedom in the symplectification process.

We write the symplectic map to be symplectified as

$$\mathcal{M} = M + H, \tag{3.125}$$

where M is the linear part, and H the higher order terms. We can distinguish three symplectification procedures: symplectify $\mathcal{M}_n$ directly, symplectify $\mathcal{M}_{L,n}$ obtained from

$$\mathcal{M}_L = I + M^{-1} \circ H, \tag{3.126}$$

or symplectify $\mathcal{M}_{R,n}$ obtained from

$$\mathcal{M}_R = I + H \circ M^{-1}. \tag{3.127}$$

In the latter two cases we first factored out the linear part from the left and right respectively. The relations among the maps are the following:

$$\mathcal{M} = M \circ \mathcal{M}_L, \tag{3.128}$$

$$\mathcal{M} = \mathcal{M}_R \circ M. \tag{3.129}$$

The question is whether these relations continue to hold for the symplectified versions of $\mathcal{M}_n$, $\mathcal{M}_{L,n}$, and $\mathcal{M}_{R,n}$. Suppose we symplectify the maps using a generator of type

α with

$$\mathrm{Jac}\,(\alpha) = \begin{pmatrix} A & B \\ C & D \end{pmatrix}. \tag{3.130}$$

The local existence conditions are

$$\det\,(CM + D) \neq 0 \tag{3.131}$$

in the first case, and

$$\det\,(C + D) \neq 0 \tag{3.132}$$

in the second and third case. Being linear, we use M for the Jacobian of M too. Equations (3.131) and (3.132) are not compatible in general. Thus in general not every type of generating function exists in all three cases. The right question to ask is the following. Suppose one uses some type of generator to symplectify a given map, using the approach of one of the three cases. Then, are there other types of generators which produce the same symplectification for the other two cases? In other words, we would like to find the appropriate type of generators such that relations (3.128) and (3.129) hold for the symplectified maps.

To this end, any generator for the first case is associated to one of the following:

$$\mathrm{Jac}\,(\alpha) = \begin{pmatrix} -JM^{-1} & J \\ \frac{1}{2}\,(I + JS)\,M^{-1} & \frac{1}{2}\,(I - JS) \end{pmatrix}. \tag{3.133}$$

Its inverse is given by

$$(\mathrm{Jac}\,(\alpha))^{-1} = \begin{pmatrix} \frac{1}{2}MJ\,(I - SJ) & M \\ -\frac{1}{2}J\,(I + SJ) & I \end{pmatrix}. \tag{3.134}$$

Denoting the generator by $F_{[S]}$, $\mathrm{Jac}\left(\nabla F_{[S]}\right)^T =_n N_{[S]}$, and the symplectification of

$\mathcal{M}_n$ by $\mathcal{M}_{[S]}$ we obtain

$$\begin{aligned}
\mathrm{Jac}\left(\mathcal{M}_{[S]}\right) &= \left[\begin{pmatrix} \frac{1}{2}MJ\left(I-SJ\right) & M \end{pmatrix}\begin{pmatrix} N_{[S]} \\ I \end{pmatrix}\right]\cdot && (3.135)\\
&\quad \left[\begin{pmatrix} -\frac{1}{2}J\left(I+SJ\right) & I \end{pmatrix}\begin{pmatrix} N_{[S]} \\ I \end{pmatrix}\right]^{-1} && (3.136)\\
&= M\cdot\left(\frac{1}{2}J\left(I-SJ\right)\cdot N_{[S]}+I\right)\cdot && (3.137)\\
&\quad \left(-\frac{1}{2}J\left(I+SJ\right)\cdot N_{[S]}+I\right)^{-1}. && (3.138)
\end{aligned}$$

Now we turn our attention to the second case. Here the possible generators belong to one of the following classes:

$$\mathrm{Jac}\left(\beta\right)=\begin{pmatrix} -J & J \\ \frac{1}{2}\left(I+J\bar{S}\right) & \frac{1}{2}\left(I-J\bar{S}\right) \end{pmatrix}. \tag{3.139}$$

Clearly its inverse is

$$\left(\mathrm{Jac}\left(\beta\right)\right)^{-1}=\begin{pmatrix} \frac{1}{2}J\left(I-\bar{S}J\right) & I \\ -\frac{1}{2}J\left(I+\bar{S}J\right) & I \end{pmatrix}. \tag{3.140}$$

Again, denoting the symplectified version of $\mathcal{M}_{L,n}$ by $\mathcal{M}_{L[\bar{S}]}$ we obtain

$$\begin{aligned}
\mathrm{Jac}\left(\mathcal{M}_{L[\bar{S}]}\right) &= \left[\begin{pmatrix} \frac{1}{2}J\left(I-\bar{S}J\right) & I \end{pmatrix}\begin{pmatrix} N_{[\bar{S}]} \\ I \end{pmatrix}\right]\cdot && (3.141)\\
&\quad \left[\begin{pmatrix} -\frac{1}{2}J\left(I+\bar{S}J\right) & I \end{pmatrix}\begin{pmatrix} N_{[\bar{S}]} \\ I \end{pmatrix}\right]^{-1} && (3.142)\\
&= \left(\frac{1}{2}J\left(I-\bar{S}J\right)\cdot N_{[\bar{S}]}+I\right)\cdot && (3.143)\\
&\quad \left(-\frac{1}{2}J\left(I+\bar{S}J\right)\cdot N_{[\bar{S}]}+I\right)^{-1}, && (3.144)
\end{aligned}$$

where we used the notation $\mathrm{Jac}\left(\nabla F_{[\bar{S}]}\right)^T =_n N_{[\bar{S}]}$. Next, we use the transformation

property (3.34) with $\mathcal{K} = M^{-1}$. It follows that

$$F_{\beta,\mathcal{M}_L} = F_{\beta\circ T_{\mathcal{K}},\mathcal{M}}. \tag{3.145}$$

Also notice that $\beta \circ T_{\mathcal{K}} = \alpha$ if and only if $\bar{S} = S$. In this case

$$N_{\left[\bar{S}\right]} = N_{[S]}. \tag{3.146}$$

Comparing (3.137) and (3.143), and using (3.146) we can conclude that

$$\mathcal{M}_{[S]} = M \circ \mathcal{M}_{L\left[\bar{S}\right]}, \tag{3.147}$$

if and only if

$$\bar{S} = S. \tag{3.148}$$

This proves that the symplectified version of (3.128) is (3.147), and holds only if (3.148) is satisfied.

We can proceed to the third case and follow the same route. To symplectify $\mathcal{M}_{R,n}$ we choose a generator type from the pool

$$\mathrm{Jac}\,(\gamma) = \begin{pmatrix} -J & J \\ \frac{1}{2}\left(I + J\tilde{S}\right) & \frac{1}{2}\left(I - J\tilde{S}\right) \end{pmatrix}, \tag{3.149}$$

with inverse

$$\left(\mathrm{Jac}\,(\gamma)\right)^{-1} = \begin{pmatrix} \frac{1}{2}J\left(I - \tilde{S}J\right) & I \\ -\frac{1}{2}J\left(I + \tilde{S}J\right) & I \end{pmatrix}. \tag{3.150}$$

If we denote the symplectification of $\mathcal{M}_{R,n}$ by $\mathcal{M}_{R[\tilde{S}]}$ we get

$$\begin{aligned}
\mathrm{Jac}\left(\mathcal{M}_{R[\tilde{S}]}\right) &= \left[\begin{pmatrix} \frac{1}{2}J\left(I-\tilde{S}J\right) & I \end{pmatrix}\begin{pmatrix} N_{[\tilde{S}]} \\ I \end{pmatrix}\right]\cdot && (3.151)\\
&\quad \left[\begin{pmatrix} -\frac{1}{2}J\left(I+\tilde{S}J\right) & I \end{pmatrix}\begin{pmatrix} N_{[\tilde{S}]} \\ I \end{pmatrix}\right]^{-1} && (3.152)\\
&= \left(\frac{1}{2}J\left(I-\tilde{S}J\right)\cdot N_{[\tilde{S}]}+I\right)\cdot && (3.153)\\
&\quad \left(-\frac{1}{2}J\left(I+\tilde{S}J\right)\cdot N_{[\tilde{S}]}+I\right)^{-1}, && (3.154)
\end{aligned}$$

using the notation $\mathrm{Jac}\left(\nabla F_{[\tilde{S}]}\right)^T =_n N_{[\tilde{S}]}$. Now using the transformation rule (3.32) with $\mathcal{A} = M^{-1}$ we obtain

$$F_{\gamma,\mathcal{M}_R} = F_{\gamma\circ T_{\mathcal{A}},\mathcal{M}}. \tag{3.155}$$

A straightforward calculation gives that

$$\mathrm{Jac}\left(\gamma\circ T_{\mathcal{A}}\right) = \begin{pmatrix} -J & JM \\ \frac{1}{2}\left(I+J\tilde{S}\right) & \frac{1}{2}\left(I-J\tilde{S}\right)M \end{pmatrix}, \tag{3.156}$$

with inverse

$$\left(\mathrm{Jac}\left(\gamma\circ T_{\mathcal{A}}\right)\right)^{-1} = \begin{pmatrix} \frac{1}{2}J\left(I-\tilde{S}J\right) & I \\ -\frac{1}{2}M^{-1}J\left(I+\tilde{S}J\right) & M^{-1} \end{pmatrix}. \tag{3.157}$$

Then, (3.153) can be expressed as

$$\mathrm{Jac}\left(\mathcal{M}_{R[\tilde{S}]}\right) = X\cdot M^{-1}, \tag{3.158}$$

where we introduced the notation

$$X = \left(\frac{1}{2}J\left(I-\tilde{S}J\right)\cdot\nabla F_{\gamma\circ T_{\mathcal{A}},\mathcal{M}}+I\right)\cdot\left(-\frac{1}{2}M^{-1}J\left(I+\tilde{S}J\right)\cdot\nabla F_{\gamma\circ T_{\mathcal{A}},\mathcal{M}}+M^{-1}\right)^{-1}. \tag{3.159}$$

But as one can see from (3.157) this is nothing else than the Jacobian of the symplectified map obtained from $\mathcal{M}_n$ and generator of type (3.156). As shown in section 3.3 this generator type for $\mathcal{M}_n$ belongs to the equivalence class represented by the symmetric matrix calculated using formula (3.107). A short calculation gives the result,

$$S = M^T \tilde{S} M. \tag{3.160}$$

Combining this result with (3.158) and (3.159) we can conclude that

$$\mathcal{M}_{[S]} = \mathcal{M}_{L[\tilde{S}]} \circ M. \tag{3.161}$$

This proves that the symplectified version of (3.129) is (3.161), and holds only if (3.160) is satisfied. Therefore, the main result of this section can be formulated as the following theorem.

Theorem 8 *The symplectified version of (3.128), i.e. (3.147), holds if and only if (3.148) is satisfied, and the symplectified version of (3.129), i.e. (3.161), holds if and only if (3.160) is satisfied.*

The main point we learned is that from the optimal symplectification point of view there is no difference which way one proceeds. Once we obtained the best type of generator for one case, the best generators for the other cases automatically follow from (3.148) and (3.160). Therefore, there is nothing to be gained by factoring out linear parts and symplectifying the nonlinear parts only. Moreover, the first case (without factorization) is the most efficient when implemented numerically on a computer.

3.4.1 Equivalence in the Case of Symplectic Maps Conjugated by Linear Symplectic Maps

Combining the left and right factorizations in linear and nonlinear parts just discussed, we can address the special case of the linear symplectic change of variables. From (3.128) and (3.129) we can infer that

$$\mathcal{M}_R = M \circ \mathcal{M}_L \circ M^{-1}, \tag{3.162}$$

and from (3.147) and (3.161) that

$$\mathcal{M}_{R[\tilde{S}]} = M \circ \mathcal{M}_{L[\bar{S}]} \circ M^{-1}, \tag{3.163}$$

if

$$\bar{S} = M^T \tilde{S} M. \tag{3.164}$$

The two maps are conjugated by a linear symplectic transformation. However, this case is very special, since both $\mathcal{M}_R$ and $\mathcal{M}_L$ are obtained from the same map $\mathcal{M}$. We could relax the conditions, and ask if any two symplectic maps are conjugated by an arbitrary linear symplectic map, then the same holds true for their symplecified counterparts. That is, suppose that $\mathcal{M}$ and $\mathcal{N}$ are symplectic maps such that

$$\mathcal{N} = \mathcal{K} \circ \mathcal{M} \circ \mathcal{K}^{-1}, \tag{3.165}$$

for some linear symplectic $\mathcal{K}$. The possible types of generating functions are associated with

$$\mathrm{Jac}\,(\alpha) = \begin{pmatrix} -JKM^{-1}K^{-1} & J \\ \frac{1}{2}\left(I + JS\right)KM^{-1}K^{-1} & \frac{1}{2}\left(I - JS\right) \end{pmatrix} \tag{3.166}$$

for $\mathcal{N}_n$, and

$$\mathrm{Jac}\,(\beta) = \begin{pmatrix} -JM^{-1} & J \\ \frac{1}{2}\left(I + J\bar{S}\right)M^{-1} & \frac{1}{2}\left(I - J\bar{S}\right) \end{pmatrix} \tag{3.167}$$

for $\mathcal{M}_n$. As before, we denoted $\mathcal{M} = M + H$ and $\mathrm{Jac}\,(\mathcal{K}) = K$. The transformation rule to be used here is

$$F_{\alpha,\mathcal{N}} = F_{\alpha\circ T_{\mathcal{K}},\mathcal{M}}, \tag{3.168}$$

where

$$\mathrm{Jac}\,(T_{\mathcal{K}}) = \begin{pmatrix} K & 0 \\ 0 & K \end{pmatrix}. \tag{3.169}$$

Following now well established procedures, it is straightforward to show that

$$\mathcal{N}_{[S]} = \mathcal{K} \circ \mathcal{M}_{\left[\bar{S}\right]} \circ \mathcal{K}^{-1} \tag{3.170}$$

holds for the symplectified maps if

$$\bar{S} = K^T S K. \tag{3.171}$$

Therefore, there is no additional freedom in the symplectification process if the symplectic map is first subjected to a linear symplectic variable change.

3.5 Implementation

In this section, the implementation of the extended generating function symplectification method to COSY INFINITY is described. The method starts with $\mathcal{M}_n$ given, and some arbitrary initial condition z. Utilizing (2.9) with α given by (3.103), the truncated α-generating function F_{n+1} is obtained. The arbitrary symmetric matrix S must be specified, fixing the type of generator utilized. All the necessary operations of map composition, map inversion, differentiation and integration are readily available in COSY. Then, notice that (2.9) can be expressed as

$$\hat{z} - M \cdot z = M \cdot J \cdot (\nabla F_n)^T \left(C \cdot (\hat{z} - M \cdot z) + z\right), \tag{3.172}$$

where we denoted $\hat{z} = \mathcal{M}_{[S]}(z)$, $\mathcal{M}_{[S]}$ representing formally the symplectified map, and

$$C = \frac{1}{2}(I + JS)M^{-1}. \tag{3.173}$$

To avoid as much as possible any problems with cancellation of digits, we denote

$$w = \hat{z} - M \cdot z, \tag{3.174}$$

which leads to

$$w = M \cdot J \cdot (\nabla F_n)^T (C \cdot w + z). \tag{3.175}$$

This can be solved by a fixed point iteration for w, and gives the final result by

$$\hat{z} = w + M \cdot z. \tag{3.176}$$

The orbit of z is then computed by iteration of the procedure (in the next step we take $\hat{z}$ as the initial condition, etc.).

Writing (3.175) as $w = f(w)$, we observe that to be able to solve (3.175) by a fixed point iteration, it is sufficient (but not necessary) for the right hand side to be contracting for a fixed z, i.e. is guaranteed to succeed if

$$|f(w_2) - f(w_1)| \leq q \cdot |w_2 - w_1|, \tag{3.177}$$

for some $q < 1$. To have a good chance of contractivity over an extended region, the derivatives of the generating functions must be small. From our experience, in general the fixed point iteration converges in the region where the generating function is defined.

We compiled a table with the number of iterations needed for convergence, for a few relevant examples that will be presented in more detail in the next chapter. The examples that we tracked are: two maps generated from random Hamiltonians, an

Using $S = 0$			
Example	Number of iterations		
	Small ampl.	Medium ampl.	Large ampl.
Random map 1	1	$[4, 10]$	$[9, 29]$
Random map 2	1	$[1, 9]$	$[3, 34]$
Anharmonic oscillator	1	$[1, 8]$	$[1, 28]$
Quadratic map	1	1	1
LHC	$[4, 5]$	$[7, 10]$	$[8, 68]$

Table 3.1: Number of iterations needed for convergence in solving (3.175) for several examples, using the generator type associated with $S = 0$. The orbits of the particles of small, medium, and large amplitude, respectively, have been followed for 100 turns, and the number of iterations needed is enclosed in the intervals appearing in the table.

Using F_1			
Example	Number of iterations		
	Small ampl.	Medium ampl.	Large ampl.
Random map 1	$[1, 4]$	$[6, 36]$	$[7, 56]$
Random map 2	$[1, 8]$	$[3, 46]$	not stable
Anharmonic oscillator	1	$[1, 8]$	$[1, 27]$
Quadratic map	$[4, 15]$	[13, n.c.]	[7, n.c.]
LHC	$[4, 7]$	$[7, 16]$	not stable

Table 3.2: Number of iterations needed for convergence in solving (3.175) for several examples, using the conventional generator type F_1. The orbits of the particles of small, medium, and large amplitude, respectively, have been followed for 100 turns, and the number of iterations needed is enclosed in the intervals appearing in the table. In the table, n.c. stands for no convergence in 100 iterations, and "not stable" means that the respective particle is predicted by the algorithm to be unstable.

anharmonic oscillator, an exactly symplectic quadratic maps, and the Large Hadron Collider with fringe fields included. For more details see next chapter. The results are summed up in Table 3.1 (using the generator associated with $S = 0$) and Table 3.2 (using the conventional F_1 type).

Of course, (3.175) can be expressed as $f(w) - w = 0$, and solved for w by Newton's method. We noticed that the results not only are sometimes dependent on the generating function type employed, but also on the numerics, that is the particular numerical method used to solve the implicit equations. Of course, if we start with an

exactly order n symplectic map, and the convergence to the solution of the implicit equations is achieved over the tracking region for both methods, then the resulting pictures are identical. However, in practice the fixed point iteration works in a more stable manner. It is faster than Newton's method when many particles are tracked simultaneously, and, in the vast majority of cases studied, its domain of convergence is larger. For maps of practical interest, Newton's method often does not converge close to the dynamic aperture, and sometimes gives misleading results. Moreover, if the symplectification starts with truncated maps that are not exactly order n symplectic, the results depend on the way the truncated generating functions are computed. It seems that the general theory provides a good order n symplectification scheme. More about the performance of the algorithm is presented in the next section, where the attention is turned to examples.

For a better overview of the theory and aspects of the implementation, the Figure below shows a flow diagram, which explains the algorithmic steps involved in the symplectic approximation/tracking process.

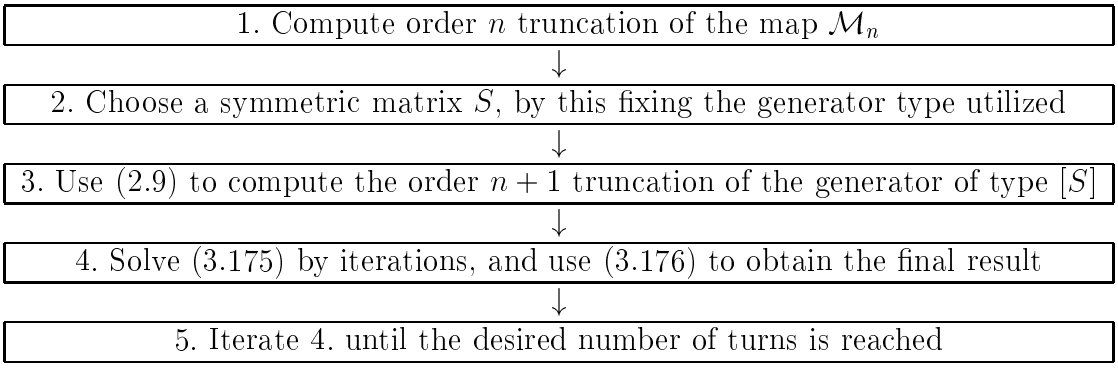

We mention that every step is efficiently implemented in COSY INFINITY, and by vectorization of the algorithm, many particles can be tracked simultaneously. Choosing different generator types, by specifying different symmetric matrices S, the tracking algorithm will give different tracking pictures.

Chapter 4

Examples

This chapter is devoted to illustrate the performance of the extended generating function symplectification method through several examples. First we generate symplectic maps from random Hamiltonians. In two dimensions this can be done easily to high orders. We can assume that these high order truncated maps are approximating the exact maps well enough to be considered numerically symplectic over a sizable phase space region. Then we can compute the generating functions, truncated as some modest order (say 7 or 11), and use them to generate exactly symplectic maps according to the above symplectification procedure. Finally, we can compare the various maps obtained this way. We will present some typical cases.

Next, we study two examples that have been studied previously in the symplectification literature: an anharmonic oscillator [16, 14], and an exactly symplectic quadratic map [51]. These are important cases, as the exact solutions are known and can be compared with the symplectified ones.

We apply our method to a lattice of the proposed Neutrino Factory [52], and the FNAL Proton Driver [53]. Although we track the muons for their lifetime (only 1000 turns), it is still an interesting case due to the wide array of nonlinear effects which the lattice exhibits [11, 12, 13]. Finally, some tracking results for the LHC are also

provided.

4.1 Maps Generated from Random Hamiltonians

We generate polynomials in two variables, starting with quadratic terms. The coefficients are chosen randomly, evenly distributed in $[-1, 1]$. Regarding the random functions as Hamiltonians, we compute their time 1 maps to very high order, say 19. The vanishing linear part of the Hamiltonians guarantee that the resulting maps will be origin preserving. We show two dimensional examples because the maps can be computed to very high orders, and generically in four or more dimensions the symplectic maps are unstable. The few stable cases that we obtained were linearly coupled and chaotic. As it is well known, chaos cannot happen in time independent one degree of freedom Hamiltonian systems. Although in $2D$ symplecticity is equivalent to area preservation, we chose to show some $2D$ examples because due to their regular features it is easier to compare the various tracking pictures involved.

At order 19 most of the resulting maps can be considered numerically symplectic over some region of phase space. Thus, we take them as the "exact" results. Then, we compute their generating function truncated at some lower order, and we use them to generate exactly symplectic maps according to the symplectification methods of the previous chapters. We use different types of generating functions, and finally we compare the resulting maps.

For one of the random seeds, the 19th order Taylor map tracking picture for 1000 turns, of some particles launched along the q axis, looks as in Figure 4.1 (the coordinate axes are always q and p). The symplectified map from the order 19th Taylor map with $S = 0$ looks almost identical; see Figure 4.2. To asses the performance of the symplectification method for this example, we show the 3rd, 7th, and 11th order

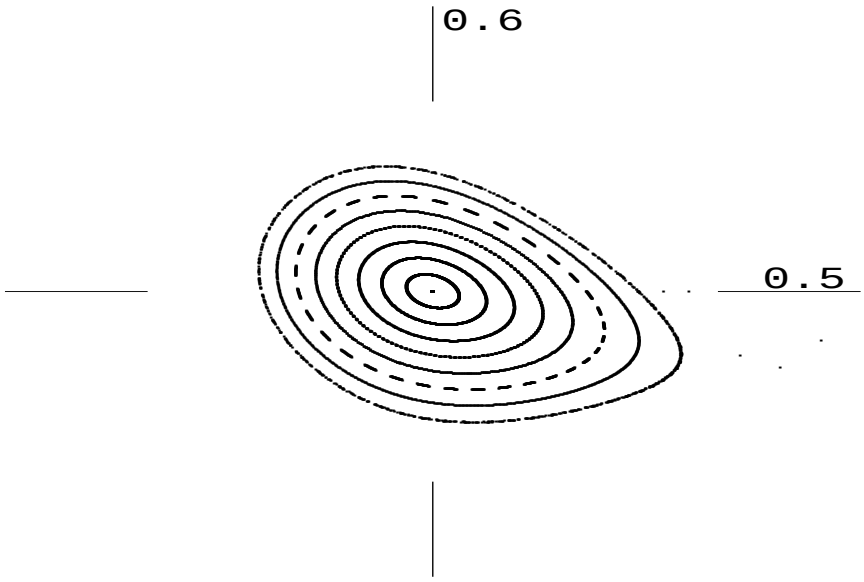

Figure 4.1: 1000 turn tracking of a random two dimensional symplectic map with the 19th order Taylor map (considered to be essentially the exact result).

Taylor maps, and the corresponding symplectified maps with $S = 0$ tracking pictures in Figure 4.3.

While the low order Taylor maps give very poor results, the symplectified maps show the right qualitative behavior right from the beginning. The dynamic aperture is overestimated, but the agreement gets better as the order is cranked up, and at order 11 we get almost the same picture as with the 19th order tracking, except perhaps slightly changed tunes of some outer particles. Therefore, at least in this case an 11th order symplectified map predicts the right dynamic aperture.

We can compare the 11th order $S = 0$ symplectified tracking picture with the conventional (Goldstein) generator types. We track using 6 different 11th order generators: F_1, F_2, F_3, and F_4 for the full map, and F_2 and F_3 for the nonlinear part only. These are the cases traditionally used in the past. The results are depicted in Figure 4.4. The superiority of the $S = 0$ method is clear.

The above random map turned out to be the most nonlinear seed. As a second

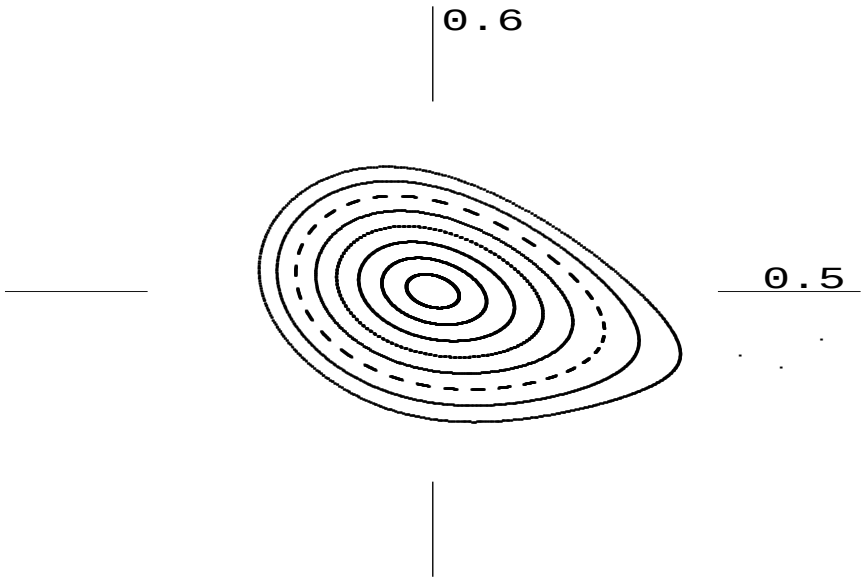

Figure 4.2: 1000 turn tracking of the random two dimensional symplectic map obtained from the 19th order Taylor map, by symplectifying it with the generator type associated with the $S = 0$ symmetric matrix.

example in this group, we show results obtained for another seed, which is much less nonlinear. First of all, the 19th order Taylor map tracking for 1000 turns of some particles, launched with vanishing momenta, is shown in Figure 4.5. Actually, already the 15th order Taylor map gives visually identical results, so we assume the order 19th map to be the exact map. As Figure 4.6 shows, the 19th order $S = 0$ symplectified map tracking gives the same result as the corresponding Taylor map, even for the tunes. Of course, the lower order symplectifications shown in Figure 4.6 give slightly worse results, but still acceptable, and give a quite accurate estimation of the dynamic aperture. For comparison, the results using the conventional generators are presented in Figure 4.7. We also studied many other seeds for random map generation, and all give similar results.

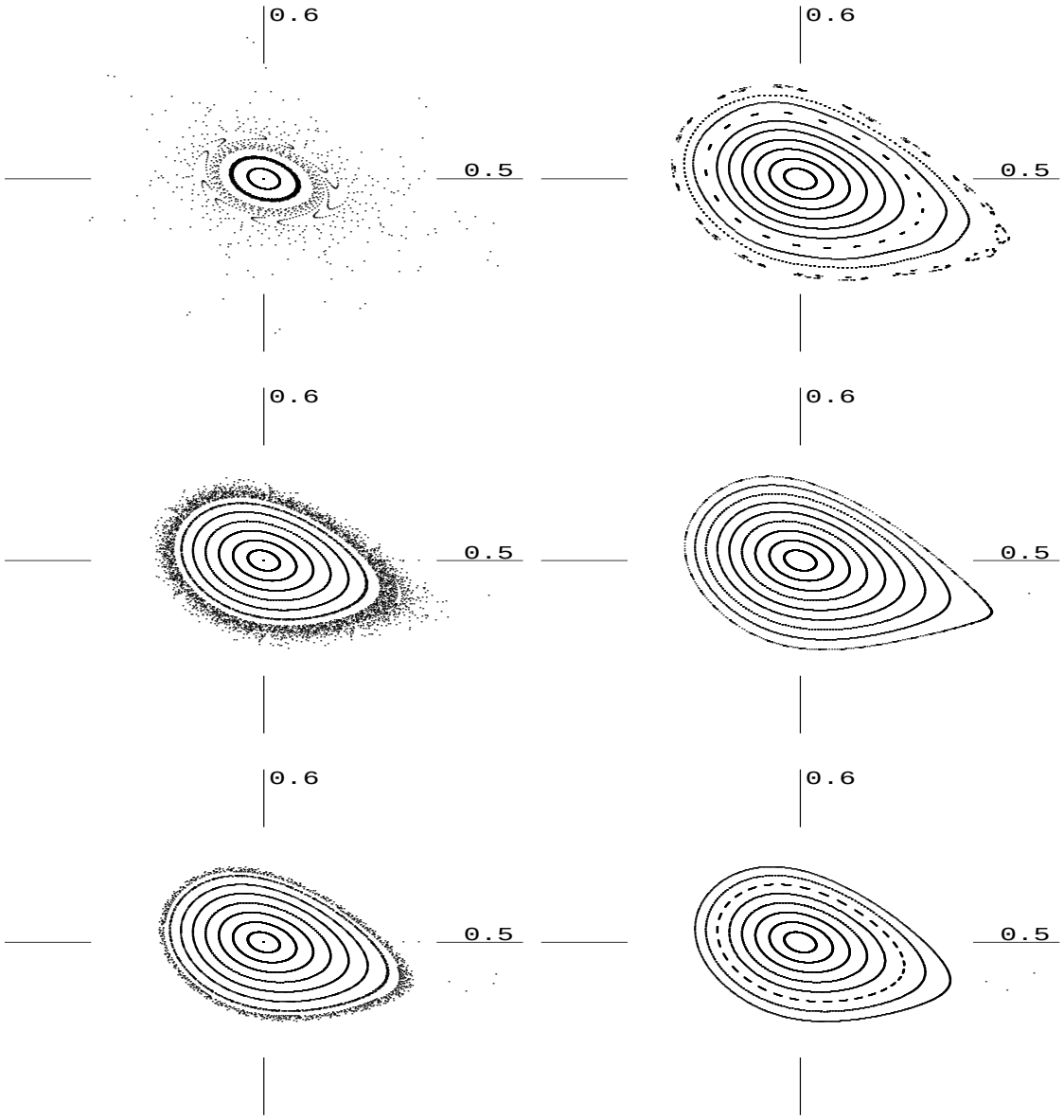

Figure 4.3: 1000 turn tracking of the random two dimensional symplectic map with the $3, 7$, and 11th order Taylor maps, and $S = 0$ symplectified map, respectively.

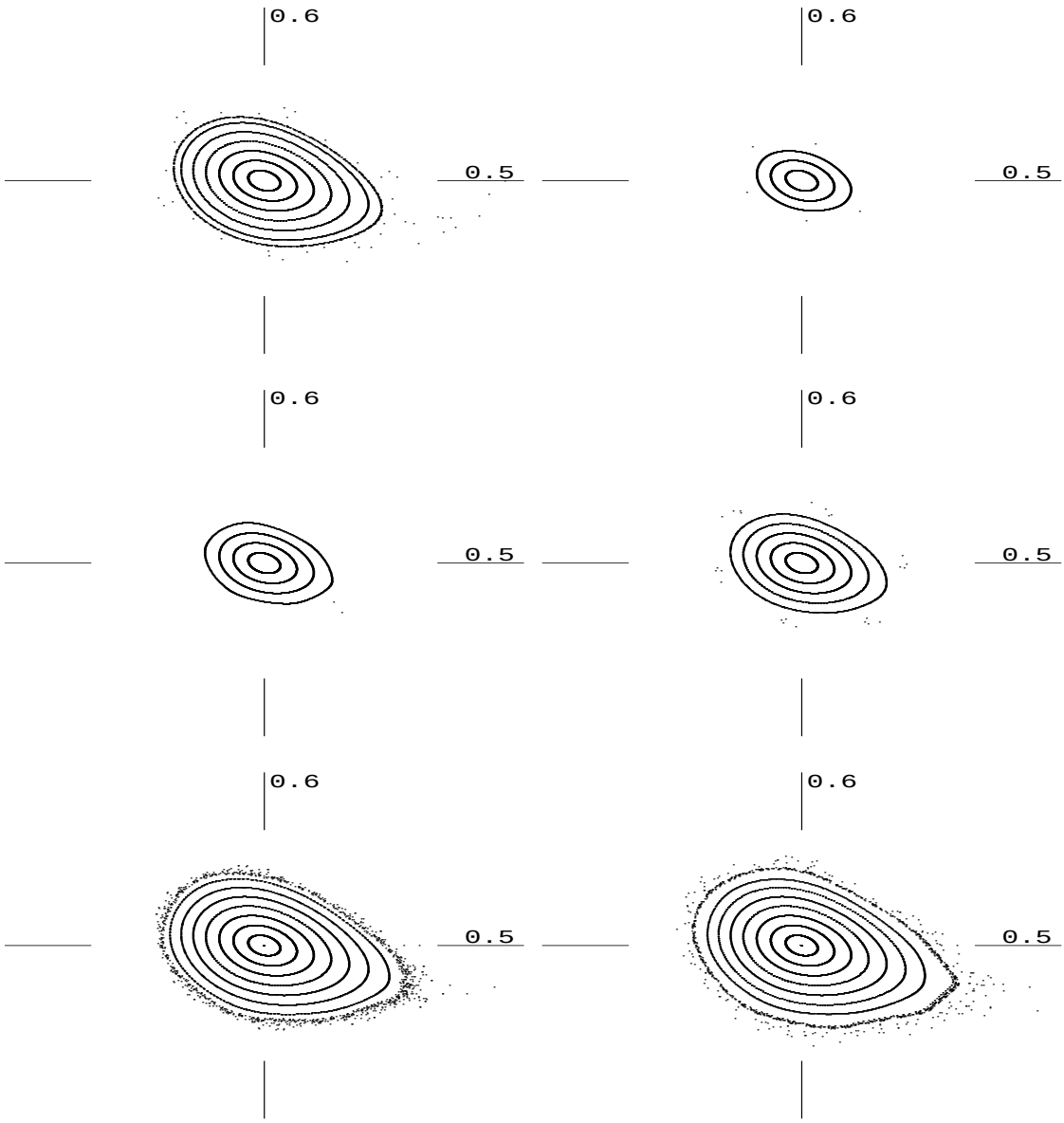

Figure 4.4: 1000 turn tracking of the random two dimensional symplectic map with the symplectified maps utilizing the F_1, F_2, F_3, F_4 generating function types for the full 11th order Taylor map, and F_2 and F_3 for the nonlinear part of the 11th order Taylor map respectively.

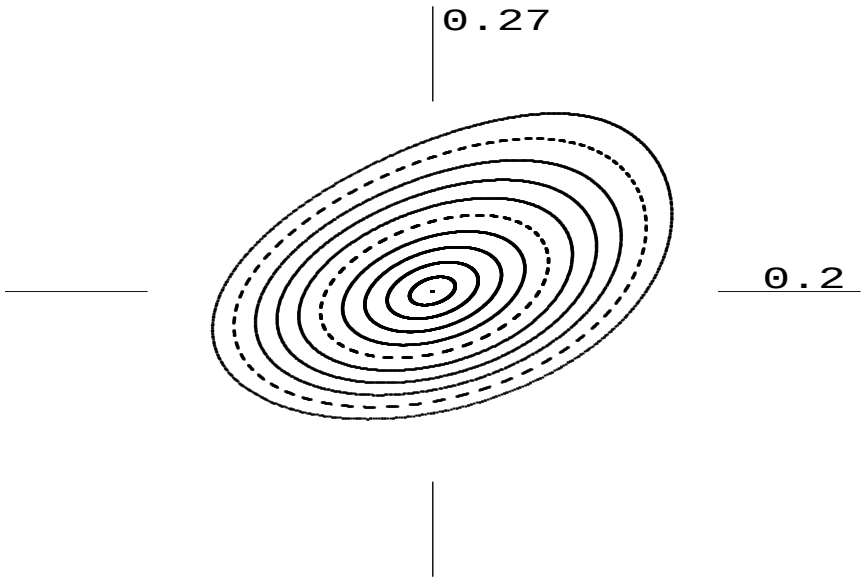

Figure 4.5: 1000 turn tracking of another random two dimensional symplectic map with the 19th order Taylor map (considered to be essentially the exact result).

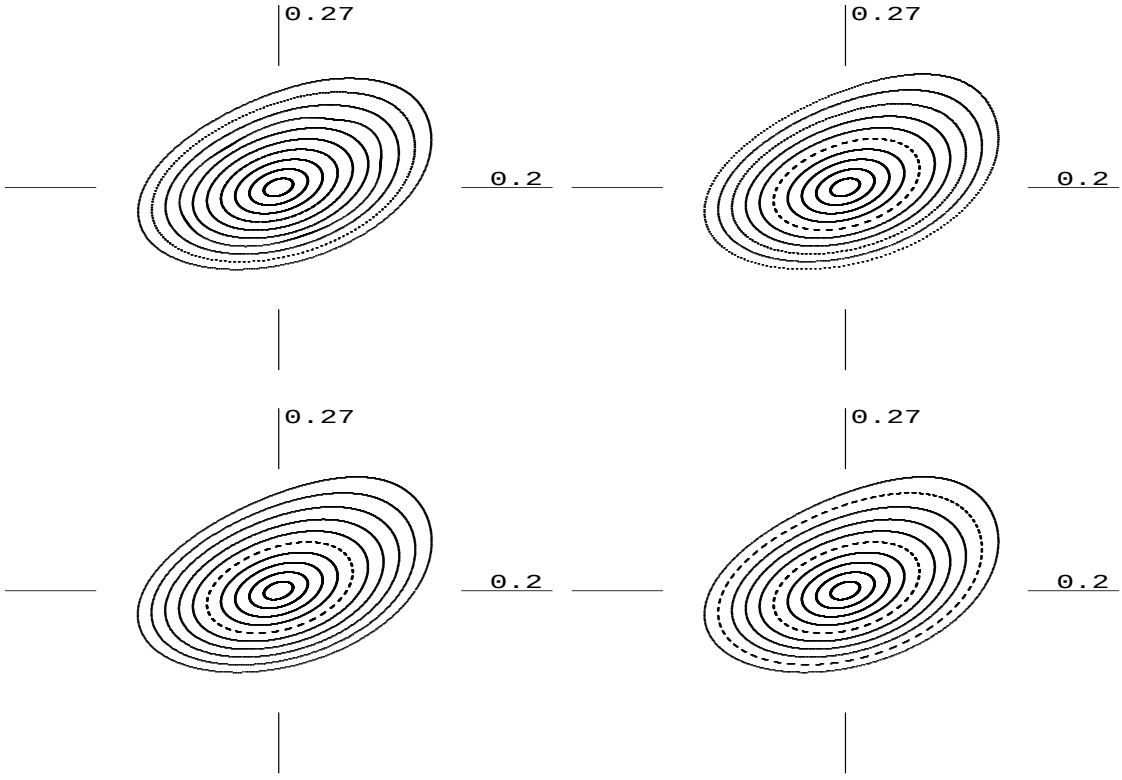

Figure 4.6: 1000 turn tracking of the second random two dimensional symplectic map with the $3, 7, 11$, and 19th order $S = 0$ symplectified maps respectively.

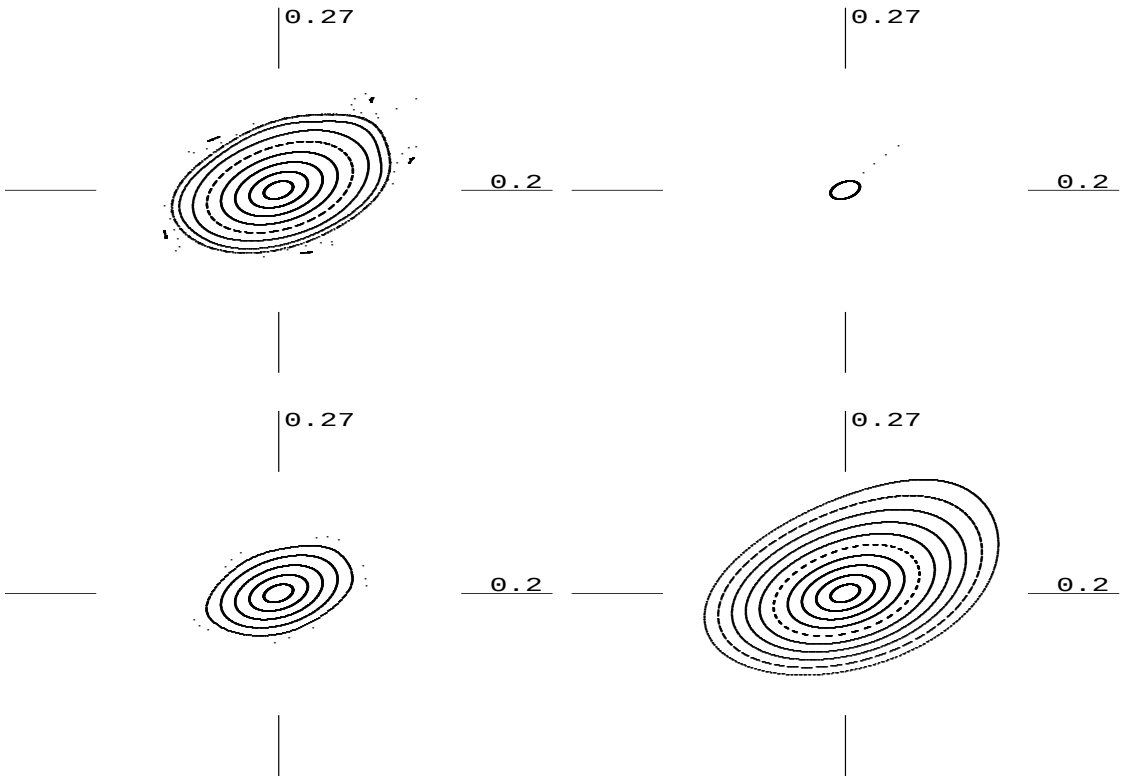

Figure 4.7: 1000 turn tracking of the second random two dimensional symplectic map with the symplectified maps using the conventional generator types F_1, F_2, F_3, and F_4 respectively.

4.2 An Anharmonic Oscillator

We consider the $2D$ anharmonic oscillator described by the Hamiltonian

$$H = \frac{1}{2}\left(p^2 + q^2\right) - \frac{1}{4}q^4, \tag{4.1}$$

which has been studied previously in [16] to compare various symplectification methods, and in [14] to study optimal Cremona symplectification. To make the comparison easier we follow the same guidelines, and present the performance of our method by symplectifying the order 3, 7 and 11 Taylor maps of the time 1 map of the flow of (4.1). We track for 1000 turns and use as initial conditions

$$\begin{cases} q = 0.1,\ 0.3,\ 0.5,\ 0.7,\ 0.9,\ 0.95,\ 0,99,\ 1.0 \\ p = 0 \end{cases} . \tag{4.2}$$

We present the order 19 Taylor map for comparison purposes. Figure 4.8 shows the orders 19 and 7 non-symplectified Taylor map tracking, and Figure 4.9 the $S = 0$ symplectified tracking pictures obtained by symplectifying the order 3, 7, 11 Taylor maps respectively. First of all, notice that this system is quite nonlinear close to the dynamic aperture. However, the symplectified tracking pictures are similar to the 19th order Taylor maps already from the order 3 symplectification. The agreement is of course better at order 7, and at order 11 also the edges at the hyperbolic fixed points are becoming visible. Moreover, the tunes of the inner particles become more accurate as the symplectification order increases.

For completeness, we also show the order 7 symplectic tracking pictures using the conventional generators in Figure 4.10. Notice that F_1 is the best conventional generator for this example. In [16] the conventional generator types F_1 and F_2 are used; F_2 after factoring out the linear part, and F_1 for the full map, including the linear part. Some unexpected discrepancies have been observed. By the general theory presented in this dissertation, the reason behind it should be clear: the two types

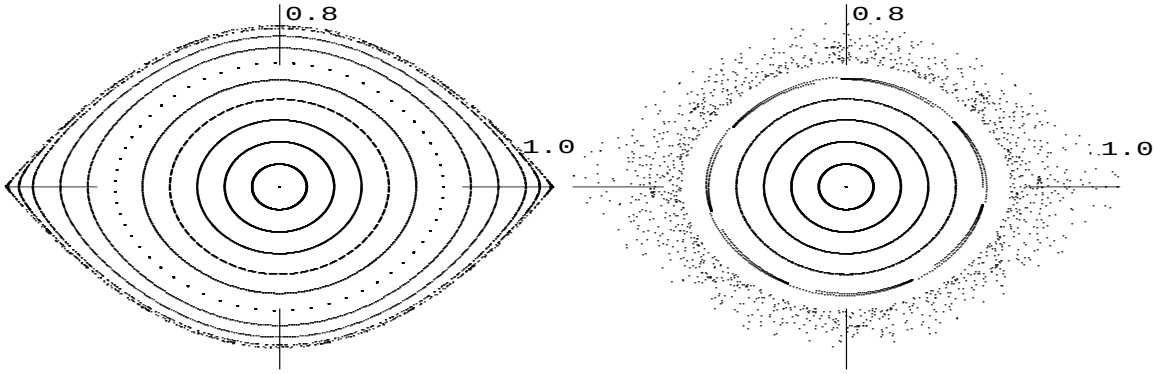

Figure 4.8: 1000 turn tracking of a anharmonic oscillator with the 19th (considered to be essentially the exact result) and 7th order Taylor maps.

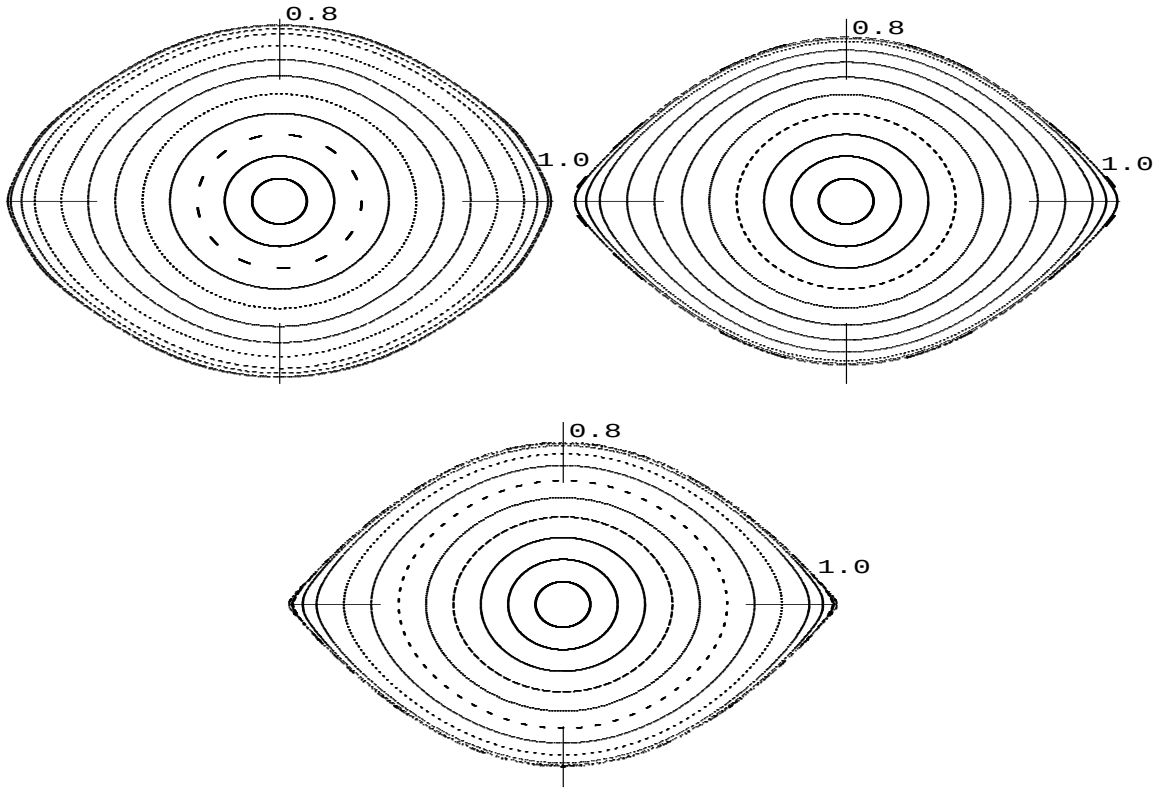

Figure 4.9: 1000 turn tracking of an anharmonic oscillator with the $3, 7$, and 11th order $S = 0$ symplectified maps respectively.

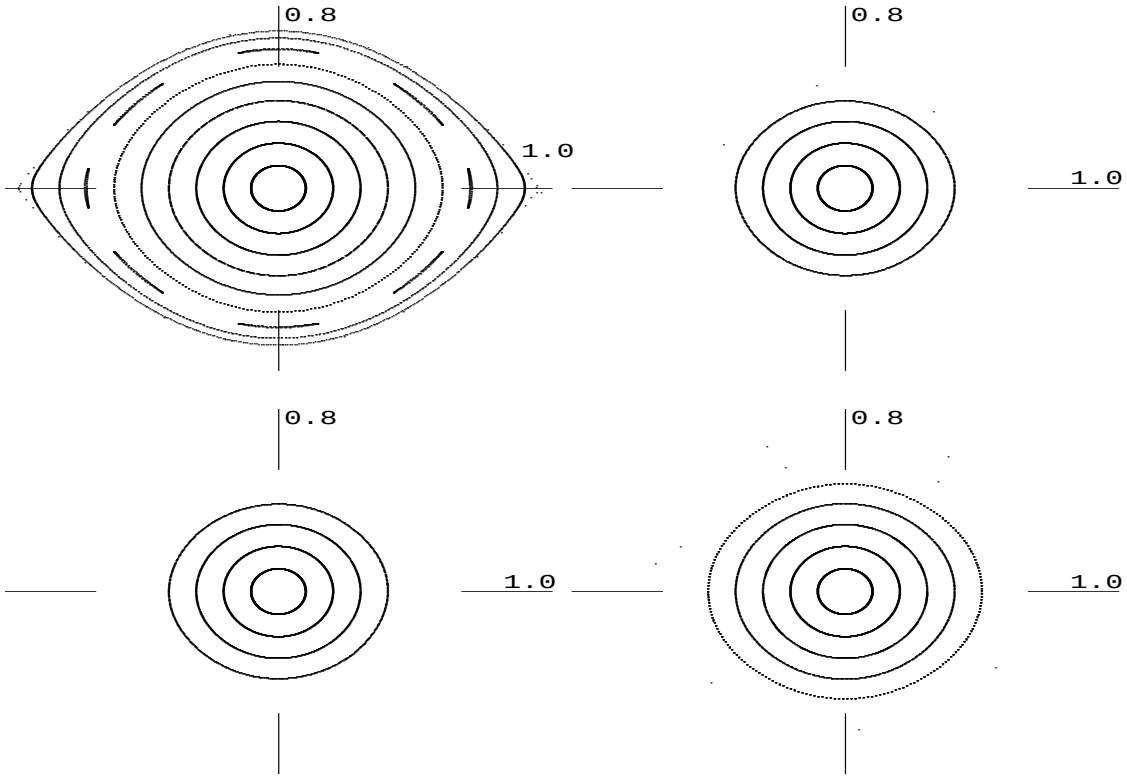

Figure 4.10: 1000 turn tracking of an anharmonic oscillator with the symplectified maps from the 7th order Taylor map, using the conventional generator types F_1, F_2, F_3, and F_4 respectively.

of generators fall into different equivalence classes. Hence, they generate different symplectic maps, with different long-term properties. In the same paper it is stated that the two unstable fixed points of the symplectified maps are moved away from $(q, p) = (\pm 1, 0)$, the locations which correspond to the exact solution. As a matter of fact, this is always the case, for any generating function symplectification method. The explanation lies in Hofer's metric, and a deep connection between fixed points of symplectic maps and critical points of generating functions (see next chapter). As a consequence, if two symplectic maps have the same fixed points, they coincide. But because symplectification can never restore the true solution, the symplectified maps will always have their fixed points moved away from the locations of the exact solution.

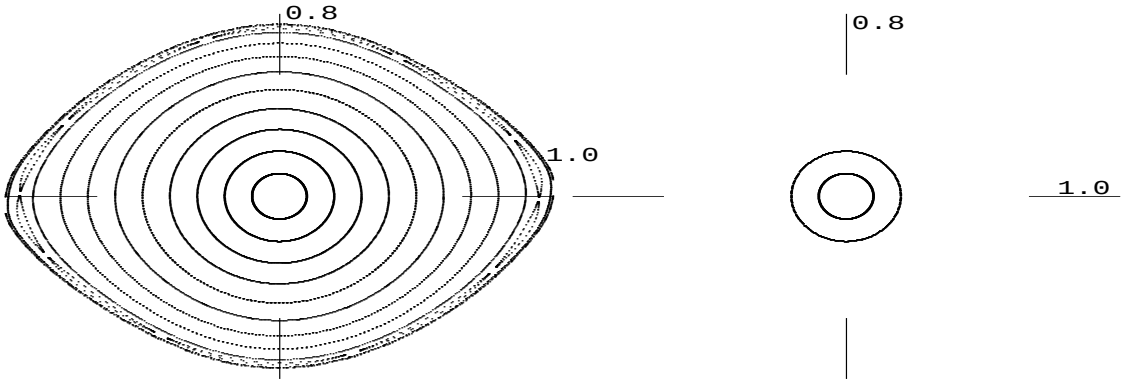

Figure 4.11: 1000 turn tracking of an anharmonic oscillator, with two random generating function types associated with symmetric matrices with entries in $[-1, 1]$ and $[-10, 10]$ respectively.

In the next step we studied random generator types, i.e. generators associated with randomly generated symmetric matrices S. In general, if the elements of S are chosen to be small, we obtain better results than if we increased the norm of S. For example see Figure 4.11 for two random types with $S_{ij} \in [-1, 1]$ and $S_{ij} \in [-10, 10]$ respectively. These figures represent typical results.

While one might say that F_1 is acceptable for estimating the dynamic aperture, but clearly $S = 0$ gives better results. So, can we find an even better generator type? We applied the following strategy: by considering the 19th order Taylor map as the exact map, and wanting to improve the agreement between the Taylor map and the symplectified map for the outermost particle (where the discrepancy is the largest, and expecting that this will not spoil the good agreement for the inner particles), starting with the $S = 0$ type of generator, we fitted the symmetric matrix S to minimize the radial correction introduced by the symplectification to the trajectory of the last particle, after one turn. We obtained the following symmetric matrix:

$$S_b = \begin{pmatrix} 0.1 & 0 \\ 0 & -0.4 \end{pmatrix}. \tag{4.3}$$

The corresponding tracking results are displayed in Figure 4.12. Comparing the various symplectic trackings with the order 19 Taylor map, we see that apparently the

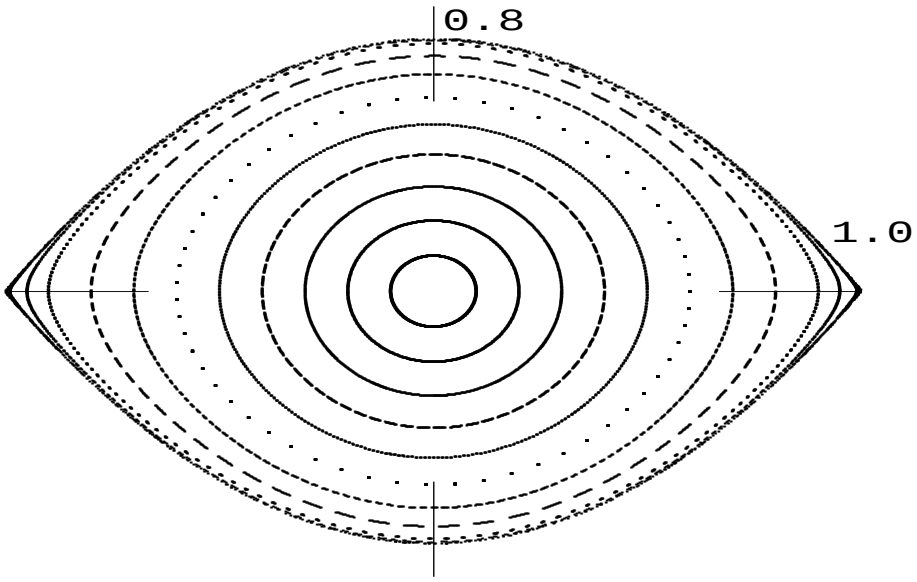

Figure 4.12: 1000 turn tracking of an anharmonic oscillator, with the generating function type associated with the symmetric matrix S_b, which was fitted to give the best results.

generator based on S_b is the best one, followed closely by the type associated to $S = 0$. Notice that the separatrix is very well reproduced, and indeed, the excellent agreement for the inner particles is not spoiled. Also, the tunes are predicted accurately over a large phase space region. Therefore, at least for this example, order 7 seems to be enough to estimate the dynamic aperture, if we use the best type of generating function symplectification.

It is worthwhile to note that by fitting S using different criteria (such as minimize radial distance over more than one turn and/or more than one particle simultaneously) we get slightly different results. In fact, only $S_b\,(1,1)$ is somewhat sensitive to these criteria (up to approximately 10% of its magnitude), but overall the tracking pictures using the different matrices look identical, or almost identical. Moreover, we start fitting these matrices from $S = 0$, and stop at the first minimum. Thus, we do not know whether S_b corresponds to a local or a global minimum. But since $S = 0$ is already a pretty good choice for an initial guess, we doubt that there exist better

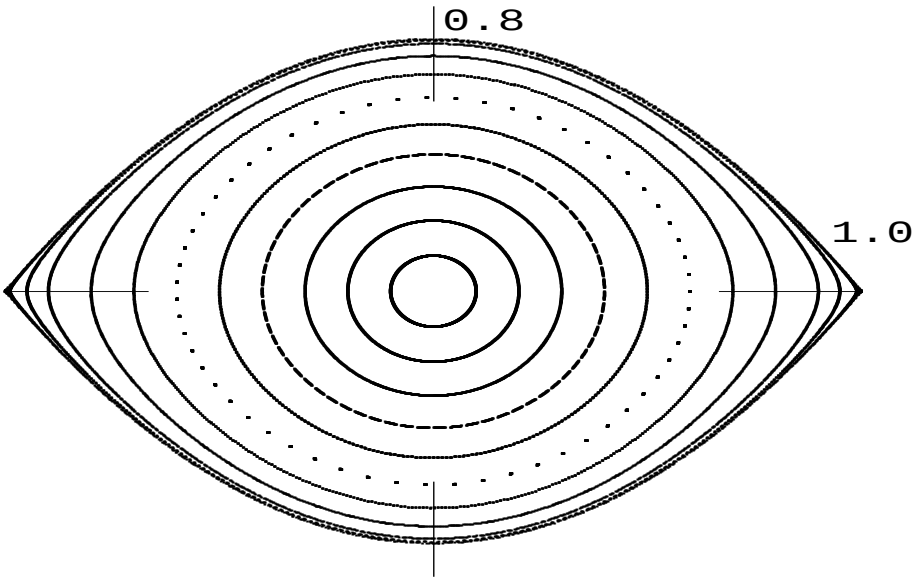

Figure 4.13: 2000 turn tracking of an anharmonic oscillator, with the generating function type associated with the symmetric matrix $S = 0$, using the 11th order 1/2 time Taylor map.

choices of symmetric matrices than S_b. The answer to why is S_b the better than $S = 0$ for this specific case will be given in the next chapter on optimal symplectification.

The high degree of nonlinearity close to the separatrix plays a significant role in the outcome of the various symplectifications. Naturally, we can compute the time 1/2 map of the same Hamiltonian flow, track it for 2000 turns, and plot every second turn. As a result, we track the same system for the same amount of time, hence the tracking pictures should look the same. However, the maps are less nonlinear, and hence the domain of definition of the generators should enlarge. We did just that with the $S = 0$ type and order 11, and obtained Figure 4.13. Now the results are much better, and a closer look reveals that the 11th order time 1/2 map symplectified with $S = 0$ is better than the 11th order time 1 or even time 1/2 map symplectified with S_b.

As a side note, we mention that the square root trick could be used to gain more confidence in the accuracy of our symplectified maps. Namely, if we track with a

symplectified map N turns ($N \approx 10^3$) and plot every turn, then track $2 \cdot N$ turns with its square root and plot every second turn, we should get the same pictures. If not, we keep taking square roots until the pictures become almost identical. Then, the resulting map can be more or less trusted for long term tracking ($N \gg 10^3$).

Finally, to get a better feeling of what the symplectification does at the local level, we plot the corrections introduced by the symplectification method to the trajectory of the stable particles over one turn. For example, Figures 4.14, 4.15, and 4.16 show the corrections (magnified by a certain factor for convenient viewing) of the F_i, $i = 1, 2, 3, 4$ and $S = 0$ types to the order 7th order Taylor approximation. The spikes point in the direction of the correction, and their length is proportional to the magnitude of the correction. We used color coding to express correction radially outwards (lighter spikes; green in the pdf file), or radially inwards (darker spikes; red in the pdf file). The three initial conditions for the three sets of pictures are $(q, p) = (0.1, 0)\,; (0.5, 0)\,; (0.9, 0)$. The general conclusion that can be drawn from these pictures is that if the Taylor map is accurate enough, the best symplectification method introduces the least amount of correction, in both radial and angular direction. Moreover, the corrections in the radial direction are usually much smaller than the correction in the angular direction (the actual values are shown in the upper part of the figures in the following order: number of particles, average radial correction, and average angular correction). This suggests that for dynamic aperture (i.e. region of stability) estimation there is a slightly lower precision needed than for the accurate prediction of the tunes (i.e. average angle advances per turn). As expected, the corrections' magnitude are increasing with distance from the origin and number of turns.

In the introduction (chapter 1), it was mentioned that one of the favorable properties of the symplectic methods is their linear global error propagation, in contrast

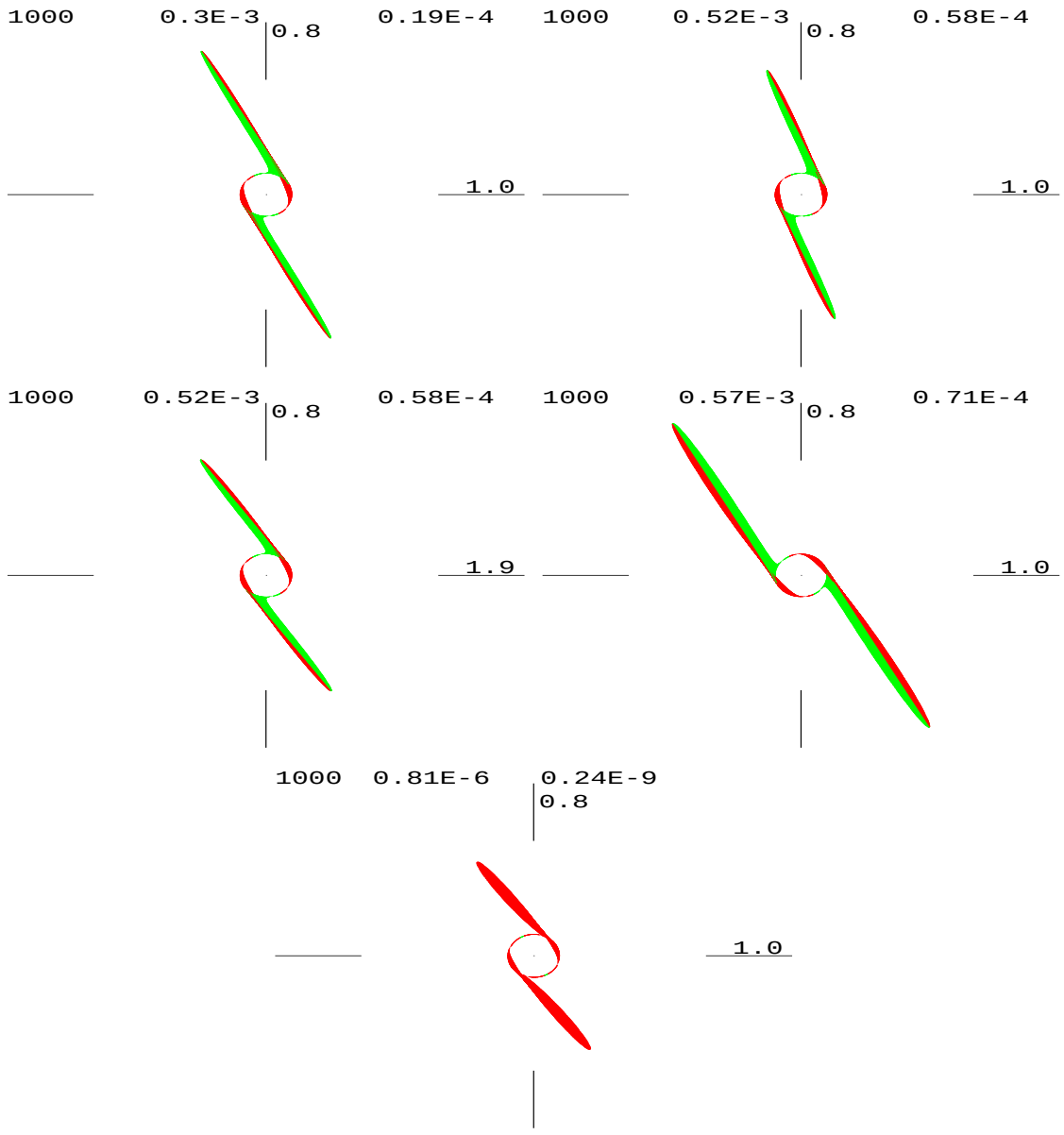

Figure 4.14: Corrections introduced by the symplectification to particles of small amplitude, which are predicted by symplectic tracking with generating function type associated with the symmetric matrix $S = 0$ to be on a invariant curve (a stable particle). The figure shows the correction with respect to the 7th order Taylor map of the symplectifications using the convential (the magnification factor is 10^3) as well as the $S = 0$ (the magnification factor is 10^6) generator types.

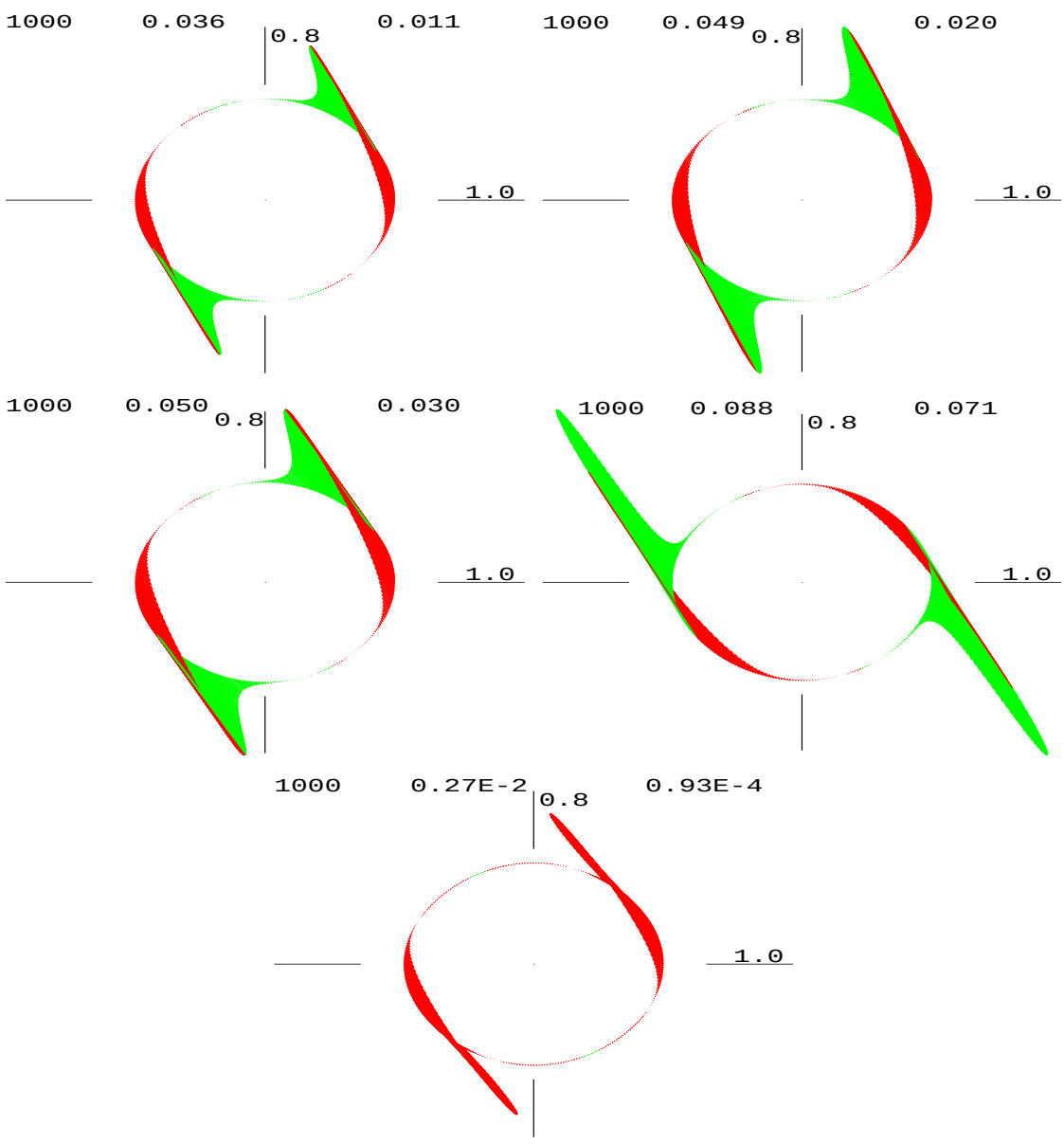

Figure 4.15: Corrections introduced by the symplectification to particles of medium amplitude, which are predicted by symplectic tracking with generating function type associated with the symmetric matrix $S = 0$ to be on a invariant curve (a stable particle). The figure shows the correction with respect to the 7th order Taylor map of the symplectifications using the convential (the magnification factor is 1) as well as the $S = 0$ (the magnification factor is 10^2) generator types.

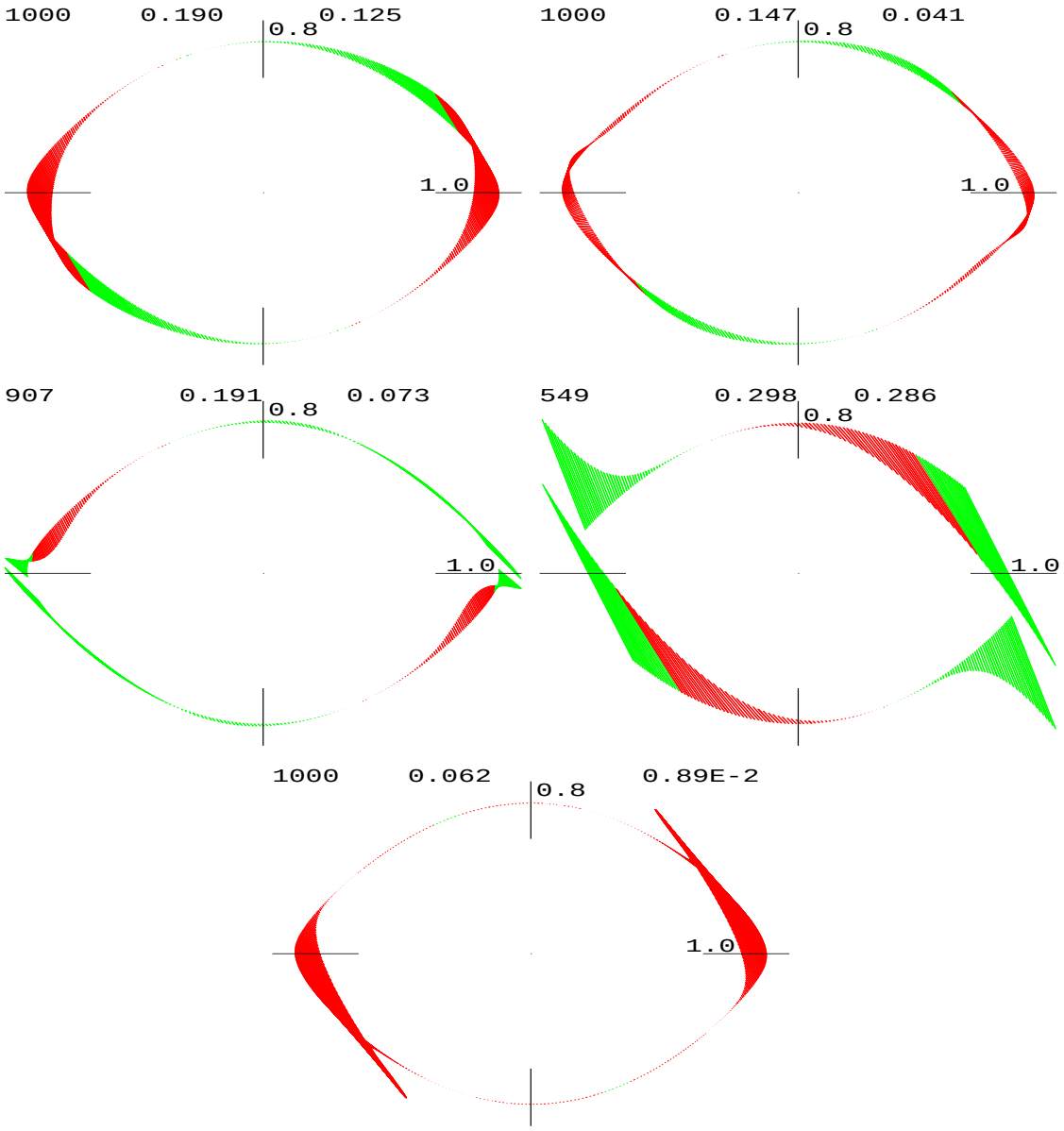

Figure 4.16: Corrections introduced by the symplectification to particles of large amplitude, which are predicted by symplectic tracking with generating function type associated with the symmetric matrix $S = 0$ to be on a invariant curve (a stable particle). The figure shows the correction with respect to the 7th order Taylor map of the symplectifications using the convential (the magnification factor is 1) as well as the $S = 0$ (the magnification factor is 10) generator types.

with quadratic error propagation of nonsymplectic methods. To illustrate quantitatively this phenomenon, we tracked a particle, with initial condition $(q, p) = (0.5, 0)$, 1000 turns through the time one map of the anharmonic oscillator's flow, using the exact solution (represented by the 19th order Taylor map), the 7th order Taylor map, and symplectic tracking with the order 7 Taylor map and generator type associated with $S = 0$. As shown in Figure 4.17, for a few tens of turns the Taylor map tracking is more accurate than the symplectic tracking, then the error of the nonsymplectic tracking grows fast, while the symplectic tracking stays at small error levels throughout the 1000 turns. The linear global error propagation of the symplectic method versus quadratic error propagation of the nonsymplectic method is clear from Figure 4.18, where we superimposed two lines with slopes one and two, respectively, for easy identification. Interestingly enough, initially, for a short period of time, the nonsymplectic method is accurate enough to pass as a "pseudo-symplectic" one by having slope one, but after ≈ 50 turns the slope suddenly becomes approximately two.

4.3 An Exactly Symplectic Quadratic Map

In [51] the following quadratic map is considered:

$$\mathcal{M} = \mathcal{N} \circ \mathcal{L}, \tag{4.4}$$

where

$$\mathcal{L} = \begin{pmatrix} \cos\theta & \sin\theta \\ -\sin\theta & \cos\theta \end{pmatrix}, \tag{4.5}$$

with $\theta = \frac{\pi}{3}$, and

$$\mathcal{N} \begin{pmatrix} q \\ p \end{pmatrix} = \begin{pmatrix} q - 3\,(q+p)^2 \\ p + 3\,(q+p)^2 \end{pmatrix}. \tag{4.6}$$

It is easy to check that it is exactly symplectic. We study this map because it is a simple map with a nontrivial behavior under iteration, and it is exactly symplec-

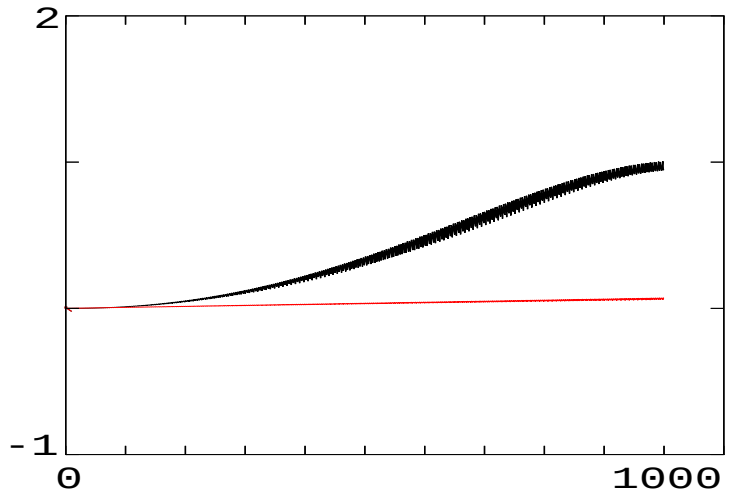

Figure 4.17: Global error propagation in the case of nonsymplectic versus symplectic tracking of a particle for 1000 turns of the anharmonic oscillator's time one map. For the tracking, the order 7 Taylor map was used for nonsymplectic tracking, and generator of type associated with $S = 0$ for the symplectic tracking. After a short transient period, the nonsymplectic method gives large errors, while the symplectic method's error stays small.

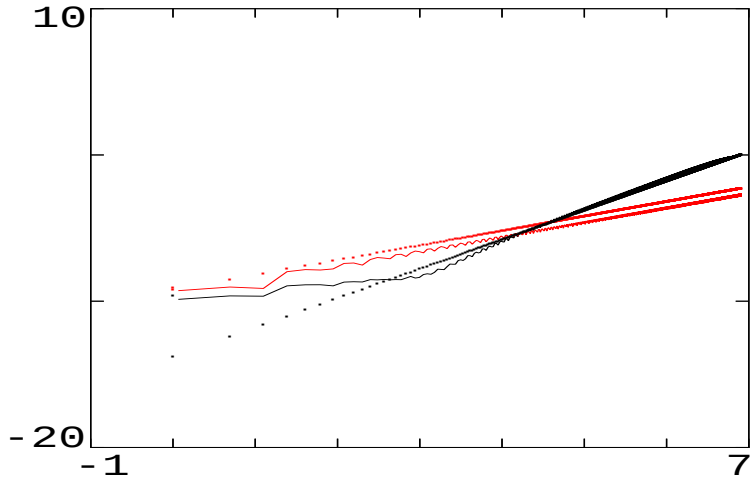

Figure 4.18: The global error propagation in a log-log scale of the case shown in Figure 4.17. After a short transient period, the nonsymplectic method's slope is two, and the symplectic method's slope is one. The dotted lines have exact slopes one and two, respectively.

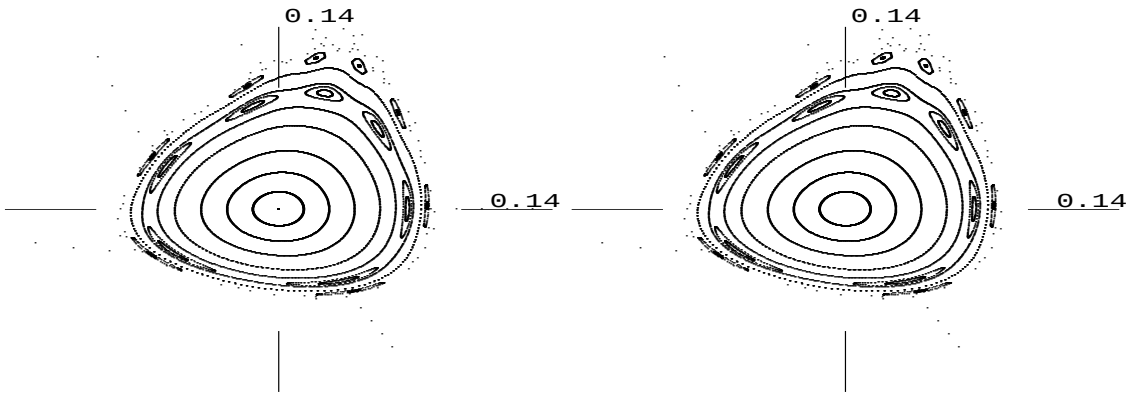

Figure 4.19: 1000 turn tracking of a quadratic symplectic map with the 3rd order Taylor map (the exact result), and the 3rd order $S = 0$ symplectified map (which also gives the exact result).

tic. Moreover, in [51] it is shown that symplectification of (4.4) using conventional generating functions gives very poor results. As in [51], we also use third order symplectification. The exact result and the $S = 0$ symplectified result for some choice of initial conditions is shown in Figure 4.19. The agreement is excellent. In fact, the results coincide; $S = 0$ gives the exact solution. As a comparison, Figure 4.20 shows the results for the Goldstein generators, and indeed they give very poor results.

The generating function of type $S = 0$ for (4.4) computed according to (2.9) is

$$\begin{aligned} F(q,p) &= 0.04903810567665787 \cdot q^3 - 0.5490381056766573 \cdot q^2 p \\ &\quad +2.049038105676657 \cdot qp^2 - 2.549038105676658 \cdot p^3. \end{aligned} \tag{4.7}$$

Moreover, it can be shown that the $S = 0$ generator type can represent exactly any quadratic symplectic map. We also mention that there exist other generator types that can be used to represent exactly any quadratic symplectic map. However, in this group there are none from the conventional, or even the Poincaré types.

It was mentioned in section 3.5 that the numerics used for solving the implicit equations also plays an important role in tracking. The tracking pictures in Figure 4.20 have been obtained using fixed point iterations. The same set of tracking pictures

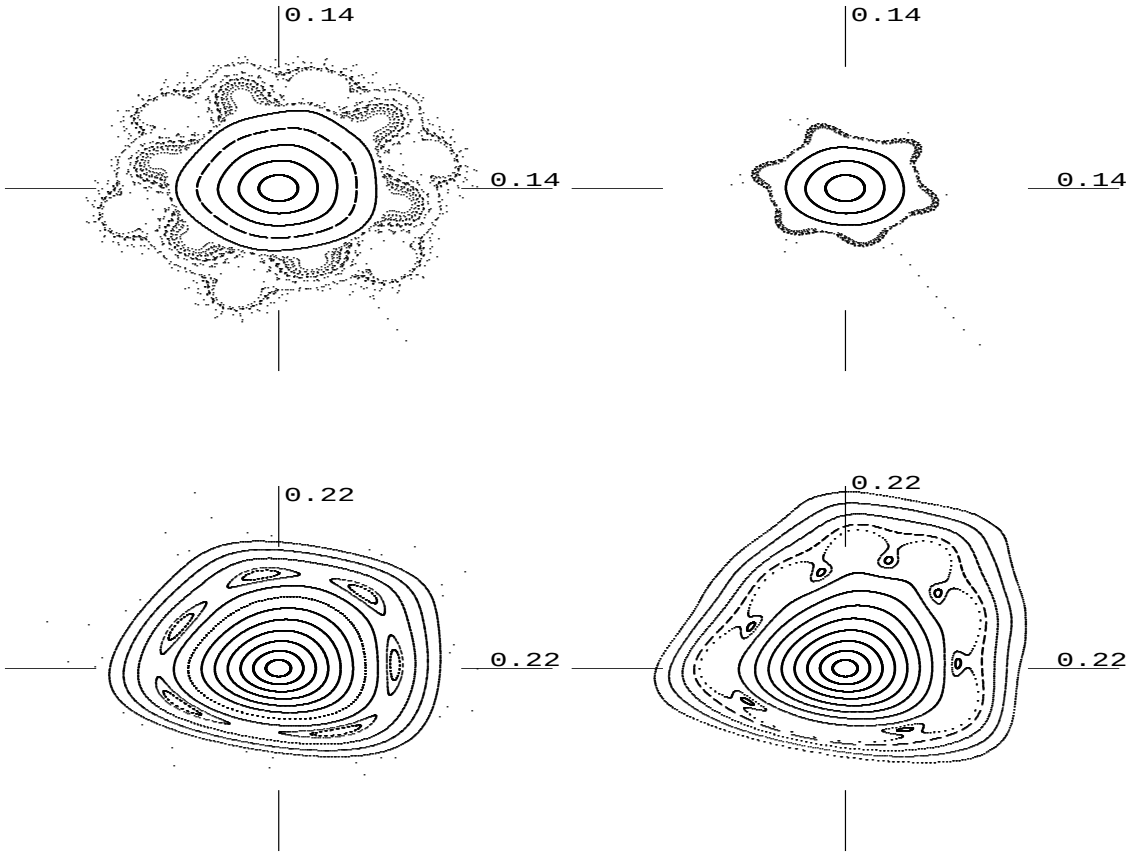

Figure 4.20: Symplectic tracking with the four conventional generator types (F_1 through F_4), for the exactly symplectic quadratic map, using fixed point iterations to solve the implicit equations.

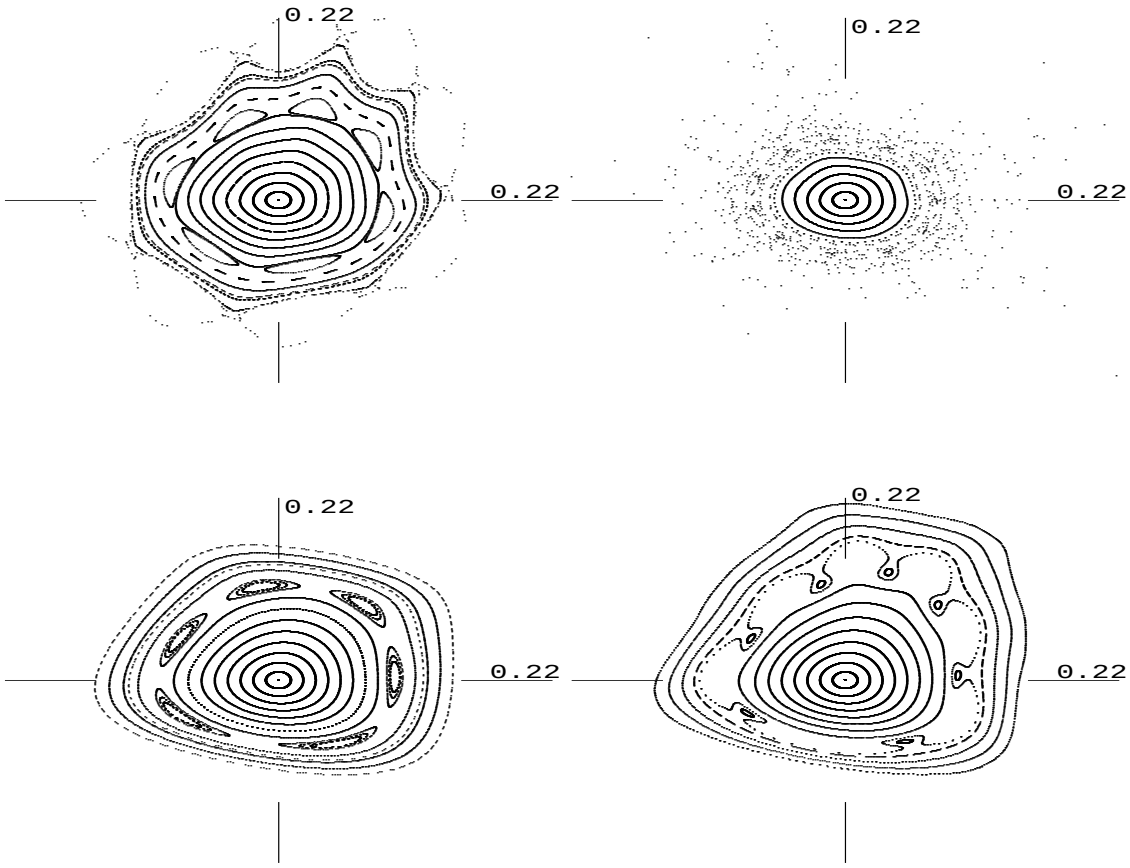

Figure 4.21: Symplectic tracking with the four conventional generator types (F_1 through F_4), for the exactly symplectic quadratic map, using Newton's method to solve the implicit equations.

obtained by solving the implicit equations utilizing Newton's methods is shown in Figure 4.21. Clearly, we obtained different pictures for F_1 through F_3, and identical pictures for F_4. This points out quantitatively the importance of the numerics, namely the size of the domain of convergence of the two methods. As expected, the F_4 case produces identical pictures, because it is the only case where both methods converge over the region of the particles tracked in this example.

4.4 Muon Accelerators

In this section we study the effects of symplectification on truncated Taylor maps of rings of the proposed Muon Collider and Neutrino Factory complex, utilizing lattices of the Neutrino Factory Storage Ring [52] and the Proton Driver [53] to illustrate the effects. For an overview of the current status of the muon collider research and development see [54], as well as the earlier feasibility study on muon colliders [55]. Since the amount of nonlinearity and emittance in the muon machines far exceed that of other machines, the muon accelerators are not comparable to most machines, and for these machines it turned out that even for short term tracking symplectification is essential.

4.4.1 A Neutrino Factory Lattice

Previous work exposed a variety of nonlinear effects in the lattice described in [52], of the proposed Neutrino Factory. Nonlinearities are due to the so-called kinematic effect, fringe fields, small circumference and large aperture. The muons' lifetime is less than 1000 turns. In spite of such a short tracking time, it is still interesting to see how the generating function symplectification method works in a case of practical interest, where nonlinearities play an important role. We computed order 8 maps of several realization of the Neutrino Factory. In the following we present side-by-side the tracking pictures obtained from order 8 Taylor map tracking and the corresponding $S = 0$ symplectic tracking.

In particular, we take 4 different realizations of the Neutrino Factory by tracking the ideal lattice with 4 sets of fringe fields which differ both in fall-off shape and length [13]. We will refer to them as case 1, 2, 3, and 4. Figure 4.22 represents the result of case 1 for some initial conditions along the horizontal axis. We see that the

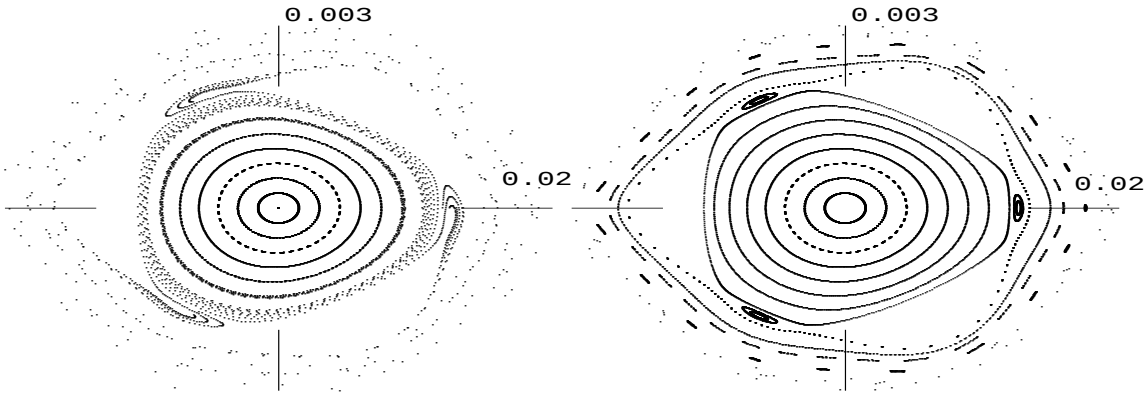

Figure 4.22: 1000 turn tracking of the case 1 of a lattice of the proposed Neutrino Factory with the 8th order Taylor map, and the corresponding $S = 0$ symplectified map.

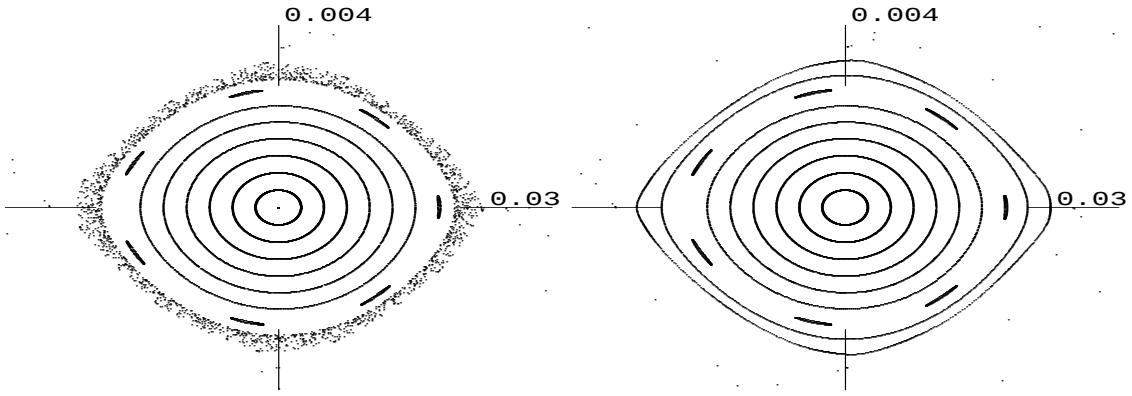

Figure 4.23: 1000 turn tracking of the case 2 of a lattice of the proposed Neutrino Factory with the 8th order Taylor map, and the corresponding $S = 0$ symplectified map.

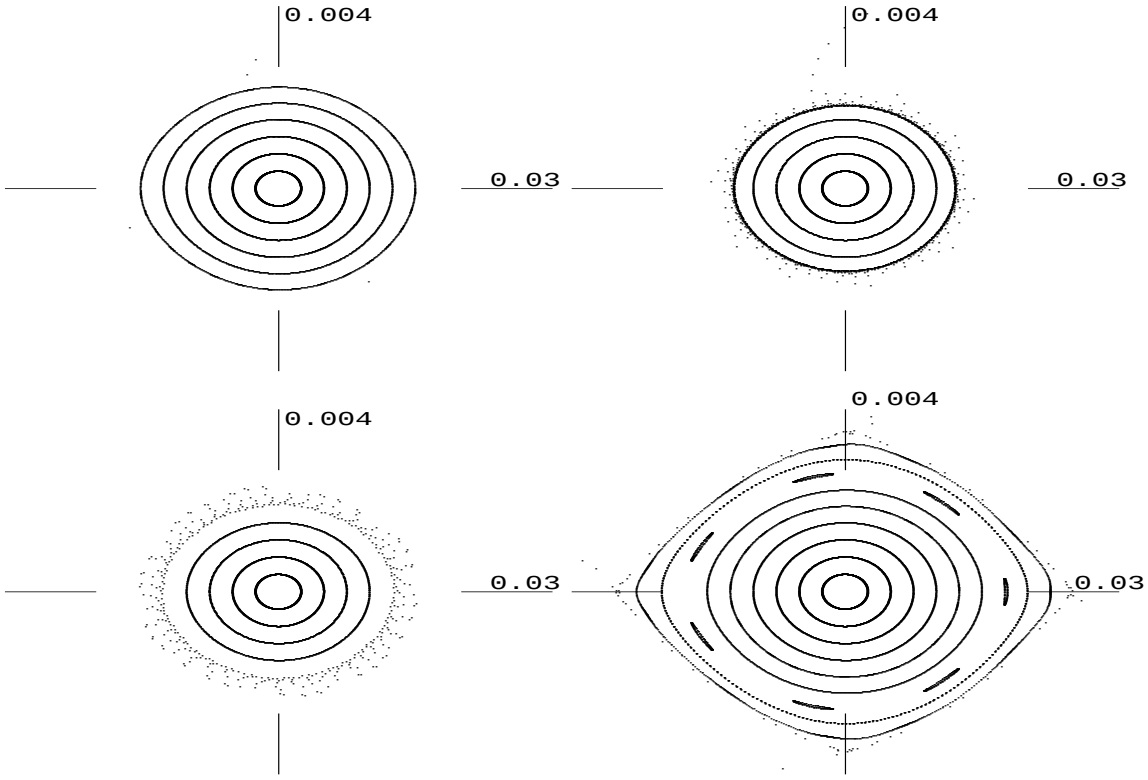

Figure 4.24: 1000 turn symplectic tracking of the case 2 of a lattice of the proposed Neutrino Factory with the conventional generating functions (F_1 through F_4).

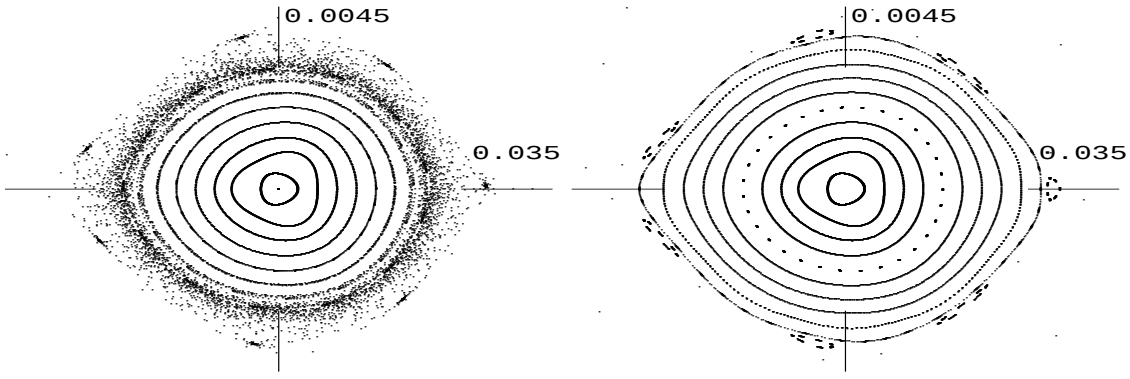

Figure 4.25: 1000 turn tracking of the case 3 of a lattice of the proposed Neutrino Factory with the 8th order Taylor map, and the corresponding $S = 0$ symplectified map.

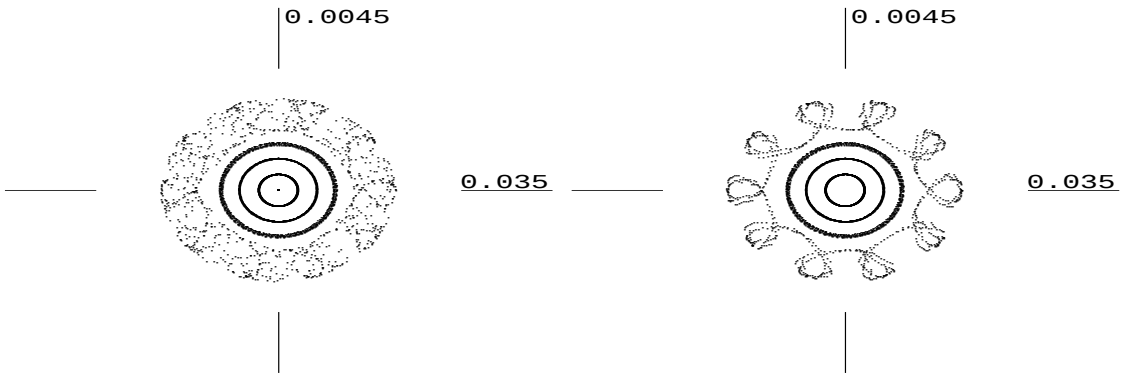

Figure 4.26: 1000 turn tracking of the case 4 of a lattice of the proposed Neutrino Factory with the 8th order Taylor map, and the corresponding $S = 0$ symplectified map.

Taylor map is not accurate enough to give a good estimation of the dynamic aperture, or to resolve the third order resonance. With the $S = 0$ symplectified tracking we obtain a clear third order resonance, bigger dynamic aperture, as well some higher order island structure. Also notice that for a few particles close to the origin, where even the 8th order Taylor map is accurate enough for short term tracking, the two pictures are alike, including the tunes. We mention that case 1 was one of the most nonlinear realizations of the Neutrino Factory.

A less nonlinear lattice is case 2. The corresponding pictures are presented in Figure 4.23. Here, the 8th order Taylor map looks more accurate than in the previous case, and has a clearly defined 7th order resonance structure. We can see that this resonance is preserved by the symplectified map, and again we get a somewhat bigger dynamic aperture. By comparison, the conventional generators for this case cannot be used to reliably estimate the DA, as depicted in Figure 4.24.

Case 3, presented in Figure 4.25, is interesting because the Taylor map predicts a chaotic region, and just on the outside rim of it something that looks like the remnants of some high order resonance. Indeed, the symplectified map confirms that there is a 7th order resonance just outside the dynamic aperture, but there is no chaotic region

whatsoever, as required by theory.

Finally, in case 4 we are looking at some particles launched along the diagonal in geometric space. As expected, Figure 4.26 shows reduced dynamic aperture, and the onset of the chaotic region. However, while the Taylor map predicts a completely chaotic trajectory, the symplectified map shows that there is still some structure left in the phase space trajectory of the outermost particle.

4.4.2 The FNAL Proton Driver

The ideal lattice of the Proton Driver is quite nonlinear. Hence, symplectification introduced considerable changes even when applied to the order 15 truncated Taylor map. The correctness of the symplectic tracking with generator type associated with $S = 0$ has been checked against accurate numerical integration, giving excellent agreement. The tracking results in the $(x - a)$ and $(y - b)$ planes without and with symplectification are depicted in Figure 4.27. Notice that the third order resonance in the $(x - a)$ figure is missing completely in the Taylor map tracking, but accurate numerical integration shown in Figure 4.28 confirms its existence, increasing the confidence level in the correctness of the symplectification approach. The particles were launched along the x and y axes respectively, and were tracked for 1000 turns.

4.5 The Large Hadron Collider (LHC)

Another interesting case for symplectification is provided by the LHC. Here we present non-symplectic tracking of the LHC v.5.1 versus symplectic tracking, with seven different generator types. In Figure 4.29, tracking 10^5 turns utilizing the order 8 Taylor map of the ideal lattice, the $S = 0$ generator type, and F_1, F_2, F_3, F_4 for the full map are presented. The same results, with a detailed account of fringe fields included in

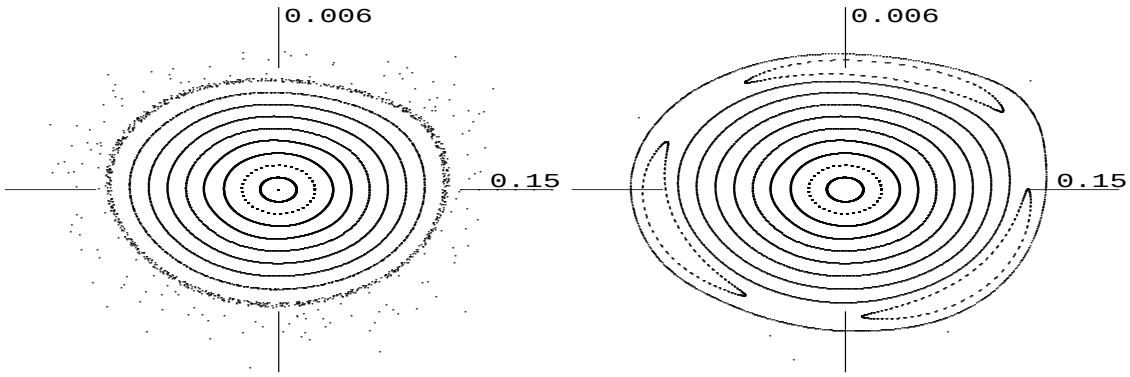

(a) $(x - a)$ tracking pictures

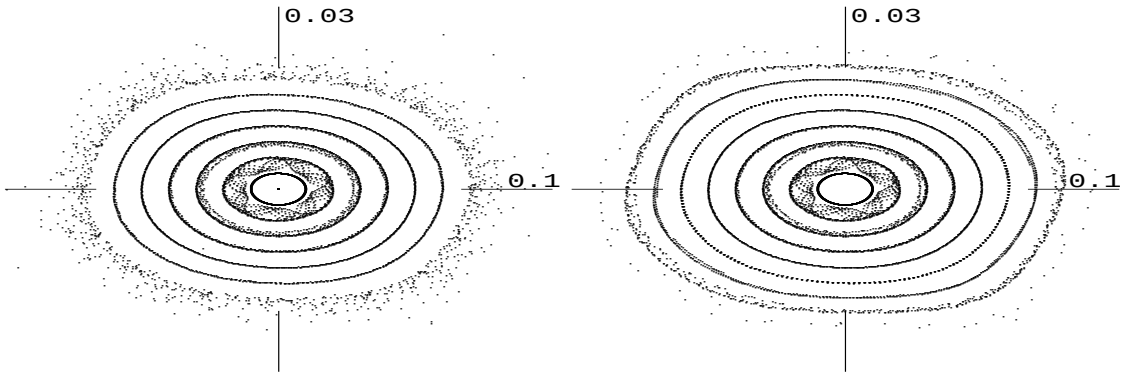

(b) $(y - b)$ tracking pictures

Figure 4.27: 1000 turn tracking of the FNAL Proton Driver with the 15th order Taylor map, and the corresponding $S = 0$ symplectified map.

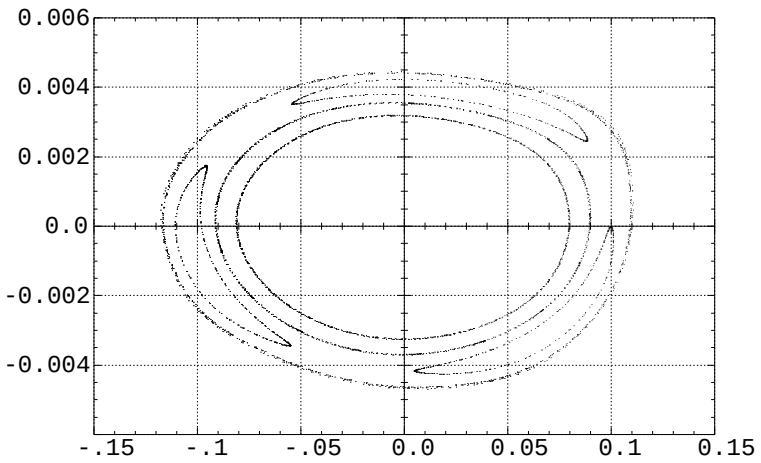

Figure 4.28: 1000 turn $(x-a)$ tracking of the FNAL Proton Driver with the element-by-element numerical integration.

the simulation (for more information on accurate fringe field maps for the LHC see chapter 10) are shown in Figure 4.30. For the sake of completeness, we depict the results without and with fringe fields for the case of F_2 and F_3 symplectified nonlinear parts of the map in Figures 4.31 and 4.32. Again, the terrible performance of some of the generator types point out the necessity of optimal symplectification studies, and shows that the right generator type ($S = 0$) gives excellent results once again.

The topic of optimal symplectification from a very general standpoint is the subject of the next chapter.

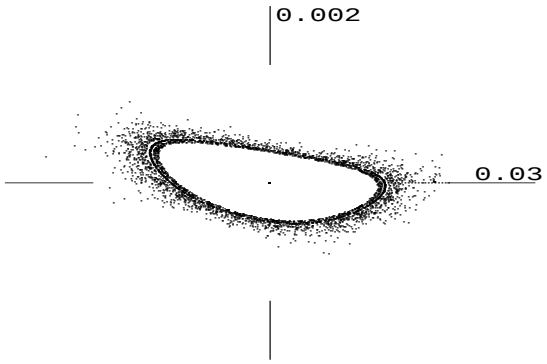

(a) 8th order Taylor map

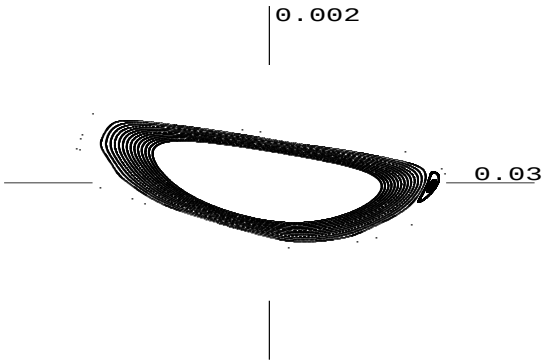

(b) $S = 0$ symplectified map

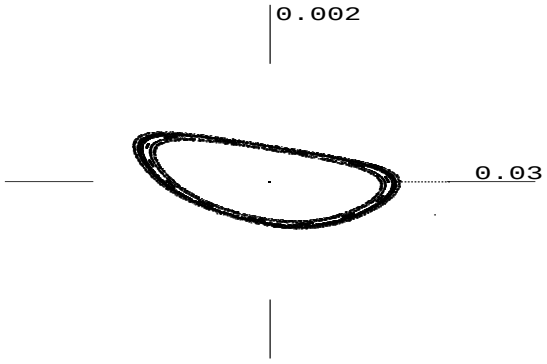

(c) F_1 symplectified full map

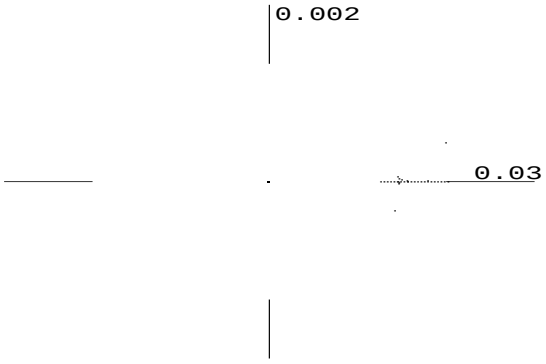

(d) F_2 symplectified full map

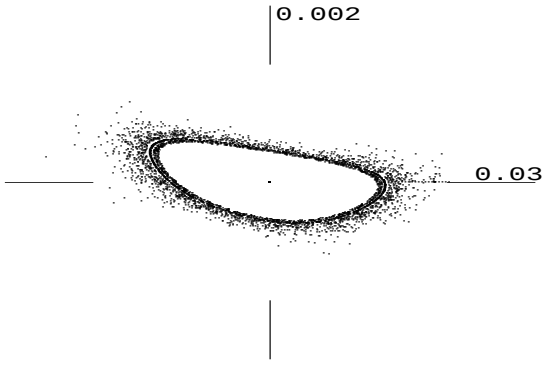

(e) F_3 symplectified full map

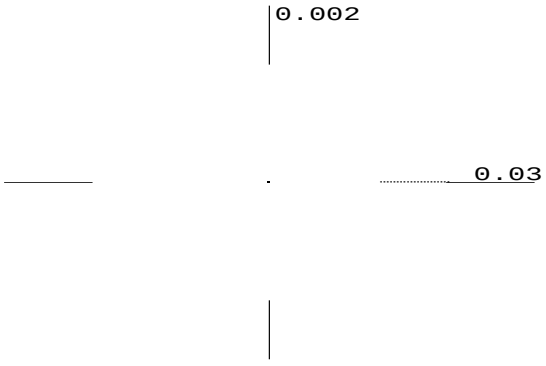

(f) F_4 symplectified full map

Figure 4.29: 10^5 turn tracking of the LHC with the 8th order Taylor map, and the corresponding various symplectified maps, without fringe fields taken into account.

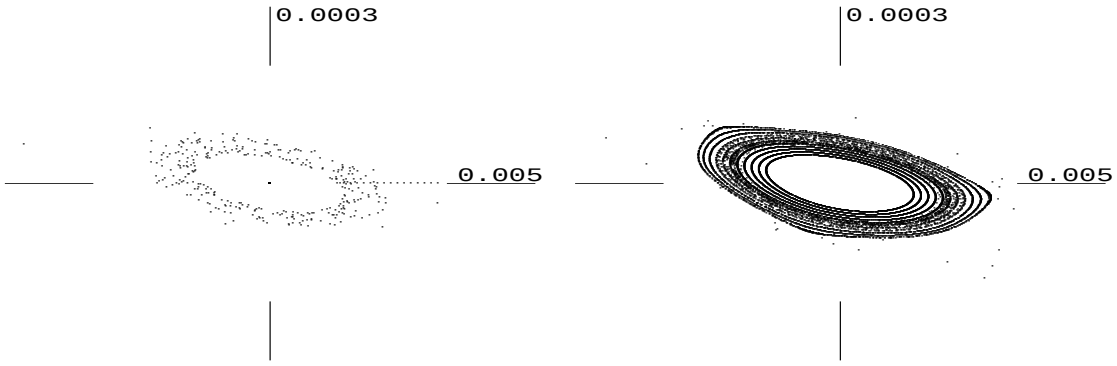

(a) 8th order Taylor map

(b) $S = 0$ symplectified map

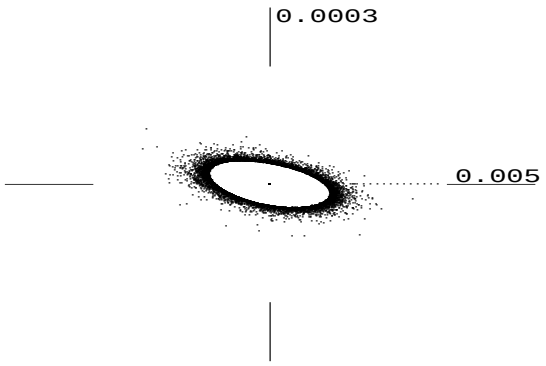

(c) F_1 symplectified full map

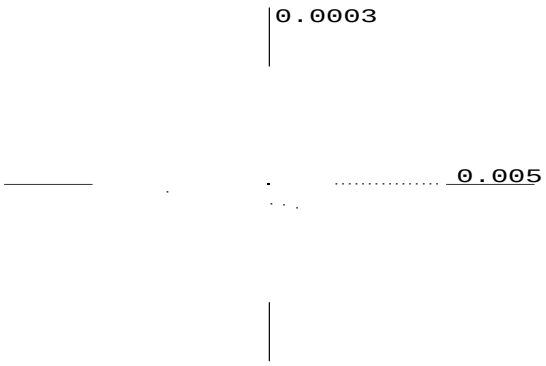

(d) F_2 symplectified full map

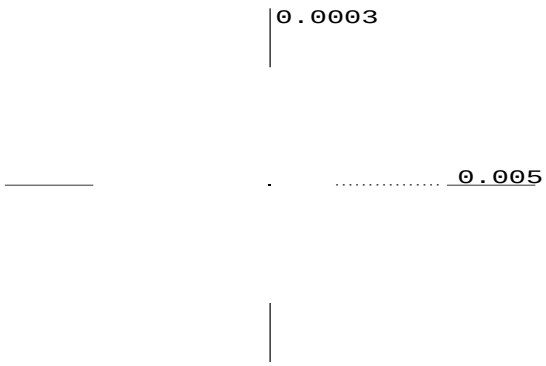

(e) F_3 symplectified full map

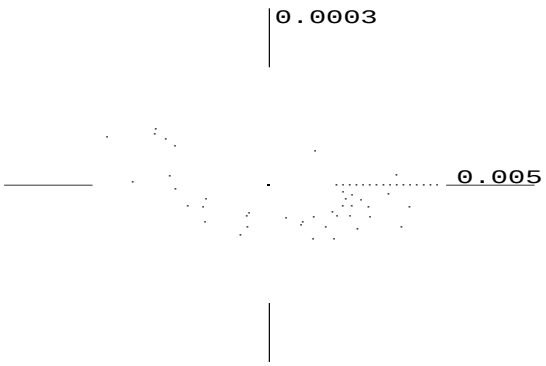

(f) F_4 symplectified full map

Figure 4.30: 10^5 turn tracking of the LHC with the 8th order Taylor map, and the corresponding various symplectified maps, with detailed fringe fields taken into account.

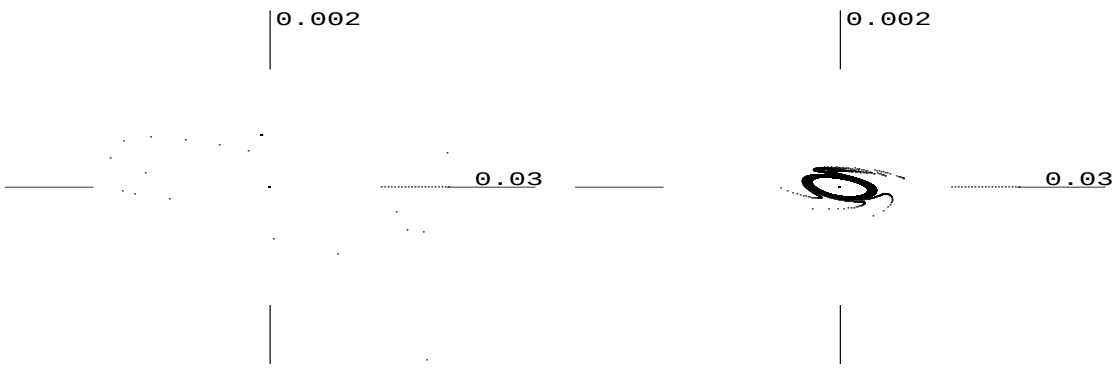

(a) F_2 symplectified nonlinear part of the map

(b) F_3 symplectified nonlinear part of the map

Figure 4.31: 10^5 turn tracking of the LHC with the F_2 and F_3 symplectified nonlinear parts of the 8th order Taylor map, without fringe fields taken into account.

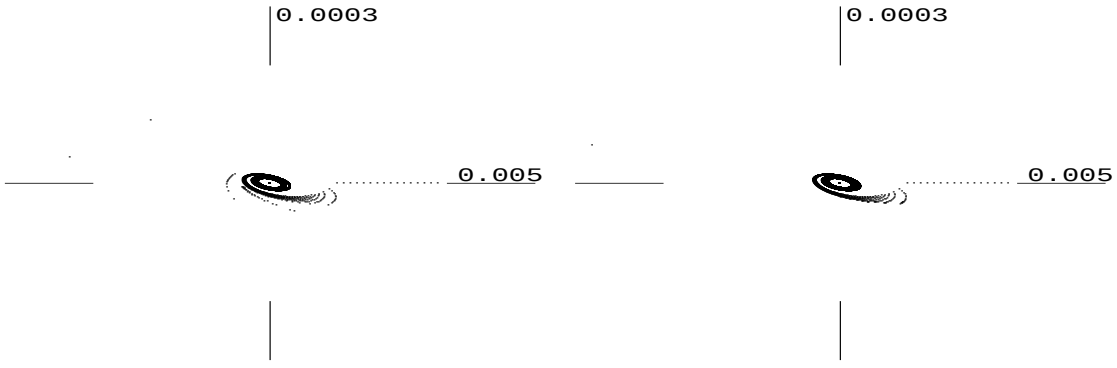

(a) F_2 symplectified nonlinear part of the map

(b) F_3 symplectified nonlinear part of the map

Figure 4.32: 10^5 turn tracking of the LHC with the F_2 and F_3 symplectified nonlinear parts of the 8th order Taylor map, with detailed fringe fields taken into account.

Chapter 5

Optimal Symplectification

Among many systems of practical interest, hadron colliders in the single particle approximation can be modeled as Hamiltonian systems. Hamiltonian systems are uniquely characterized by their symplecticity [10]. One of the fundamental quantities in accelerator physics is the dynamic aperture (DA), which, roughly, is the region of space containing stable particle orbits over long times. Since the system is so complex that an exact solution is not within reach, simulations are needed to estimate the DA [13, 56]. This can be achieved by iteration of the so-called one-turn map, i.e. Poincaré section map, of the system. Unfortunately, only some approximation of the one-turn map, as, for example, the order n truncation of its Taylor series, is available [24]. While the Taylor map preserves the symplecticity up to order n terms in the expansion, in general fails to be exactly symplectic. The numerical simulations in chapter 4 show that the truncation often generates inaccurate results. Therefore, restoration of the exact symplecticity of the one-turn map is desirable.

There are several symplectification methods [14, 15, 57]. While every method produces exactly symplectic maps, the results are not equivalent. The symplectified maps depend on the specifics of the methods. Several examples are presented in chapter 4 using the formalism of generating functions of canonical transformations. For

some generators, the results are not satisfactory. Therefore, it is not only important to symplectify, but also to symplectify the right way. The purpose of this chapter is to give a precise meaning for how to symplectify "the right way" [58].

5.1 Formulation of the Problem

As with any approximation method, a criterion for closeness is needed; mathematically speaking, a suitable metric is necessary. In our case, the metric should provide a way to measure distances between Hamiltonian symplectic maps, and should have some desirable properties, namely:

1. The symplectification should work well for every particle in a given Poincaré section,

2. The outcome of the symplectification should not depend on the specific Poincaré section used,

3. The symplectification should work just as well after any $N > 1$ turns as after one turn, and

4. Based on the previous three conditions, the assessment of the optimality of the symplectification should be unambiguous.

These conditions can be captured by the requirement that if a symplectification method yields the best result, say $\mathcal{M}$, with respect to the metric, then the same symplectification gives the same result for $\mathcal{A} \circ \mathcal{M} \circ \mathcal{A}^{-1}$, $\mathcal{A}$ being any symplectic map, which entails coordinate independence of the metric. It is hoped that such special purpose metrics would capture better the details of the dynamics than general purpose metrics (as, for example, the well-known C^0 metric), and would give an

as unambiguous as possible way to measure distances. Therefore, mathematically speaking, we would like to have a bi-invariant metric for Hamiltonian symplectic maps. The importance of bi-invariant metrics has been pointed out also in [59]. It also can be thought of as a certain generalization of subsection 3.4.1, where it has been shown that linear symplectic variable changes do not matter, to the nonlinear case. The question is whether such a metric exists at all. Indeed, existence of such a metric is highly nontrivial over an infinite dimensional non-compact Lie group, like the Lie group of symplectic maps. A negative example from the field of motion planning for robotic systems is provided by [60], where it is shown that over the relevant Lie group, i.e. $SE(3)$, no such "natural and unequivocal concept of distance" exists. Hence the results are task or designer biased.

5.2 Hofer's Metric and the Optimality Condition

Fortunately, there exists an outstanding metric that satisfies our needs, and symplectic topology provides a way to formulate the necessary conditions for optimal symplectification. This is astonishing, since despite Hamiltonian systems have been studied for such a long time, there was no symplectic topology 25 years ago. Now symplectic topology is a very lively research field, and we will use and extend some results concerning Hofer's metric. In [18], a surprising intrinsic metric has been introduced, now called Hofer's metric, on the space of compactly supported Hamiltonian symplectomorphisms, $\mathrm{Ham}^c(\mathbb{R}^{2n})$. Recall that a symplectic map is called Hamiltonian if it is the time one map of the flow of some function defined on phase space. The fact that such a Finsler metric exists on a non-compact infinite dimensional Lie group points out the special nature of Hamiltonian systems.

5.2.1 Hofer's Metric

We give a short description of this norm [45]. In general, let G be a Lie group with Lie algebra L. A norm $\| \cdot \|$ on L is called invariant if it is invariant under the adjoint action of G

$$\| \xi \| = \| g^{-1} \xi g \| \tag{5.1}$$

(defined through the exponential of ξ at $t = 0$) for every $\xi \in L$ and every $g \in G$. Any such norm gives rise to a bi-invariant intrinsic metric on the Lie group via

$$d(g_0, g_1) = \inf_g \int_0^1 \| \dot{g}(t) g(t)^{-1} \| dt \tag{5.2}$$

for $g_0, g_1 \in G$. The infimum is taken over any smooth path $g : [0, 1] \to G$ connecting $g_0 = g(0)$ to $g_1 = g(1)$.

Specifically, the compactly supported Hamiltonian vector fields of $\mathbb{R}^{2n}$ can be identified with the space of compactly supported functions $C_c^\infty(\mathbb{R}^{2n})$ via the isomorphism mentioned in subsection 2.2.1. The velocity vector of (5.2) is the Hamiltonian vector field. Hence, Hofer defined the following L^∞-type norm on compactly supported Hamiltonian functions

$$||X_{H_t}|| \triangleq \sup_{z \in \mathbb{R}^{2n}} H_t(z) - \inf_{z \in \mathbb{R}^{2n}} H_t(z) \tag{5.3}$$

For convenience we denote it as $||H_t||$. This norm is called the oscillation norm. The adjoint actions are the symplectic variable changes. For the Hamiltonian functions the adjoint actions are the transformations $H \longmapsto H \circ \psi$, for every $H \in C_c^\infty(\mathbb{R}^{2n})$ and every $\psi \in \mathrm{Symp}(\mathbb{R}^{2n}, J)$. The oscillation norm is obviously invariant under the adjoint action

$$||H_t|| = ||H_t \circ \psi|| \tag{5.4}$$

In fact, the norm stays invariant under the larger diffeomorphism group of $\mathbb{R}^{2n}$. The induced length spectrum for paths $\{\phi_t\}$, $t \in [0,1]$ in $\mathrm{Ham}^c(\mathbb{R}^{2n})$ is given by

$$\ell\{\phi_t\} = \int_0^1 ||H_t|| dt \tag{5.5}$$

where H_t is the, possibly time dependent, generating Hamiltonian. For any two $\varphi, \psi \in \mathrm{Ham}^c(\mathbb{R}^{2n})$, the distance between them is defined as

$$\rho(\varphi, \psi) = \inf_{\phi_0=\varphi, \phi_1=\psi} \ell\{\phi_t\} = \inf_{\phi_0=\varphi, \phi_1=\psi} \int_0^1 ||H_t|| dt \tag{5.6}$$

The infimum is taken over all smooth paths in $\mathrm{Ham}^c(\mathbb{R}^{2n})$ from φ to ψ. The following proposition holds [46]:

Proposition 9 *For all $\phi, \varphi, \psi \in \mathrm{Ham}^c(\mathbb{R}^{2n})$ the following hold:*

- $\rho(\phi, \varphi) \geq 0$,
- $\rho(\phi, \varphi) = \rho(\varphi, \phi)$,
- $\rho(\phi, \psi) \leq \rho(\phi, \varphi) + \rho(\varphi, \psi)$,
- $\rho(\phi, \mathcal{I}) = \rho(\varphi \circ \phi \circ \varphi^{-1}, \mathcal{I})$,
- $\rho(\psi \circ \phi, \psi \circ \varphi) = \rho(\phi, \varphi) = \rho(\phi \circ \psi, \varphi \circ \psi)$
- *the map $t \to \rho(\phi_t, \mathcal{I})$ is uniformly continuous.*

The first three properties mean that ρ is a pseudo-metric. The highly nontrivial fact is [46]:

Theorem 10 *Let $\phi, \varphi \in \mathrm{Ham}^c(\mathbb{R}^{2n})$. Then*

$$\rho(\phi, \varphi) = 0 \quad \Leftrightarrow \quad \phi = \varphi \tag{5.7}$$

Therefore, Hofer's metric ρ is an essentially unique, genuine, intrinsic, bi-invariant, Finsler metric, i.e. it satisfies the positive definiteness, separation and symmetry axioms, the triangle inequality, and the fifth statement of the above proposition. It has been shown in [61] that all the invariant L_p norms, $1 \leq p < \infty$,

$$||H||_p = \left(\int_{\mathbb{R}^{2n}} |H|^p \omega^n \right)^{1/p} \tag{5.8}$$

give rise to pseudo-metrics, but not genuine metrics. So, the only non-trivial case is $p = \infty$. We also mention that varying the metric in the t direction gives equivalent metrics. Thus Hofer's metric satisfies all the conditions we wanted to, and can be used for our purposes.

Assume that $\mathcal{M}$ is the exact one-turn map of our system, $\mathcal{M}_n$ its order n Taylor approximation, and $\mathcal{N}$ is an exactly symplectic map produced from $\mathcal{M}_n$ by some symplectification method. In practice $\mathcal{M}$ and $\mathcal{N}$ will not be compactly supported. In fact, a priori it is not even clear that $\mathcal{N}$ will be Hamiltonian since it is the symplectification of some non-symplectic map. However, we need $\mathcal{M}, \mathcal{N} \in \mathrm{Ham}^c(\mathbb{R}^{2n})$ to be able to use Hofer's metric. The problem can be solved as follows. From the practical point of view, the particles in the accelerator are constrained to move within the evacuated beam pipes, and any particle that hits the tube is lost. Mathematically this can be modeled as a cut-off of the particles' Hamiltonian. Indeed, choosing suitable bump functions [43], it is possible to replace the original Hamiltonian with another one which agrees with the original Hamiltonian inside the beam tube, it is zero outside, and has arbitrary fast fall-off. Moreover, we are interested in the dynamics in this finite region of phase space only. These compactly supported Hamiltonians will generate, as time one maps of their flows, compactly supported Hamiltonian symplectic maps which will agree with the original maps over the desired region. The arbitrary fast decay of the cutoff function guarantees that this effect does not influence the

numerical results (since this region of the phase space can be made arbitrarily small, in particular smaller than any floating point number that can be represented on a computer). Therefore, for all practical purposes, this region can be taken as a delta function, as it saves the complication of working with compactly supported maps in practice. Knowing that every symplectic map can be interpolated by the flow of some Hamiltonian in time one, the problem is solved. Indeed, in $\mathbb{R}^{2n}$ the group of symplectic maps coincides with the group of Hamiltonian maps. For completeness, the next subsection gives more details about the connectedness of the group of Hamiltonian symplectic maps.

5.2.2 Connectedness of the Group of Hamiltonian Symplectic Maps

There is a lot of information scattered in the literature on the connectedness of the group of symplectic and Hamiltonian maps [41, 45, 46]. There is also some confusion regarding certain aspects of this topic. For self consistency, the most important results are presented in this subsection.

It follows from the existence of generating functions (or the so-called Weinstein charts) that the group of symplectic maps (compactly supported symplectic maps) are locally contractible, and consequently are locally connected by smooth arcs. Then, the identity components consist of all symplectic maps which are isotopic to the identity through symplectic maps (compactly supported symplectic maps). Smooth isotopies are in one-to-one correspondence with families of smooth vector fields, i.e. if ϕ_t is such an isotopy, then it gives rise to the vector fields

$$X_t = \frac{d\phi_t}{dt} \circ \phi_t^{-1}. \tag{5.9}$$

If the isotopy is symplectic, then so is the vector field. On simply connected manifolds, the symplectic vector fields are Hamiltonian (in general, on connected manifolds, only

locally Hamiltonian). Therefore, on $\mathbb{R}^{2n}$ every symplectic isotopy is Hamiltonian. Moreover, it can be shown that in this case the group of symplectic and Hamiltonian maps coincide. Indeed, given any $\mathcal{M} \in \mathrm{Symp}\,(\mathbb{R}^{2n})$, to show that it is Hamiltonian, according to the above discussion, it is enough to show that $\mathcal{M}$ is the endpoint of a symplectic isotopy.

Denote the constant part of $\mathcal{M}$ by c, i.e. $\mathcal{M}\,(0) = c$. Homotop $\mathcal{M} = c + \mathcal{M}_0$ to an origin preserving symplectic map by $\mathcal{M}_t = tc + \mathcal{M}^0$, $t \in [0,1]$. We have that $\mathcal{M}_t$ is symplectic for each t and $\mathcal{M}^0\,(0) = 0$. Using the Alexander trick, an arc can be found from the linear part of $\mathcal{M}^0$, $\mathcal{L}$, to $\mathcal{M}^0$, that is

$$\mathcal{M}_t^0 = \frac{1}{t}\mathcal{M}^0 \circ t\mathcal{I}, \tag{5.10}$$

for $t \in (0,1]$. It is easy to see that $\mathcal{M}_t^0$ is symplectic for each t (the Alexander trick being in fact only a change of scale), and from the Taylor expansion of $\mathcal{M}_t^0$ is follows that

$$\lim_{t\to 0} \mathcal{M}_t^0 = \mathcal{L}. \tag{5.11}$$

Furthermore, $L = \mathrm{Jac}\,(\mathcal{L}) \in \mathrm{Sp}\,(2n,\mathbb{R})$, and it is well-known that $\mathrm{Sp}\,(2n,\mathbb{R})$ is contractible. There are several ways to see this. For example, any $L \in \mathrm{Sp}\,(2n,\mathbb{R})$ can be written as

$$L = e^{J\mathcal{S}_1} e^{J\mathcal{S}_2}, \tag{5.12}$$

where S_1, S_2 are symmetric matrices [62]. Therefore, it is enough to define the arc

$$\mathcal{L}_t = e^{t\mathcal{J}\mathcal{S}_1} \circ e^{t\mathcal{J}\mathcal{S}_2}, \tag{5.13}$$

$t \in [0,1]$ to obtain the final part of the total isotopy. Putting together the different parts by juxtaposition of paths, we obtain the following piecewise smooth isotopy:

$$\mathcal{M}_t = \begin{cases} \mathcal{L}_t,\ t \in [0,1/3]\,, \\ \mathcal{M}_t^0,\ t \in (1/3,2/3], \\ tc + \mathcal{M}^0,\ t \in (2/3,1]. \end{cases} \tag{5.14}$$

By replacing the parameter t by a smooth function $f : [0.1] \to [0,1]$ such that it is constant in the neighborhoods of the non-smooth points, we finally obtain a smooth isotopy from the identity to $\mathcal{M}$, showing that every $\mathcal{M} \in \mathrm{Symp}\left(\mathbb{R}^{2n}\right)$ is in fact $\in \mathrm{Ham}\left(\mathbb{R}^{2n}\right)$.

The next natural question is the following: if $\mathcal{M} \in \mathrm{Symp}^c\left(\mathbb{R}^{2n}\right)$, then is it true that $\mathcal{M} \in \mathrm{Ham}^c\left(\mathbb{R}^{2n}\right)$? In general, the answer is not known. It is true for $n < 3$ [50]. Moreover, it is known that $\mathrm{Ham}^c\left(\mathbb{R}^{2n}\right)$ is the C^0 closure of $\mathrm{Symp}^c\left(\mathbb{R}^{2n}\right)$ for any n. Again, there are several ways to see this. Perhaps the easiest is to notice that for any compactly supported diffeomorphism ϕ such that $\mathrm{supp}(\phi) \subset D$, and any diffeomorphism θ, $\mathrm{supp}\left(\theta \circ \phi \circ \theta^{-1}\right) \subset \theta\left(D\right)$. It follows that any $\mathcal{M} \in \mathrm{Symp}^c\left(\mathbb{R}^{2n}\right)$ can be conformally rescaled to have support in an arbitrary small neighborhood of a point. Then, the Alexander trick (5.10) gives an isotopy from $\mathcal{M}$ to an element in $\mathrm{Symp}^c\left(\mathbb{R}^{2n}\right)$ arbitrarily C^0-close to the identity. Therefore, for computational purposes we can always interchange symplectic with Hamiltonian, even in the compactly supported case.

5.2.3 The Optimality Condition

To this end, Hofer's metric can be applied to the problems of interest to us. Therefore, optimal symplectification can be defined as the symplectification method that minimizes the distance in Hofer's metric between the exact map and the symplectified maps. That is, if the set of all possible symplectification methods is denoted by Σ, the best result is achieved by any symplectic map $\mathcal{N}_{opt}$ which satisfies

$$\rho\left(\mathcal{M}, \mathcal{N}_{opt}\right) = \inf_{i \in \Sigma} \rho\left(\mathcal{M}, \mathcal{N}_i\right). \tag{5.15}$$

While being very general, there is a problem with this formulation of the optimal symplectification, namely it is not very useful for practical computations. The reason

is that in general it is not known yet how to compute the Hofer distance between two arbitrary maps in $\mathrm{Ham}^c(\mathbb{R}^{2n})$. The difficulty lies in the necessity of consideration of all the Hamiltonians generating the two maps, or equivalently, the paths in $\mathrm{Ham}^c(\mathbb{R}^{2n})$ from $\mathcal{M}$ to $\mathcal{N}_i$. However, by the nature of our optimality condition, we are interested only in the maps $\mathcal{N}_i$ that are already close to $\mathcal{M}$ in some sense. Obviously, this necessary condition can be achieved by sufficiently increasing the value of n, the degree of the polynomials $\mathcal{M}_n$ with which the exact maps are initially approximated. Thus it would be sufficient if a suitable neighborhood of $\mathcal{M}$ can be parametrized in such a way that (5.15) becomes computable. Clearly, any symplectic map that does not fit into this neighborhood cannot be optimal.

5.3 Link to the Extended Generating Function Theory

Indeed, parametrization of a neighborhood of $\mathcal{M}$ is possible in the C^1 topology, utilizing the theory of generating functions. The first results in this direction have been obtained in [63] for Hamiltonian maps C^1 close to identity and Poincaré's generating function, and then it was extended to Hamiltonian maps C^1 close to identity and all compactly supported generating functions in [64] and [45]. While the approach of [64] is more general, as it holds on any symplectic manifold, we are only interested in $\mathbb{R}^{2n}$, and the method of [63] lends itself more easily to generalizations. The main idea is to replace the Hamiltonian maps by their generating functions, and try to express Hofer's metric between two maps as some norm of the difference of their generating functions. In [63] this was proven to be possible in some cases. However, in the extended theory of generating functions of chapter 2 it was shown that in fact there exist uncountably many generator types for any symplectic map, some of which are not compactly supported. To be able to decide which generating function type

provides the optimal symplectification, the result of [63] must be generalized to every generator type.

More precisely, introducing a map Φ_α that sends a symplectic map $\mathcal{M}$ into its generating function F of type α, we prove that Φ_α is an isometry. Formally, we can state the result as the following theorem:

Theorem 11 *There exists a neighborhood $\mathcal{E}$ of any $\mathcal{M} \in \mathrm{Ham}^c(\mathbb{R}^{2n})$, and a neighborhood $\mathcal{Z}$ of 0 in $C_c^\infty(\mathbb{R}^{2n})$ such that the map*

$$\Phi_\alpha : \mathcal{E} \to \mathcal{Z} \qquad \Phi_\alpha(\mathcal{M}) = F \tag{5.16}$$

is isometric. That is, for every $F, G \in \mathcal{Z}$,

$$\rho(\mathcal{M}, \mathcal{N}) = \frac{1}{|\mu|}||\Phi_\alpha(\mathcal{M}) - \Phi_\alpha(\mathcal{N})|| = \frac{1}{|\mu|}||F - G||. \tag{5.17}$$

As a consequence, the inverse of the isometry takes any function from $(\mathcal{Z}, ||\cdot||)$ into a Hamiltonian symplectomorphism in $(\mathcal{E}, \rho)$ depending on α. This shows that, considering the space $(\mathcal{Z}, ||\cdot||)$ a flat space (in which straight lines are minimal geodesics), their image under $\Phi_\alpha^{-1} : \mathcal{Z} \to \mathcal{E}$ in $\mathrm{Ham}^c(\mathbb{R}^{2n})$ remain locally flat minimal geodesics. That is why this results is called the local flatness phenomenon.

The proof uses three main ingredients. First, there is an intimate relationship between fixed points of symplectic maps and critical points of generating functions, which is presented in the next subsection. Second, the proof in [63] is based on the Hamilton-Jacobi equation. In subsection 5.3.2 the generalized Hamilton-Jacobi is derived, adapted to our situation. It provides the time evolution of any generator type. Finally, the proof uses a theorem of Siburg [65], which is stated without proof in subsection 5.3.3. The theorem essentially states that paths without nontrivial fixed points are absolutely length minimizing for Hofer's metric.

5.3.1 The Fixed Point-Critical Point Relationship

In this subsection we study an interesting property of generating functions. A point z_f is called a fixed point of the symplectic map $\mathcal{M}$ if it acts on it as the identity map, that is $\mathcal{M}(z_f) = z_f$. It follows that the iterates of the map have the same fixed points,

$$\mathcal{M}^k(z_f) = \mathcal{M}^{k-1} \circ \mathcal{M}(z_f) = \mathcal{M}^{k-1}(z_f) = ... = \mathcal{M}(z_f) = z_f. \tag{5.18}$$

Moreover, the inverse $\mathcal{M}^{-1}$ also has the same fixed points,

$$\mathcal{M}^{-1}(z_f) = \mathcal{M}^{-1} \circ \mathcal{M}(z_f) = z_f. \tag{5.19}$$

To sum up, we can say that any integer power of a symplectic map has the same fixed points as the map itself. Thus the set of fixed points form a topological invariant of the map under iteration. Generating functions can be connected with these fixed points. For start, let us consider a special class of generating functions. We assume that the generating functions are globally defined, otherwise the theory is valid for the fixed points in the regions where it is defined. The critical points of functions in this set are the fixed points of the symplectic maps, and conversely, the fixed points of the map are critical points of the function. If the symplectic maps are compactly supported, then these generating functions are exactly the generating functions with compact support. This can be easily seen if we argue geometrically. Recall that the symplectic map is a Lagrangian submanifold in the product manifold. Then, the fixed points of the map are exactly the intersection points of this submanifold with the diagonal. On the other hand, the critical points of the generating function are the intersection points of the Lagrangian submanifold determined by the function with the zero section. Now, if we identify the diagonal with the zero section by α, the fixed points of the map will go into critical points of the generating functions.

Explicitly, given a symplectic map, we can choose only αs that satisfy the transversality condition. On the other hand, identification of the diagonal with the zero section requires that

$$\alpha\left(\Delta\right) = Z, \tag{5.20}$$

which further restricts the pool of αs. A necessary condition is that the generating functions in this class can generate the identity map. If the map is close enough to the identity, then also the transversality condition is satisfied automatically. Equation (5.20) can be expanded as

$$\left(\begin{array}{c} \alpha_1 \circ \left(\begin{array}{c} \mathcal{I} \\ \mathcal{I} \end{array} \right) \\ \alpha_2 \circ \left(\begin{array}{c} \mathcal{I} \\ \mathcal{I} \end{array} \right) \end{array} \right) (z) = \left(\begin{array}{c} 0 \\ \mathcal{I} \end{array} \right) (w)\,. \tag{5.21}$$

Applying z_f to (2.107), we obtain that

$$\nabla F \circ \alpha_2 \circ \left(\begin{array}{c} \mathcal{M} \\ \mathcal{I} \end{array} \right) (z_f) = \alpha_1 \circ \left(\begin{array}{c} \mathcal{M} \\ \mathcal{I} \end{array} \right) (z_f)\,, \tag{5.22}$$

which is equivalent to

$$\nabla F \circ \alpha_2 \circ \left(\begin{array}{c} \mathcal{I} \\ \mathcal{I} \end{array} \right) (z_f) = \alpha_1 \circ \left(\begin{array}{c} \mathcal{I} \\ \mathcal{I} \end{array} \right) (z_f)\,. \tag{5.23}$$

Using (5.21) we arrive to

$$\nabla F\left(w_f\right) = 0, \tag{5.24}$$

where w_f is given by z_f and the identification process. From the explicit constraints we will see that actually $w_f = z_f$. Hence, the fixed points of the map are critical points of the generating functions from this set.

The next question is whether this is true conversely: are all the critical points of generating functions in this set fixed points of the map? As has been shown in section

2.4,

$$\mathcal{M} = \left(\alpha^1 \circ \begin{pmatrix} \nabla F \\ \mathcal{I} \end{pmatrix}\right) \circ \left(\alpha^2 \circ \begin{pmatrix} \nabla F \\ \mathcal{I} \end{pmatrix}\right)^{-1}, \tag{5.25}$$

or

$$\mathcal{M} \circ \left(\alpha^2 \circ \begin{pmatrix} \nabla F \\ \mathcal{I} \end{pmatrix}\right)(w_c) = \left(\alpha^1 \circ \begin{pmatrix} \nabla F \\ \mathcal{I} \end{pmatrix}\right)(w_c), \tag{5.26}$$

where w_c are the critical points of F. From (5.20) it follows that

$$\alpha^{-1}(Z) = \Delta, \tag{5.27}$$

$$\begin{pmatrix} \alpha^1 \circ \begin{pmatrix} 0 \\ \mathcal{I} \end{pmatrix} \\ \alpha^2 \circ \begin{pmatrix} 0 \\ \mathcal{I} \end{pmatrix} \end{pmatrix}(w) = \begin{pmatrix} \mathcal{I} \\ \mathcal{I} \end{pmatrix}(z). \tag{5.28}$$

Combining what we have derived sofar, we are able to answer the question about critical points. Using $\nabla F(w_c) = 0$, from (5.26) and (5.28) we obtain

$$\mathcal{M}(z_c) = z_c. \tag{5.29}$$

Again, z_c is the point corresponding to w_c via the identification, and we will see that $z_c = w_c$. Hence, w_c are fixed points of the symplectic map. In conclusion, there is a one-to-one correspondence between fixed points of the map and critical points of the generating functions in this set.

Now we elaborate in the direction of finding the explicit constraints for this class of generating functions. Beside the constraints (2.123-2.125) we have another set given by (5.21), which in terms of the entries in the Jacobian of α read

$$A(z,z) + B(z,z) = 0, \tag{5.30}$$

$$C(z,z) + D(z,z) = I. \tag{5.31}$$

But we already know from chapter 3 that, with $M = I$, this set is nothing else than generating functions constructed via any α of the form

$$\alpha = \begin{pmatrix} -\mu J & \mu J \\ \frac{1}{2}(I + JS) & \frac{1}{2}(I - JS) \end{pmatrix} \quad \begin{matrix} \mu \in \mathbb{R}^{\times} \\ S = S^T \end{matrix}. \tag{5.32}$$

The critical points of these generators are in one-to-one correspondence with the fixed points of the map. Now it is straightforward to check that for any generating function in this set indeed $w_f = z_f$ and $z_c = w_c$.

The above results can be extended to any generating function, with the condition that it can be used to generate the identity map. The difference between the above set and the other generating functions is that they will not identify the diagonal with the zero section, but some other section. However, this little inconvenience can be circumvented by noticing that subtracting from the generating function the function that generates the identity map, we get almost the same results. That is, suppose we have the following:

$$\nabla F \circ \alpha_2 \circ \begin{pmatrix} \mathcal{M} \\ \mathcal{I} \end{pmatrix}(z) = \alpha_1 \circ \begin{pmatrix} \mathcal{M} \\ \mathcal{I} \end{pmatrix}(z), \tag{5.33}$$

$$\nabla F_0 \circ \alpha_2 \circ \begin{pmatrix} \mathcal{I} \\ \mathcal{I} \end{pmatrix}(z) = \alpha_1 \circ \begin{pmatrix} \mathcal{I} \\ \mathcal{I} \end{pmatrix}(z), \tag{5.34}$$

where we denoted by F_0 the same type of generating function as F, but which generates the identity map. Then, if $z = z_f$, the right hand sides are the same, and we obtain that

$$\nabla (F - F_0)(w_f) = 0. \tag{5.35}$$

The fixed points can be obtained from

$$z_f = \left(\alpha_2 \circ \begin{pmatrix} \mathcal{I} \\ \mathcal{I} \end{pmatrix}\right)^{-1}(w_f). \tag{5.36}$$

So, there is still a one-to-one correspondence between fixed points of symplectic maps and critical points of generating functions in the above modified sense. Of course, in the case of the (5.32) set $F_0 = 0$, and the previous results can be recovered.

Finally, to put the results in the form that we will need them to prove the theorem, consider the case when the same generator type α exists for two symplectic maps $\mathcal{M}$ and $\mathcal{N}$. It follows that

$$\nabla F \circ \alpha_2 \circ \begin{pmatrix} \mathcal{M} \\ \mathcal{I} \end{pmatrix} (z) = \alpha_1 \circ \begin{pmatrix} \mathcal{M} \\ \mathcal{I} \end{pmatrix} (z) \,, \tag{5.37}$$

$$\nabla G \circ \alpha_2 \circ \begin{pmatrix} \mathcal{N} \\ \mathcal{I} \end{pmatrix} (z) = \alpha_1 \circ \begin{pmatrix} \mathcal{N} \\ \mathcal{I} \end{pmatrix} (z) \,. \tag{5.38}$$

Then, on the set of common fixed points z_f of $\mathcal{M}$ and $\mathcal{N}$ we obtain that

$$\nabla \left(F - G \right) (w_f) = 0. \tag{5.39}$$

5.3.2 The Generalized Hamilton-Jacobi Equation and Applications

In this subsection we prove the most general Hamilton-Jacobi equation, associated to the time evolution of any generating function. As we have seen, critical points of generating functions are closely related to fixed points of the map. But more can be said. We will show that, actually every generating function of compact support assumes the same value at the fixed points of the map. These numbers are called the action of the fixed points, that is, if z_f is a fixed point of $\mathcal{M}$, define $\mathcal{A}\left(z_f, \mathcal{M}, \mu\right)$ as the value taken by any generating function. Call the set of all such numbers, as z_f spans all the fixed points, the action spectrum of $\mathcal{M}$

$$\sigma_\mu \left(\mathcal{M} \right) = \left\{ \mathcal{A}\left(z_f, \mathcal{M}, \mu\right) \ \middle| \ \mathcal{M}\left(z_f\right) = z_f \right\}. \tag{5.40}$$

The spectrum depends parametrically on the conformality factor μ of α, and is a symplectic invariant of the map. To show the claim, we need to prove that the

generating functions satisfy a generalized Hamilton-Jacobi equation. Based on the proof in [28] for linear αs, here we present the general proof. Assume that the flow is generated by the time-dependent Hamiltonian H_t, and the corresponding time t maps can be represented at any moment by a time-dependent generating function F_t. We claim the following.

Theorem 12 *The following Hamilton-Jacobi equation is satisfied for any $w \in \mathbb{R}^{2n}$:*

$$\frac{\partial}{\partial t} F_t(w) = \mu H_t \circ \left(\alpha^1 \circ \begin{pmatrix} \mathcal{N}_t \\ \mathcal{I} \end{pmatrix} \right)(w), \tag{5.41}$$

where F_t is the generating function associated to any α satisfying (2.123-2.125), and $\mathcal{N}_t = (\nabla F_t)^T$ at every moment t.

Proof. We are situated in the $(\mathbb{R}^{4n}, J_{4n})$ symplectic space, with symplectic coordinates $(w, \hat{w})$. Consider the extended phase space $\mathbb{R}^{4n+2}$ by including the canonical pair of variables $\left(t, -\bar{H}_t\right)$. The symplectic structure modifies to

$$\omega = \omega_0 - dt \wedge d\bar{H}_t, \tag{5.42}$$

the differential form of Cartan. Take the one-form

$$\lambda_e = \hat{w} dw + \bar{H}_t dt, \tag{5.43}$$

where $\bar{H}_t = \mu H_t \circ \left(\alpha^1 \circ \begin{pmatrix} \mathcal{N}_t \\ \mathcal{I} \end{pmatrix} \right)$. We prove that λ_e is closed. We have that

$$\begin{aligned} d\lambda_e &= \sum_{i,j=1}^{2n} \frac{\partial \hat{w}_i}{\partial w_j} dw_j \wedge dw_i + \sum_{i=1}^{2n} \frac{\partial \hat{w}_i}{\partial t} dt \wedge dw_i + \sum_{i=1}^{2n} \frac{\partial \bar{H}_t}{\partial w_i} dw_i \wedge dt + \frac{\partial \bar{H}_t}{\partial t} dt \wedge dt \\ &= \sum_{i<j}^{2n} \left(Jac\left(\mathcal{N}_t\right) - \left(Jac\left(\mathcal{N}_t\right)^T \right) \right) dw_j \wedge dw_i + \sum_{i=1}^{2n} \left(\frac{\partial \hat{w}_i}{\partial t} - \frac{\partial \bar{H}_t}{\partial w_i} \right) dt \wedge dw_i \\ &= \sum_{i=1}^{2n} \left(\frac{\partial \hat{w}_i}{\partial t} - \frac{\partial \bar{H}_t}{\partial w_i} \right) dt \wedge dw_i. \end{aligned} \tag{5.44}$$

On the other hand

$$\frac{d\hat{w}}{dt} = \dot{\mathcal{N}}_t(w) = \mathrm{Jac}\left(\mathcal{N}_t(w)\right) \cdot \dot{w} + \frac{\partial \hat{w}}{\partial t}, \tag{5.45}$$

$$\frac{\partial \hat{w}}{\partial t} = \dot{\mathcal{N}}_t(w) - \mathrm{Jac}\left(\mathcal{N}_t(w)\right) \cdot \dot{w}. \tag{5.46}$$

Recall that

$$w = \alpha_2 \circ \begin{pmatrix} \mathcal{M}_t \\ \mathcal{I} \end{pmatrix}(z), \tag{5.47}$$

$$\hat{w} = \alpha_1 \circ \begin{pmatrix} \mathcal{M}_t \\ \mathcal{I} \end{pmatrix}(z), \tag{5.48}$$

and $\hat{z} = \mathcal{M}_t(z)$ is the solution of the initial value problem

$$\frac{d\hat{z}}{dt} = J\nabla_{\hat{z}} H_t(\hat{z}), \tag{5.49}$$

$$\hat{z}(t=0) = z. \tag{5.50}$$

We compute

$$\frac{\partial \bar{H}_t}{\partial w}(w) = \mu \nabla_w \left(H_t \circ \left(\alpha^1 \circ \begin{pmatrix} \mathcal{N}_t \\ \mathcal{I} \end{pmatrix} \right) \right)(w) \tag{5.51}$$

$$= \mu \left[\mathrm{Jac}\left(\alpha^1 \circ \begin{pmatrix} \mathcal{N}_t \\ \mathcal{I} \end{pmatrix} \right)(w) \right]^T \cdot \nabla_{\hat{z}} H(\hat{z}) \tag{5.52}$$

$$= \mu \left[\begin{pmatrix} A^\alpha & B^\alpha \end{pmatrix} \cdot \begin{pmatrix} N_t \\ I \end{pmatrix} \right]^T \cdot \nabla_{\hat{z}} H(\hat{z}) \tag{5.53}$$

$$= \mu \left(A^\alpha N_t + B^\alpha \right)^T \cdot \nabla_{\hat{z}} H(\hat{z}) \tag{5.54}$$

$$= \mu \left(N_t A^{\alpha T} + B^{\alpha T} \right) \cdot \nabla_{\hat{z}} H(\hat{z}), \tag{5.55}$$

where in the second row we used $\hat{z} = \alpha^1 \circ \begin{pmatrix} \mathcal{N}_t \\ \mathcal{I} \end{pmatrix}(w)$, in the third row $\mathrm{Jac}(\mathcal{N}_t) = N_t$ and the notation for the Jacobian of α^{-1}

$$\alpha^{\#} = \mathrm{Jac}\left(\alpha^{-1}\right) = \begin{pmatrix} A^\alpha & B^\alpha \\ C^\alpha & D^\alpha \end{pmatrix}. \tag{5.56}$$

In the last row the fact that N_t is symmetric, $N_t^T = N_t$ is also utilized. We can express $\alpha^{\#}$ in terms of entries of $\alpha_{\#}$. From (2.113) it follows that

$$\alpha^{\#} = -\frac{1}{\mu}\tilde{J}_{4n}\alpha_{\#}^T J_{4n} \tag{5.57}$$

$$= -\frac{1}{\mu}\begin{pmatrix} J_{2n} & 0_{2n} \\ 0_{2n} & -J_{2n} \end{pmatrix}\begin{pmatrix} A^T & C^T \\ B^T & D^T \end{pmatrix}\begin{pmatrix} 0_{2n} & I_{2n} \\ -I_{2n} & 0_{2n} \end{pmatrix}, \tag{5.58}$$

which reads explicitly

$$A^{\alpha} = \frac{1}{\mu}J_{2n}C^T, \qquad B^{\alpha} = -\frac{1}{\mu}J_{2n}A^T, \tag{5.59}$$

$$C^{\alpha} = -\frac{1}{\mu}J_{2n}D^T, \qquad D^{\alpha} = \frac{1}{\mu}J_{2n}B^T. \tag{5.60}$$

Finally, we obtain

$$\frac{\partial \bar{H}_t}{\partial w}(w) = \mu\left(N_t A^{\alpha T} + B^{\alpha T}\right)\cdot \nabla_{\hat{z}} H_t(\hat{z}) \tag{5.61}$$

$$= (A - N_t C)\cdot J\nabla_{\hat{z}} H_t(\hat{z}). \tag{5.62}$$

Analogously, the calculation of $\frac{\partial \hat{w}}{\partial t}$ proceeds as follows

$$\frac{\partial \hat{w}}{\partial t} = \frac{d}{dt}\left(\alpha_1(\hat{z}, z)\right) - N_t \cdot \frac{d}{dt}\left(\alpha_2(\hat{z}, z)\right) \tag{5.63}$$

$$= \frac{\partial \alpha_1(\hat{z}, z)}{\partial \hat{z}}\cdot\frac{d\hat{z}}{dt} - N_t \cdot \frac{\partial \alpha_2(\hat{z}, z)}{\partial \hat{z}}\cdot\frac{d\hat{z}}{dt} \tag{5.64}$$

$$= (A - N_t C)\cdot J\nabla_{\hat{z}} H_t(\hat{z}). \tag{5.65}$$

Hence, $d\lambda_e = 0$. The vanishing first cohomology class guarantees the existence of a function $F_t(w)$ such that

$$dF_t(w) = \lambda_e = \hat{w}dw + \bar{H}_t(w)\,dt, \tag{5.66}$$

$$\frac{\partial F_t(w)}{\partial w}dw + \frac{\partial F_t(w)}{\partial t}dt = \hat{w}dw + \bar{H}_t(w)\,dt. \tag{5.67}$$

Comparing coefficients, we get that indeed $F_t(w)$ is the generating function

$$\nabla F_t(w) = \mathcal{N}_t(w) = \hat{w}, \tag{5.68}$$

and the advertised result

$$\frac{\partial F_t(w)}{\partial t} = \mu H_t \circ \left(\alpha^1 \circ \begin{pmatrix} \mathcal{N}_t \\ \mathcal{I} \end{pmatrix}\right)(w). \tag{5.69}$$

■

Finally, as an application, it can be shown that compactly supported generating functions assume the same value at the fixed points of the symplectic map. Notice that the right hand side of (5.69) can be expressed as

$$H_t \circ \left(\alpha^1 \circ \begin{pmatrix} \mathcal{N}_t \\ \mathcal{I} \end{pmatrix}\right)(w) = H_t \circ \left(\alpha^1 \circ \alpha \circ \begin{pmatrix} \mathcal{M}_t \\ \mathcal{I} \end{pmatrix}(z)\right) \tag{5.70}$$

$$= H_t \circ \mathcal{M}_t(z). \tag{5.71}$$

In the derivation we used the following

$$\alpha^{-1} \circ \alpha = \begin{pmatrix} \alpha^1 \circ \alpha \\ \alpha^2 \circ \alpha \end{pmatrix} = \mathcal{I}. \tag{5.72}$$

Therefore, $\alpha^1 \circ \alpha$ is the identity for the first $2n$ components and 0 for the second $2n$ components. Also, if we consider only time-independent Hamiltonians, H is invariant under its own flow at any time, $H = H \circ \mathcal{M}_t$, since H is constant along the solutions of the Hamiltonian dynamical system. Reparametrization with respect to time, such that $\mathcal{M}$ is the time 1 flow of H_t, and integration of (5.66) gives

$$F \circ \alpha_2 \circ \begin{pmatrix} \mathcal{M} \\ \mathcal{I} \end{pmatrix}(z) - F_0 \circ \alpha_2 \circ \begin{pmatrix} \mathcal{I} \\ \mathcal{I} \end{pmatrix}(z) = \tag{5.73}$$

$$\int_{w(0)}^{w(1)} \nabla F(w) \cdot dw + \mu \int_0^1 H_t \circ \mathcal{M}_t(z)\, dt. \tag{5.74}$$

We used $\mathcal{M}_0 = \mathcal{I}$, and the notation $F_1 = F$. If $z = z_f$, the first term on the right hand side is vanishing because in this case $w(0) = w(1)$ as can be seen from (5.47). Hence, we get

$$(F - F_0)(w_f) = \mu \int_0^1 H_t \circ \mathcal{M}_t(z_f)\, dt, \tag{5.75}$$

with

$$w_f = \alpha_2 \circ \begin{pmatrix} \mathcal{I} \\ \mathcal{I} \end{pmatrix} (z_f) \,. \tag{5.76}$$

In particular, for compactly supported generating functions (5.75) takes the form

$$F(z_f) = \mu \int_0^1 H_t \circ \mathcal{M}_t (z_f)\, dt = \mathcal{A}(z_f, \mathcal{M}, \mu) \,. \tag{5.77}$$

This means that generating functions in this set, with the same conformality factor, take the same value at the fixed points of the symplectic map. In general, the other generating functions, after subtracting the part that generates the identity, take the same value at points that are in one-to-one correspondence with the fixed points. In [45] it is shown that the action of a fixed point is related to the area enclosed by certain loops, thus is no surprise that the action depends parametrically on the conformality factor.

It is also known that the action spectrum of compactly supported Hamiltonian maps is compact and nowhere dense, and in general does not depend continuously with respect to $\mathcal{M}$. For details we refer the reader to [46]. On the other hand, Weinstein proved that the fixed points of a perturbed symplectic map are close to the fixed points of the unperturbed map [32]. A related result is due to Viterbo, who proved that any compactly supported symplectic map has infinitely many periodic points inside its support [66].

5.3.3 Siburg's Theorem

Some preparation is needed before the theorem statement.

Definition 3 *Let $I \subset \mathbb{R}$ be a connected subset with non-empty interior. A smooth path $\{\phi_t\} : I \to \mathrm{Ham}^c(\mathbb{R}^{2n})$ is called regular if $X_{H_t} \neq 0$ for every $t \in I$.*

Definition 4 *Let* $\{\phi_t\} : I \to \mathrm{Ham}^c(\mathbb{R}^{2n})$ *be a smooth regular path.*

- $\{\phi_t\}$ *is called a minimal geodesic if for all* $a, b \in I$*, such that* $a < b$*,*

$$\ell\{\phi_t\}|_{[a,b]} = \rho(\phi_a, \phi_b) \tag{5.78}$$

holds.

- $\{\phi_t\}$ *is called a geodesic if for every* $t \in I$ *there exists a neighborhood* $U \subset I$ *of* t *such that* $\{\phi_t\}|_U$ *is a minimal geodesic.*

The following proposition is proved in [63].

Proposition 13 *Let* $H : [a, b] \times \mathbb{R}^{2n} \to \mathbb{R}$ *be a smooth compactly supported function. The following two conditions are equivalent:*

- $\int_a^b ||H_t|| dt = ||\int_a^b H_t(z)\, dt||$
- *There exist two points* z_-*,* $z_+ \in \mathbb{R}^{2n}$ *such that* $\sup_z H_t = H_t(z_+)$ *and* $\inf_z H_t = H_t(z_-)$*, for all* $t \in [a, b]$*.*

Definition 5 *A function* $H_t(z)$ *which satisfies one of the conditions in the proposition above is called quasi-autonomous. Each autonomous path is quasi-autonomous.*

We are interested under what conditions the length-minimizing property of a path is achieved. Lalonde and McDuff [64] proved the necessary condition, which holds for any symplectic manifold.

Theorem 14 *A regular path* $\{\phi_t\}$*,* $t \in I$*, in* $\mathrm{Ham}^c(\mathbb{R}^{2n})$ *is a geodesic if and only if its generating Hamiltonian has at least one fixed maximum and one fixed minimum at each moment.*

Hence, every geodesic is generated by quasi-autonomous Hamiltonian functions. To prove that a path is length-minimizing is much harder. Fortunately, in $\mathbb{R}^{2n}$ one can obtain more results than in the general case. First, we need another definition.

Definition 6 *A fixed point, z_f, of a map $\phi_1 \in \mathrm{Ham}^c(\mathbb{R}^{2n})$ is called constant if it is a fixed point of its flow, that is $\phi_t z_f = z_f$, for every $t \in [0,1]$.*

We say that a smooth path $\{\phi_{t\in[0,1]}\}$ starting at the identity has no non-constant fixed points if for any fixed $\tau \in (0,1]$ and z_f such that

$$\phi_\tau(z_f) = z_f \Rightarrow \phi_t(z_f) = z_f \tag{5.79}$$

for any $t \in [0,1]$. In case $\{\phi_{t\in[0,1]}\}$ does not start at the identity, (5.79) should be modified to

$$\phi_\tau(z_f) = \phi_0(z_f) \Rightarrow \phi_t(z_f) = \phi_0(z_f). \tag{5.80}$$

We are ready to state the following theorem [65].

Theorem 15 *Any regular path $\{\phi_{t\in[0,1]}\}$ in $\mathrm{Ham}^c(\mathbb{R}^{2n})$ that is generated by a quasi-autonomous Hamiltonian, and has no non-constant fixed points in time less than 1, is a minimal geodesic, that is absolutely length-minimizing for Hofer's metric.*

It is conjectured that a similar theorem holds for any symplectic manifold. The case of autonomous Hamiltonians has been proved recently [67].

5.3.4 Proof of the Main Theorem

Now we are ready to derive the so-called local flatness phenomenon. We want to measure the distance between two compactly supported Hamiltonian symplectic maps, say φ and ψ. Suppose that for some type α the two generating functions

associated with α for φ and ψ are F_α and G_α. Take the convex combination of the two generating functions

$$S_t = (1-t)\, F_\alpha + tG_\alpha = F_\alpha + t\,(G_\alpha - F_\alpha)\,. \tag{5.81}$$

The corresponding path $\{\phi_t\}$ in $\mathrm{Ham}^c\,(\mathbb{R}^{2n})$ is generated by a Hamiltonian H_t. The path satisfies the following relations: $\phi_0 = \varphi$ and $\phi_1 = \psi$. Noticing that $S_0 = F_\alpha$, if z_f is a fixed point of ϕ_τ, for some fixed $\tau \in (0,1]$, according to (5.39) it follows that

$$\nabla\,(S_\tau - S_0)\,(w_f) = \tau \cdot \nabla\,(G_\alpha - F_\alpha)\,(w_f) = 0, \tag{5.82}$$

that is w_f is a critical point of $G_\alpha - F_\alpha$. Obviously, this implies that w_f remains a critical point of $G_\alpha - F_\alpha$ for any $t \in [0,1]$, which in turn means that z_f is a fixed point of ϕ_t for any $t \in [0,1]$. Indeed, as in (5.36), it follows that in this case

$$z_f = \left(\alpha_2 \circ \begin{pmatrix} \varphi \\ \mathcal{I} \end{pmatrix}\right)^{-1} (w_f)\,. \tag{5.83}$$

According to subsection 5.3.1, we just proved that all the fixed points of $\left\{\phi_{t\in[0,1]}\right\}$ are constant. Also, a careful look at the Hamilton-Jacobi equation (5.69) reveals that the path $\left\{\phi_{t\in[0,1]}\right\}$ is generated by quasi-autonomous Hamiltonians. Since, as follows from above, the left hand side is quasi-autonomous, the right hand side must be quasi-autonomous too. Moreover, the points where the left hand side achieves its maximum and minimum values are critical points of $G_\alpha - F_\alpha$; hence at these points $\mathcal{N}_t\,(w_c) = \nabla S_t\,(w_c) = \nabla F_\alpha\,(w_c)$ is time independent, showing that indeed H_t is quasi-autonomous. We remark that the same arguments show that paths with these properties are never unique, as in the definition of S_t any function of t such that $f\,(0) = 0$ and $f\,(1) = 1$ can be taken instead of t. In our specific case, i.e. $f\,(t) = t$, in fact autonomous paths are obtained. As a side note, this shows that symplectic maps close to identity always can be generated by autonomous Hamiltonians.

To this end, the conditions of theorem (15) are satisfied, and the Hamilton-Jacobi equation provides a method to compute the distance between symplectic maps. Using (5.71) in (5.69), taking norms on both sides of (5.69), and using the invariance of the oscillation norm under the adjoint action, we obtain

$$||G_\alpha - F_\alpha|| = ||\mu H_t \circ \mathcal{M}_t|| = |\mu|||H_t||. \tag{5.84}$$

Integration gives

$$||G_\alpha - F_\alpha|| = |\mu| \cdot \ell\left\{\phi_t\right\}, \tag{5.85}$$

and according to Siburg's theorem we finally arrive at

$$\rho\left(\varphi, \psi\right) = \frac{1}{|\mu|}||G_\alpha - F_\alpha||. \tag{5.86}$$

In summary, as long as the same type of generating function exists for two compactly supported Hamiltonian maps, the Hofer distance between them can be measured as the oscillation norm of the difference between their generators. From our point of view, it is very important that this result holds for any generator type, subject to the existence condition. This is always the case if φ and ψ are sufficiently close in the C^1 topology. However, it is a local result in the sense that it does not provide a way to compute Hofer's distance between any two arbitrary Hamiltonian maps. It is worthwhile to note that for any autonomous Hamiltonian H, there exists an $\varepsilon > 0$ such that the time 1 flow of εH has only constant fixed points [45]. Also, it automatically follows that flows of quasi-autonomous Hamiltonian systems are geodesics, that is they minimize length on sufficiently small time intervals. It was known from [46] that this is true for autonomous Hamiltonians, and examples of time dependent (quasi-autonomous) Hamiltonians can be found in [68].

5.4 The Best Generating Function Type

Now we are ready to transfer the problem of solving (5.15) to solving

$$\rho\left(\mathcal{M},\mathcal{N}_{opt}\right)=\inf_{i\in\Sigma}\frac{1}{|\mu|}||\Phi_{\alpha}\left(\mathcal{M}\right)-\Phi_{\alpha}\left(\mathcal{N}_{i}\right)||. \tag{5.87}$$

Denote $\Phi_{\alpha}\left(\mathcal{M}\right)=F^{\alpha}$. Unfortunately, F^{α} is unknown, and to minimize the right hand side of (5.87) a good approximation of F^{α} is needed. All the information about the system that is available in practice is contained in $\mathcal{M}_{n}$. This entails that, with some a priori fixed α, the best approximation for F^{α} is obtained by solving as accurately as possible (2.9). The necessary operations of truncated map computation, map composition and order m inversion, and integration are readily available in the code COSY INFINITY [24], and, as a consequence, the order m Taylor expansion of F^{α}, F_{m}^{α}, can be easily obtained. Then, it follows that the best result is achieved by the symplectic map $\mathcal{N}_{opt}$ which satisfies

$$\rho\left(\mathcal{M},\mathcal{N}_{opt}\right)=\inf_{\alpha\in\Sigma}\frac{1}{|\mu|}||F^{\alpha}-F_{m}^{\alpha}||, \tag{5.88}$$

where $\Phi_{\alpha}\left(\mathcal{N}_{i}\right)=F_{m}^{\alpha}$. Apparently, minimization of the right hand side of (5.88) is equivalent to the choice of the generating function type that achieves this minimization. It is worthwhile to note that, due to the one-to-one correspondence between generating functions of a fixed type and symplectic maps, $\rho\left(\mathcal{M},\mathcal{N}_{opt}\right)>0$ always, which means that the true solution can never be recovered by symplectification. Therefore, the differences among symplectification methods is caused by the truncation of the generating functions. However, F_{m}^{α} is the most that can be computed in practice. Hence, we can state the following conclusion:

Optimal symplectification with respect to Hofer's metric is achieved by the order n truncated generating function type that has the smallest oscillation norm of the terms neglected, above order m.

Thus, the remaining question is that, based on this limited information, which generator type will give optimal results in general? To answer this question we need to pick a generator type, or equivalently an α, that minimizes $||F^{\alpha}-F_m^{\alpha}||/\mu$. Again, for an arbitrary $\mathcal{M}$ this turns out to be a difficult problem, because in general nonlinear αs would be required, and it is difficult to construct useful nonlinear maps that satisfy (2.6). For accelerator physics applications this turns out not to be a problem since the maps of interest are in general weakly nonlinear maps around equilibrium points. For these types of maps linear choices of α are sufficient, which simplifies the construction of generating functions. Also, in principle any nonlinear Hamiltonian map can be split into a composition of Hamiltonian maps which are only weakly nonlinear. Therefore, the final step is to find the linear α, which can be considered as matrices, such that $||F^{\alpha} - F_m^{\alpha}||/\mu$ is minimized in general.

One of the main results of chapter 3 is that the set of linear maps satisfying (2.6) can be organized into equivalence classes, meaning that for symplectification purposes the following are the only independent generator types:

$$\alpha = \begin{pmatrix} -JM^{-1} & J \\ \frac{1}{2}(I + JS)M^{-1} & \frac{1}{2}(I - JS) \end{pmatrix}, \tag{5.89}$$

where M is the linear part of $\mathcal{M}$, and S represent arbitrary symmetric matrices. For a given $\mathcal{M}$ with linear part M, the classes characterized by some symmetric matrix S is denoted by $[S]$. We note that M is know from $\mathcal{M}_n$, and $\mu = 1$ for every α from (5.89). Thus optimal symplectification is map dependent, that is, there is a different optimal symplectification for every symplectic map having a different linear part. Then, which class $[S]$ gives the optimal symplectification for symplectic maps having the same linear part? To answer the question, first is observed that instead of the requirement of minimization of $||F^{\alpha} - F_m^{\alpha}||$, minimization of $||F^{\alpha}||$ could be required. The two requirements are not strictly equivalent. In one direction there is

no problem; if we require F^α to be small, it follows that the tail $F^\alpha - F^\alpha_m$ will be also small. Indeed, the only way that $F^\alpha - F^\alpha_m$ will not be small for some m when F^α is small is by cancellation of large terms in the Taylor expansion of F^α. However, as it will be seen below, this cannot happen due to the fact that C^0 smallness implies C^1 smallness. The other direction is not necessarily always true, that is, in general a small $F^\alpha - F^\alpha_m$ does not imply a small F^α. However, as have been shown in subsection 2.2.5, a large F^α does imply in general a small domain of definition of F^α. For further studies that support this conclusion, utilizing several examples, see [44]. It was shown that, indeed, lower bounds for the domains of generating functions can be guaranteed to enclose the dynamic aperture, if the corresponding types are small enough. Since we are interested in estimation of the DA, the generating functions should be defined in a rather large domain in phase space. Putting together the facts, we can conclude that for our purpose it is sufficient if $||F^\alpha||$ is minimized.

To this end, notice that, with the notations $\hat{z} = \mathcal{M}(z)$ and $w = \alpha_2(\hat{z}, z)$, (2.9) can be expressed as

$$\nabla_w F^\alpha(w) = \alpha_1(\hat{z}, z). \tag{5.90}$$

Integration, which can be along an arbitrary path according to Stokes' theorem, gives

$$F^\alpha(w) = \int_0^w \alpha_1(\hat{z}, z) \cdot dw'. \tag{5.91}$$

Taking norms on both sides of the equation the following estimate is obtained:

$$\| F^\alpha \| \leq \| \alpha_1 \circ \begin{pmatrix} \mathcal{M} \\ \mathcal{I} \end{pmatrix} \| \cdot \| \alpha_2 \circ \begin{pmatrix} \mathcal{M} \\ \mathcal{I} \end{pmatrix} \|. \tag{5.92}$$

It is rather straightforward to check from (2.9) and (5.89) that

$$\alpha_1(\hat{z}, z) = 0 + \mathcal{O}(z^2), \tag{5.93}$$

$$\alpha_2(\hat{z}, z) = I \cdot z + \frac{1}{2}(I + JS) \cdot \mathcal{O}(z^2). \tag{5.94}$$

From these equations it can be inferred that indeed C^0 smallness implies C^1 smallness. Therefore, $\alpha_1(\hat{z}, z)$ is already small if $\mathcal{M}$ is weakly nonlinear, and its norm does not depend on the type of generating function. Hence, minimization of $||F^\alpha||$ in the end is equivalent to minimization of $I + (I + JS)/2 \cdot \mathcal{O}(z^2)$. The only free parameter is the symmetric matrix S. Because the $\mathcal{O}(z^2)$ comes from the nonlinear part of the symplectic map $\mathcal{M}$, a simple calculation shows that $S = 0$ is the best choice if $\mathcal{M}$ is allowed to be free.

To see this, denote the Jacobian of $\mathcal{M}$ by $M + N$, where N is the nonlinear part. Because $\mathcal{M}$ is symplectic, we have the following relation:

$$N^T JN + N^T JM + M^T JN = 0. \tag{5.95}$$

We also observe that minimization of (5.94) and of

$$\| J \left(I + \frac{1}{2} (I + JS) \cdot N \right) \| \tag{5.96}$$

are equivalent, since J just reorders the entries. Suppose we found some S such that

$$J \left(I + \frac{1}{2} (I + JS) \cdot N \right) = J + \frac{1}{2} JN - \frac{1}{2} SN \approx 0. \tag{5.97}$$

Hence we have the relations

$$M^T JN \approx M^T SN - 2M^T J, \tag{5.98}$$

$$N^T JM \approx N^T SM + 2JM, \tag{5.99}$$

which inserted into (5.95) gives

$$\left[N^T JN \right] + \left[M^T SN + N^T SM \right] + \left[2JM - 2M^T J \right] \approx 0. \tag{5.100}$$

We separated the terms into three groups: the first contains 4th and higher order terms, the second group starts with second order terms, and the last group is purely linear. Therefore, S cannot influence the linear part of (5.100). Also, in the region

of interest to us the second and third order terms dominate over fourth and higher order terms. In fact, there is a good chance that in the region where fourth order terms dominate, the generating function is not even defined anymore, especially since we are working with Taylor expansions. Hence, for best results, we have to choose S in such a way to minimize the second and third order terms in (5.100). Clearly, this is achieved for any $\mathcal{M}$ by

$$S = 0. \tag{5.101}$$

With this result, it can be concluded that the optimal symplectification is achieved by the class of generators $[S]$ obeying $S = 0$, and associated with the following α:

$$\alpha_{opt} = \begin{pmatrix} -JM^{-1} & J \\ \frac{1}{2}M^{-1} & \frac{1}{2}I \end{pmatrix}. \tag{5.102}$$

Interestingly enough, it turns out that if in α_{opt} the linear part M is replaced with the unit matrix I, the resulting matrix gives a valid generator type, which exists for symplectic maps close enough to identity. It was first used by Poincaré in the restricted three body problem for a completely different purpose [39], and hence called the Poincaré generating function. Our α_{opt} can be regarded as a dynamically adjusted Poincaré generator, to symplectic maps not having identity as linear parts. That is why we call it the EXtended POincaré (EXPO for short) generating function type. Finally, the best symplectified map $\mathcal{N}_{opt}$, in the sense presented in this chapter, is obtained if the symplectification is performed using the EXPO generator type, i.e.

$$\mathcal{N}_{opt} \equiv \mathcal{N}_{EXPO}. \tag{5.103}$$

Many examples of EXPO can be found in chapter 4. Indeed, the pictures confirm the conclusions of the optimal symplectification theory, i.e. EXPO is in general by far superior to any other generator type studied, including the traditionally used

conventional Goldstein types. It is expected that the EXPO will become the method of choice for symplectic tracking in COSY INFINITY.

5.5 Some Further Remarks

In general, Hofer's metric is rather little understood. It determines a kind of C^{-1} topology on $\mathrm{Ham}^c(\mathbb{R}^{2n})$, and gives rise to a paradox. Sikorav [69] showed that every one-parameter subgroup of $\mathrm{Ham}^c(\mathbb{R}^{2n})$ remains a bounded distance from the identity. So, we could draw the paradoxical conclusion that, according to the theorem proved in subsection 5.3.4, every point has a flat neighborhood, but in some sense a positive curvature is apparent. In any case, geometry on the group of Hamiltonian symplectomorphisms with respect to Hofer's metric gives rise to a different way of thinking about Hamiltonian dynamics, and we can expect quite some progress in this direction in the near future. The understanding of the global features and properties of Hofer's metric could give insight into the long term properties of Hamiltonian systems, and perhaps provide an exciting method to compute the region of stability without the time intensive tracking.

Finally, we mention that there exists another, related metric on $\mathrm{Ham}^c(\mathbb{R}^{2n})$, introduced in [66]. However, in [63] and [65] it was proved that they coincide locally on $\mathbb{R}^{2n}$, so we need not consider it. We use Hofer's metric because it is easier to work with.

Put in a different perspective, according to (5.88), since we are working with Taylor expansions of generating functions, the best generating function is which has the fastest convergence inside its support. The first thought to minimize the left hand side is to choose the conformality factor μ as large as possible. However, this is deceiving as has been seen in section 3.2. Here, another method is presented to the

same effect. Consider any admissible α, of the form (5.32) with $\mu = 1$. Compute the corresponding distance from (5.88). For another α in the same class, which differs just by $\mu \gg 1$, the corresponding generating function is equivalent to the generating function of α with $\mu = 1$, subjected to the transformation $\alpha_1 \longmapsto \mu\alpha_1$. However, we have seen in the section on transformation properties of generating functions that this transformation is equivalent to $F \longmapsto \mu F$. Hence, we get the same distance in both cases. At the same time, consider the transformation $\alpha_2 \longmapsto \mu\alpha_2$. It follows from (3.27) that the generating functions transform according to $F \longmapsto \mu F \circ \mu^{-1}\mathcal{I}$. The simultaneous transformations $\alpha_1 \longmapsto \mu\alpha_1$ and $\alpha_2 \longmapsto \mu^{-1}\alpha_2$ leave the conformality factor equal to 1 and give $F \longmapsto F \circ \mu\mathcal{I}$, according to (3.21). Hence, inserting them into (5.88), again we get the same distances. It follows that the conformality factor does not add any flexibility. Therefore, the conformality factor does not influence the outcome of the symplectification, hence $\mu = 1$ is always assumed.

As a side note, we mention that the conformality factor does play a role in the numerical stability of the algorithms. For example, if a generating function with $\| S \| \gg 1$ is computed, (some entries in) the primitive function might be scaled down to zero on a computer (which in reality are tiny, but still non-zero), and it might be obtained that the generating function vanishes, which is obviously wrong. This follows from the fact that $I/2 + JS/2 \approx JS/2$ if $\| S \| \gg 1$, and if we write $S \propto 2\mu I$, then μ can be considered as a conformality factor induced by the transformation $\alpha_2 \longmapsto \mu\alpha_2$, which in turn induces the $F \longmapsto \mu F \circ \mu^{-1}\mathcal{I}$ transformation of the primitive function. Hence, if $\mu \gg 1$ numerical problems arise in the nonlinear part of F. This constitutes another reason for working with $\mu = 1$ only.

Intuitively, Hofer's metric measures what is the minimal Hamiltonian needed, averaged over time, to generate a symplectic map from identity. Actually, Hofer himself calls the distance from the identity of a map the symplectic energy of the

map. In view of the KAM theorem for symplectic integration methods [70, 2], which roughly says that the behavior of symplectic maps obtained by symplectic integration applied to a integrable system should be close to the integrable system (at least in the region where invariant tori still exist), this provides a strong support for our closeness criterion for optimal symplectification based on Hofer's metric, and points out that Hofer's metric is a natural choice.

There is an alternative interpretation of Hofer's metric applied to beam dynamics. Notice that, due to bi-invariance of Hofer's metric we have

$$\rho\left(\mathcal{M},\mathcal{N}\right)=\rho\left(\mathcal{N}^{-1}\circ\mathcal{M},\mathcal{I}\right). \tag{5.104}$$

Therefore, by computing the distance between symplectic maps in Hofer's metric, actually what is computed is the minimum Hamiltonian needed to generate the initial conditions of $\mathcal{N}$ from the initial conditions of $\mathcal{M}$, such that both $\mathcal{M}$ and $\mathcal{N}$ applied to the respective initial conditions give the same final results. If the result of the norm minimization is small, the two sets of initial conditions are connected by a map close to identity, hence the two sets are close to each other. From a practical point of view this can be considered as not knowing exactly the properties of the injected beam. Such small uncertainties always occur in practice, and to be able to build robust accelerators, one should look for realizations that are not too sensitive to small errors. This is done by considering different error sources, each realization of the errors giving a different symplectic map. The incoming beam quality can be considered one type of such an error effect. Hence, from this viewpoint it does not matter whether $\mathcal{M}$ or $\mathcal{N}$ is used for the simulation of the accelerator.

The optimality condition can be given a nice geometric interpretation. Minimizing the norm of the generating function is equivalent with finding the generating function type, which maps the Lagrangian submanifold determined by the symplectic map as

close as possible to the zero section. In fact, for any symplectic map, a generating function type can be found, such that it is globally defined and it is identically zero. This corresponds to the case when the corresponding generator type maps the Lagrangian submanifold exactly to the zero section. However, in practice this observation is worthless, because the problem of finding the respective type of generator is equivalent with representing the symplectic map on a computer, rendering the symplectification procedure pointless. To see this, just replace in (5.89) M with the total map $\mathcal{M}$. Nevertheless, the observation it is very useful in another sense. In the present chapter the optimality condition has been formulated for the most general case, but the solution has been found only for generator types of linear α, which was enough for the symplectic maps of practical interest, i.e. weakly nonlinear. In case $\mathcal{M}$ is strongly nonlinear, nonlinear αa are needed to map the respective Lagrangian submanifolds closer to the zero section. Thus, nonlinear α type of generators become a necessity, since with nonlinear αs the Lagrangian submanifolds can be mapped closer to the zero section than with any linear α generator type. This observation hints towards the right direction to look for the appropriate nonlinear αs.

There are also other interesting consequences of these results, specifically concerning symplectic integration. The only difference between symplectic integration and symplectic tracking is the method for obtaining the truncated generating function. In the case of symplectic tracking, it is obtained from $\mathcal{M}_n$ using (2.9). In symplectic integration, it is obtained by direct solution of the generalized Hamilton-Jacobi equation (5.69). Thus, in this case, the linear part M is not known. Therefore, the prescription for optimal symplectic integration is to use Poincaré's generating function and a sufficiently small time step (by this keeping the linear part of the resulting symplectic map as close as possible to identity). Moreover, if the Poincaré generator is expanded in a power series in the time step, from the Hamilton-Jacobi equation it

follows that, as first order approximation in time $F_P(w) = H(z)$. The corresponding integration method then reduces to the well-known implicit midpoint rule.

To conclude this chapter, we would like to make a clearer connection between Hofer's metric and the visual aspects of the assessment of optimality of symplectification. That is, while the optimal symplectification theory says that in general EXPO is optimal, it has been seen that, in the case of the anharmonic oscillator of section 4.2, the generator type S_b gave visually (or equivalently, in a C^0 sense) better results than EXPO. What is the explanation in the light of the optimal symplectification theory? Well, S_b is "more optimal" than EXPO because over the region which includes all trajectories of interest, the Hofer distance between the exact map and the symplectified map with S_b is smaller than the distance between the exact map and the map symplectified with EXPO. Unfortunately, we cannot compute Hofer's distance exactly. However, considering the 19th order Taylor map as the exact solution, according to (5.86) we can approximate the distance very accurately from

$$d_{EXPO} \approx \| F_{19}^{EXPO} - F_{11}^{EXPO} \|, \tag{5.105}$$

and

$$d_{S_b} \approx \| F_{19}^{S_b} - F_{11}^{S_b} \|, \tag{5.106}$$

respectively. We plotted $F_{19} - F_{11}$ (magnified by some constant factor) with Mathematica for the two cases, and we obtained Figure 5.1. We can read off the plots

$$d_{EXPO} \approx 3, \tag{5.107}$$

$$d_b \approx 1. \tag{5.108}$$

Obviously, S_b is better than EXPO. Notice that the sharp deviation from zero of the distance function occurs only in the region close to the dynamic aperture, where we already noticed most of the discrepancies among the various maps. This observation

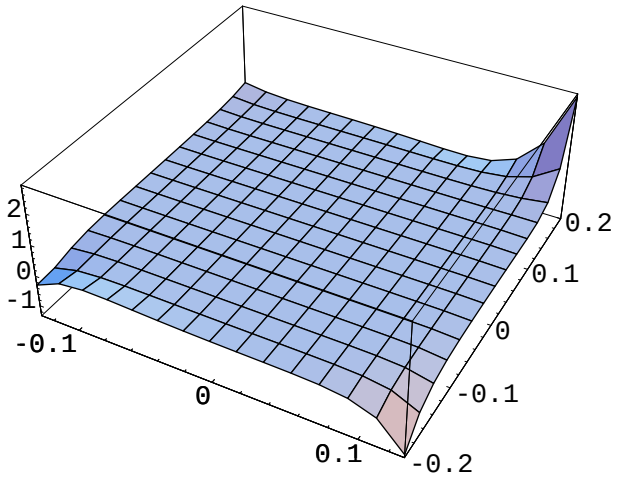

(a) EXPO symplectification

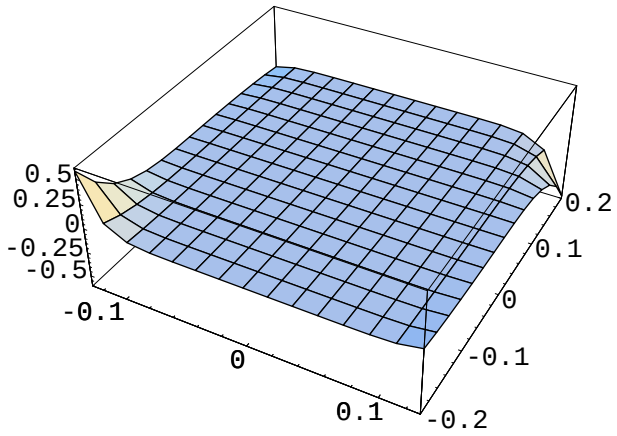

(b) S_b symplectification

Figure 5.1: Plot of Hofer's distance between the exact and the symplectified maps over the region enclosing the dynamic aperture of the anharmonic oscillator studied in section 4.2.

opens the prospect of using Hofer's metric as a local indicator beside the global one that we already know.

Chapter 6

Summary of Part I

The extended theory of generating functions of canonical transformations was developed. Using a modified definition of the generating function, it was showed that there are many more generating functions than commonly known, and some always are defined globally. The set of generating functions turned out to be very degenerate from the symplectification point of view. However, employing some transformation properties of the generating functions, it was possible to reduce the pool of generating functions to equivalence classes associated with linear conformal symplectic maps. The remaining independent types were characterized by symmetric matrices. Also, it was proved that by choosing appropriate types of generators, there is no advantage in factoring out linear parts and symplectifying only nonlinear parts, or first subjecting the map to be symplectified to a linear symplectic coordinate change.

The performance of this symplectification method was illustrated by a variety of examples. It was showed that different generator types often give significantly different long term behavior of the symplectified maps. This fact pointed out the necessity for optimal generating function symplectification studies, which were solved in a very general setting based on Hofer's metric.

Using Hofer's metric, a condition for optimal symplectification was given. After

a few manipulations, Hofer's metric for Hamiltonian symplectic maps was expressed in terms of associated generating functions. Therefore, finding the best symplectified map turned out to be equivalent to finding the appropriate generator type. It was shown that the generator type which satisfies the optimality condition in general is given by (5.102), and it was called the EXPO type. Consequently, the symplectic map $\mathcal{N}_{EXPO}$, obtained by symplectification of $\mathcal{M}_n$ using EXPO, gives optimal results in general. However, these results do not exclude the existence of custom tailored generator types that give better results for *specific* symplectic maps. EXPO is not only optimal, but it is also fast due to its simplicity, implementation using fixed point iterations, and vectorization.

Throughout part I methods of symplectic geometry and topology have been utilized. The unifying concept behind these methods is the flows of Hamiltonian systems. The accelerators of interest to us can be modeled as Hamiltonian systems. The time evolution of these systems (i.e. the flow, or the particle orbits) can be regarded as curves on the space of Hamiltonian symplectic maps. The geometric properties of these curves with respect to Hofer's metric are deeply related to the dynamics. In this dissertation we exposed and exploited several aspects of this relationship. More precisely, the Hamiltonian system representing the real accelerator lattice is replaced by another Hamiltonian system, and instead of simulating approximately the real accelerator, we track exactly a nearby accelerator, where closeness is measured in Hofer's metric. Then we hope that the perturbations so introduced are small enough that in the light of the KAM theorem most invariant tori, and hence most of the geometric structures, survive, and it leads to a more reliable and faster estimation of the dynamic aperture.

Finally, while the results obtained in this dissertation have been derived with accelerator physics motivation in mind, their relevance go beyond beam physics, and

directly apply to any other weakly nonlinear problem in Hamiltonian dynamics.

Part II

Accurate Simulation of Fringe Field Effects

Chapter 7

Introduction and Theoretical Background

In part I it was shown that symplectification of the truncated Taylor maps, in general, is necessary, and it must be done by using the appropriate generating function type, EXPO. As a prerequisite of symplectification, it was assumed that the truncated, order n symplectic, Taylor maps represent the systems well over short times. If this is not the case, it is easy to find examples for which no symplectification can give good results. For example, consider two truncated Taylor maps representing two different systems, which agree through order n, but differ by a large amount starting at order $n+1$. This can happen, for example, if the amplitude dependent tune shifts of both systems agree up to order n, but only one of the system has some very large tune shifts at order $n+1$. This entails that no symplectification can predict the behavior of the system with large tune shifts, if the order n truncated Taylor map is used for symplectification. The reason is that important information was neglected about the system, which renders the order n truncated Taylor map inaccurate, even for short times. Therefore, for successful symplectic tracking, the order n needs to be high enough (the exact value being system dependent), and every relevant effect must be incorporated into the Taylor map. One of the effects that requires more sophisticated

methods for their inclusion in the one-turn Taylor map, are the effects of fringe fields. In part II of this dissertation, the theory relevant for accurate fringe field effects simulation is developed, the effects are studied generically in chapter 8, new methods for multipole decomposition of superconducting magnets are introduced in chapter 9, and the results are applied to a few examples. For the LHC, a detailed study draws some conclusions about the effects of realistic fringe fields on the nonlinear dynamics of particles in chapter 10.

Due to the diversity of the field of nonlinear beam optics, the mathematical methods employed and the formalisms utilized can be very different depending on the specific design requirements. One of the topics for which traditionally very different approaches have been carried out in different subfields are the fringe fields, or end fields. For the purpose of simulations of large storage rings, fringe field effects are often neglected. Sometimes this is a quite good approximation. However, strictly speaking, it is an unphysical model, as the electromagnetic fields of the model do not satisfy Maxwell's equations. The simplest method to take fringe fields into account is to approximate their effect with a kick (i.e. impulsive momentum change, while position is unchanged) characterized by the integrated field value [71]. While this model may alleviate some problems, it is not a cure, and more sophisticated models are needed for accurate simulations. Besides the kick, the effect of the fringe fields has been characterized by a sudden shift in position at the so-called effective field boundary [72, 73, 74, 75]. For a specific field falloff, in [76] the third order aberrations and their scaling with fringe field extension have been computed for the quadrupole. Also, leading order hard edge fringe field effects have been studied in [77]. Fringe fields have been shown to adversely affect the PEP-II dynamic aperture [78]. However, an extensive study of fringe field effects has so far not been available.

The nonlinearities due to fringe fields have been well-known in the field of high

resolution particle spectrographs for a long time [74, 79]. Also, as recently has been shown, they tend to become significant in small rings, especially at larger emittances [11, 12]. The latter studies motivated us to look more deeply, at a fundamental level, at the fringe field effects.

The introduction of the methods used to study the fringe field effects, first requires the development of a theoretical framework. In the following we assume straight optical axis, and a source-free region surrounding the axis. In this divergence-free, curl-free region of the magnets it is possible to derive the magnetic field components from a magnetic scalar potential that satisfies the Laplace equation. The general solution expanded in cylindrical coordinates with axial coordinate s, in the so-called multipole expansion form is [80]

$$V_B = \sum_{k,l=0}^{\infty} \left(b_{k,l}(s) \sin l\phi + a_{k,l}(s) \cos l\phi\right) r^k. \tag{7.1}$$

The functions $b_{l,l}(s)$ are called the normal and $a_{l,l}(s)$ the skew multipoles, respectively. The components, according to $l = 0, 1, 2, 3, ...$ are called the solenoid, dipole, quadrupole, sextupole, etc. components, respectively. Defining $\theta_{k,l}(s)$ and $M_{k,l}(s)$ by

$$\tan \theta_{k,l}(s) = -\frac{b_{k,l}(s)}{a_{k,l}(s)}, \tag{7.2}$$

$$M_{k,l}(s) = \sqrt{b_{k,l}^2(s) + a_{k,l}^2(s)}, \tag{7.3}$$

we have an equivalent form

$$V_B = \sum_{k,l=0}^{\infty} M_{k,l}(s) \cos\left(l\phi + \theta_{k,l}(s)\right) r^k, \tag{7.4}$$

which shows that any normal (skew) component can be obtained from the corresponding skew (normal) component by an s-dependent rotation around the s axis.

The link between the two forms in the other direction is

$$\begin{aligned} b_{k,l}(s) &= -M_{k,l}(s)\sin\theta_{k,l}(s) \\ a_{k,l}(s) &= M_{k,l}(s)\cos\theta_{k,l}(s). \end{aligned} \tag{7.5}$$

Inserting (7.1) in the Laplace equation in cylindrical coordinates

$$\Delta V_B = \frac{1}{r}\frac{\partial}{\partial r}\left(\frac{r\partial V_B}{\partial r}\right) + \frac{1}{r^2}\frac{\partial^2 V_B}{\partial \phi^2} + \frac{\partial^2 V_B}{\partial s^2} = 0, \tag{7.6}$$

we obtain

$$\sum_{k,l=0}^{\infty}\left[\left(b_{k,l}(s)(k^2-l^2)+b''_{k-2,l}(s)\right)\sin l\phi + \left(a_{k,l}(s)(k^2-l^2)+a''_{k-2,l}(s)\right)\cos l\phi\right] r^{k-2} = 0, \tag{7.7}$$

using the convention that the coefficients vanish for negative indices. Due to the fact that the above equation must hold for every r and ϕ, and the sin and cos are linearly independent, it follows that

$$b_{k,l}(s)(k^2-l^2) + b''_{k-2,l}(s) = 0 \tag{7.8}$$

$$a_{k,l}(s)(k^2-l^2) + a''_{k-2,l}(s) = 0. \tag{7.9}$$

Furthermore, it can be shown that the following recurrence relations hold:

$$b_{l+2n,l}(s) = \frac{b^{(2n)}_{l,l}(s)}{\Pi_{\nu=1}^{n}\left(l^2-(l+2\nu)^2\right)} \tag{7.10}$$

$$a_{l+2n,l}(s) = \frac{a^{(2n)}_{l,l}(s)}{\Pi_{\nu=1}^{n}\left(l^2-(l+2\nu)^2\right)}, \tag{7.11}$$

and the coefficients that cannot be obtained by these relations are zero. The terms that contain s-derivatives are called pseudo-multipoles. It is worth mentioning that, as one can see from (7.2), the recurrence relations (7.10) do not hold in general for

$M_{k,l}(s)$. However, when the $\theta_{k,l}$s are s-independent, (7.10) holds for $M_{k,l}(s)$. Inserting relations (7.10) in (7.1), we get for the potential

$$V_B = \sum_{l=0}^{\infty} \left(f_l(r,s) \sin l\phi + g_l(r,s) \cos l\phi \right) r^l, \tag{7.12}$$

where

$$\begin{aligned} f_l(r,s) &= \sum_{n=0}^{\infty} b_{l+2n,l}(s) r^{2n} = \sum_{n=0}^{\infty} \frac{b_{l,l}^{(2n)}(s)}{\Pi_{\nu=1}^{n} \left(l^2 - (l+2\nu)^2 \right)} r^{2n} \qquad (7.13) \\ &= b_{l,l}(s) - \frac{b_{l,l}^{(2)}(s)}{4(l+1)} r^2 + \frac{b_{l,l}^{(4)}(s)}{32(l+1)(l+2)} r^4 - \frac{b_{l,l}^{(6)}(s)}{384(l+1)(l+2)(l+3)} r^6 + \ldots \\ g_l(r,s) &= \sum_{n=0}^{\infty} a_{l+2n,l}(s) r^{2n} = \sum_{n=0}^{\infty} \frac{a_{l,l}^{(2n)}(s)}{\Pi_{\nu=1}^{n} \left(l^2 - (l+2\nu)^2 \right)} r^{2n} \qquad (7.14) \\ &= a_{l,l}(s) - \frac{a_{l,l}^{(2)}(s)}{4(l+1)} r^2 + \frac{a_{l,l}^{(4)}(s)}{32(l+1)(l+2)} r^4 - \frac{a_{l,l}^{(6)}(s)}{384(l+1)(l+2)(l+3)} r^6 + \ldots \end{aligned}$$

The functions $f_l(r,s)$ and $g_l(r,s)$ represent the "out of axis" expansion of the multipoles. The magnetic field components in cylindrical coordinates can be calculated using the well known formulas

$$B_r = -\frac{\partial V_B}{\partial r} \tag{7.15}$$

$$B_\phi = -\frac{1}{r} \frac{\partial V_B}{\partial \phi} \tag{7.16}$$

$$B_s = -\frac{\partial V_B}{\partial s}, \tag{7.17}$$

resulting the expressions

$$B_r(r,\phi,s) = \tilde{g}_0(r,s) + \sum_{l=1}^{\infty} \left[\tilde{f}_l(r,s) \sin l\phi + \tilde{g}_l(r,s) \cos l\phi \right] r^{l-1} \tag{7.18}$$

$$B_\phi(r,\phi,s) = \sum_{l=1}^{\infty} \left[l \left(f_l(r,s) \cos l\phi - g_l(r,s) \sin l\phi \right) \right] r^{l-1} \tag{7.19}$$

$$B_s(r,\phi,s) = \sum_{l=0}^{\infty} \left[f_l^{'}(r,s) \sin l\phi + g_l^{'}(r,s) \cos l\phi \right] r^l, \tag{7.20}$$

where prime denotes derivative with respect to s and

$$\tilde{f}_l(r,s) = \sum_{n=0}^{\infty}(l+2n)b_{l+2n,l}(s)r^{2n} = \sum_{n=0}^{\infty}\frac{(l+2n)b_{l,l}^{(2n)}(s)}{\Pi_{\nu=1}^{n}\left(l^2-(l+2\nu)^2\right)}r^{2n} \tag{7.21}$$

$$= lb_{l,l}(s) - \frac{(l+2)b_{l,l}^{(2)}(s)}{4(l+1)}r^2 + \frac{(l+4)b_{l,l}^{(4)}(s)}{32(l+1)(l+2)}r^4 - \frac{(l+6)b_{l,l}^{(6)}(s)}{384(l+1)(l+2)(l+3)}r^6 + \ldots$$

$$\tilde{g}_l(r,s) = \sum_{n=0}^{\infty}(l+2n)a_{l+2n,l}(s)r^{2n} = \sum_{n=0}^{\infty}\frac{(l+2n)a_{l,l}^{(2n)}(s)}{\Pi_{\nu=1}^{n}\left(l^2-(l+2\nu)^2\right)}r^{2n} \tag{7.22}$$

$$= la_{l,l}(s) - \frac{(l+2)a_{l,l}^{(2)}(s)}{4(l+1)}r^2 + \frac{(l+4)a_{l,l}^{(4)}(s)}{32(l+1)(l+2)}r^4 - \frac{(l+6)a_{l,l}^{(6)}(s)}{384(l+1)(l+2)(l+3)}r^6 + \ldots$$

It can be seen that every multipole, except for $l=0$, is multiplied by r^{l-1}. For the special case $l=0$, we obtain

$$B_r(r,s) = \tilde{g}_0(r,s) = -\sum_{k=1}^{\infty}(-1)^{k+1}\frac{k}{2^{2k-1}k!k!}a_{0,0}^{(2k)}(s)r^{2k-1} \tag{7.23}$$

$$B_\phi(r,s) = 0 \tag{7.24}$$

$$B_s(r,s) = -\sum_{k=0}^{\infty}(-1)^{k+1}\frac{1}{2^{2k}k!k!}a_{0,0}^{(2k+1)}(s)r^{2k}. \tag{7.25}$$

In the Differential Algebraic (DA) picture, the field calculations are done locally, as Taylor expansions of the fields with respect to the Cartesian coordinates x, y, s. Hence, we need the following equations relating the cylindrical and Cartesian components of the magnetic fields:

$$B_x(r,\phi,s) = B_r(r,\phi,s)\cos\phi - B_\phi(r,\phi,s)\sin\phi \tag{7.26}$$

$$B_y(r,\phi,s) = B_r(r,\phi,s)\sin\phi + B_\phi(r,\phi,s)\cos\phi, \tag{7.27}$$

and $B_s(r,\phi,s)$ is unchanged.

Chapter 8

Generic Effects

For a better understanding of the fringe field effects, we start their study in this chapter, by performing a study of the effects that one may miss by not considering the influence of the fringe fields. We keep the study generic, and use lattices of the muon storage rings, which, however, are available only at a preliminary design stage, and to illustrate general trends in small footprint (i.e. small effective area occupied by the accelerator), large acceptance rings. Specifically, we use a version of the proposed 30 GeV Neutrino Factory [52], and of the FNAL Proton Driver [53].

The fringe fields' falloff are modeled by a six parameter Enge function

$$F(s) = \frac{1}{1 + \exp\left(\sum_{i=1}^{6} a_i \left(s/D\right)^{i-1}\right)}, \tag{8.1}$$

where s is the arclength along the reference trajectory, used as the independent variable. D denotes the full aperture of the magnet, and the a_i $(i = 1, 2, ..., 6)$ are called Enge coefficients. For practical calculations, the Enge coefficients are either fitted to represent measured data [81], or obtained by multipole decomposition of detailed field computations as in chapter 9. We look at fringe field effects as a function of magnet aperture and falloff shape. This is achieved by varying the magnet apertures D, and the Enge coefficients a_i.

The fringe field effects can be particularly easily studied in the map picture using Differential Algebraic methods [82, 9, 10]. The consequences of the fringe field effects influence all orders of the motion, beginning with the linear behavior. The pseudo-multipole nonlinearities of the fringe fields couple to higher derivatives of the multipole strengths. In practice this entails that fringe field effects become more and more relevant the more the particles are away from the axis of the elements, which, of course, is directly connected to the emittance of the beam. Also, it is clear that the falloff shapes, and implicitly the apertures, have an influence on the induced nonlinearities. Complete treatment, to any order, of detailed fringe field effects is possible in the code COSY INFINITY [83, 84, 24, 85]. To quantify the effects, we compute linear tunes, amplitude dependent tune shifts, chromaticities, resonance strengths, and estimate dynamic apertures. In the following sections we present observations related to aperture (section 8.1) and shape dependent effects (sections 8.2 and 8.3). In section 8.4 it is presented briefly that neglect of the high order pseudo-multipoles can also give misleading simulation results. Moreover, in section 8.5 it is pointed out that, in general, symplectification is not sufficient to undo the errors made in neglecting important information about the system (such as higher order pseudo-multipoles).

8.1 Aperture Dependent Effects on Linear Tunes and Chromaticities

In some perturbation theories the linear or first order effects are not considered. In others, the first order effect is characterized by a kick [71], or as a sudden change in position and momentum at the so-called effective field boundary [74]. Here, using the 30 GeV Neutrino Factory lattice, we compute with COSY INFINITY the linear tunes and chromaticities as a function of the magnet apertures. We assume that all

	Dipole	Quadrupole	Sextupole
a_1	0.478959	0.296471	0.176659
a_2	1.911289	4.533219	7.153079
a_3	−1.185953	−2.270982	−3.113116
a_4	1.630554	1.068627	3.444311
a_5	−1.082657	−0.036391	−1.976740
a_6	0.318111	0.022261	0.540068

Table 8.1: Enge coefficients of the default fringe field falloff used in COSY INFINITY for dipoles, quadrupoles, and sextupoles, respectively.

the magnets have the same aperture, and the falloff is given by the Enge coefficients of Table 8.1 [86]. We will call them hereafter the default Enge coefficients. It is important to note that the Enge function model can be used for a global fit of the magnetic fields, including the out of axis expansion. This has been demonstrated in several real situations, as for example the NSCL's S800 spectrograph [87], the GSI QD kaon spectrometer [88], and even the rather peculiar LHC HGQ lead end [81].

The aperture is varied between 1 mm and 300 mm. Fig. 8.1 gives the results for the x and y center tunes (tunes in the linear approximation). In the stable regions the tunes change continuously and monotonically with the aperture. However, in general there is a nonlinear relationship between center tunes and the aperture. As the linear motion is uncoupled, for linear stability the absolute values of the traces of the $x - a$ (horizontal phase plane) and $y - b$ (vertical phase plane) submatrices respectively need to be less then 2. The variables a, b are scaled momenta, conjugate to x and y, respectively. The nonlinear dependence of the traces on the apertures is also clear from Fig. 8.2. The trend regarding chromaticities is included in Fig. 8.3 and 8.4.

It has been noticed that the main impact of the fringe fields is coming from only a few matching quadrupoles in the arcs [12]. We repeated the computations of this section for the same ring, with the respective matching quadrupole fringe fields turned

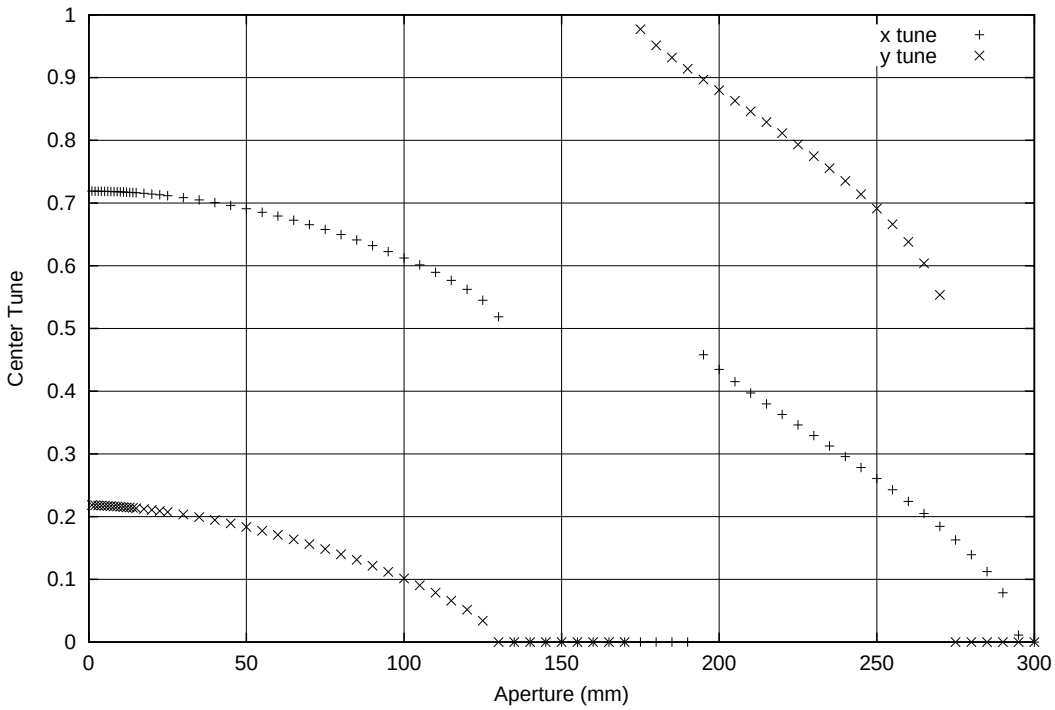

Figure 8.1: Center tunes as a function of aperture. The fringe field shape is given by the default Enge coefficients.

off. As one can see from Fig. 8.5 and 8.6, the results are different only quantitatively, but qualitatively the situation remains the same.

8.2 The Sharp Cutoff Limit

As already mentioned, the sharp cutoff, or hard-edge, approximation is a contradiction in itself, as far the physics goes. However, as a purely mathematical approximation, it still can be analyzed in some detail. Qualitatively, it can be characterized as follows. The function that describes the falloff is called the cutoff function, or a bump function. It is well-known in the mathematical literature [43, 89] that infinitely often continuously differentiable (C^∞ smooth) bump functions can be found such that they take the value 1 on one closed set, and assume the value zero on the complement of another closed set; one of the closed sets lying in the interior of the other closed

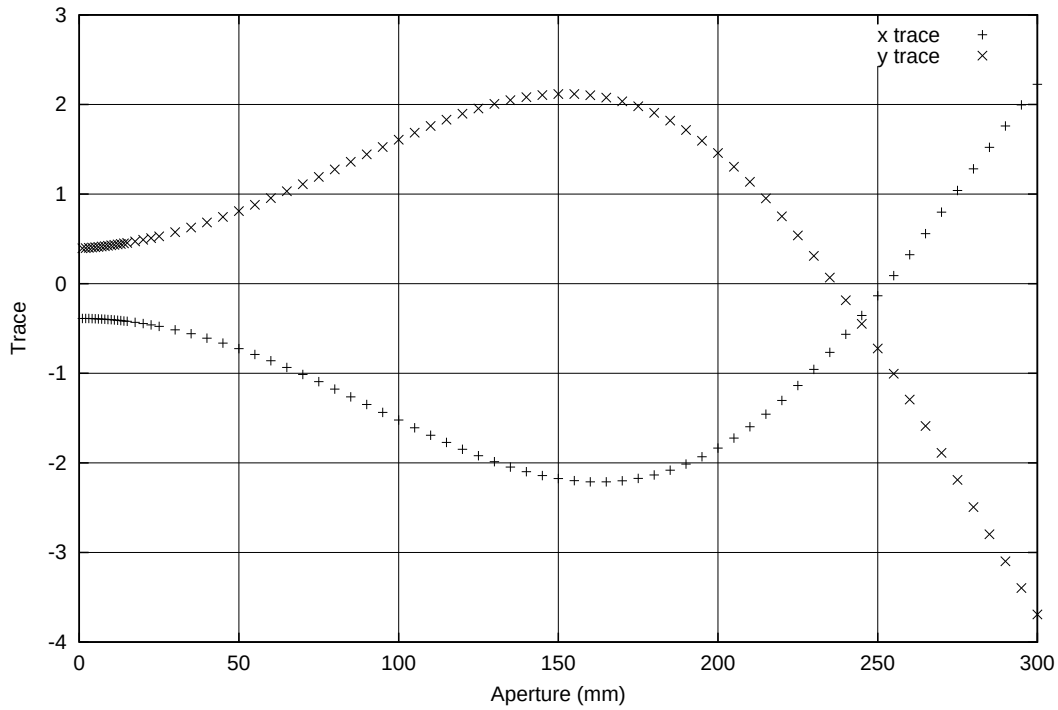

Figure 8.2: Traces of the $x - a$ and $y - b$ submatrices versus aperture. The fringe field shape is given by the default Enge coefficients.

set. For our case the inner closed set can be taken as the region of the main field of the magnet, and the complement of the outer closed set the region where the fields practically vanish. Furthermore, the two sets are arbitrary except the already mentioned conditions. This means that the two sets can be taken arbitrarily close to each other in some sense (for example in the Hausdorff metric). Thus, the falloff speed can be arbitrarily fast, and at the same time the smoothness can be kept intact.

This is why the sharp cutoff limit gives satisfactory numerical results when fringe fields are not important: in principle, the falloff regions' width always can be taken smaller than the smallest step of any integrator, and thus escapes from any numerical issues. On the other hand, as a rigorous mathematical limit, the sharp cutoff limit corresponds to the case where the two closed sets "touch" each other. In this case, any bump function tends to the sum of two Heaviside functions, which then end up in

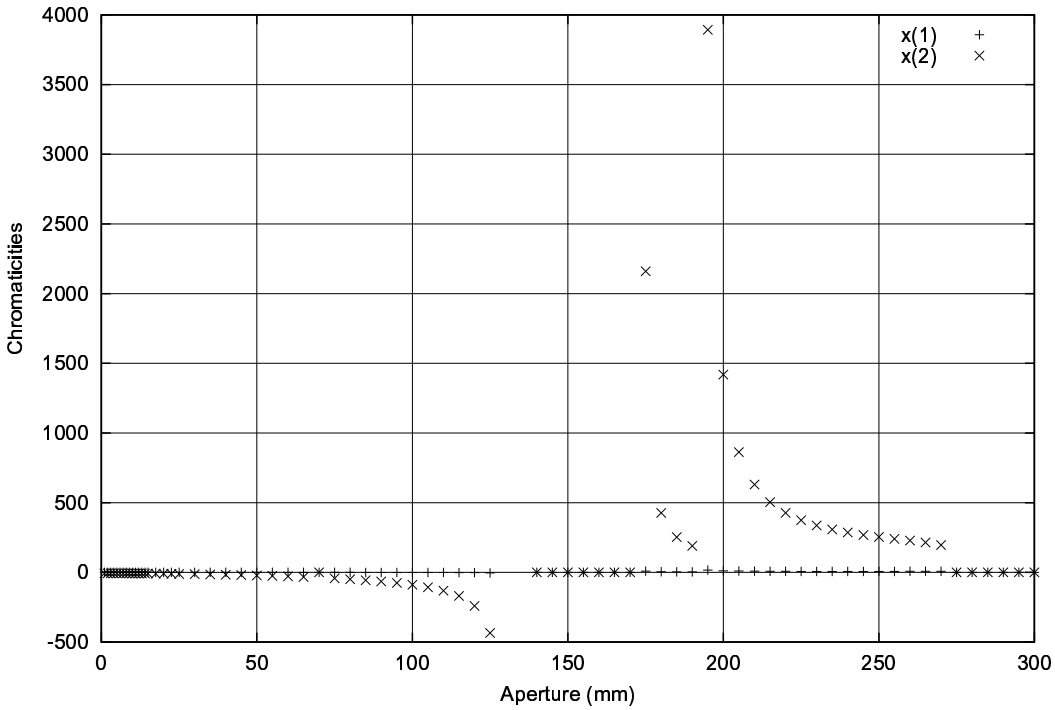

Figure 8.3: First and second order x chromaticities as a function of aperture. The fringe field shape is given by the default Enge coefficients.

the Hamiltonian. However, as it is well-known, the dynamics is not governed by the Hamiltonian itself, but by its gradient. The Heaviside function's derivative being the Dirac delta function, it follows that the sharp cutoff limit gives rise to divergences. The divergences show up as blowing up of some of the map elements, and, as a consequence, some of the tune shifts and resonance strengths.

Hence, blow-up of amplitude dependent tune shifts in the sharp cutoff limit occurs regardless of the exact shape of the falloff. However, in the perturbative order-by-order approach, the divergence can occur at different orders depending on the specific fields involved. For the case of the homogeneous dipole, it has been derived [90] that the lowest order map element that causes divergence is $(b|yyy)$, that is the element that shows how the final angle in the vertical phase plane depends on the initial position in the vertical direction.

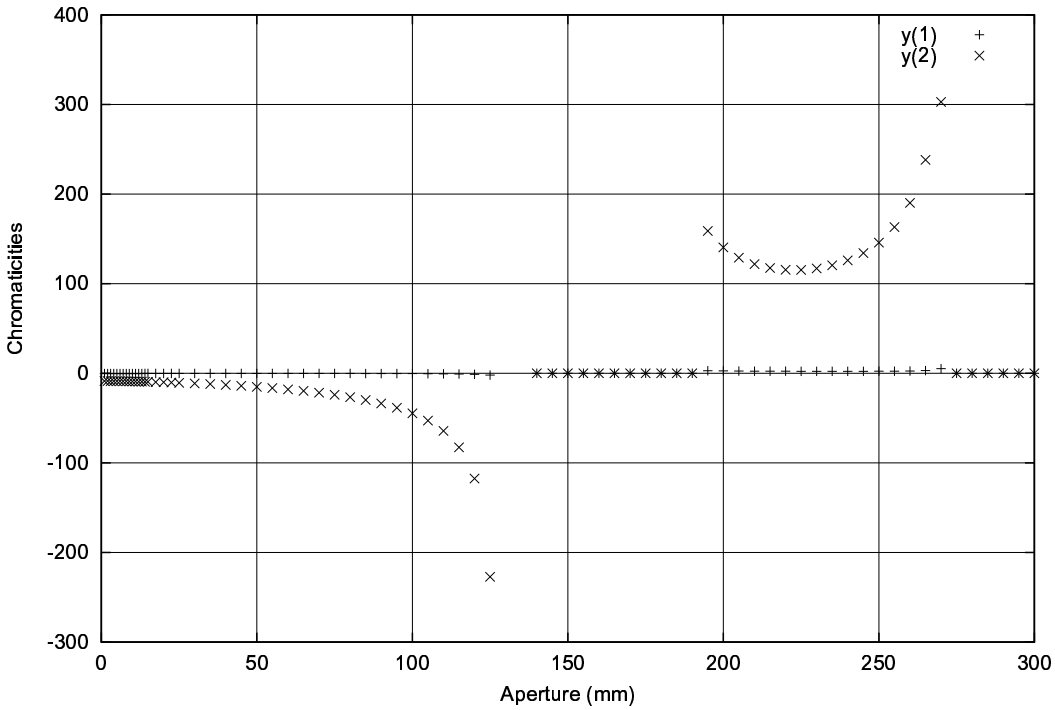

Figure 8.4: First and second order y chromaticities as a function of aperture. The fringe field shape is given by the default Enge coefficients.

For multipoles with straight optical axis, the divergences occur at higher orders. Recently, under some simplifying assumptions, estimates for the second order amplitude dependent tune shifts of a quadrupole fringe field have been calculated [91]. It is shown that, in the integrated field approximation, the second order tune shifts tend to a finite non-zero value in the sharp cutoff approximation. This is derived from a few integrals that are part of the integrated Hamiltonian, and taking limits as the extension of the fringe region goes to zero. Within its domain of validity, the estimate gives good agreement with the exact values computed by COSY INFINITY, at least for the cases studied.

The second order tune shifts (i.e. the quantities that represent the quadratic dependence of the tunes on the amplitudes) are functions of the third order map elements. To compute the third order map elements of a quadrupole, integrals of the

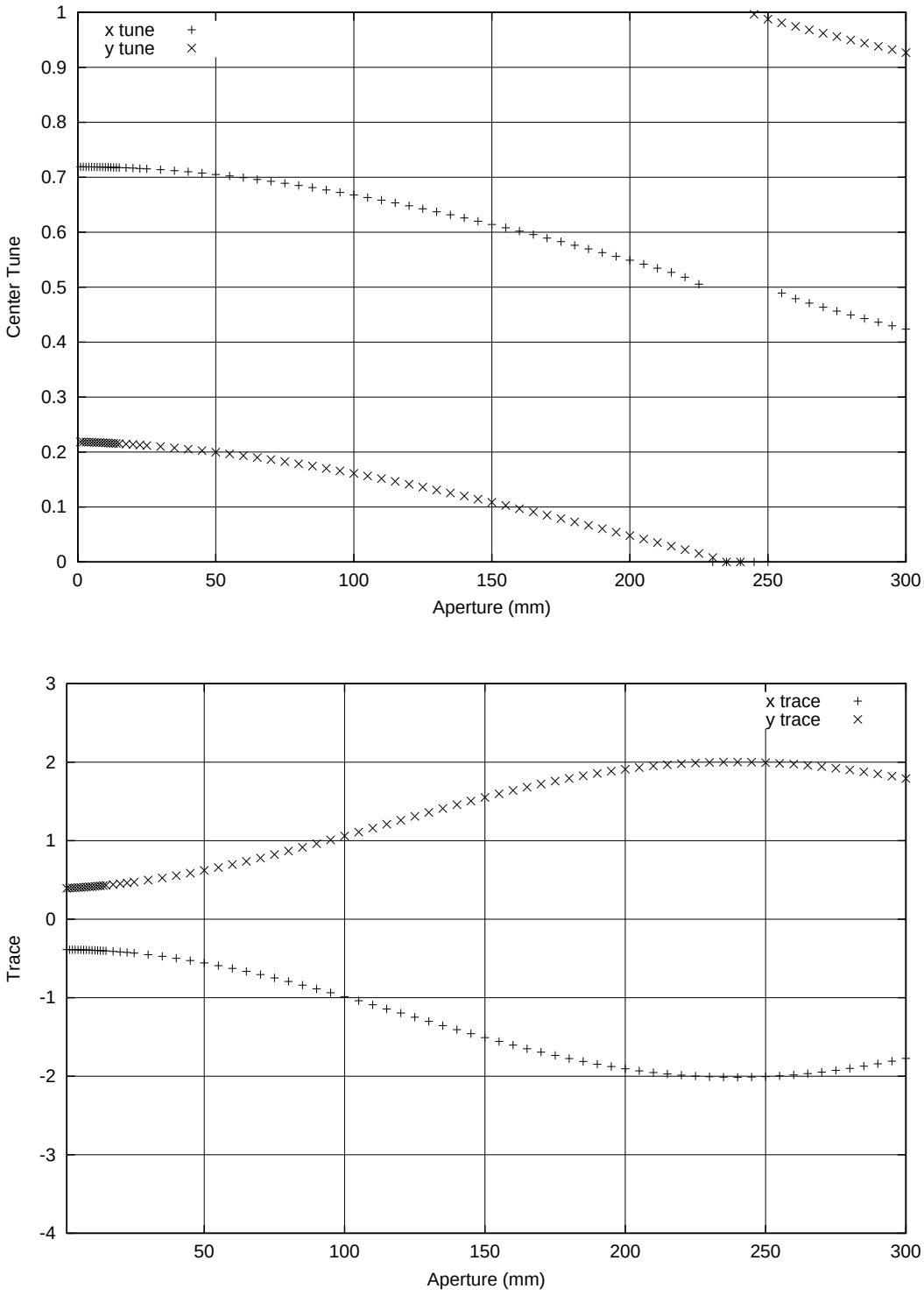

Figure 8.5: Same as Fig. 8.1 (top), and Fig. 8.2 (bottom), but without the matching section, where most of the fringe field effects are concentrated.

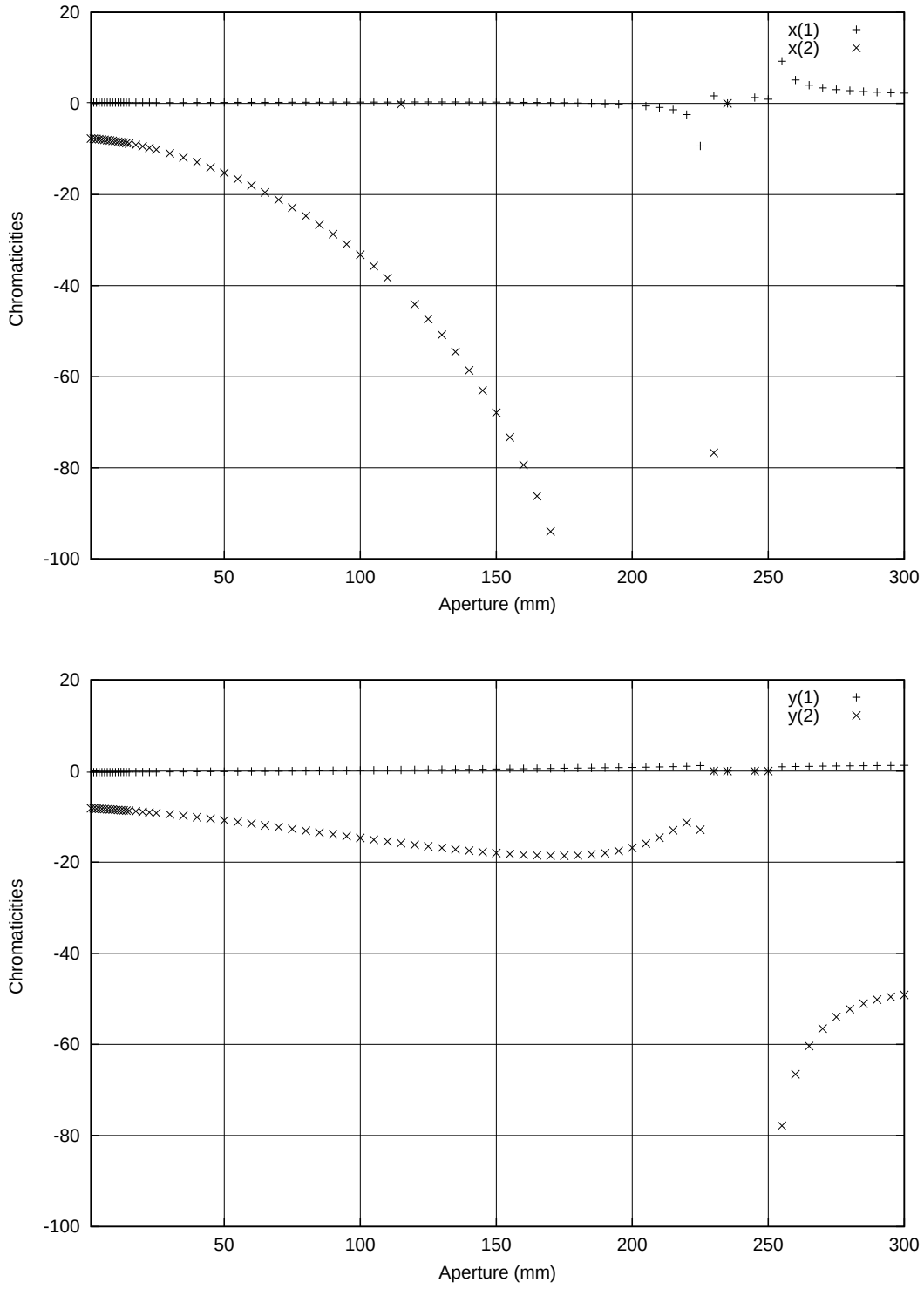

Figure 8.6: Same as Fig. 8.3 (top), and Fig. 8.4 (bottom), but without the matching section, where most of the fringe field effects are concentrated.

type

$$I_2 = \int_{s_b}^{s_e} r^3(s)\, b''_{2,2}(s)\, ds \tag{8.2}$$

appear, where $b''_{2,2}(s)$ is the second order derivative with respect to s of the quadrupole strength, and s_b and s_e are the beginning and end of the fringe field, respectively. The function $r(s)$ is the initially unknown orbit. To evaluate the above integral within the framework of perturbation theory, one can distinguish two cases. In the approximation that the orbit does not change over the fringe region, that is $r(s)$ =constant over $s \in [s_b, s_e]$, the result is $I_2 = r^3(s_b)\left(b'_{2,2}(s_e) - b'_{2,2}(s_b)\right)$. Because at the beginning and end, the fringe fields have assumed their plateaus $b(s) = 0$ and $b(s) = 1$, respectively, we have $b'_{2,2}(s_e) = b'_{2,2}(s_b) = 0$, and hence altogether $I_2 = 0$. This approximation yields the prediction that there are no second order tune shifts, independent of the specific shape of $b_{2,2}(s)$.

On the other hand, we obtain a different, and more precise, answer performing perturbation theory successively over small equidistant subintervals of the interval $[s_b, s_e]$, which in the limit of all subintervals going to zero leads to the correct result in much the same way as numerical integration schemes. Again we assume perturbatively that $r(s)$ is constant over the interval in question, which in the i-th step of the perturbation theory spans $s \in [s_i, s_{i+1}]$. If $\Delta s = s_{i+1} - s_i$ is small enough, this approximation will become better and better. However, unavoidably $r(s)$ will change slightly over different time steps. Consider the specific case of performing N sub-steps

of the perturbation theory. Then an estimate for I_2 is

$$I_2 \approx \sum_{i=1}^{N} r^3(s_i) \int_{s_i}^{s_{i+1}} b''_{2,2}(s)\, ds = \sum_{i=1}^{N} r^3(s_i) \left(b'_{2,2}(s_{i+1}) - b'_{2,2}(s_i) \right) \tag{8.3}$$

$$= -r^3(s_1)\, b'_{2,2}(s_1) - \left[\sum_{i=1}^{N} b'_{2,2}(s_{i+1}) \left(r^3(s_{i+1}) - r^3(s_i) \right) \right] \tag{8.4}$$

$$+ r^3(s_N)\, b'_{2,2}(s_{N+1}) \tag{8.5}$$

$$= -\sum_{i=1}^{N} b'_{2,2}(s_{i+1}) \left(r^3(s_{i+1}) - r^3(s_i) \right) \tag{8.6}$$

where we used as before that $b'_{2,2}(s_1) = b'_{2,2}(s_{N+1}) = 0$. Performing a Taylor expansion of $r(s_{i+1})$ we have

$$r^3(s_{i+1}) - r^3(s_i) = \sum_{j=1}^{\infty} \frac{(\Delta s)^j}{j!} \left(r^3 \right)^{(j)}(s_i) \tag{8.7}$$

and therefore, the estimate becomes

$$I_2 \approx -\sum_{i=1}^{N} b'_{2,2}(s_{i+1}) \sum_{j=1}^{\infty} \frac{(\Delta s)^j}{j!} \left(r^3 \right)^{(j)}(s_i). \tag{8.8}$$

To estimate the behavior of I_2 as a function of aperture D, we first observe that the derivative $b'_{2,2}(s)$ scales with $1/D$, and thus

$$b'_{2,2}(s_{i+1}) \propto \frac{c_{i+1}}{D}, \tag{8.9}$$

where c_{i+1} are suitable constants; similarly, we have

$$\Delta s = s_{i+1} - s_i = \frac{s_e - s_b}{N} \propto \frac{D}{N}. \tag{8.10}$$

Inserting (8.9) and (8.10) in (8.8) we obtain

$$I_2 \approx -\sum_{i=1}^{N} c_{i+1} \sum_{j=1}^{\infty} \frac{D^{j-1}}{j! N^j} \left(r^3 \right)^{(j)}(s_i). \tag{8.11}$$

In the sharp cutoff approximation, $D \to 0$, only the $j = 1$ terms survive the limit. Thus, finally we obtain the qualitative behavior

$$I_2 \approx -\sum_{i=1}^{N} c_{i+1}^{*} \cdot \left(r^3\right)' (s_i) \tag{8.12}$$

where we absorbed various constants into c_{i+1}^{*}. Instead of being zero, the integral now approaches a constant and usually nonzero value as $D \to 0$. Therefore, the convergence to a constant of the second order quadrupole tune shifts in the sharp cutoff limit can be qualitatively understood. We mention that the limits of the extension of the fringe fields or the size of the apertures going to zero are equivalent.

On the other hand, in the case of fourth order tune shifts in the sharp cutoff limit we obtain completely different qualitative behavior. The fourth order tune shifts are functions of fifth order map elements. In this case we need to estimate integrals of the type

$$I_4 = \int_{s_b}^{s_e} r^5 (s)\, b_{2,2}^{(4)} (s)\, ds \tag{8.13}$$

containing fourth order derivatives of $b_{2,2}(s)$. Proceeding the same way as above we obtain that

$$I_4 \approx -\sum_{i=1}^{N} k_{i+1} \sum_{j=1}^{\infty} \frac{D^{j-3}}{j! N^j} \left(r^5\right)^{(j)} (s_i)\,, \tag{8.14}$$

due to the fact that the third order derivatives $b_{2,2}^{(3)}(s_{i+1})$ scale with $1/D^3$. Hence, we obtain that in the sharp cutoff limit the integral diverges as

$$I_4 \approx \frac{a}{D^2} + \frac{b}{D} + c, \tag{8.15}$$

for some constants a, b, c. In a log-log plot the slope of the resulting curve will be between 0 and 2 depending on the exact values of a, b and c. Generalizing this argument to a rectilinear $2l$-pole, we see that the first divergence occurs always at order $2l + 1$.

The perturbative view employed in the above arguments can reveal the qualitative behavior of the situation, yet is less fruitful for the quantitative study of the effects to very high orders of the motion, which would require the treatment of more and more integrals like those appearing above. In the map picture employed in COSY INFINITY, all dynamics can be solved by the ability of the DA approach to obtain the map to any order of interest, and then to obtain the tune shifts of interest to any order using DA-based normal form methods.

For the example of the default COSY falloff, we explicitly obtained the divergence of the second and fourth order amplitude dependent tune shifts. See Figure 8.7 and 8.8. Only one second order tune shift blows up, which shows that the single map element responsible for this effect comes from the dipoles' $(b|yyy)$. This behavior can be seen in the logarithmic scale plots of Figure 8.9, where the slope 1 seems to be the limiting maximum slope. Although the constants $k_i\,(D)$ in general will be different at every time step, we expect that the divergence of some of the fifth order quadrupole map elements will be roughly with the second power of the aperture. As it turns out, this implies also the divergence of the amplitude dependent tune shifts, and the logarithmic plots reveal the blow-up with slope at most 3 (Figure 8.10).

We performed the same studies for the ring with the matching quadrupoles' fringe fields turned off. As expected, qualitatively we obtained the same results. The main difference is that the blow-up of the fourth order tune shifts begin at somewhat smaller apertures.

8.3 Shape Dependent Effects

Rescaling of the length of the fringe field region, for example by changing the aperture, is a first example of shape dependent effect. This has been studied in section 8.1.

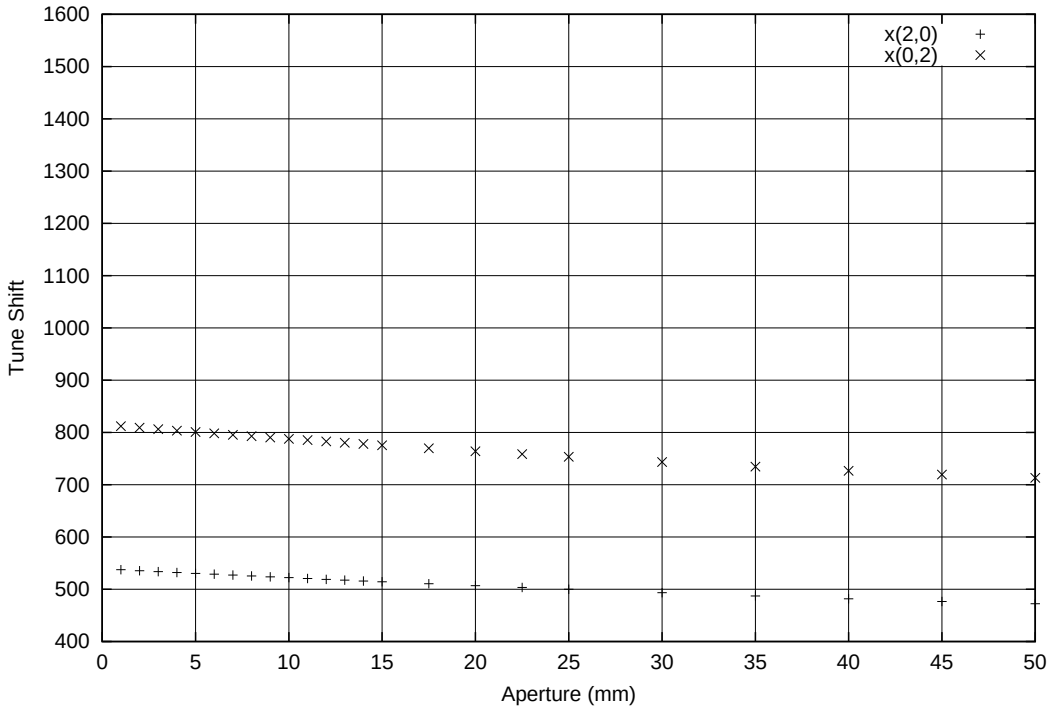

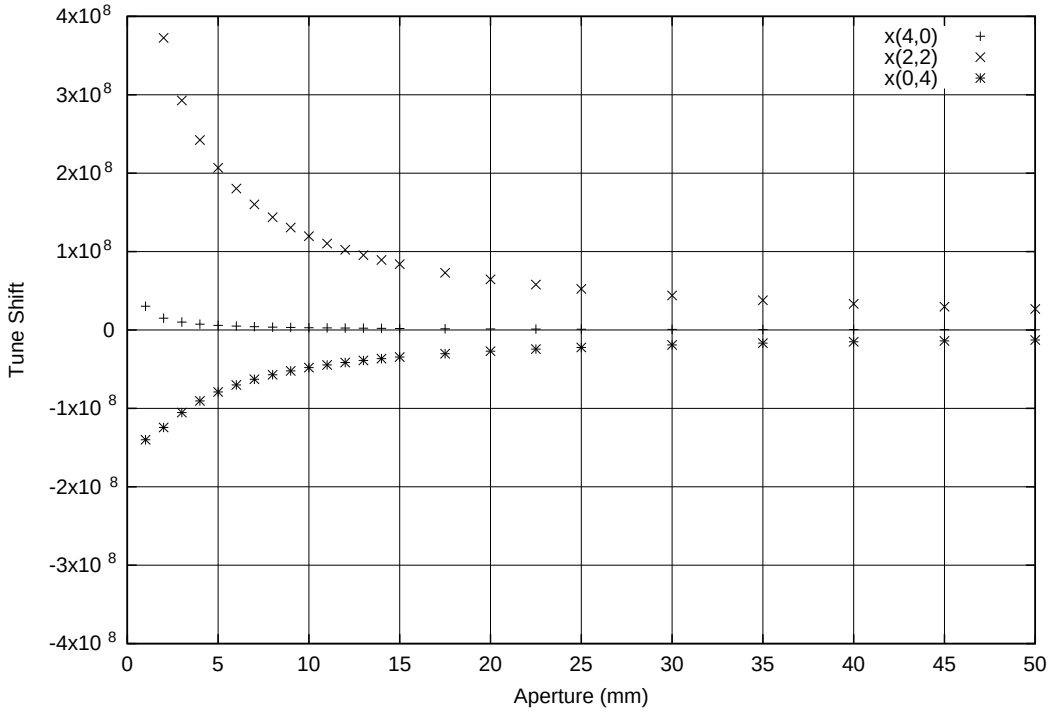

Figure 8.7: Convergence to a constant of the second order (top) and blow-up of the fourth order (bottom) amplitude dependent tune shifts in the x tune. The fringe field shape is given by the default Enge coefficients.

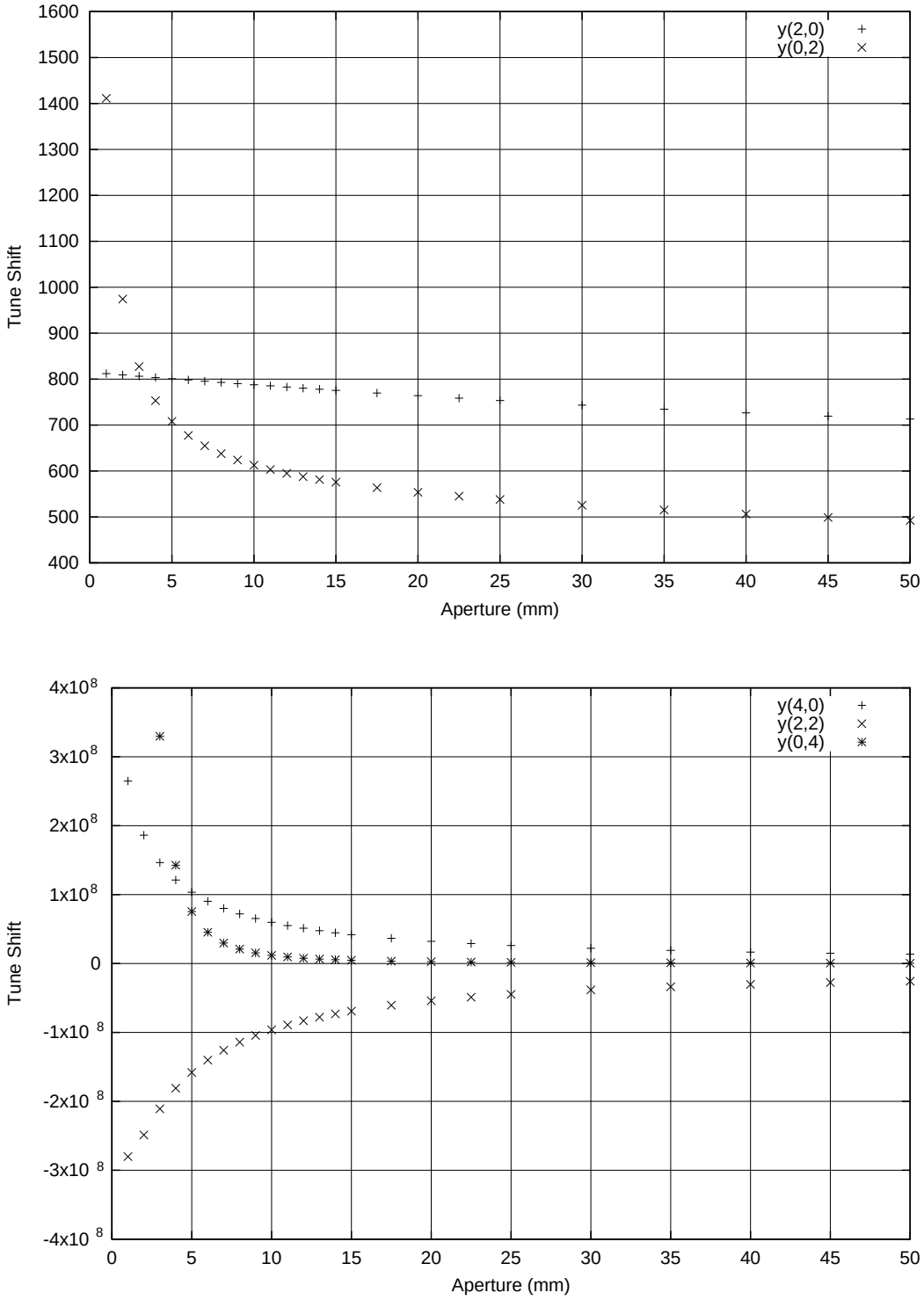

Figure 8.8: Blow-up of the second (top) and fourth (bottom) order amplitude dependent tune shifts in the y tune. The fringe field shape is given by the default Enge coefficients.

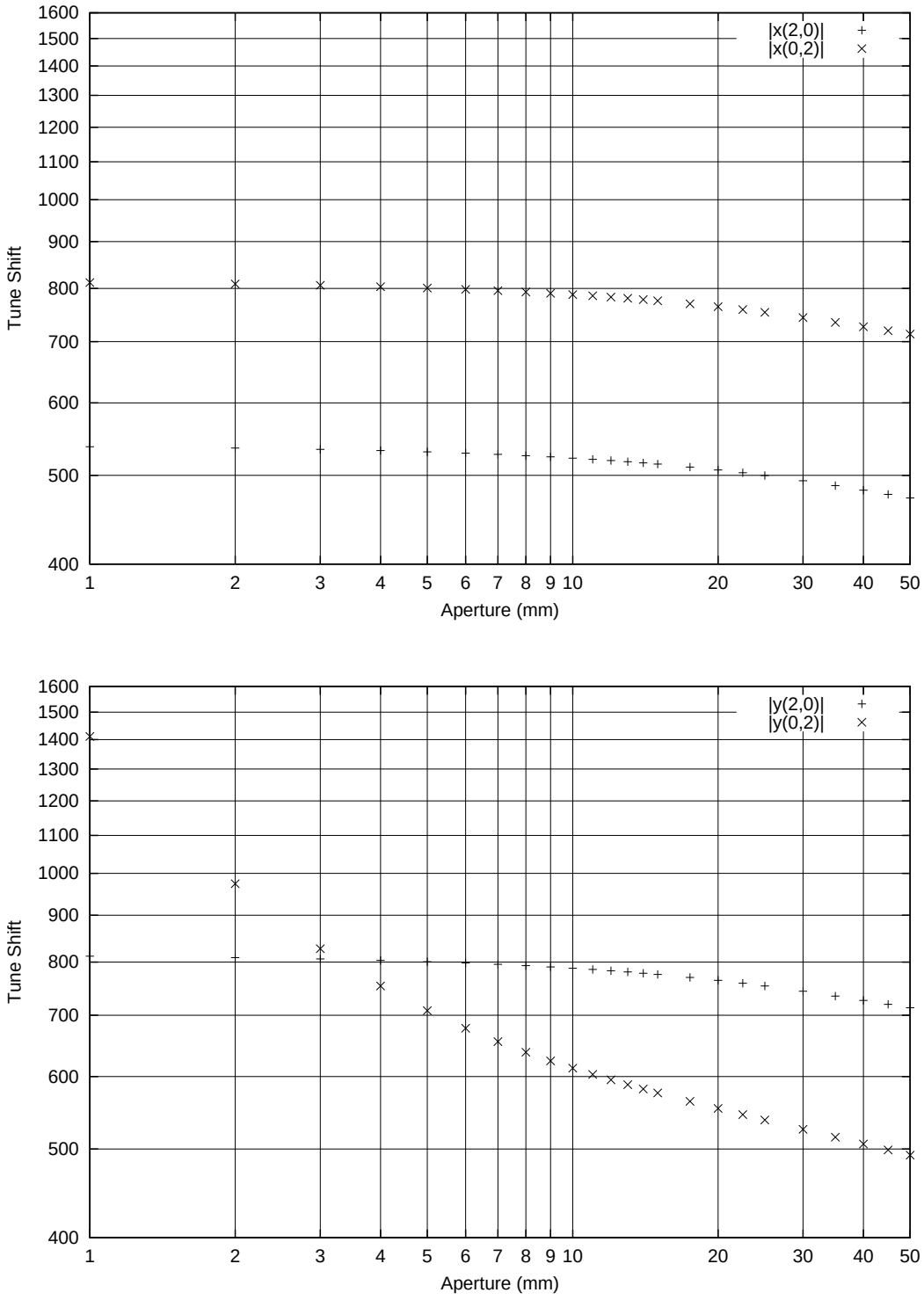

Figure 8.9: Second order amplitude dependent tune shifts as a function of aperture in log-log scale. x tune shifts are on the top, and y tune shifts are on the bottom. The maximum slope is around 1.

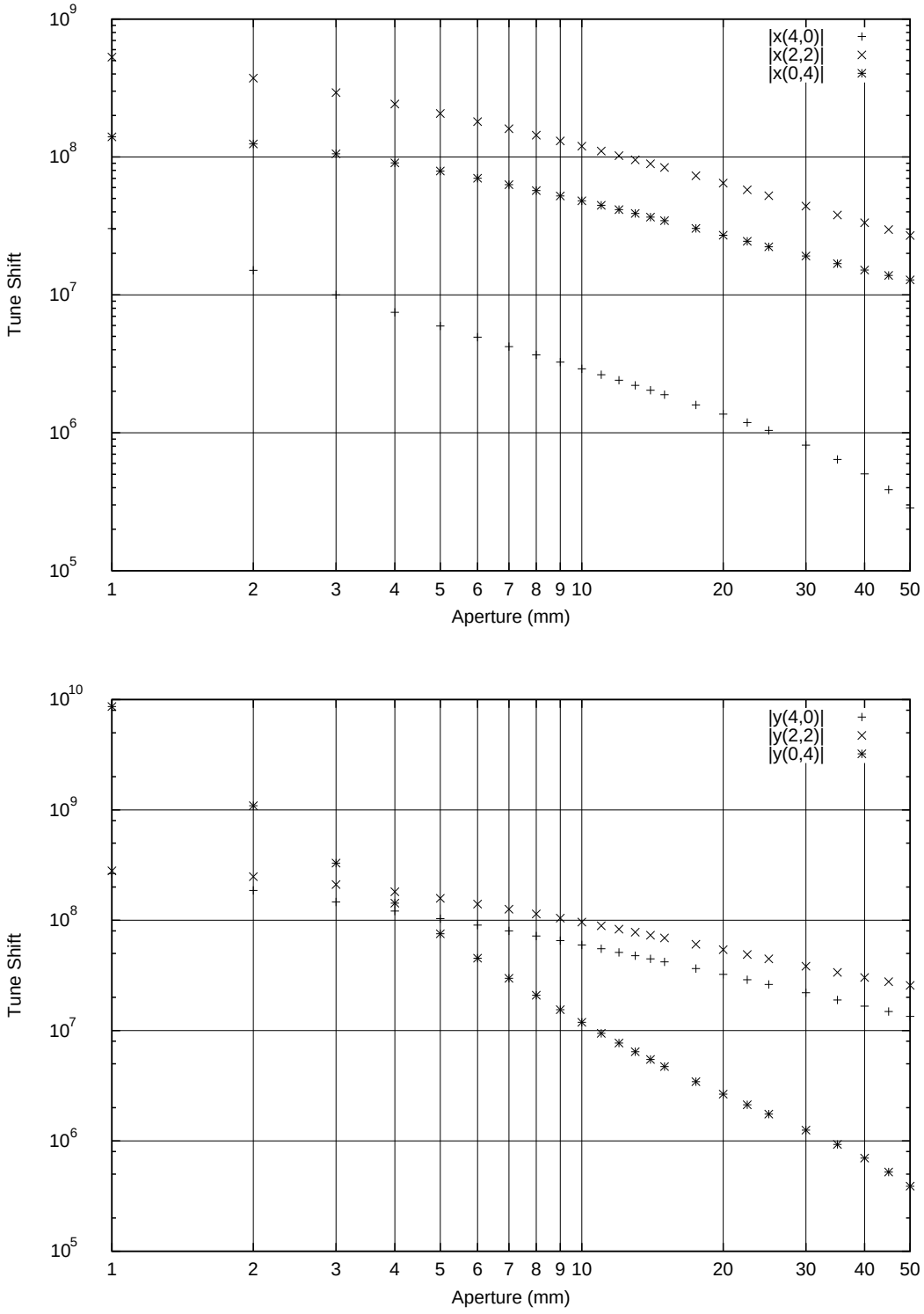

Figure 8.10: Fourth order amplitude dependent tune shifts as a function of aperture in log-log scale. x tune shifts are on the top, and y tune shifts are on the bottom. The maximum slope is around 3.

	Dipole	Quadrupole	Sextupole
a_1	-0.003183	0.00004	-0.000117
a_2	1.911302	4.518219	7.135786

Table 8.2: Enge function with only two parameters, computed by slightly modifying the second default Enge coefficient (a_2), such that the corresponding Enge function has the same integral as the default six parameter one.

In this section we are interested in falloff shape alterations, modulo translation and rescaling. It can be achieved by different sets of Enge coefficients for the same lattice and different falloffs only for the quadrupoles. Also, the same falloff is assumed at both ends.

For example, one may want to choose a benign Enge function. This can be achieved by utilizing only the first two coefficients instead of 6. Furthermore, one may want the same effective field boundary in both cases. Hence, for the Enge coefficients of the default case we obtain the values listed in Table 8.2. In the following we list two other sets, taken from fitting measured or simulated magnetic field data of specific quadrupoles. The Large Hadron Collider's High Gradient Quadrupoles of the interaction regions have been designed by G. Sabbi of Fermilab. Based on the magnet end design described in [92] we obtained the Enge coefficients listed in Table 8.3 [81]. Finally, another set has been obtained by F. Méot [88] for a warm, large aperture (diameter $\sim 30\ cm$) quadrupole that belongs to a QD kaon spectrometer in operation at GSI; the values are $a_1 = 0.1122$, $a_2 = 6.2671$, $a_3 = -1.4982$, $a_4 = 3.5882$, $a_5 = -2.1209$, $a_6 = 1.723$. These fits represent the fields globally as well as along the optical axis.

Altogether, there is a total of 6 cases according to the above sets: quadrupoles with default dipole, default quadrupole and default sextupole, LHC HGQ lead end, two parameter default quadrupole Enge function, and GSI QD spectrometer type fringe fields. For each case we computed the maps at four different apertures: 25, 50,

	Lead end	Return end
a_1	-0.939436	-0.585368
a_2	3.824163	3.603682
a_3	3.882214	2.037629
a_4	1.776737	0.768748
a_5	0.296383	0.216590
a_6	0.013670	0.035435

Table 8.3: Enge coefficients fitted for the LHC HGQ lead and return ends, respectively.

75 and 100 mm. Using the map we obtained the tune shifts and resonance strengths via normal form methods [10], and the dynamic apertures by symplectic tracking with the order 8 map. For the tracking we followed the prescription of the optimal generating function symplectification (EXPO), described in part I.

Table 8.4 represents the results of the computation of some of the amplitude dependent tune shifts in the horizontal plane in all of the 6 cases for an aperture of 25 mm. The same data is given in Tables 8.5, 8.6 and 8.7 for apertures of 50, 75, and 100 mm. Interestingly, there are only moderate changes, with both aperture and shape, of the second order tune shifts, with the exception of a few cases where significant changes can be observed. For example, the LHC HGQ type fringe fields, and to a lesser extent the default dipole type, differ significantly from the other types when the aperture is around 75 mm. Also, the small tune shift with horizontal action of the LHC HGQ type for aperture 25 mm is somewhat surprising. On the other hand, starting with the fourth order, the tune shifts depend significantly on the details of the fringe field shape.

In general, the results on the dynamic aperture and resonance strengths point in the same direction. Here we include only some of the representative cases. We will present the results for the 75 mm aperture for all the 6 fringe field shapes. The tracking pictures show the horizontal phase plane of on-energy particles launched

Aperture = 25 mm					
Type of fringe field	Amplitude dependent tune shifts				
	$(\nu_x \vert J_x)$	$(\nu_x \vert J_y)$	$(\nu_x \vert J_x^2)$	$(\nu_x \vert J_x J_y)$	$\left(\nu_x \vert J_y^2\right)$
Default dipole	479	722	541992	56513171	−26570420
Default quadrupole	500	753	1040229	52370674	−22335176
Default sextupole	513	774	−177824	−536329	−404400
LHC HGQ lead end	138	773	4930507	−200333148	100929561
2 para. Enge func.	499	751	950741	37684628	−15400818
GSI QD	514	776	1455256	63871881	−26392343

Table 8.4: A few amplitude dependent tune shifts for the 25 mm aperture case. All 6 studied fringe field falloff shapes are included.

Aperture = 50 mm					
Type of fringe field	Amplitude dependent tune shifts				
	$(\nu_x \vert J_x)$	$(\nu_x \vert J_y)$	$(\nu_x \vert J_x^2)$	$(\nu_x \vert J_x J_y)$	$\left(\nu_x \vert J_y^2\right)$
Default dipole	480	738	−424782	44639316	−2501083
Default quadrupole	472	713	284406	26926490	−12828937
Default sextupole	492	741	727021	26941101	−10996773
LHC HGQ lead end	411	953	−19501	−65824924	23955356
2 para. Enge func.	469	707	246449	18213525	−8614039
GSI QD	494	746	522581	32686302	−14724215

Table 8.5: A few amplitude dependent tune shifts for the 50 mm aperture case. All 6 studied fringe field falloff shapes are included.

Aperture = 75 mm					
Type of fringe field	Amplitude dependent tune shifts				
	$(\nu_x \vert J_x)$	$(\nu_x \vert J_y)$	$(\nu_x \vert J_x^2)$	$(\nu_x \vert J_x J_y)$	$\left(\nu_x \vert J_y^2\right)$
Default dipole	957	1466	−16023679	456668857	−293452875
Default quadrupole	475	718	−416016	−1258842	−952296
Default sextupole	477	720	−239001	−721214	−544239
LHC HGQ lead end	1261	1773	−54679213	−227089388	−22890174
2 para. Enge func.	459	702	551115	12895677	−6894978
GSI QD	480	762	65222	36938218	4364284

Table 8.6: A few amplitude dependent tune shifts for the 75 mm aperture case. All 6 studied fringe field falloff shapes are included.

Aperture = 100 mm					
Type of fringe field	Amplitude dependent tune shifts				
	$(\nu_x \vert J_x)$	$(\nu_x \vert J_y)$	$(\nu_x \vert J_x^2)$	$(\nu_x \vert J_x J_y)$	$(\nu_x \vert J_y^2)$
Default dipole	unstable				
Default quadrupole	532	834	-1043654	-3274271	-2568105
Default sextupole	463	678	80182	28804518	7992446
LHC HGQ lead end	426	621	-1958026	-21897965	5483897
2 para. Enge func.	483	757	-909438	6770949	-8894670
GSI QD	488	749	-313590	16526843	-10581676

Table 8.7: A few amplitude dependent tune shifts for the 100 mm aperture case. All 6 studied fringe field falloff shapes are included.

along the x axis with vanishing transversal momenta. The resonance strengths have been calculated along the diagonal in action space, at a value that approximately corresponds to the dynamic aperture.

We grouped the dynamic aperture pictures in Fig. 8.11, and the resonance strengths pictures in Fig. 8.12 for the 75 mm aperture case. Notice that there is no really good correlation between the three different quantities computed. The lattice with dipole type fringe field has larger than average amplitude dependent tune shifts and resonance strengths, which results in a smaller dynamic aperture. On the other hand, the LHC HGQ type fringe fields result in even larger tune shifts, but the tracking shows a relatively clean looking phase space with an average dynamic aperture. Furthermore, in spite of the quadrupole type fringe fields having larger resonance strengths than the sextupole type, the dynamic apertures and the second order tune shifts are approximately equal. Even between the maximum value of the resonance strengths of the 6 parameter, respectively the two parameter default quadrupole type Enge function there is a factor 5 difference in the resonance strengths, but they produce similar dynamic apertures. This may serve as an indication that it is wise to study fringe field effects on a case-by-case basis.

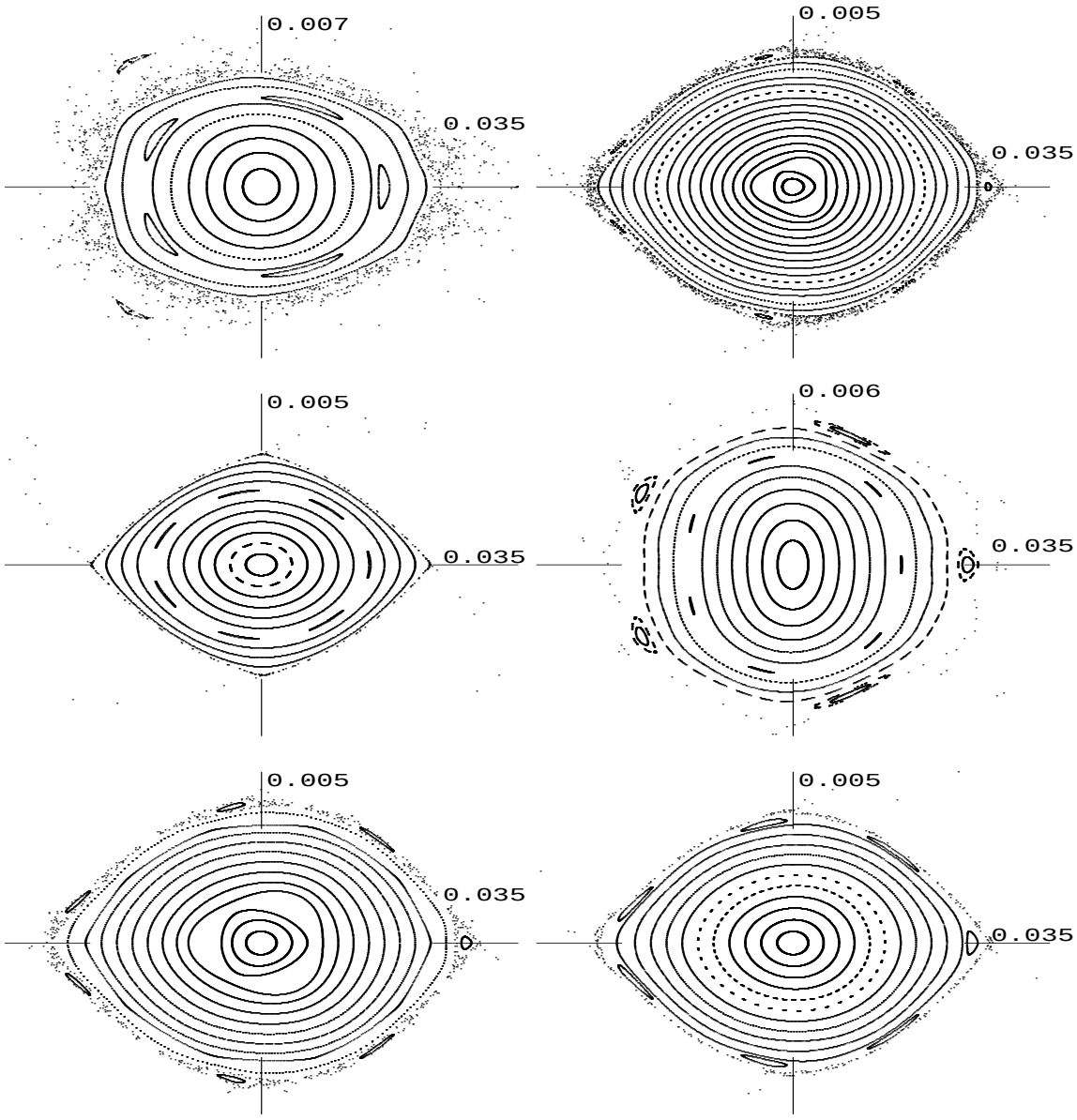

Figure 8.11: Tracking pictures of on-energy particles launched along the x-axis with vanishing transversal momenta, magnet aperture of 75 mm, for all six types of fringe fields. From left to right and from top to bottom the following fringe field types are depicted: default dipole, default quadrupole, default sextupole, LHC HGQ lead end, two parameter Enge function, and GSI QD spectrograph.

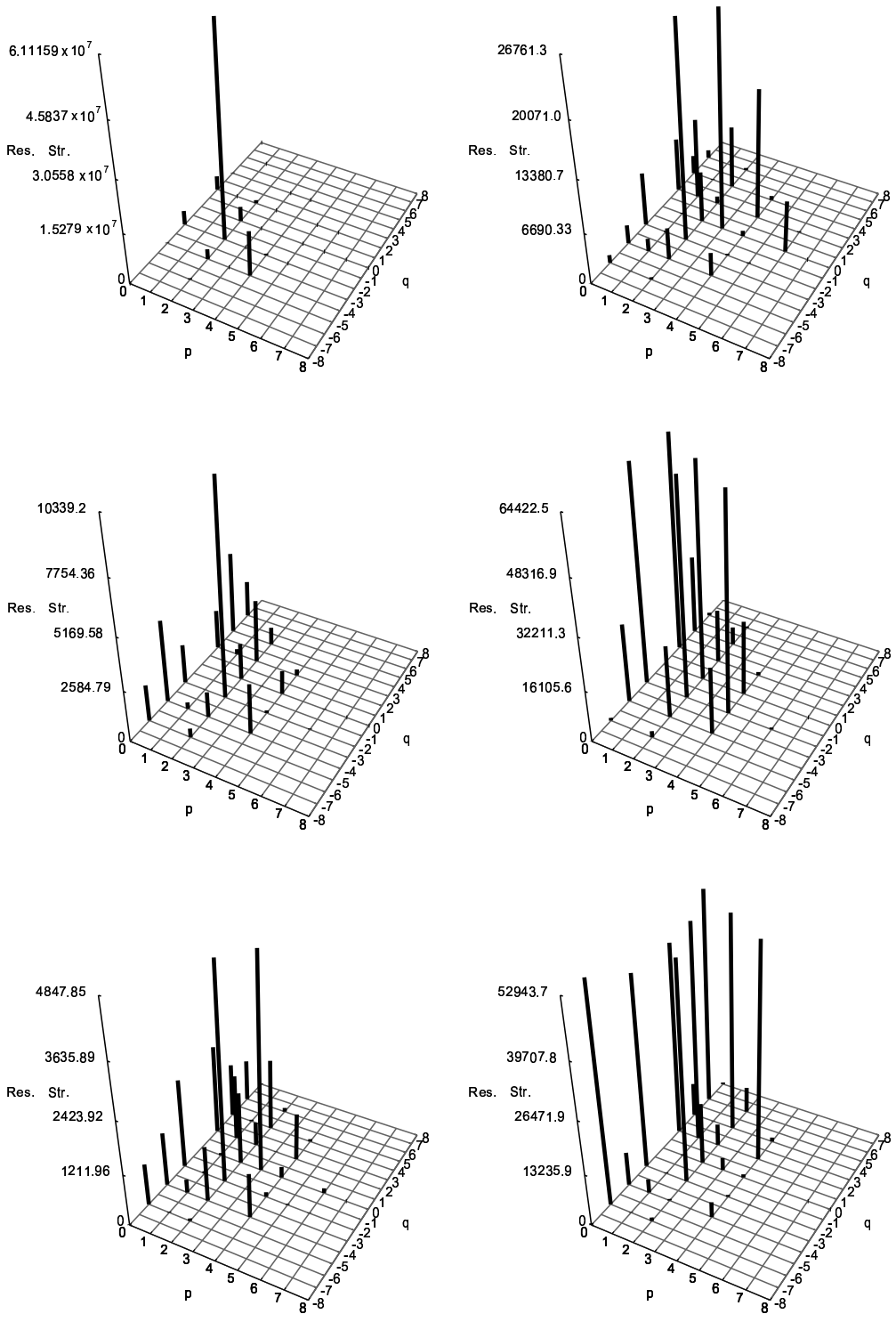

Figure 8.12: Resonance strengths of on-energy particles along the diagonal in action space, at a distance from the origin that corresponds to the approximate dynamic aperture, magnet aperture of 75 mm, for all six types of fringe fields. From left to right and from top to bottom the following fringe field types are depicted: default dipole, default quadrupole, default sextupole, LHC HGQ lead end, two parameter Enge function, and GSI QD spectrograph.

8.4 Nonlinear Effects Due to Pseudo-Multipoles

High order terms in the map arise from intrinsic nonlinearities, as for example in the map of a pure quadrupole, and from nonlinearities related to s-dependent effects, as in the case of fringe fields. For an accurate representation of the system, the maps have to be computed to a sufficiently high order. However, the exact value of the order needed is system dependent.

It follows from (7.12) that in the regions of s-dependent fields the potential is given by a double infinite series. However, at least in the case of an ideal lattice, the normal and skew multipole strengths vanish for sufficiently high l. To compute the order n map of the system, it is necessary to know the potential to order $n+1$, which in particular requires the knowledge of high order derivatives of the falloff, a frequently non-trivial task outside the Differential Algebraic framework [93]. The question arises whether the truncation of the pseudo-potential expansion in (7.13) and (7.14) at various orders less then $n+1$ makes a difference. We studied this question by tracking a lattice of the proposed Neutrino Factory with fringe field effects taken into account. First, it was verified that in this case the order eleven map is sufficient. In Figure 8.13 we present the results of tracking for 1000 turns through lattices in which the potential has been truncated at orders 4, 6, and 8. For lattices with potential truncation higher than order 8 we obtained similar pictures with the order 8 case. These pictures are to be compared with the order eleven symplectic tracking that is shown in Figure 8.14.

It was shown in [11] that fringe fields effects are significant for this lattice. Figures 8.13 and 8.14 show that the pseudo-multipole part of fringe fields are also important, up to reasonably high orders. Therefore, again we arrive to the conclusion that it is important to simulate fringe field effects as accurately as possible.

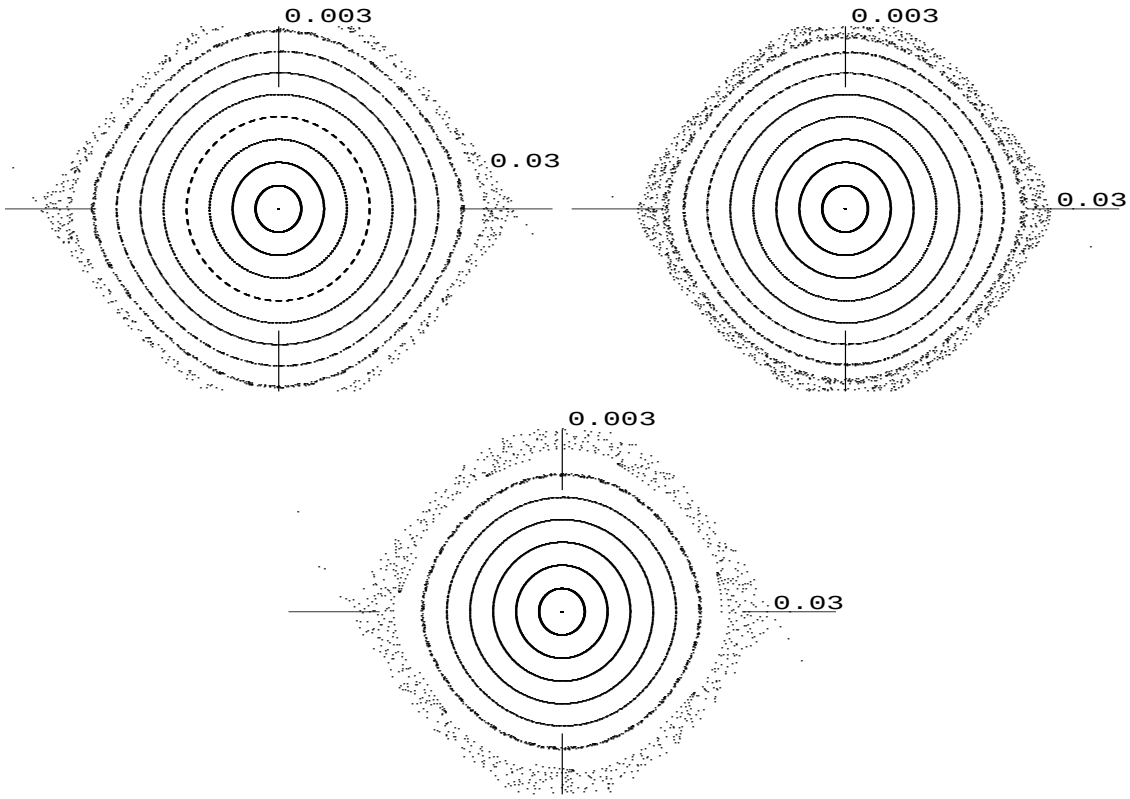

Figure 8.13: Tracking pictures of the Neutrino Factory, with the potential truncated in the pseudo- potential part at orders: 4 for (a), 6 for (b), and 8 for (c).

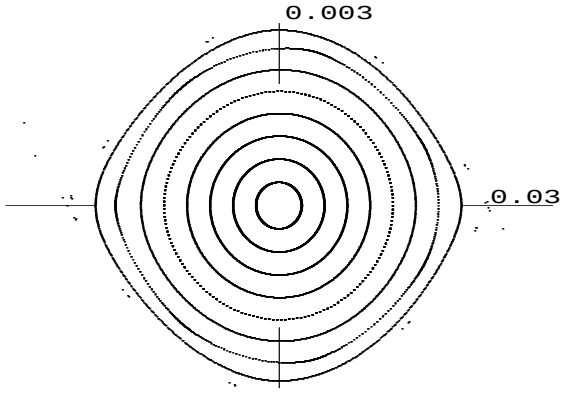

Figure 8.14: Symplectic tracking picture (map and potential expansion at full order) of the Neutrino Factory for the same initial conditions as in Figure 8.13.

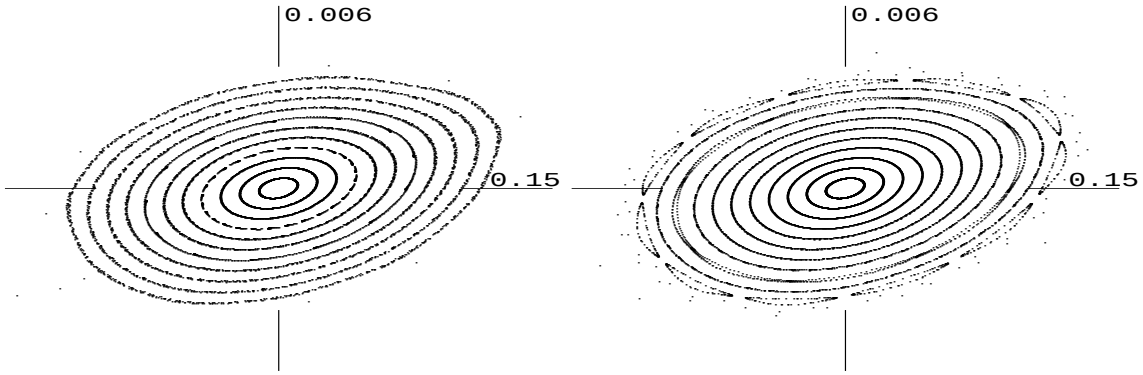

Figure 8.15: Symplectic tracking pictures of the Proton Driver, for -4% momentum offset, (a) with full potential, and (b) with 6th order potential truncation.

8.5 Symplectification

Close to the dynamic aperture, both the Neutrino Factory and the Proton Driver lattices are quite nonlinear. As a consequence, even for short term tracking, symplectification of maps turned out to be appropriate; in the case of the Proton Driver even for Taylor maps up to order 18 and without fringe field effects. Also, it turned out that fringe fields are not as important for the Proton Driver as are for the Neutrino Factory. In cases when fringe field effects were taken into account, we studied the question whether symplectification alone can restore the information neglected by truncating the pseudo-potential part of the expansion at lower orders than the needed map order. For the example of the Proton Driver, differences between the two symplectic tracking pictures are still noticeable. Here we present the case with full potential and momentum offset -4%, and the same system, but potential truncated at order 6 (Figure 8.15). Therefore, even for cases when fringe fields are not very detrimental, the effects of high order pseudo-multipoles are visible, and symplectification cannot undo the errors made in neglecting them.

8.6 Summary

Recognizing that fringe fields might be important for the design of some of the proposed machines and accelerators under construction, we undertook a systematic study of the effects that one could expect. Using the example of the proposed 30 GeV Neutrino Factory, we experimented with 6 different types of fringe fields at many different aperture settings. The main message of this chapter is that fringe fields induce a variety of effects, and it is not always straightforward to anticipate their effects without accurate simulation studies. The results point out that it is important to decide ahead of time on the end field designs for the proposed machines. We used fringe fields modelled by Enge functions for the Neutrino Factory because at this stage the exact shape is not known, as no model exists yet. As we mentioned, there is such a model for the LHC HGQs. Using Differential Algebraic techniques, it is possible to compute the multipole decomposition and accurate fringe field maps, up to arbitrary order, for such a model, as shown in chapter 9. Once the necessary maps are available, the subsequent dynamical studies can proceed with no additional overhead compared to the case when no fringe field effects are taken into account. This includes normal form based quantities like tune shifts, resonance strengths and resonance webs, and tracking (see chapter 10 for a case study of the LHC). It is also worthwhile to note that symplectic tracking with fringe fields is of the same level of effort as without fringe fields, as was shown in part I. In conclusion, a study of fringe field effects appears to be indicated for a detailed analysis of any ring lattice.

In the last two sections we considered the question of the implications of truncation of some pseudo-multipoles, and of the symplectification of the so resulting maps. It is well known that symplectic integration methods have many favorable properties, and in general it is necessary to maintain symplecticity when tracking Hamiltonian

dynamics (see part I). However, as examples show, symplecticity alone cannot make up for fundamental errors made at the level of representation of the system by its individual elements, such as truncating the higher order pseudo-multipoles.

We studied more specifically the lattices of the Neutrino Factory and the Proton Driver. Figures 8.17 and 8.16 show some tracking pictures without and with fringe fields for both lattices, from which it follows that the default fringe fields induce the shrinkage of the DA by a factor of 10 for the Neutrino Factory, and does not have almost any effect on the DA of the Proton Driver.

In summary, we examined the order of the map needed, nonsymplectic versus symplectic tracking, off-energy tracking, full fringe field effects, and the influence of the truncation of the expansion of the potential into pseudo multipoles. Accurate modeling of Muon Accelerators requires the correct treatment of the equations of the motion, in which the potentials are included in accordance to Maxwell's equations. Moreover, a sufficiently high order map is needed, especially for off-energy tracking, and symplectic tracking is essential.

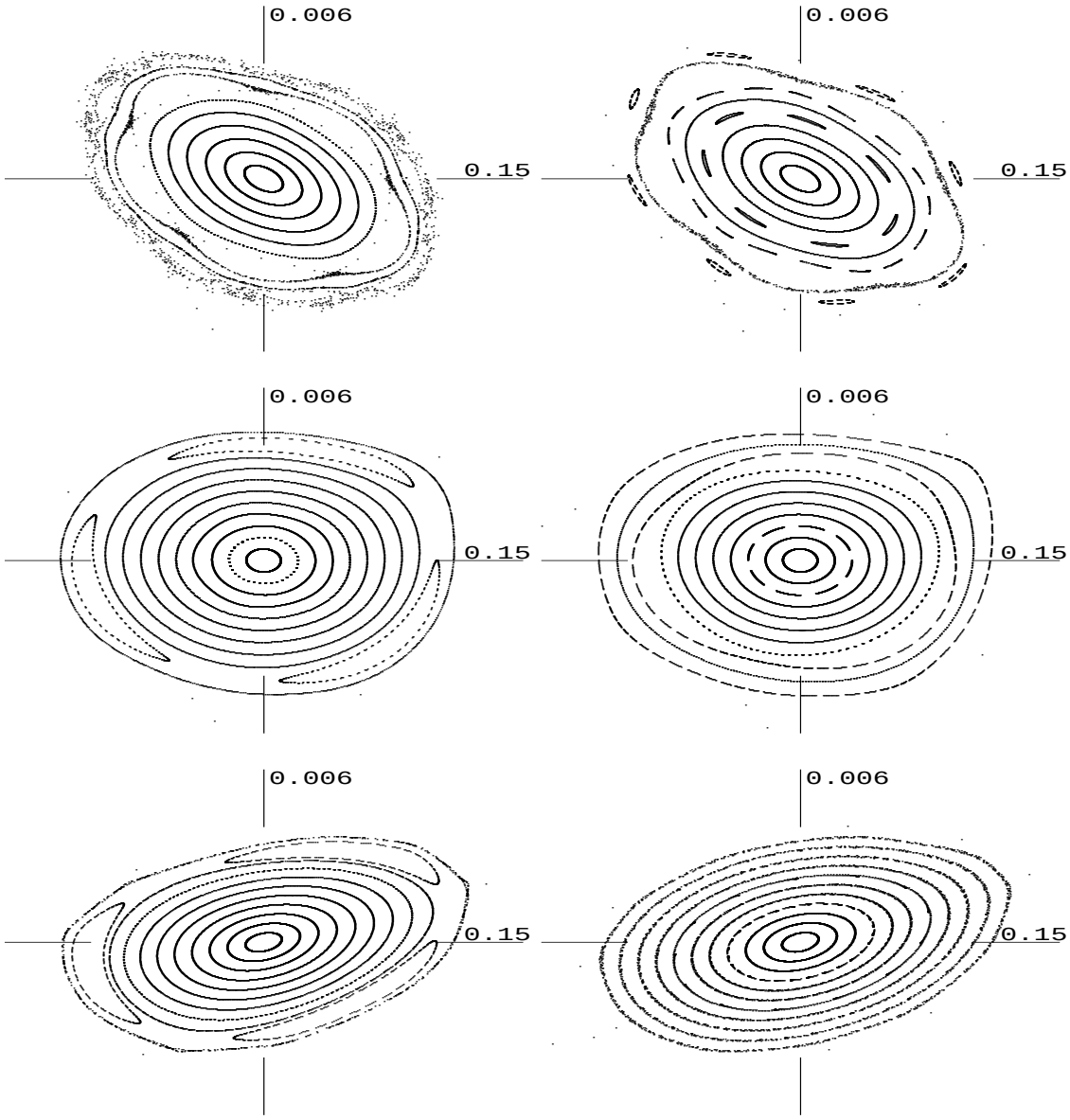

Figure 8.16: Tracking pictures of the Proton Driver without and with default fringe fields, and momentum offsets of 0 and ±4%, respectively.

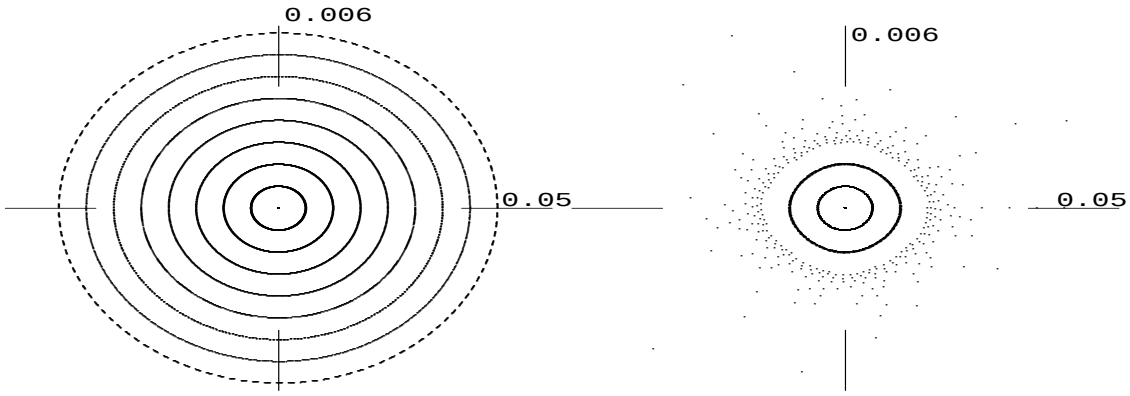

Figure 8.17: Tracking of the Neutrino Factory without and with default fringe fields.

Chapter 9

Multipole Decomposition of Magnets Represented by Wire-Currents

The performance of the modern high energy accelerators, such as the Large Hadron Collider to be built at CERN, depends critically on the field quality of the superconducting magnets employed to guide and focus the circulating beam [94]. The nonlinearities of these magnets drive resonances, rendering the motion of particles at large amplitudes unstable [95]. The shrinkage of the useful region in space, called the dynamic aperture, due to magnet nonlinearities is very detrimental to the stringent high luminosity requirements, so a careful design of these magnets is in order. The design is performed by sophisticated codes like ROXIE [96]. The accurate placement of the superconducting wires, followed by extensive optimization produces an analytical model of the magnet. Using the Biot-Savart law, the resulting magnetic field is computed on the surface of a coaxial cylinder with the optical axis, and subsequently Fourier analyzed numerically to reveal its multipole content. Several iterations are necessary to obtain a magnet model that satisfies the design specifications. However, once the magnet model is ready, the dynamical studies can use only the multipole data output of the magnet design codes, usually organized in tables, which contain

the integrated values of the multipoles [92]. This is satisfactory for the dynamical studies of the so-called straight sections, where the fields are independent of the arclength s, which is used as the independent variable. However, it is not necessarily accurate enough for the end regions, the fringe fields, where the s dependence of the fields could result in unusual local dynamics not revealed by the integrated values. In this chapter, the theory that solves this problem is developed, by computing the magnetic fields, and their multipole content, based on Differential Algebraic methods. This method allows not just the extraction of the multipole strengths, but also their full s-dependence, allowing analytical computation of s-derivatives, which are necessary for "exact" fringe field map computations. The first steps in this direction have been done in [97]. Here we present the theory in its full generality. In section 9.1 we derive an improved, numerically stable version of the Biot-Savart law for straight line current wires in $3D$ and explain the principle of DA based field computation. Section 9.2 develops two methods for multipole extraction. The importance of enforcing Maxwell's equations is presented in section 9.3. In fact, there are two methods to enforce Maxwell's equations: a local (section 9.3.1) and a global (section 9.3.2) approach. Finally, section 9.5 contains examples of multipoles, and section 9.6 applications to map computation.

9.1 Biot-Savart Law and Field Computation

The magnetic field computation is based on the Biot-Savart law. As will be shown in section 9.2, to solve the equations of the motion, and hence to get the map of a magnetic element it is necessary to compute not just the value of the field at a certain point in space, but also its derivatives, i.e. its Taylor expansion. So, why do we want to use Differential Algebraic methods [82, 9] to achieve this? In principle, it is possible to get the derivatives analytically and implement it in some code to evaluate them.

Order	$\frac{\partial^n B_y}{\partial x^n}(0,0,0)$			
n	Comp. t [sec]	Mem. used [$bytes$]	Fortran lines	Eval. t[msec]
0	0.02	890672	4	0.3
1	0.09	912192	20	0.8
2	0.33	1025616	69	2.4
3	0.94	1306056	188	7.0
4	2.50	1931872	457	16.0
5	6.26	3213192	1009	36.0
6	12.95	5709304	2078	72.9
7	27.23	10274512	4059	140.9
8	50.16	18590928	7567	267.0
9	96.73	33132056	13603	480.0

Table 9.1: Results of transforming the analytic derivatives of the Biot-Savart law, computed with Mathematica, to Fortran code.

We did it using Mathematica. The results are presented in Table 9.1. We mention that the calculations have been done in only one variable (x), for one field component (B_y), and one single line current. On every computer we tried, Mathematica ran out of memory at the computation of the order 10 derivative. Therefore, it is clear that for realistic magnet models, consisting of several 10^5 line currents, in at least 2 variables up to high orders this way is practically intractable. As a comparison, Table 9.2 shows how fast is the DA method, and at the same time preserves the accuracy of the computed derivatives. Technically, all we need to get the Taylor expansion of the field components around a specified point in space, is the evaluation in DA of the Biot-Savart law.

While the exact form of the formula is not critical for the evaluation of the magnetic field value at a certain point in the space, as long it is mathematically accurate, it does have a significant influence when it is used to compute also the Taylor expansion of the field around a point. This is exactly what we attempt by evaluating it in DA. Some of the shortcomings of a naive implementation have been pointed out in [97]. Another numerical instability has been noticed by us when we utilized it at a

Order	$\frac{\partial^n B_y}{\partial x^n}(0,0,0)$
n	Evaluation time in μsec up to order n
1	4.8
5	6.8
10	10.7
15	20.5
20	47.8
25	93.7

Table 9.2: Computation time of the Taylor expansion of the y-component of the magnetic field in DA at various orders.

point where some of the wire currents were exactly or almost colinear with the point of expansion. Therefore, we made several modifications to the standard form of the Biot-Savart law, and found a numerically stable version which has a good behavior in any situation.

As a consequence of Ampère's law, the elementary magnetic flux density at a point $\vec{r}$ generated by a filamentary current wire $d\vec{l}$ situated at $\vec{r}'$ is given by the Biot-Savart formula

$$d\vec{B} = \frac{\mu_0 I}{4\pi} \frac{d\vec{l} \times (\vec{r} - \vec{r}')}{|\vec{r} - \vec{r}'|^3}. \tag{9.1}$$

To compute the magnetic field generated by an extended straight line current we parametrize the line by $\lambda \in [0,1]$ and define $\vec{r}'(\lambda) = \vec{r}_s + \lambda\vec{l}$ and $\vec{r}_e = \vec{r}_s + \vec{l}$, where $\vec{r}_s$, $\vec{r}_e$ represent the starting and endpoint respectively of the line current to the point $\vec{r}$.

Integrating over the line

$$\vec{B} = kI \int \frac{d\vec{l} \times \vec{r}'}{|\vec{r}'|^3} = kI \int_0^1 \frac{\vec{l} \times \left(\vec{r}_s + \lambda\vec{l}\right)}{\left|\vec{r}_s + \lambda\vec{l}\right|^3} d\lambda = kI \left(\vec{l} \times \vec{r}_s\right) \int_0^1 \frac{d\lambda}{\left|\vec{r}_s + \lambda\vec{l}\right|^3}, \tag{9.2}$$

with $k = -\mu_0/(4\pi)$. Introducing the shorthand notations $a = |\vec{r}_s|^2$, $b = 2\vec{r}_s \cdot \vec{l}$,

$c = \left|\vec{l}\right|^2$, the integral gives the result

$$\int_0^1 \frac{d\lambda}{\left(a + b\lambda + c\lambda^2\right)^{3/2}} = \frac{1}{b^2 - 4ac}\left(\frac{2b}{\sqrt{a}} - \frac{2b}{\sqrt{a+b+c}} - \frac{4c}{\sqrt{a+b+c}}\right). \tag{9.3}$$

While mathematically accurate, this formula exhibits several severe numerical pitfalls that restrict its direct practical use, in particular when high-order derivatives are to be computed. Indeed, first the formula apparently exhibits a problem of cancellation of closeby numbers if $b + c \ll a$. Introduction of the quantity $\varepsilon = (b + c)/a$ yields

$$\vec{B} = \frac{kI\left(\vec{l} \times \vec{r}_s\right)}{\sqrt{a}\left(b^2 - 4ac\right)}\left[2b\left(1 - \frac{1}{\sqrt{1+\varepsilon}}\right) - \frac{4c}{\sqrt{1+\varepsilon}}\right]. \tag{9.4}$$

The first problem can be substantially alleviated now by observing that

$$1 - \frac{1}{\sqrt{1+\varepsilon}} = \frac{\varepsilon}{1 + \varepsilon + \sqrt{1+\varepsilon}}, \tag{9.5}$$

which yields the formula

$$\vec{B} = \frac{kI\left(\vec{l} \times \vec{r}_s\right)}{\sqrt{a}\left(b^2 - 4ac\right)}\left[\frac{2b\varepsilon}{1 + \varepsilon + \sqrt{1+\varepsilon}} - \frac{4c}{\sqrt{1+\varepsilon}}\right]. \tag{9.6}$$

However, there is a second numerical difficulty if the line current and the observation point are lying exactly or almost on the same line, because in this case b^2 and $4ac$ assume similar values, which makes the evaluation of $b^2 - 4ac$ prone to numerical inaccuracies. To avoid this effect we rewrite the formula in terms of the angle θ between $\vec{l}$ and $\vec{r}_s$. The relations among the angle and the products of vectors are

$$|\sin\theta| = \frac{\left|\vec{l} \times \vec{r}_s\right|}{\left|\vec{l}\right| \cdot |\vec{r}_s|}, \tag{9.7}$$

$$\cos\theta = \frac{\vec{l} \cdot \vec{r}_s}{\left|\vec{l}\right| \cdot |\vec{r}_s|}. \tag{9.8}$$

This implies the relationships

$$b^2 - 4ac = -4\left|\vec{r}_s\right|^2 \left|\vec{l}\right|^2 \sin^2\theta, \tag{9.9}$$

$$\frac{2b\varepsilon}{1+\varepsilon+\sqrt{1+\varepsilon}} - \frac{4c}{\sqrt{1+\varepsilon}} = \frac{4\left|\vec{r}_s\right|\left|\vec{l}\right|\cos\theta\left(2\left|\vec{r}_s\right|\left|\vec{l}\right|\cos\theta + \left|\vec{l}\right|^2\right)}{\left|\vec{r}_e\right|\left(\left|\vec{r}_e\right| + \left|\vec{r}_s\right|\right)} - \frac{4\left|\vec{l}\right|^2\left|\vec{r}_s\right|}{\left|\vec{r}_e\right|}.$$

Finally, we obtain the magnetic field expressed in terms of $\vec{r}_s$ and $\vec{l}$ as

$$\vec{B} = -\frac{kI\left(\vec{l}\times\vec{r}_s\right)}{\left|\vec{r}_s\right|^2\left|\vec{r}_s+\vec{l}\right|\left(\left|\vec{r}_s+\vec{l}\right| + \left|\vec{r}_s\right|\right)}\left[-\left|\vec{r}_s\right| + \frac{\left|\vec{r}_s\right|\cos^2\theta + \left|\vec{l}\right|\cos\theta - \left|\vec{r}_s+\vec{l}\right|}{\sin^2\theta}\right] \tag{9.10}$$

Denoting $\left|\vec{r}_s\right|\cos^2\theta + \left|\vec{l}\right|\cos\theta = \alpha$ and $\left|\vec{r}_s+\vec{l}\right| = \beta$, we manage to eliminate the $\sin^2\theta$ term in the denominator with the help of the identity $\alpha - \beta = \left(\alpha^2-\beta^2\right)/\left(\alpha+\beta\right)$. Direct calculation shows that $\alpha^2 - \beta^2 = -\sin^2\theta\left(\left|\vec{r}_s\right|^2\cos^2\theta + \left|\vec{r}_s+\vec{l}\right|^2\right)$. Altogether we obtain the final result

$$\vec{B} = \frac{kI\left(\vec{l}\times\vec{r}_s\right)}{\left|\vec{r}_s\right|^2\left|\vec{r}_s+\vec{l}\right|\left(\left|\vec{r}_s+\vec{l}\right| + \left|\vec{r}_s\right|\right)}\left[\left|\vec{r}_s\right| + \frac{\left|\vec{r}_s\right|^2\cos^2\theta + \left|\vec{r}_s+\vec{l}\right|^2}{\left|\vec{r}_s\right|\cos^2\theta + \left|\vec{l}\right|\cos\theta + \left|\vec{r}_s+\vec{l}\right|}\right]. \tag{9.11}$$

The only case where this is numerically unstable is when $\left|\vec{r}_s\right|\cos^2\theta + \left|\vec{l}\right|\cos\theta + \left|\vec{r}_s+\vec{l}\right|$ approaches zero, that is $\theta \to \pi$ and $\left|\vec{r}_s\right| \leq \left|\vec{l}\right|$; but this corresponds to a point in the close proximity of the wire.

The necessary ingredients for the DA field calculation are the above formula and the analytic model of the magnet, consisting of line wire currents. To this end, the entire field in space is calculated by summing up the fields created by wire currents. At each step, the evaluation of (9.11) in DA yields not only the value of the magnetic field at the respective point, but also its derivatives, that is the Taylor expansion with

$B_x\,(x,s,y)$			$B_y\,(x,s,y)$		
Coefficient	Order	Exp. (x,s,y)	Coefficient	Order	Exp. (x,s,y)
0.93844739E-11	0	0 0 0	-.83395100E-11	0	0 0 0
0.10229458E-09	1	1 0 0	17.49010593690	1	1 0 0
0.14301198E-09	1	0 1 0	-.13045929E-09	1	0 1 0
17.49010593689	1	0 0 1	0.95844482E-10	1	0 0 1
-.60674194E-09	2	2 0 0	0.55438195E-09	2	2 0 0
0.36025250E-08	2	1 1 0	-3.80475173597	2	1 1 0
0.12053635E-08	2	0 2 0	-.11068638E-08	2	0 2 0
-.20145723E-08	2	1 0 1	0.19416855E-08	2	1 0 1
-3.80475173613	2	0 1 1	0.34442337E-08	2	0 1 1
-.59862145E-09	2	0 0 2	0.55248205E-09	2	0 0 2
-.22827223E-07	3	3 0 0	-1.66625730542	3	3 0 0
-.92745885E-09	3	2 1 0	0.12449044E-09	3	2 1 0
0.71839210E-07	3	1 2 0	9.99754389589	3	1 2 0
0.55577595E-09	3	0 3 0	-.21654983E-10	3	0 3 0
-4.99877197923	3	2 0 1	-.30524801E-08	3	2 0 1
-.11331539E-06	3	1 1 1	0.11068027E-06	3	1 1 1
9.99754389364	3	0 2 1	0.69547317E-07	3	0 2 1
-.33575741E-08	3	1 0 2	-4.99877197953	3	1 0 2
-.739876993E-09	3	0 1 2	-.59531324E-10	3	0 1 2
-1.66625730477	3	0 0 3	-.22164947E-07	3	0 0 3

Table 9.3: Taylor expansion of the magnetic field components B_x and B_y. The columns represent the expansion coefficients, the order in the expansion and the exponents of (x,s,y), respectively.

respect to coordinates. The result for the return end of the Large Hadron Collider's High Gradient Quadrupole, up to order 3, is presented in Table 9.3. The correctness of our results have been checked against data obtained from Fermilab. The Fermilab data contains the values of the components of the field on the surface of a coaxial cylinder with the optical axis, and have been supplied by G. Sabbi.

To show that the Biot-Savart law implementation based on (9.11) is much more stable then, for example, based on (9.6), we use as indicator the s component of the curl of the field. From Table 9.4 it is clear that the naive implementation goes wrong as low as second order in the curl. Due to lack of space, we presented the result only

$\left(\nabla \times \vec{B}\right)_s$ from (9.11)			$\left(\nabla \times \vec{B}\right)_s$ from (9.6)		
Coefficient	Order	Exp. (x, s, y)	Coefficient	Order	Exp. (x, s, y)
0.64481753E-11	0	0 0 0	0.64517280E-11	0	0 0 0
0.31233362E-08	1	1 0 0	0.31233356E-08	1	1 0 0
0.15774093E-09	1	0 1 0	0.15770096E-09	1	0 1 0
0.31389284E-08	1	0 0 1	0.31389279E-08	1	0 0 1
0.62971751E-07	2	2 0 0	0.336831253164	2	2 0 0
0.11356437E-06	2	1 1 0	0.11356393E-06	2	1 1 0
0.22546586E-08	2	0 2 0	0.22374493E-08	2	0 2 0
0.61018801E-09	2	1 0 1	0.61014426E-09	2	1 0 1
0.11216003E-06	2	0 1 1	0.11215921E-06	2	0 1 1
-.65226274E-07	2	0 0 2	-.336831255411	2	0 0 2
-.10351639E-06	3	3 0 0	0.84829867E-06	3	3 0 0
0.36038492E-05	3	2 1 0	-1010523.36223	3	2 1 0
0.23104571E-05	3	1 2 0	0.44302147E-06	3	1 2 0
0.23642363E-07	3	0 3 0	-.31176547E-04	3	0 3 0
-.19778205E-05	3	2 0 1	-.38402254E-05	3	2 0 1
0.94348351E-08	3	1 1 1	0.94491708E-08	3	1 1 1
0.22561792E-05	3	0 2 1	0.62955066E-05	3	0 2 1
-.199990078E-05	3	1 0 2	-.20901225E-05	3	1 0 2
-.367474004E-05	3	0 1 2	1010523.36227	3	0 1 2
-.927884933E-07	3	0 0 3	0.50706360E-05	3	0 0 3

Table 9.4: Comparison of the s component of the curl, up to order 3, computed by two different implementations of the Biot-Savart law ((9.11) and (9.6), respectively).

up to order 3, but our results show that the behavior of (9.11) is good up to very high orders. Also, we mention that probably this is the most straightforward and accurate way to compute the curl and hence verify whether Maxwell's equations are satisfied.

9.2 Multipole Extraction Algorithms

9.2.1 The Direct Method

Using the field computation of the preceding section, it is possible to extract the multipole content of magnetic fields directly, in a very elegant way that is arbitrary in order.

Obviously, if we evaluate the above equations in the midplane ($y = \phi = 0$), then

$$B_r(r, \phi = 0, s) \mid_{r \mapsto x} = B_x(x, y = 0, s), \tag{9.12}$$

$$B_\phi(r, \phi = 0, s) \mid_{r \mapsto x} = B_y(x, y = 0, s). \tag{9.13}$$

Therefore, all the information we need to extract the multipoles up to the order of calculation are the Cartesian components of the fields in the midplane

$$B_x(x, y = 0, s) = \tilde{g}_0(x, s) + \sum_{l=1}^{\infty} \tilde{g}_l(x, s) \cdot x^{l-1}, \tag{9.14}$$

$$B_y(x, y = 0, s) = \sum_{l=1}^{\infty} l f_l(x, s) \cdot x^{l-1}. \tag{9.15}$$

This is possible due to the previously mentioned fact that any multipole strength of order l is multiplied by x^{l-1}. Starting at $l = 1$, $a_{1,1}(s)$ is extracted as the x-independent part of B_x, and analogously $b_{1,1}(s)$ from B_y. Evaluating $a_{1,1}(s)$ and $b_{1,1}(s)$ at $s = 0$ yields the skew and normal dipole components, respectively. From $a_{1,1}(s)$ and $b_{1,1}(s)$ the functions $f_1(x, s)$, $\tilde{g}_1(x, s)$ are generated up to the order of calculation and subtracted from $B_x(x, y = 0, s)$, and $B_y(x, y = 0, s)$, respectively. This cancels the pseudo-multipoles generated by the s-dependence of $a_{1,1}(s)$ and $b_{1,1}(s)$ (see (7.10)), which otherwise would make the distinction between sextupole terms and pseudo-dipole terms impossible. The procedure can be iterated for the higher order multipoles, up to the order of calculation. After the k-th step, the remainder of the field components should contain just $(k + 1)$-th and higher order multipoles.

However, there is an additional problem in the case of solenoidal fields (the case $l = 0$). In this case, we have an $a_{0,0}(s)$ in the potential, but its contribution vanishes from the field components B_x and B_y, so the function $\tilde{g}_0(x, s)$ cannot be generated from the information available in B_x and B_y. Fortunately, it can be generated from

the B_s component, which evaluated at $x = y = 0$ yields $a'_{0,0}(s)$. From this function we can calculate $a_{0,0}(s)$ up to a constant and generate the $l = 0$ contribution to B_x, $\tilde{g}_0(x, s)$. Once this is subtracted from B_x, the method works as previously described, starting with $l = 1$.

Finally, two notes: the method relies on the fact that the magnetic field can be generated by a magnetic scalar potential that satisfies the Laplace equation. Therefore, it is really important that the curl of the field vanishes. If the fields are calculated from line currents by the Biot-Savart law, that means that the model should consist only of closed circuits to ensure vanishing curl. Maxwellification of the field ensures a better numerical stability of the algorithm. Secondly, only in the regions where the magnetic field is not s-dependent the functions f_l and g_l are equal to the true multipoles, and $l f_l = \tilde{f}_l$, $l g_l = \tilde{g}_l$, an assumption that is sometimes made even for the s-dependent region too.

9.2.2 Multipole Extraction by Analytical Fourier Transform

There is an alternate way to extract the multipoles. The field computation being performed in COSY in Cartesian coordinates (x, y, s), it is possible to perform an analytical pseudo-Fourier transform, i.e. a series of coordinate transformation in DA, keeping throughout the r and s dependences. This is done by our S-Dependent Differential Algebraic Analytical Fourier Transform briefly presented below.

Initially, the field components are in the form of (9.33). The first transformation is $(x, y, s) \mapsto (r, \cos\phi, \sin\phi, s)$ by $x = r\cos\phi$ and $y = r\sin\phi$. At the same time, using (9.35), we switch to cylindrical coordinates, obtaining the field components in the form of (9.39). Note that we are going from a 3 variable representation to a 4 variable one, hence some of the information in the new representation will turn out to be redundant for our purpose. The next transformation is $(r, \cos\phi, \sin\phi, s) \mapsto (r, e^{i\phi}, e^{-i\phi}, s)$, that

is a complex exponential representation, using $\cos\phi = \left(e^{i\phi} + e^{-i\phi}\right)/2$ and $\sin\phi = \left(e^{i\phi} - e^{-i\phi}\right)/(2i)$.

We show in section 9.4 that it does not matter which field component is used for Fourier transformation, so assume that we are working with B_r. Then, we have it at this stage in the form $B_r(r, e^{i\phi}, e^{-i\phi}, s)$.

Now, in principle, it is possible to recombine various products of powers of $e^{i\phi}$ and $e^{-i\phi}$ to trigonometric functions involving multiple angles. However, the key point is to notice that we can obtain the true multipoles by setting $e^{i\phi} = 0$. This is true due to the fact that all the terms of the form $e^{iq\phi}e^{-ip\phi}$, with $q, p \neq 0$, are responsible for the pseudo-multipoles. This becomes clear if one takes a closer look at (9.43). By setting $e^{i\phi}$ to zero, we get rid of all the pseudo-multipole terms and we are going back to a 3 variable representation

$$B_r(r, e^{-i\phi}, s) = \sum_{l=1}^{n+1} z_l(s) e^{-il\phi} r^{l-1}, \tag{9.16}$$

where $z_l(s)$ are complex functions of s. By comparison with (9.57) it is obvious that one term of (9.16) can come only from $\left[A_l(s)\cos l\phi + B_l(s)\sin l\phi\right] r^{l-1}$, which also can be expressed as

$$\left[e^{-il\phi}\left(\frac{B_l(s)}{2} + i\frac{A_l(s)}{2}\right) + e^{il\phi}\left(\frac{B_l(s)}{2} - i\frac{A_l(s)}{2}\right)\right] r^{l-1}. \tag{9.17}$$

After setting $e^{il\phi}$ to zero and comparison with (9.16) we obtain the result $B_l(s) = 2\,\mathrm{Re}\left(z_l(s)\right)$ and $A_l(s) = 2\,\mathrm{Im}\left(z_l(s)\right)$. As a final step, we take the true multipoles as given by

$$b_{l,l}(s) = \frac{2}{l}\,\mathrm{Re}\left(z_l(s)\right), \tag{9.18}$$

$$a_{l,l}(s) = \frac{2}{l}\,\mathrm{Im}\left(z_l(s)\right). \tag{9.19}$$

9.3 Enforcing Maxwell's Equations

9.3.1 Local Maxwellification

Given a magnet model consisting of line currents, it is possible to compute the magnetic field generated by the Biot-Savart law in the DA framework as a local Taylor expansion with respect to the Cartesian coordinates (x, y, s), as has been demonstrated in section 9.1. The magnetic field should be divergence and curl-free in the regions of interest, as implied by Maxwell's equations in a source-free region: $\nabla \cdot \vec{B} = 0$ and $\nabla \times \vec{B} = 0$. This is the case only when the magnet model consist of closed loops of current. Realistic magnet models, as for example the LHC HGQ end regions as modeled by the code ROXIE and supplied by G. Sabbi of FNAL, are not closed due to presence of image currents, "leads" and separate treatment of the two end regions (lead end and return end). One way to fix this problem is to input as much physical intuition as possible to close the magnet model, compute the field generated by this model, which should differ as little as possible from the original model. This is the first step of Maxwellification. Obviously, the solution is not unique due to infinitely many ways of closing the model. The closing is important to guarantee vanishing curl, as it is required by the Maxwell equations, and in this case the field is derivable from a scalar potential. From the DA computational point of view it is also important, because it is enough to compute the field components only in the midplane (see section 9.2). The computer time needed for computing a magnet model of several 10^5 line currents to high order in one end region of the LHC HGQ's scales much worse with the increase of the number of variables than with the increase of line currents, which should be linear. Besides computer time, the second step of the Maxwellification provides a way to correct for small computational errors or magnet model imperfections. One specific example is the method of the next section. Al-

though the curl is already small, as shown in Table 9.4, the numerical stability of the multipole extraction algorithm is improved by local Maxwellification of the field, which is described below.

If we restrict ourselves to elements with straight optical axis for simplicity, the second step of Maxwellification proceeds as follows. Given $B_x(x,0,s)$, $B_y(x,0,s)$, $B_s(x,0,s)$ ($y=0$ representing the midplane) we can compute the field components in the whole space. From a scalar potential $V(x,y,s)$ that satisfies the Laplace equation

$$\frac{\partial^2 V(x,y,s)}{\partial x^2} + \frac{\partial^2 V(x,y,s)}{\partial y^2} + \frac{\partial^2 V(x,y,s)}{\partial s^2} = 0, \tag{9.20}$$

the field results from the well-known relation $\vec{B}(x,y,s) = \nabla V(x,y,s)$ (we neglect the sign which is irrelevant in our discussion). We transform the Laplace equation to a fixed point problem by isolating the y derivative term and integrating with respect to y

$$\frac{\partial^2 V(x,y,s)}{\partial y^2} = -\left(\frac{\partial^2 V(x,y,s)}{\partial x^2} + \frac{\partial^2 V(x,y,s)}{\partial s^2}\right) \tag{9.21}$$

$$\Rightarrow \quad \int_0^{y'} \frac{\partial^2 V(x,y'',s)}{\partial y''^2} dy'' = -\int_0^{y'} \left(\frac{\partial^2 V(x,y'',s)}{\partial x^2} + \frac{\partial^2 V(x,y'',s)}{\partial s^2}\right) dy'' \tag{9.22}$$

$$\Rightarrow \quad \frac{\partial V(x,y',s)}{\partial y'} = \left.\frac{\partial V(x,y'',s)}{\partial y''}\right|_{y''=0} - \int_0^{y'} \left(\frac{\partial^2 V(x,y'',s)}{\partial x^2} + \frac{\partial^2 V(x,y'',s)}{\partial s^2}\right) dy''.$$

Integrating once more

$$\int_0^{y} \frac{\partial V(x,y',s)}{\partial y'} dy' = V(x,y,s) - V(x,0,s) \tag{9.23}$$

$$\Rightarrow V(x,y,s) = V(x,0,s) + \int_0^{y} \left.\frac{\partial V(x,y'',s)}{\partial y''}\right|_{y''=0} dy' - \tag{9.24}$$

$$\int_0^{y}\int_0^{y'} \left(\frac{\partial^2 V(x,y'',s)}{\partial x^2} + \frac{\partial^2 V(x,y'',s)}{\partial s^2}\right) dy'' dy', \tag{9.25}$$

we obtain a fixed point problem for $V(x, y, s)$. In the DA picture it converges to the exact solution in $[n/2]$ steps, where n is the order of computation [98]. Since the Laplace equation is a second order PDE, we need two initial conditions. One is immediate from

$$\int_0^y \left.\frac{\partial V(x, y'', s)}{\partial y''}\right|_{y''=0} dy' = yB_y(x, 0, s), \tag{9.26}$$

because by definition $\partial V/\partial y = B_y$. This is already known, and the other initial condition to be calculated is the potential in the midplane $V(x, 0, s)$.

In the ideal case the potential in the midplane is computed by a path integral, along an arbitrary path. This is the case when the curl of the initial field is exactly vanishing. Due to various causes previously mentioned this is almost never true. Nevertheless, the curl it is usually small. Then, one should use a path along which the field is deemed more accurately computed, yielding a potential, and subsequently field components that are close to the original, and curl that is vanishing. Hence the name Maxwellification.

Most of the time it is not obvious where the fields are computed more accurately. Then, one could try different paths and choose the one giving the smallest change in the field components. Convenient choices of paths are along the sides or diagonal of a rectangle in the midplane with opposite corners at $(0, 0)$ and (x, s). In the midplane we have $dV(\vec{r}) = \vec{B}(\vec{r}) \cdot d\vec{r}$, where $\vec{r} = (x, 0, s)$. Integrating, we get

$$V(\vec{r}) = V(\vec{0}) + \int_0^{\vec{r}} \vec{B}\,(\vec{r}') \cdot d\vec{r}'. \tag{9.27}$$

We can neglect the immaterial constant $V(\vec{0})$, and integration along the sides in one direction gives

$$V(x, 0, s) = \int_0^x B_x(x', 0, 0)dx' + \int_0^s B_s(x, 0, s')ds'. \tag{9.28}$$

Integration along the sides in the other direction gives

$$V(x,0,s) = \int_0^s B_s(0,0,s')ds' + \int_0^x B_x(x',0,s)dx'. \tag{9.29}$$

For integration along the diagonal we set $\vec{r}' = \lambda\vec{r}$ with $\lambda \in [0,1]$. Then, $d\vec{r}' = \vec{r}d\lambda$ and

$$V(x,0,s) = x\int_0^1 B_x(\lambda x,0,\lambda s)d\lambda + s\int_0^1 B_s(\lambda x,0,\lambda s)d\lambda. \tag{9.30}$$

One can check by direct calculation that indeed $B_x(x,0,s) = \frac{\partial V(x,0,s)}{\partial x}$ and $B_s(x,0,s) = \frac{\partial V(x,0,s)}{\partial s}$. This completes the Maxwellification procedure. Once we have $V(x,y,s)$ we can compute the field components satisfying Maxwell's equations in the whole region of interest by mere differentiation.

In DA, the field components are computed as local Taylor expansions, so the method provides a local Maxwellification. That's why, beside choosing the right path, it might be useful to average over a certain region to decide which approach is the best. Finally, it should be obvious how to extend all the equations in the case of full $3D$ Maxwellification, if originally the field components are given in all 3 variables (x,y,s). For example, (9.28) is extended as

$$V(x,y,s) = \int_0^x B_x(x',0,0)dx' + \int_0^s B_s(x,0,s')ds' + \int_0^y B_y(x,y',s)dy', \tag{9.31}$$

and in the same way in other cases. In this situation, of course, there are many more path choices and no fixed point transformation of the Laplace equation is needed.

As an example, in Table 9.5 we present the s component of the curl of the Maxwellified field of Table 9.3. We mention that the now we present the results up to order 12 in the curl and the first non-vanishing element occurs at order 6. Also, notice the improvement in comparison with the curl in Table 9.4.

$\left(\nabla \times \vec{B}\right)_s$ after Maxwellification		
Coefficient	Order	Exp. (x, s, y)
-.4547473508864641E-12	6	2 0 4
-.1455191522836685E-10	7	2 1 4
0.3051757812500000E-04	8	6 0 2
-.2328306436538696E-09	8	4 2 2
-.3051757812500000E-04	8	2 0 6
0.1862645149230957E-08	9	4 3 2
-.1862645149230957E-08	10	6 2 2
-.1490116119384766E-07	10	4 4 2
-.1490116119384766E-07	10	2 4 4
-.1455191522836685E-10	10	2 0 8
-.2842170943040401E-13	11	5 0 6
0.1490116119384766E-07	11	4 1 6
-.3552713678800501E-14	11	2 0 9
0.5960464477539063E-07	12	2 2 8

Table 9.5: The s component of the curl, up to order 12, after Maxwellification of the field in Table 9.3.

9.3.2 Global Maxwellification

We saw that local Maxwellification is possible based on a closed magnet model consisting of line currents. One might imagine cases when the magnet model is not closed, and for some reason it is practically impossible to close it, or the actual closings change the original fields significantly. For such cases the S-Dependent Differential Algebraic Analytical Fourier Transform (SDDAAFT) of subsection 9.2.2 provides a way for global Maxwellification and minimal modification of the original fields in a neighborhood of the optical axis. The only drawback compared to the previous method is that we need the field computation of the unclosed model in all 3 variables (x, y, s), which implies increased computer time.

We start with the magnetic field vector $\vec{B}(x, y, s)$ representing the field of an unclosed magnet model computed using Biot-Savart law. Therefore, $\nabla \cdot \vec{B} = 0$ and $\nabla \times \vec{B} \neq 0$. Then, there exists another vector $\vec{R}(x, y, s)$, which stands for the field

generated by fictitious line currents representing the closings of the model. Obviously, $\vec{R}$ is not unique, due to infinitely many possibilities of closing. It follows that $\nabla \cdot \vec{R} = 0$ and $\nabla \times \left(\vec{B} + \vec{R}\right) = 0$. Taking the cross product $\nabla \times \nabla \times \left(\vec{B} + \vec{R}\right) = \nabla \left(\nabla \cdot \left(\vec{B} + \vec{R}\right)\right) - \Delta \left(\vec{B} + \vec{R}\right) = 0$, we obtain $\Delta \left(B_i + R_i\right) = 0$; B_i and R_i being the components in cylindrical coordinates of $\vec{B}$ and $\vec{R}$. Now, we know from the general theory what is the structure of a function in cylindrical coordinates that satisfies the Laplace equation. Hence, we get

$$R_i(r, \phi, s) = \sum_{l=0}^{\infty} \left(f_{i,l}(r, s) \sin l\phi + g_{i,l}(r, s) \cos l\phi\right) r^l - B_i(r, \phi, s). \tag{9.32}$$

Apparently, we get the smallest R_i in the vicinity of the optical axis if we choose the free parameters in $f_{i,l}(r, s)$ and $g_{i,l}(r, s)$, the true multipoles, such that they cancel the corresponding terms in B_i. This way we fix uniquely the true multipoles, that are anyway the dominating part, and let R_i to contribute only for the pseudo-multipole parts. Here we define as being a true multipole of order l the s-dependent function that is the coefficient of $r^{l-1} \cos l\phi$ or $r^{l-1} \sin l\phi$, respectively, in the expression of B_i. This definition makes sense, since it reduces to the usual definitions in the case when the fields are derivable from a magnetic scalar potential.

Once the principle is understood, in practice we do not need to calculate explicitly R_i. It is enough to have B_i and extract the relevant terms, the true multipoles, then the out of axis expansion is performed, the potential is built up and the new fields are computed. The new fields will satisfy Maxwell's equation; hence the name global Maxwellification.

Still, one thing remains to be proved. The solution is really unique if we prove that the true multipoles are invariant with respect to which component of the original field we choose, B_r or B_ϕ. This result is easily obtained in case we impose the vanishing curl and divergence conditions, as has been shown in the direct method. It can be

shown that this is also the case without imposing any constraints on the coefficients. This is the subject of section 9.4.

All the methods described have been implemented in the DA based code COSY INFINITY [83, 84, 24].

9.4 Structure of B_r and B_ϕ for Non-Maxwellian Fields

We start with the Cartesian components

$$B_x(x,y,s) = \sum_{i,j=0}^{n} a_{ij}(s) x^i y^j, \tag{9.33}$$

$$B_y(x,y,s) = \sum_{i,j=0}^{n} b_{ij}(s) x^i y^j, \tag{9.34}$$

as given by the field computation, without imposing any relations among the a_{ij}'s and b_{ij}'s due to Maxwell's equations; n is the order of computation. Transformation to cylindrical coordinates gives

$$B_r = B_x \cos\phi + B_y \sin\phi, \tag{9.35}$$

$$B_\phi = -B_x \sin\phi + B_y \cos\phi, \tag{9.36}$$

$$x = r\cos\phi, \tag{9.37}$$

$$y = r\sin\phi. \tag{9.38}$$

Inserting (9.33) in (9.35) we obtain

$$B_r(r,\phi,s) = \sum_{i,j=0}^{n} r^{i+j} \cos^i\phi \sin^j\phi \left(a_{ij}(s)\cos\phi + b_{ij}(s)\sin\phi\right), \tag{9.39}$$

$$B_\phi(r,\phi,s) = \sum_{i,j=0}^{n} r^{i+j} \cos^i\phi \sin^j\phi \left(-a_{ij}(s)\sin\phi + b_{ij}(s)\cos\phi\right). \tag{9.40}$$

The next step is to transform the products of trigonometric functions into a sum of trigonometric functions involving multiple angles, i.e.

$$\cos^{i+1}\phi \sin^{j}\phi = \sum_{k=0}^{i+j+1} \alpha_k^{(j)} \cos k\phi + \beta_k^{(j)} \sin k\phi, \tag{9.41}$$

$$\cos^{i}\phi \sin^{j+1}\phi = \sum_{k=0}^{i+j+1} \gamma_k^{(j)} \cos k\phi + \delta_k^{(j)} \sin k\phi, \tag{9.42}$$

where $\alpha_k^{(j)}$, $\beta_k^{(j)}$, $\gamma_k^{(j)}$, $\delta_k^{(j)}$ are real constants depending on j. Hence, we obtain

$$B_r = \sum_{i,j=0}^{n} r^{i+j} \left[\begin{array}{c} a_{ij}(s) \sum_{k=0}^{i+j+1} \left(\alpha_k^{(j)} \cos k\phi + \beta_k^{(j)} \sin k\phi \right) + \\ b_{ij}(s) \sum_{k=0}^{i+j+1} \left(\gamma_k^{(j)} \cos k\phi + \delta_k^{(j)} \sin k\phi \right) \end{array} \right], \tag{9.43}$$

$$B_\phi = \sum_{i,j=0}^{n} r^{i+j} \left[\begin{array}{c} -a_{ij}(s) \sum_{k=0}^{i+j+1} \left(\gamma_k^{(j)} \cos k\phi + \delta_k^{(j)} \sin k\phi \right) + \\ b_{ij}(s) \sum_{k=0}^{i+j+1} \left(\alpha_k^{(j)} \cos k\phi + \beta_k^{(j)} \sin k\phi \right) \end{array} \right]. \tag{9.44}$$

Now we can use the definition of the multipoles to retain in B_r and B_ϕ just the true multipoles: we need to keep only the terms with $k = i + j + 1$, all others giving rise to pseudo-multipoles. We neglect the solenoidal terms, which are always treated best separately from B_s. Then, the components of the field containing just the true multipoles are

$$\tilde{B}_r = \sum_{i,j=0}^{n} r^{i+j} \left[\begin{array}{c} a_{ij}(s) \left(\alpha_{i+j+1}^{(j)} \cos\left(i+j+1\right)\phi + \beta_{i+j+1}^{(j)} \sin\left(i+j+1\right)\phi \right) \\ +b_{ij}(s) \left(\gamma_{i+j+1}^{(j)} \cos\left(i+j+1\right)\phi + \delta_{i+j+1}^{(j)} \sin\left(i+j+1\right)\phi \right) \end{array} \right],$$

$$\tilde{B}_\phi = \sum_{i,j=0}^{n} r^{i+j} \left[\begin{array}{c} -a_{ij}(s) \left(\gamma_{i+j+1}^{(j)} \cos\left(i+j+1\right)\phi + \delta_{i+j+1}^{(j)} \sin\left(i+j+1\right)\phi \right) \\ +b_{ij}(s) \left(\alpha_{i+j+1}^{(j)} \cos\left(i+j+1\right)\phi + \beta_{i+j+1}^{(j)} \sin\left(i+j+1\right)\phi \right) \end{array} \right],$$

or by rearranging terms the results are

$$\tilde{B}_r = \sum_{i,j=0}^{n} r^{i+j} \left[\begin{array}{c} \left(a_{ij}(s)\alpha_{i+j+1}^{(j)} + b_{ij}(s)\gamma_{i+j+1}^{(j)}\right)\cos\left(i+j+1\right)\phi \\ +\left(a_{ij}(s)\beta_{i+j+1}^{(j)} + b_{ij}(s)\delta_{i+j+1}^{(j)}\right)\sin\left(i+j+1\right)\phi \end{array} \right], \quad (9.45)$$

$$\tilde{B}_\phi = \sum_{i,j=0}^{n} r^{i+j} \left[\begin{array}{c} \left(-a_{ij}(s)\gamma_{i+j+1}^{(j)} + b_{ij}(s)\alpha_{i+j+1}^{(j)}\right)\cos\left(i+j+1\right)\phi \\ +\left(-a_{ij}(s)\delta_{i+j+1}^{(j)} + b_{ij}(s)\beta_{i+j+1}^{(j)}\right)\sin\left(i+j+1\right)\phi \end{array} \right]. \quad (9.46)$$

By expanding the trigonometric functions in terms of exponentials, it can be seen that: for j even we get

$$\alpha_{i+j+1}^{(j)} = 2^{-(i+j)}\left(-1\right)^{j/2}, \quad (9.47)$$

$$\beta_{i+j+1}^{(j)} = 0, \quad (9.48)$$

$$\gamma_{i+j+1}^{(j)} = 0, \quad (9.49)$$

$$\delta_{i+j+1}^{(j)} = 2^{-(i+j)}\left(-1\right)^{j/2}, \quad (9.50)$$

and for j odd

$$\alpha_{i+j+1}^{(j)} = 0, \quad (9.51)$$

$$\beta_{i+j+1}^{(j)} = 2^{-(i+j)}\left(-1\right)^{(j-1)/2}, \quad (9.52)$$

$$\gamma_{i+j+1}^{(j)} = -2^{-(i+j)}\left(-1\right)^{(j-1)/2}, \quad (9.53)$$

$$\delta_{i+j+1}^{(j)} = 0. \quad (9.54)$$

Separation of the double sum into summation over i, and j-even, respectively j-odd leads to

$$\tilde{B}_r = \sum_{i=0}^{n} \left\{ \begin{array}{l} \sum_{j=0\ j-even}^{n} r^{i+j} \left[\begin{array}{c} a_{ij}(s)\cos\left(i+j+1\right)\phi) + \\ b_{ij}(s)\sin(i+j+1)\phi \end{array} \right] 2^{-(i+j)}\left(-1\right)^{j/2} + \\ \sum_{j=1\ j-odd}^{n} r^{i+j} \left[\begin{array}{c} -b_{ij}(s)\cos\left(i+j+1\right)\phi) + \\ a_{ij}(s)\sin(i+j+1)\phi \end{array} \right] 2^{-(i+j)}\left(-1\right)^{(j-1)/2} \end{array} \right\},$$

$$\tilde{B}_\phi = \sum_{i=0}^{n} \left\{ \begin{array}{l} \sum_{j=0\ j-even}^{n} r^{i+j} \left[\begin{array}{c} b_{ij}(s)\cos\left(i+j+1\right)\phi) - \\ a_{ij}(s)\sin(i+j+1)\phi \end{array} \right] 2^{-(i+j)}\left(-1\right)^{j/2} + \\ \sum_{j=1\ j-odd}^{n} r^{i+j} \left[\begin{array}{c} a_{ij}(s)\cos\left(i+j+1\right)\phi) + \\ b_{ij}(s)\sin(i+j+1)\phi \end{array} \right] 2^{-(i+j)}\left(-1\right)^{(j-1)/2} \end{array} \right\}.$$

The symmetry of the above equations is clear. $\tilde{B}_r$ and $\tilde{B}_\phi$ have the same number of terms, and if the symmetry holds term by term, then it also holds for their sum. By introducing a new index $l = i + j$ we obtain relations of the form

$$\tilde{B}_r = \sum_{l=0}^{n} \left[A_l(s)\cos(l+1)\phi + B_l(s)\sin(l+1)\phi\right] r^l, \tag{9.55}$$

$$\tilde{B}_\phi = \sum_{l=0}^{n} \left[B_l(s)\cos(l+1)\phi - A_l(s)\sin(l+1)\phi\right] r^l. \tag{9.56}$$

where $A_l(s)$, $B_l(s)$ are sums over $a_{ij}(s)$, $b_{ij}(s)$ with $i + j = l$. Shifting the origin of summation to make comparison easier with the direct method, and using the convention that the $l = 1$ component corresponds to dipole gives the final form

$$\tilde{B}_r(r,\phi,s) = \sum_{l=1}^{n+1} \left[A_l(s)\cos l\phi + B_l(s)\sin l\phi\right] r^{l-1}, \tag{9.57}$$

$$\tilde{B}_\phi(r,\phi,s) = \sum_{l=1}^{n+1} \left[B_l(s)\cos l\phi - A_l(s)\sin l\phi\right] r^{l-1}. \tag{9.58}$$

By identification, it is apparent that (9.57) is of the same form as the field components derived from a scalar potential, containing only the true multipoles. For example, up to order 5 we can derive the following relations:

$$A_1(s) = a_{00}(s), \tag{9.59}$$

$$A_2(s) = \frac{1}{2}\left(a_{10}(s) - b_{01}(s)\right), \tag{9.60}$$

$$A_3(s) = \frac{1}{4}\left(a_{20}(s) - b_{11}(s) - a_{02}(s)\right), \tag{9.61}$$

$$A_4(s) = \frac{1}{8}\left(a_{30}(s) - b_{21}(s) - a_{12}(s) + b_{03}(s)\right), \tag{9.62}$$

$$A_5(s) = \frac{1}{16}\left(a_{40}(s) - b_{31}(s) - a_{22}(s) + b_{13}(s) + a_{04}(s)\right); \tag{9.63}$$

$$B_1(s) = b_{00}(s), \tag{9.64}$$

$$B_2(s) = \frac{1}{2}\left(b_{10}(s) + a_{01}(s)\right), \tag{9.65}$$

$$B_3(s) = \frac{1}{4}\left(b_{20}(s) + a_{11}(s) - b_{02}(s)\right), \tag{9.66}$$

$$B_4(s) = \frac{1}{8}\left(b_{30}(s) + a_{21}(s) - b_{12}(s) - a_{03}(s)\right), \tag{9.67}$$

$$B_5(s) = \frac{1}{16}\left(b_{40}(s) + a_{31}(s) - b_{22}(s) - a_{13}(s) + b_{04}(s)\right). \tag{9.68}$$

The differences between the constrained cases (by the Maxwell equations) and arbitrary coefficients now can be analyzed. Clearly, the dipole component will give the same result in every method. The differences start to show up at the quadrupole component. For example, the normal quadrupole is given in general by $B_2(s) = \frac{1}{2}\left(b_{10}(s) + a_{01}(s)\right)$. If we impose $\nabla \cdot \vec{B} = 0$, as it is always the case for magnetic field computations, it gives just $a_{10}(s) + b_{01}(s) + c'_{00}(s) = 0$, that is, it does not impose any constraints between $b_{10}(s)$ and $a_{01}(s)$. On the other hand, if $\nabla \times \vec{B} = 0$, the s component imposes: $b_{10}(s) = a_{01}(s)$. If the curl is not vanishing, i.e. $b_{10}(s) \neq a_{01}(s)$, the method will take as the quadrupole component the average value. The same type of analysis can be performed on higher order multipoles to emphasize the importance of vanishing curl.

As a conclusion, we proved that the method can be used for global Maxwellification, with a unique solution, that alters the original fields by a minimal amount. However, we remind the reader that $\tilde{B}_r$ and $\tilde{B}_\phi$ do not contain all the terms, the whole field expressions for B_r and B_ϕ have contributions from pseudo-multipoles that cannot be written in the form of (7.18) in case of non-vanishing curl.

9.5 Examples of Exact Multipole Decompositions

Using the methods developed in this chapter, we computed the multipole strengths as a function of s for the LHC interaction region's High Gradient Quadrupoles. These

quadrupoles have two end regions, the lead end (Figure 9.1) and the return end (Figure 9.2), where the fields are s-dependent.

We computed the multipoles up to 28-poles for both ends. The field computation has been performed up to order 13, at 1 cm equally spaced points along the optical axis. Figure 9.3 shows the allowed (due to symmetry considerations) normal and skew multipole strengths as functions of s, for the lead end. The same data is depicted in Figure 9.4 for the return end. Notice that the skew multipoles vanish for the return end.

As previously mentioned, the map computation needs also the s-derivatives of the multipoles. These are easily obtained as a by-product of the multipole extraction algorithms, because we always keep their s dependence; derivative computation in DA in an elementary operation. It yields very accurate results without the need to resort to numerical differentiation. The even order s derivatives (which enter the potential expansion (7.12)) of multipoles presented in Figures 9.3 and 9.4 are shown in Figures 9.5, 9.6. and 9.7 (for lead end's $b_2(s)$, $b_6(s)$, and $b_{10}(s)$), Figures 9.8, 9.9, and 9.10 (for lead end's $a_2(s)$, $a_6(s)$, and $a_{10}(s)$), and Figures 9.11, 9.12, and 9.13 (for return end's $b_2(s)$, $b_6(s)$, and $b_{10}(s)$). The multipoles and their derivatives have been interpolated for plotting by a derivative preserving interpolation scheme. Also, the two multipole extraction algorithms were checked against each other and found to be in complete agreement.

The importance of vanishing curl has been stressed at several points throughout the chapter. To show the influence on the extracted quadrupole strength and its derivatives of the effect of non-vanishing curl, we compare two cases: multipole extracted from a magnet model that generates field with non-vanishing curl, and multipole extracted from the same magnet model after all the open-ended wires have

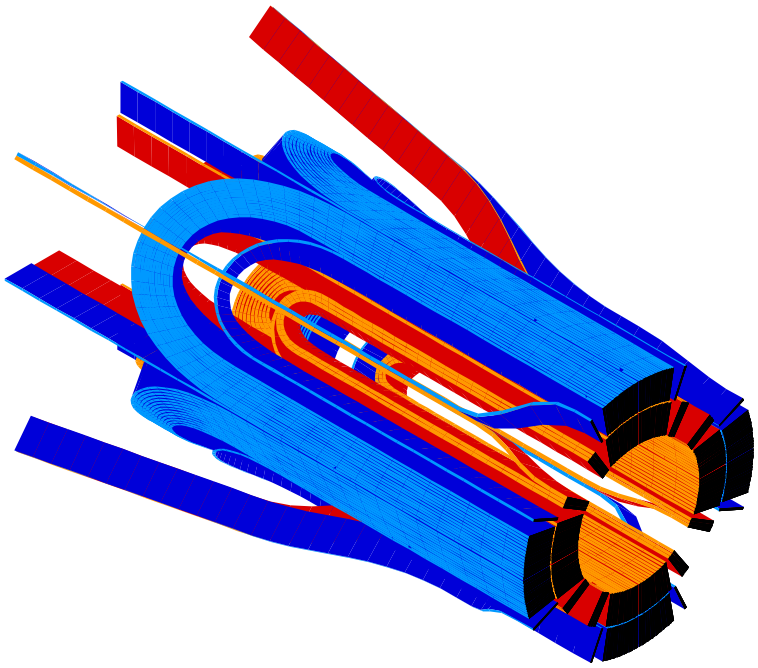

Figure 9.1: Lead End of the High Gradient Quadrupoles of the Large Hadron Collider.

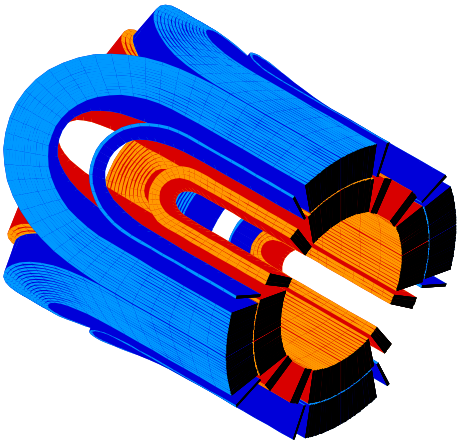

Figure 9.2: Return End of the High Gradient Quadrupoles of the Large Hadron Collider.

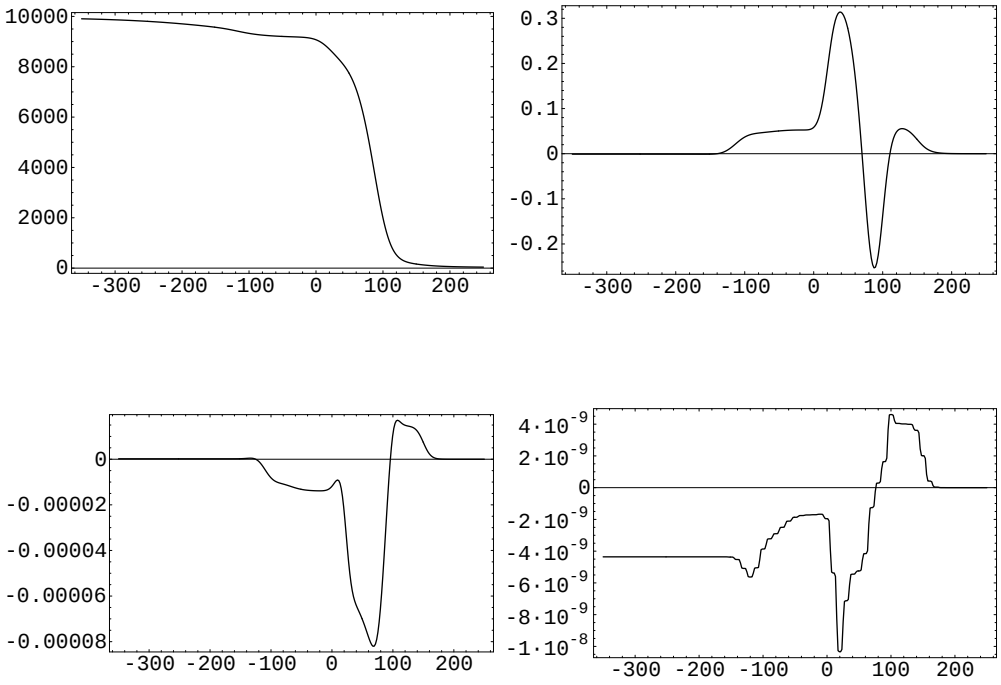

(b) Normal multipoles: $b_2(s)$, $b_6(s)$, $b_{10}(s)$, and $b_{14}(s)$.

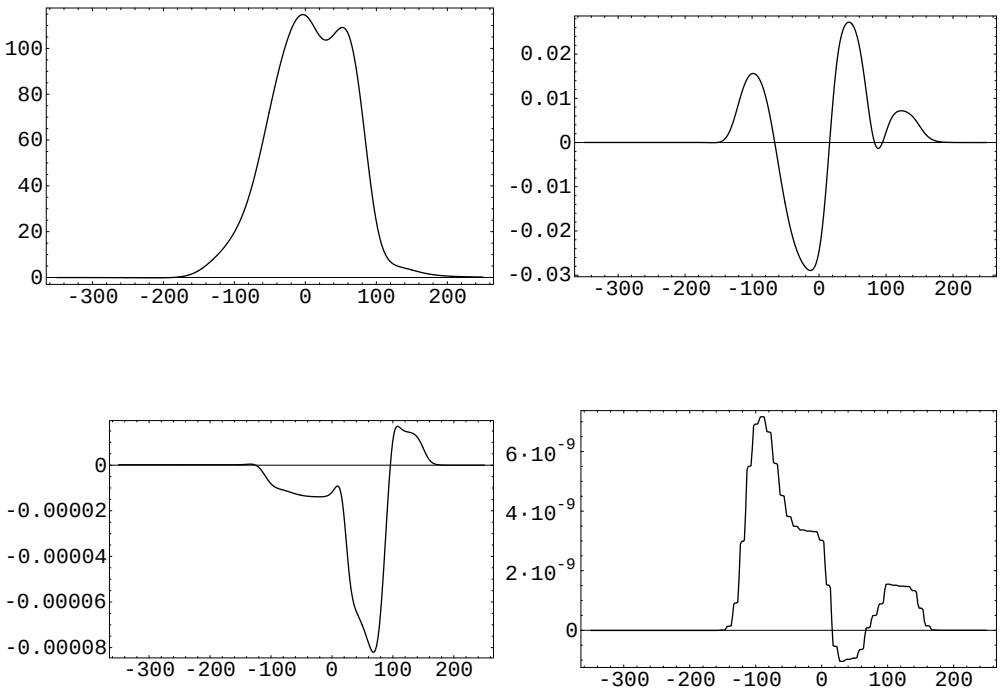

(d) Skew multipoles: $a_2(s)$, $a_6(s)$, $a_{10}(s)$, and $a_{14}(s)$.

Figure 9.3: Multipole strengths of the lead end as functions of s.

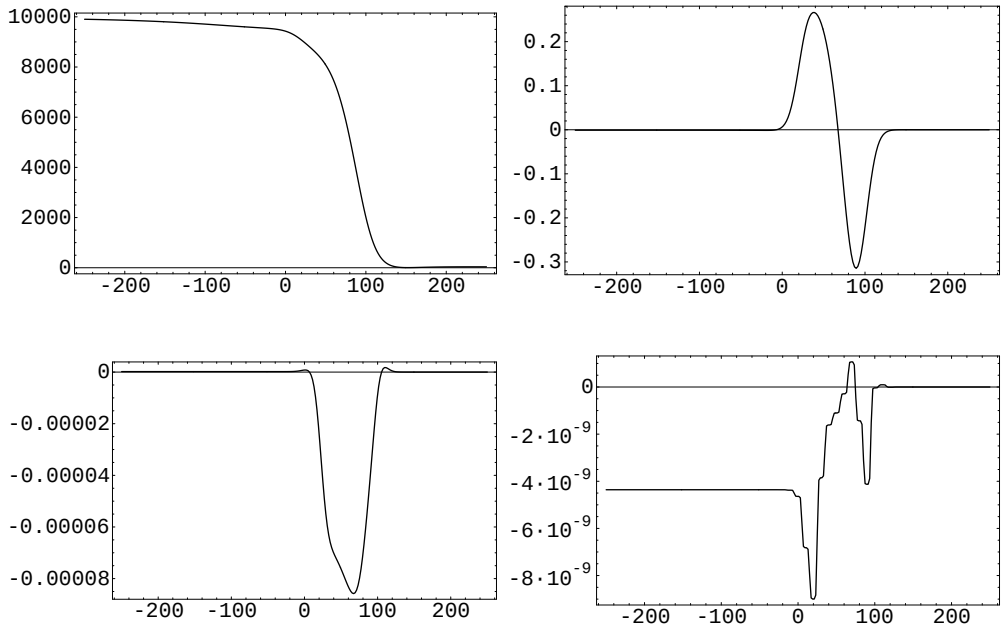

Figure 9.4: Normal multipole strengths of the return end as functions of s: $b_2(s)$, $b_6(s)$, $b_{10}(s)$, and $b_{14}(s)$.

been closed at "infinity" (in practice meaning far away from the observation points). The result is contained in Figure 9.14. It can be seen that, although the agreement is pretty good for the quadrupole strength, the small differences are amplified for the higher order derivatives.

9.6 Computation of Fringe Field Maps

As an application of the multipole decompositions, we describe very accurate high-order map computations of s-dependent fields. There are two ways to calculate maps. In the first case the following three steps are needed: using the analytical magnet model, the field expansions at selected support points along the optical axis are computed. In case it is necessary, the Maxwellification is included in this step. Then follows the extraction of the multipoles. Finally, the multipoles are interpolated by Gaussian interpolation [99], and using the integration algorithm of COSY, described

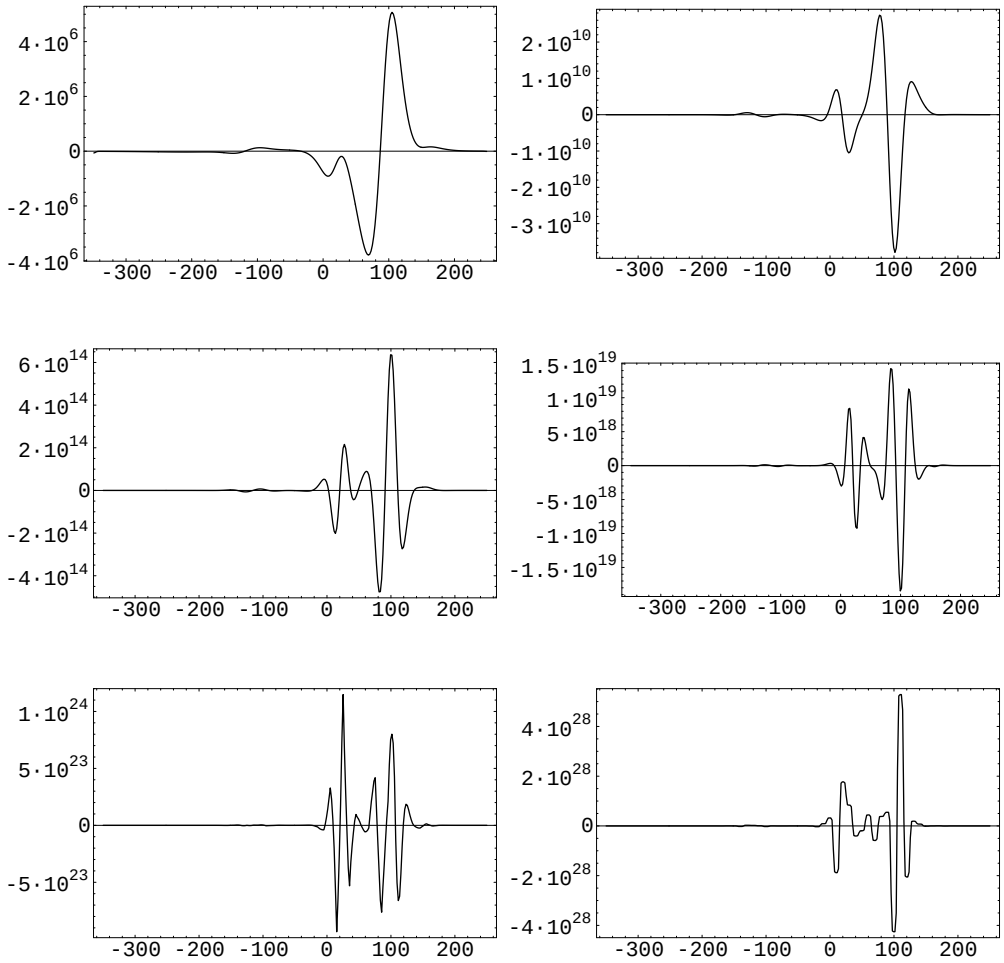

Figure 9.5: The even order s-derivatives of the lead end's $b_2(s)$. Shown are ${b_2}^{(2)}(s)$, ${b_2}^{(4)}(s)$, ${b_2}^{(6)}(s)$, ${b_2}^{(8)}(s)$, ${b_2}^{(10)}(s)$, and ${b_2}^{(12)}(s)$.

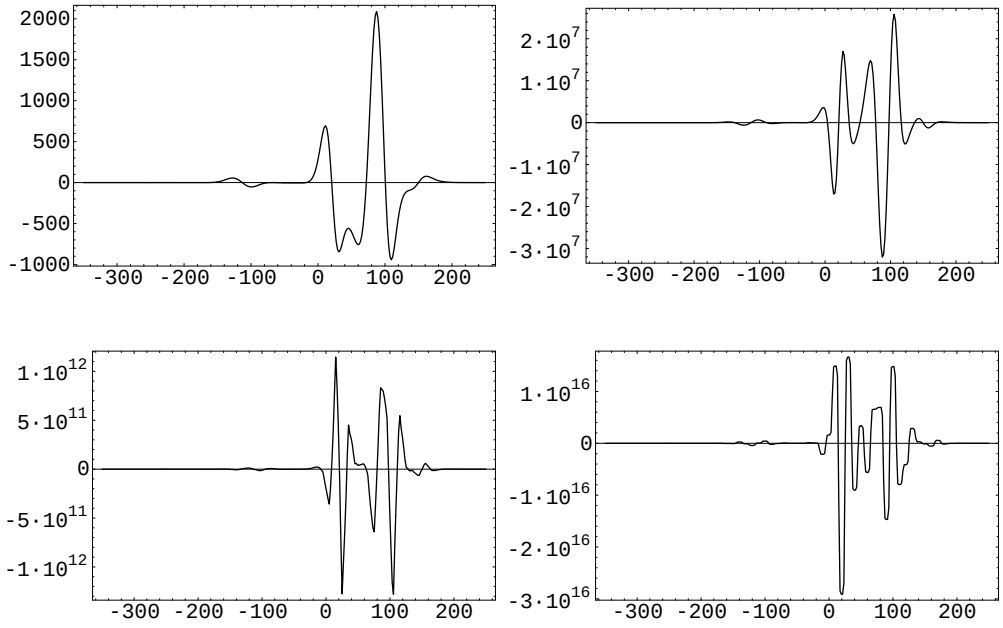

Figure 9.6: The even order s-derivatives of the lead end's $b_6(s)$. Shown are ${b_6}^{(2)}(s)$, ${b_6}^{(4)}(s)$, ${b_6}^{(6)}(s)$, and ${b_6}^{(8)}(s)$.

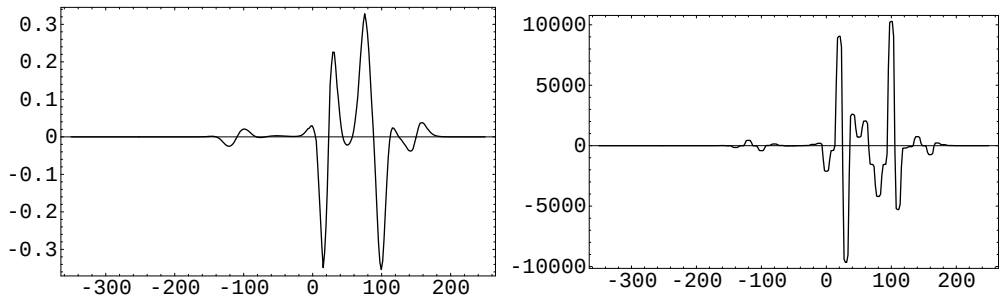

Figure 9.7: The even order s-derivatives of the lead end's $b_{10}(s)$. Shown are ${b_{10}}^{(2)}(s)$ and ${b_{10}}^{(4)}(s)$.

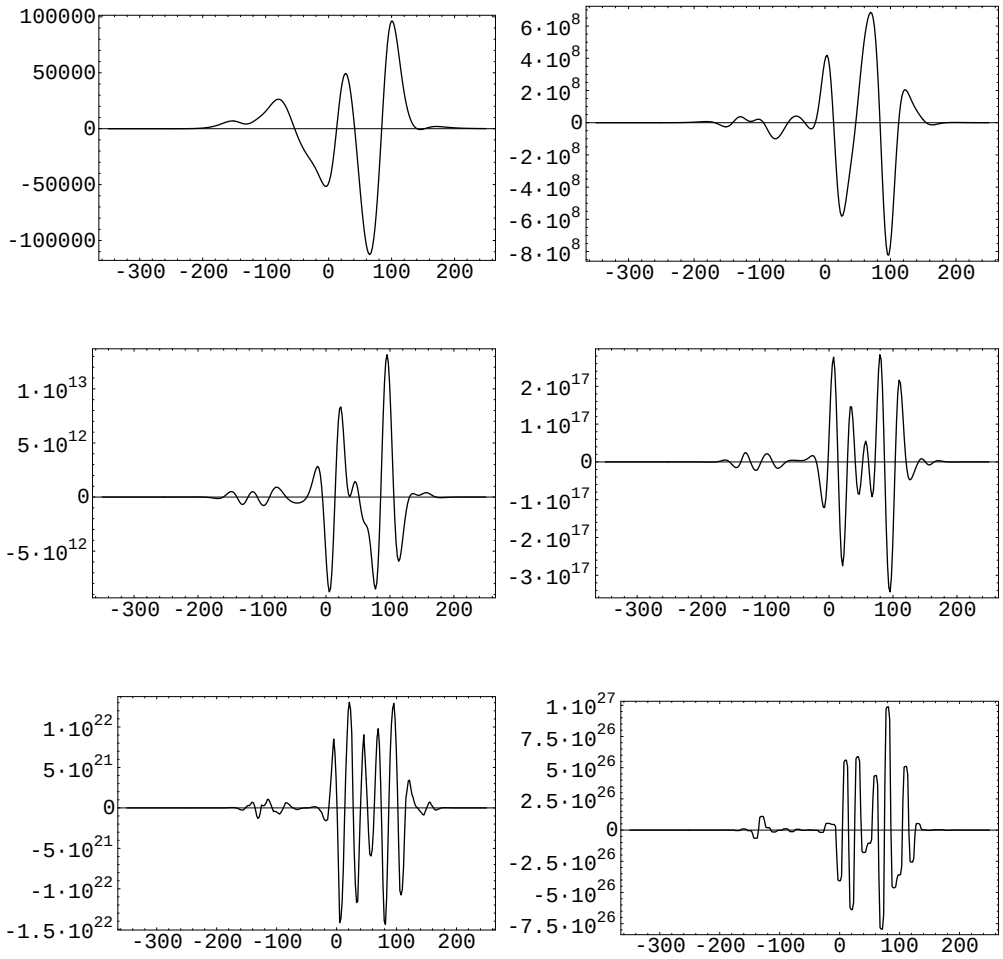

Figure 9.8: The even order s-derivatives of the lead end's $a_2(s)$. Shown are ${a_2}^{(2)}(s)$, ${a_2}^{(4)}(s)$, ${a_2}^{(6)}(s)$, ${a_2}^{(8)}(s)$, ${a_2}^{(10)}(s)$, and ${a_2}^{(12)}(s)$.

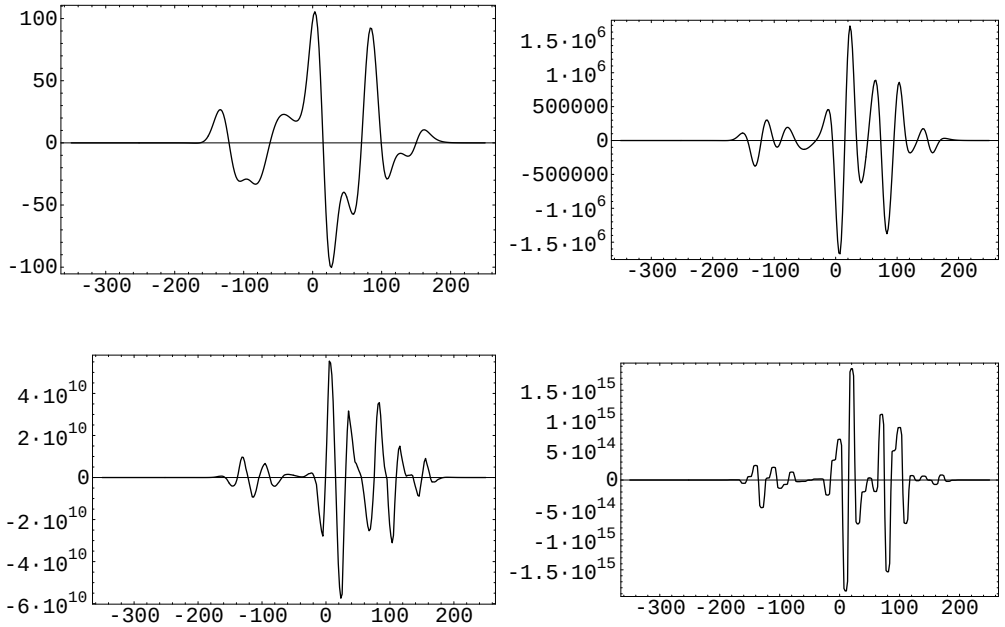

Figure 9.9: The even order s-derivatives of the lead end's $a_6(s)$. Shown are ${a_6}^{(2)}(s)$, ${a_6}^{(4)}(s)$, ${a_6}^{(6)}(s)$, and ${a_6}^{(8)}(s)$.

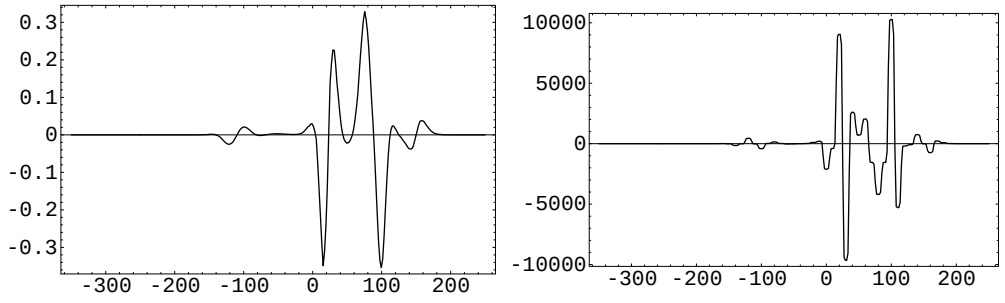

Figure 9.10: The even order s-derivatives of the lead end's $a_{10}(s)$. Shown are ${a_{10}}^{(2)}(s)$ and ${a_{10}}^{(4)}(s)$.

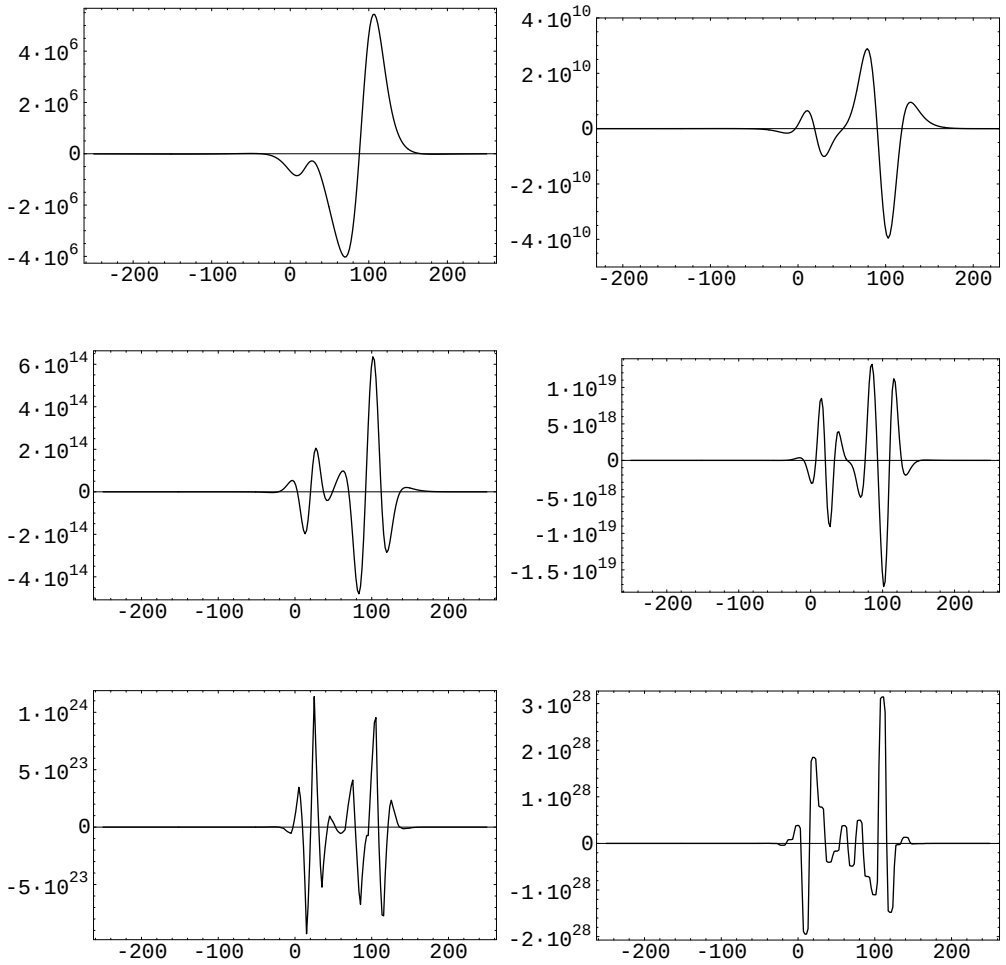

Figure 9.11: The even order s-derivatives of the return end's $b_2(s)$. Shown are ${b_2}^{(2)}(s)$, ${b_2}^{(4)}(s)$, ${b_2}^{(6)}(s)$, ${b_2}^{(8)}(s)$, ${b_2}^{(10)}(s)$, and ${b_2}^{(12)}(s)$.

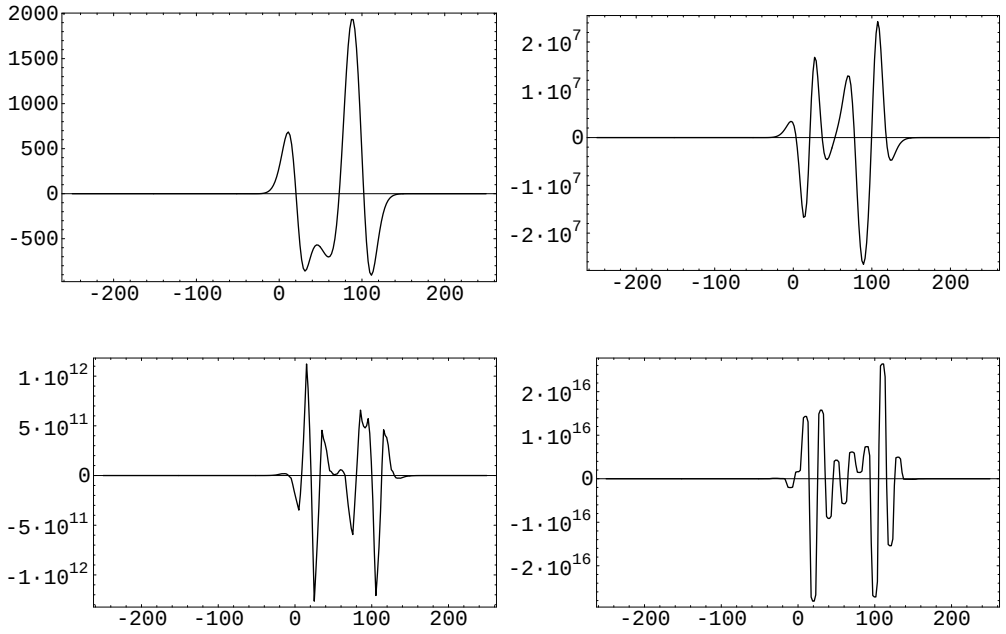

Figure 9.12: The even order s-derivatives of the return end's $b_6(s)$. Shown are ${b_6}^{(2)}(s)$, ${b_6}^{(4)}(s)$, ${b_6}^{(6)}(s)$, and ${b_6}^{(8)}(s)$.

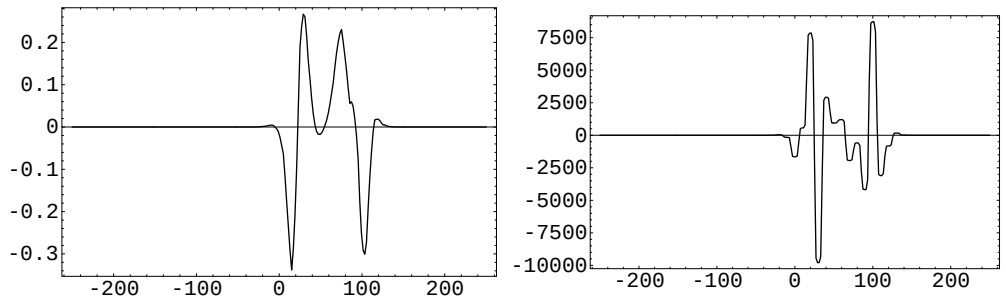

Figure 9.13: The even order s-derivatives of the return end's $b_{10}(s)$. Shown are ${b_{10}}^{(2)}(s)$ and ${b_{10}}^{(4)}(s)$.

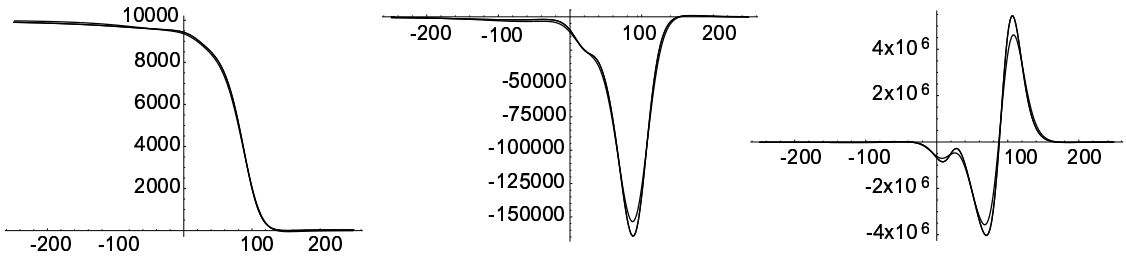

Figure 9.14: The lead end's normal quadrupole strength, and its first and second s-derivatives, extracted from Maxwellian and non-Maxwellian fields, respectively, and superimposed on the same pictures.

Order	Opening aberrations $(x\|a^n)$	
n	Return end	Lead end
2	0	0
3	0.2497609620388847	0.2995410193258450
4	0.6293863605053251E-13	-.3054844395050998E-13
5	0.1903231022089257	0.1962270889999381
6	0.6911276300083234E-12	-.6125473066348172E-12
7	0.1699451387437771	0.9019387229287767E-01
8	-.1364626459777126E-09	0.2013346179046971E-09

Table 9.6: Opening aberrations, $(x|a^n)$, for the return and lead ends' exit focusing maps.

in [24], the map is generated.

The alternate way's first step is the same. However, the scalar potential at support points is anyway computed in the process of Maxwellification. We can use this potential to integrate the equations of the motion, with an interpolation scheme that preserves the derivatives at the support points, yielding the map.

Both methods have been implemented in COSY, and they give essentially the same results. Especially at high orders, the Gaussian method is faster due to the smoothing properties of Gaussian interpolation [99]. Although to list the whole map it would be too long, to get a feeling of the resulting fringe field maps for the above mentioned end regions we list the opening aberrations in both ends up to order 8 in Table 9.6. Once we have the maps, they can be employed for dynamics studies, which is actually the final purpose of the whole theory and methods developed in this chapter. We applied the methods to study the fringe field effects in the LHC. Some of the results are presented in chapter 10.

Chapter 10

Fringe Field Effects on the Nonlinear Dynamics of the LHC

Recently, many studies have been published on single particle dynamics in the Large Hadron Collider to be built at CERN. See [100] and references therein. Specifically, at collision energy it has been shown that the dynamics is dominated by the interaction region's high gradient quadrupole triplets. This is due to large variations of the β functions across the quadrupoles. The studies concentrate on many possible realizations of the LHC lattice, that is, on computing the effects of the so-called systematic and random body errors, and perhaps other effects like crossing angle, beam-beam interaction, misalignment, etc. The fringe fields, traditionally, are taken into account at most at the level of lumped thin lenses (kicks), characterized by integrated multipole strengths. However, it is not obvious whether this simplistic approach is enough to give an accurate account of the dynamics under the influence of fringe fields. This chapter attempts to fill this gap, by assessing the impact of fringe fields via very accurate fringe field maps, at least for the LHC, and specifically for the low-β insertion quadrupoles shown in Figures 9.1 and 9.2.

We showed in chapter 9 how to take into account the local structure of s-dependent fields, resulting in the computation of very accurate fringe field maps. We use the

fringe field maps computed with the methods of section 9.6 to study systematically their effect on the nonlinear dynamics of the LHC. Starting from a simplistic model of the lattice, we gradually include more and more effects (described in more detail in the next section) and study their influence measured by tune-shifts, resonance strengths and sometimes resonance webs. We keep an eye on the importance of the exact shape of fringe fields and relative importance with respect to body errors. Results concerning off-energy particles are included too.

10.1 Methods of Analysis

We use as measures for the dynamics indicators that have been proven effective in predicting the performance of existing accelerators, and were useful for construction of correction schemes for proposed machines. We will employ tune footprint, tune shift, resonance strength and resonance web calculations. All of them are based on normal forms of symplectic maps. We assume that the LHC is accurately described by the n-th order Taylor expansion of the system's true map, $\mathcal{M}$. Because hadron accelerators can be regarded as large Hamiltonian systems, the truncated map will be symplectic to order n. It means that relative to some symplectic coordinates $\vec{z}$ its Jacobian, M, satisfies the symplectic condition to order n

$$M^T J M = J. \tag{10.1}$$

The truncated map can be subjected to an order by order symplectic change of variables that finally yields its normal form. That is, there exist symplectic maps $\mathcal{A}_n$ such that

$$\mathcal{N} = \mathcal{A}_n \circ \mathcal{M} \circ \mathcal{A}_n^{-1}, \tag{10.2}$$

The symplectic map $\mathcal{N}$ takes a particularly simple interpretation; it is a rotation with radius dependent frequency. See [101] for details. The angles of advancement of a

point on a torus after one application of the map are called the tunes of the respective particle. Its deviation from the tune of a particle with 0 amplitude (the linear tune) is called the tune-shift. Due to the fact that the normal form of a symplectic map is unique, also the tune-shifts are uniquely defined. We compute these quantities for the various cases studied. In general, for good performance of accelerators, large tune-shifts are to be avoided.

In this setting, the resonance condition is defined as

$$\vec{k} \cdot \vec{\mu} \left(\vec{J}, \vec{\delta} \right) = m \pmod{2\pi}, \tag{10.3}$$

for a vector of integers $\vec{k}$ and integer m. The tunes are denoted by $\vec{\mu}$, $\vec{J}$ represents the action variables (the radii), and $\vec{\delta}$ the parameters. Although the normal form transformation can be used to compute the tunes only in the non-resonant case, it is our hope that extrapolation of the results close to the resonant case can give insight into the dynamics of resonant orbits. For this purpose, we study (10.3) as a function of $\vec{J}$. By adding to the right hand side a small quantity $\varepsilon \ll 1$, with fixed maximum value, we plot in action space the actions $\vec{J}$ that satisfy the resonant condition. This gives insight into the resonance orbit structure of the phase space directly. This picture of the location and width of resonance lines is called the resonance web. The intuitive interpretation of the role of ε is that it translates a fixed, small distance in tune space around exactly resonant orbits into oscillation of the action variables around exactly resonant orbits. The amount of oscillation gives a measure of the width of the resonance lines. Overlapping of resonance lines are considered signs of chaos, which is not necessarily bad in theory, but it is usually in practice. Often, the dynamic aperture is close to the chaotic boundary. Hence, the closeness of the resonance lines to the origin in action space again can be a useful indicator.

It is not straightforward to explain the method of computing the resonance strengths

without getting into unnecessary details. This is partly due to the fact that the resonance strengths are not defined uniquely. Usually it is based on the normalizing map, $\mathcal{A}_n$, which is known to not be unique. Moreover, the manipulation of the elements of $\mathcal{A}_n$ is somewhat arbitrary. Nevertheless, as a general rule, the resonance strengths are directly proportional to the nonlinearity of the underlying map and its distance from resonances, measured by the resonance denominators, which are the left hand sides of (10.3). For more details of a method similar in spirit to our calculation we refer the reader to [102]. The difference between the two methods is that we do not use Lie algebraic techniques, but we work directly with the Taylor expansions of the components of the normalizing map. Despite all this, the correction of dominating resonances proved to be an effective tool for improving the performance of accelerators. We could say that, although the exact numerical values of the resonance strengths do not really have relevance (as they are method dependent), the qualitative picture it is useful (for example identifying the dominating resonances).

We mention that none of the above indicators have an absolute correlation with the behavior of particles in accelerators. In some cases one of them can have a better correlation with the dynamic aperture, in other cases another indicator, or none. However, altogether probably they can reveal the gross features of the dynamics, and are useful in practice.

10.2 Cases Studied

All maps, fringe field and rest of the lattice (LHC v.5.1), have been computed at order 8 using the code COSY INFINITY [24]. Due to sensitivity to numerical errors, especially at high orders, of the tune-shift computation, and occurrence of large numbers in the maps, we performed all the calculations in quadruple pre-

cision on an Alpha workstation. The effects of RF cavities have been neglected, i.e. we computed the maps in two transversal degrees of freedom, with energy as a parameter. At the specific location of the lattice where we fixed the Poincaré section, the r.m.s. beam sizes are $\sigma_x = 1.267 \cdot 10^{-4} m$ and $\sigma_y = 2.981 \cdot 10^{-4} m$, respectively. It is also known from the design specifications that the r.m.s. normalized emittance is $\varepsilon_N = 3.75 \cdot 10^{-6} m \cdot r$ and the r.m.s. energy deviation is $\sigma_E = 1.1 \cdot 10^{-4}$. For body errors we used the table MQXB (FNAL High Gradient Quad) Reference Harmonics at Collision v. 2.0, available on the WWW at the address http://www.agsrhichome.bnl.gov/LHC/fnal/v2.0/hgq_col_v2p0.txt. The detailed analysis of the body errors were not the main purpose of our studies, so we used only one seed for the random body errors, which gives "average" results in some sense (for example, dynamic aperture). For the systematic part of the errors we employed their full uncertainty, with the two possible signs. That is, if we denote by $\langle b_n \rangle$ the average value of a multipole, then the multipole value due to uncertainty lies between $-d\left(b_n\right) + \langle b_n \rangle \leq b_n \leq +d\left(b_n\right) + \langle b_n \rangle$. Hereafter we will refer to the two cases of full uncertainty by their sign, $(-)$ or $(+)$.

To assess the importance of fringe field shape, we use two different models. One is the "detailed" shape, based on the exact shape of the fringe field computed using the model HGQS01 [92]. The other is a "default" fringe field shape, as implemented in the code COSY Infinity, based on the falloff modeled by an Enge function [24]. The detailed fringe fields detune the ideal lattice and also introduce linear coupling between the planes. To obtain meaningful results we have to retune and decouple the lattice. We achieve this in a rather elegant way using an ideal local correction. Moreover, the method provides a way to keep the design linear lattice completely

unchanged. It is done by splitting the fringe field maps into two parts

$$M_{ff} = L_{ff} + N_{ff}, \tag{10.4}$$

where L_{ff} is the linear part and N_{ff} is the nonlinear part. Application of the inverse of the linear map, which can be thought of as the zero length insertion ideal local corrector, we obtain for the fringe field map

$$\tilde{M}_{ff} = I + L_{ff}^{-1} \circ N_{ff}, \tag{10.5}$$

where I is the identity map. The identity as linear part ensures that the linear layout of the lattice remains unchanged. Of course, we would get a slightly different result if we were to apply L_{ff}^{-1} from the right. However, L_{ff} is close to identity, so L_{ff}^{-1} is also close to identity, and hence almost commutes with the nonlinear part. Again, this is an ideal case, and it is very likely that any real world correction scheme would introduce more nonlinearities in the map of the system. This method has been implemented in COSY INFINITY as a new fringe field mode. As a final remark, we mention that it is enough to compute only the exit focusing fringe field maps, and obtain the other variants by mirroring operations and rotations. Also, we use the same symmetry based tricks to get the correct maps for the proposed layout of the interaction regions, which includes rotations of quadrupoles around their vertical axis. The respective procedures are described in section 10.4.

Table 10.1 contains all the cases studied, starting from the simple to the more complex. In the following section we describe the results obtained for each of them. We will refer to the specific case by their number in the table.

10.3 Results and Discussion

The results shed light on the relative importance of intrinsic nonlinearities of the ideal lattice, the fringe field induced nonlinearities, and body errors induced nonlinearities.

CASE	SYSTEM
1	Interaction regions at order 8, rest linear Fringe fields and body errors OFF
2	Interaction regions at order 8, rest linear HGQ detailed fringe fields ON
3	Interaction regions at order 8, rest linear Only quadrupole components of HGQ fringe fields ON
4	Interaction regions at order 8, rest linear HGQ default fringe fields ON
5	Whole lattice at order 8 Fringe fields and body errors OFF
6	Whole lattice at order 8 detailed fringe fields for HGQ, and default fringe fields for rest of ring ON; body errors OFF
7	Whole lattice at order 8 fringe fields OFF, body errors (−) ON
8	Whole lattice at order 8 fringe fields OFF, body errors (+) ON
9	Whole lattice at order 8 fringe fields from case 6 ON, and body errors (−) ON
10	Whole lattice at order 8 fringe fields from case 6 ON, and body errors (+) ON

Table 10.1: The various LHC realization cases studied.

The tunes are visualized in two different ways. The $2D$ pictures represent the usual tune footprint style, and the $3D$ pictures show the tune shift of particles as a function of initial amplitudes in geometric space, in units of r.m.s. beam sizes, up to 6σ. The tune-shifts in the $3D$ pictures are all in units of 10^{-4}. The resonance strengths are computed close to the expected dynamic aperture, along the diagonal in action space. The units are arbitrary, and we denote $\vec{k} = (q, p)$. Also, for cases 9 and 10 we computed the resonance strengths on a grid of points to identify the dominating resonances in different locations of phase space. Every case is subdivided in 3 subcases according to energy: $\delta = -2.5\sigma_E, 0, +2.5\sigma_E$. For the computation of resonance webs we used a maximum value of $\varepsilon = 10^{-3}$. The size of the beam at the expected dynamic aperture is approximately $J_x = J_y = 5 \cdot 10^{-4} m$.

We start with the most simple case. Case 1 represents the linear LHC lattice with only the intrinsic nonlinearities of the interaction region quadrupoles added. As we expected, Figures 10.1, 10.2 and 10.3 show that the nonlinearities are insignificant.

The tune footprints have regular shapes, but practically vanishing in size. For off-energy particles the dominating resonance is $(2, 0)$, which is 2 orders of magnitude bigger than the dominating resonance for on-energy particles, $(2, -2)$.

Case 2 is actually case 1, to which we add the detailed fringe fields of the High Gradient Quadrupoles of the interaction regions. The acceptance guidelines require a tune shift of less than 10^{-3} at 6σ.

We can see that the nonlinearities introduced by the fringe fields are considerable. See Figures 10.4, 10.5 and 10.6. However, tune shifts are still inside the safe region. Also, the tune footprints get bigger and have highly irregular shapes. Maximum values of tune shifts and size of tune footprints decrease as the energy increases. The sharpest decrease with energy is experienced by particles with small initial y and large

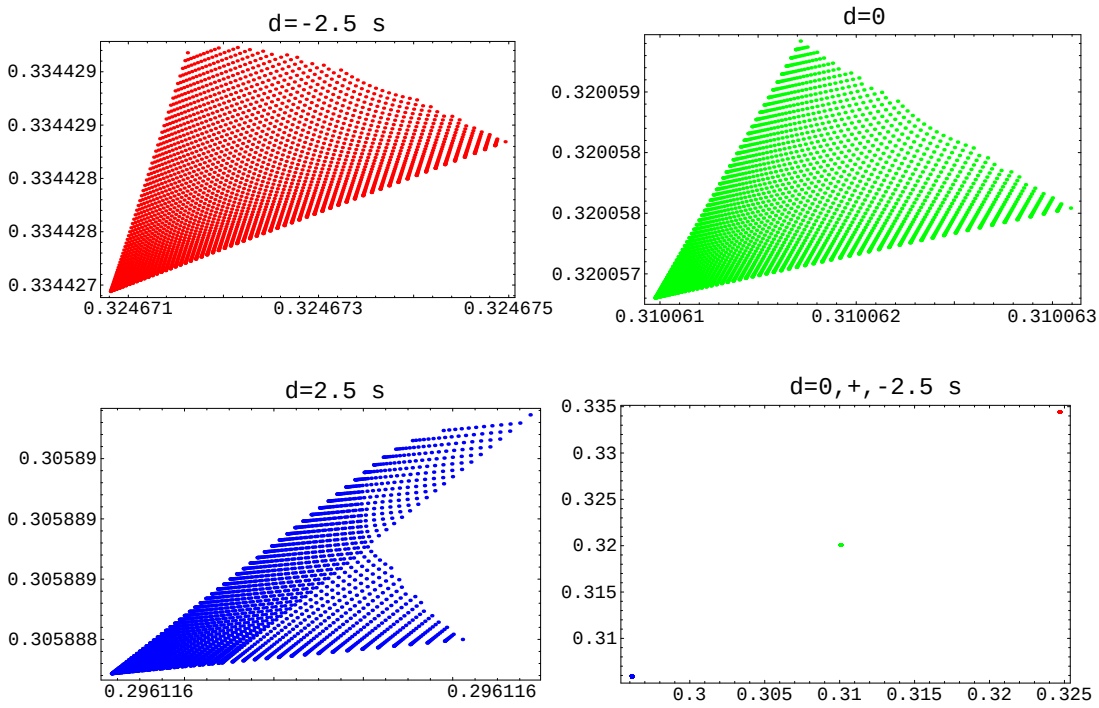

Figure 10.1: Tune footprints for the LHC case 1.

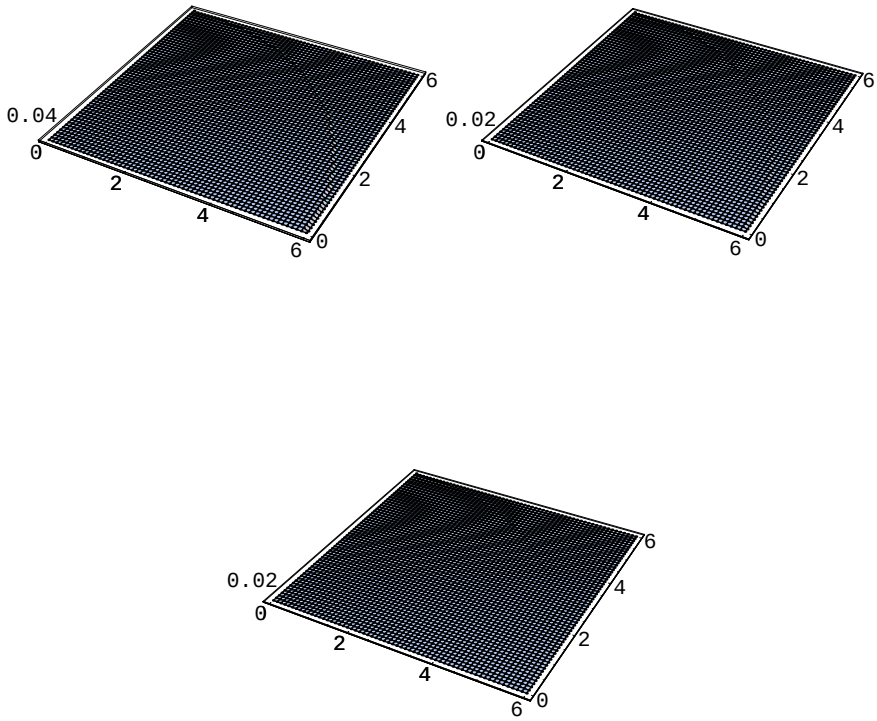

Figure 10.2: Tune shifts for the LHC case 1.

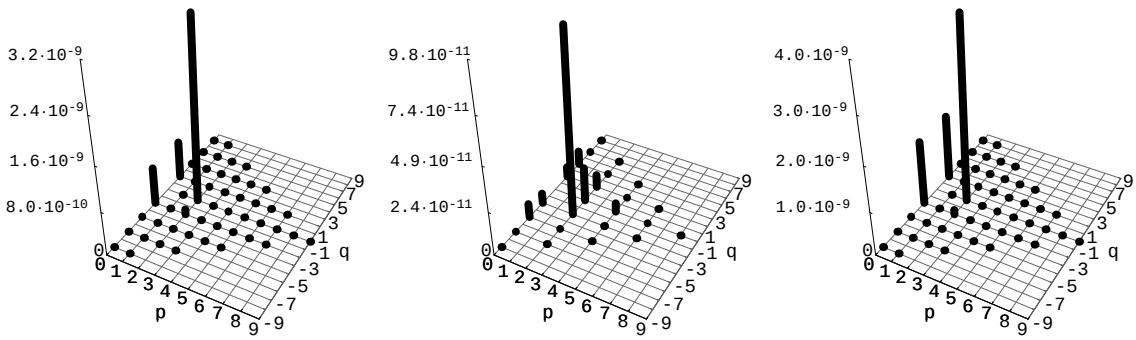

Figure 10.3: Resonance strengths for the LHC case 1.

initial x. Dominating resonances are the $(2, -2)$, also encountered in case 1, and a newly excited resonance, the $(1, -1)$. There is an increase in the absolute values of the resonance strengths, compared with case 1. The resonances are almost invariant with respect to energy. Also, their magnitudes are slightly increasing with energy, an opposite tendency when compared to tune shifts.

Next, we studied what is the relative importance of the quadrupole components with respect to the rest of the multipoles. Therefore, case 3 is case 2 without the sextupole components in the fringe fields. For the results, see Figures 10.7, 10.8 and 10.9.

We notice a 5 times decrease for the maximum tune shift for negative energy dispersion particles, and some more modest decreases for the other particles. The tune footprints are becoming a little bit smaller and regular, triangle shaped, hence the irregularities of case 2 are caused by the sextupole components in the fringe fields. Overall, the importance of the sextupole components are decreasing as the energy increases. There are noticeable differences between resonance strengths of cases 3 and 2. The magnitudes drop by 2 orders of magnitude, and become comparable with off-energy particle's resonance strengths of case 1. Moreover, they are not invariant anymore with respect to energy. While the dominating resonance, regardless of en-

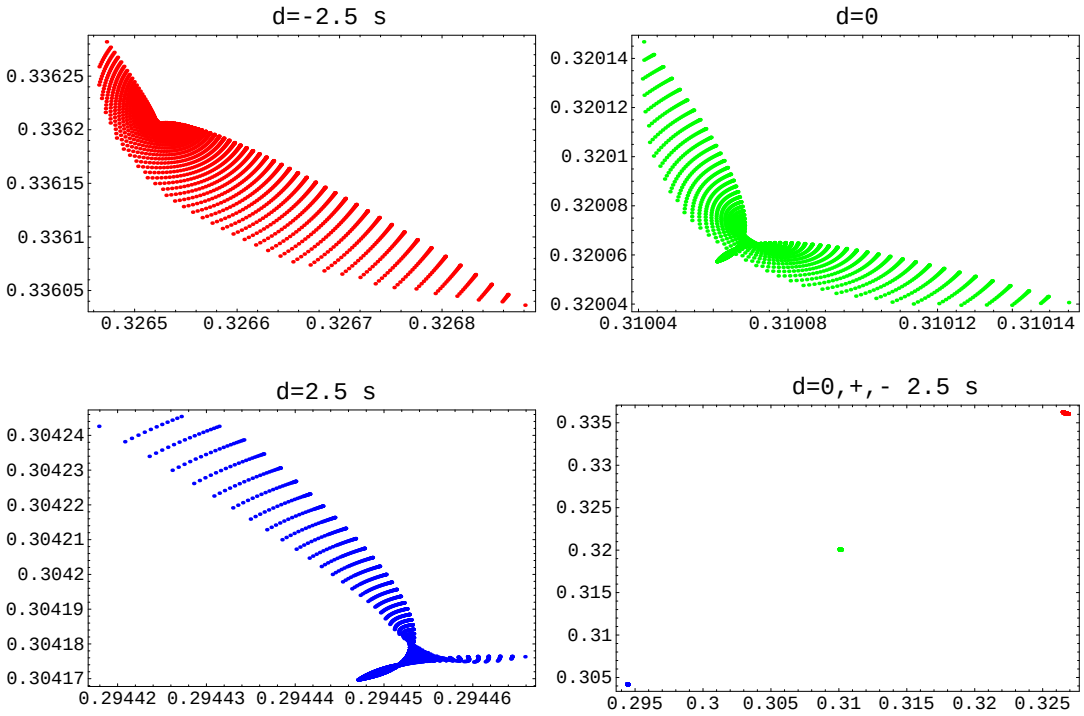

Figure 10.4: Tune footprints for the LHC case 2.

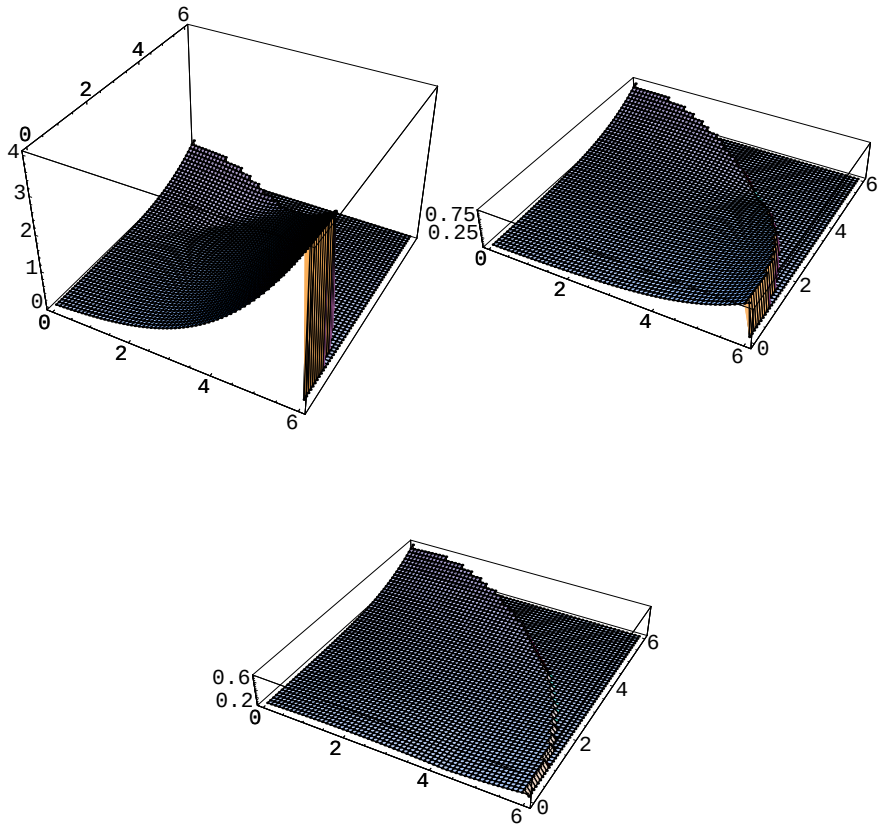

Figure 10.5: Tune shifts for the LHC case 2.

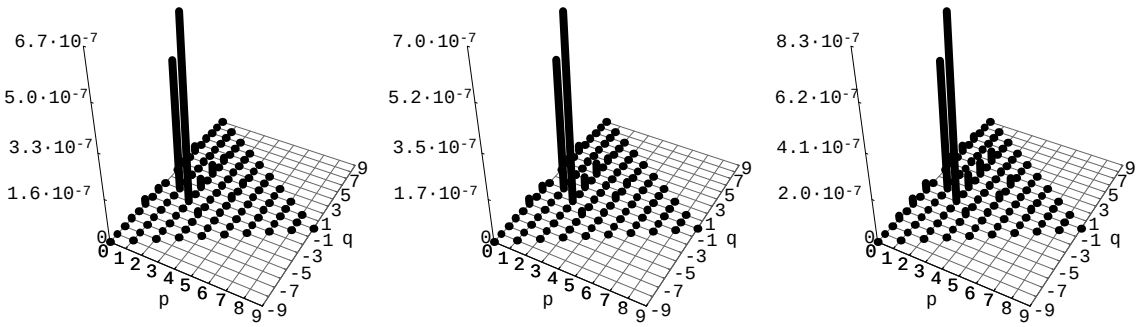

Figure 10.6: Resonance strengths for the LHC case 2.

ergy, is $(2, -2)$, which we carried along since case 1, again $(2, 0)$ from case 1 makes its appearance for off-energy particles, and $(1, -1)$ completely disappears. We conclude that the intrinsic nonlinearities of the quadrupoles excite the $(2, 0)$ and $(2, -2)$ resonances, all components of the fringe fields contribute to the $(2, -2)$ resonance, making it the dominating one, and the $(1, -1)$ resonance is excited only by the sextupole components, which is comparable in magnitude with $(2, -2)$. The magnitudes of the resonance strengths hold the slightly increasing behavior with energy.

Now we turn our attention to the question of the exact shape of the fringe fields. For easy comparison we created case 4, which is case 3 with the detailed fringe fields, containing only the quadrupole components, replaced by a generic fringe field shape, that has a falloff modeled by an Enge function with 6 parameters.

As one can see, the differences between the set of Figures of case 3, Figures 10.7, 10.8 and 10.9, and the Figures of case 4, Figures 10.10, 10.11 and 10.12, are marginal. The pictures are almost identical, with a small decrease in all the indicators for the generic fringe field. We conclude that, at least for the main component of the fringe fields, the exact shape is not critical.

As the next step, we studied the nonlinearities of the ideal lattice, that is no errors at all, only the intrinsic nonlinearities of the whole ring up to order 8. This is case 5,

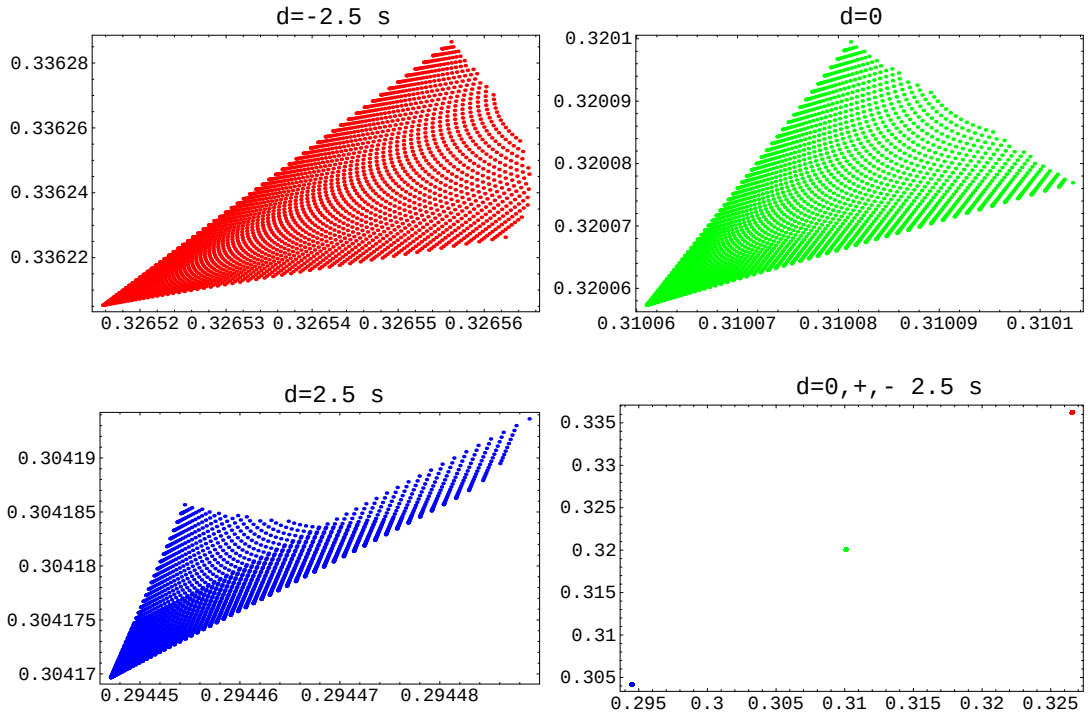

Figure 10.7: Tune footprints for the LHC case 3.

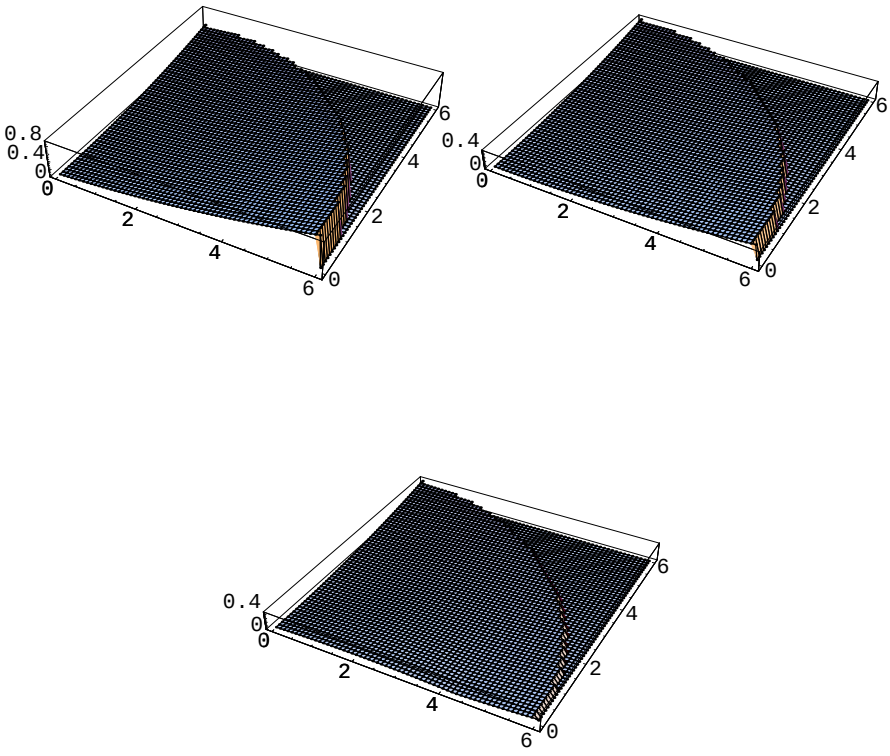

Figure 10.8: Tune shifts for the LHC case 3.

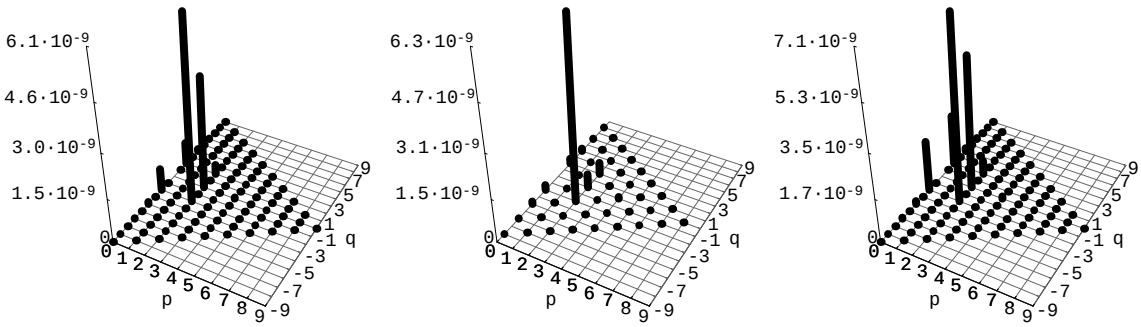

Figure 10.9: Resonance strengths for the LHC case 3.

and the relevant Figures are 10.13, 10.14, 10.15 and 10.16.

The effects of the intrinsic nonlinearities of the whole lattice are comparable with those created by the fringe fields of the interaction regions. In the case of $\delta < 0$ the fringe fields cause a bigger maximum tune-shift, while for $\delta \geq 0$ the intrinsic nonlinearities are marginally bigger. Also, the tune footprints are roughly the same, but in this case the shapes are regular, triangle shaped. However, the resonance strengths are more than one order of magnitude smaller than in case 2, and they are almost invariant with respect to energy. Many more resonances are excited than in the previous cases, with $(2, -2)$ remaining the dominant one. Other excited resonances are $(1, 2)$, $(1, 0)$ and a few smaller: $(1, -2)$, $(3, 0)$ and $(2, 0)$. The $(2, 0)$ is almost completely missing for $\delta = 0$, hence it is excited mostly by off-energy particles. The resonance web shows the chaotic boundary to be at approximately $3 \cdot 10^{-3} m$. A beam of $\simeq 12\sigma_{x,y}$ occupies $\simeq 4 - 5 \cdot 10^{-4} m$ in this picture, therefore this region is completely free of low order resonances. We estimated the following resonances to be the "thickest", in decreasing order: $(1, -1)$, $(2, -2)$, $(3, -3)$, $(4, -4)$, $(6, 1)$ and $(8, -1)$.

Case 6 represents case 2 and case 5 superimposed, and additionally generic fringe fields are set on for the remaining of the ring.

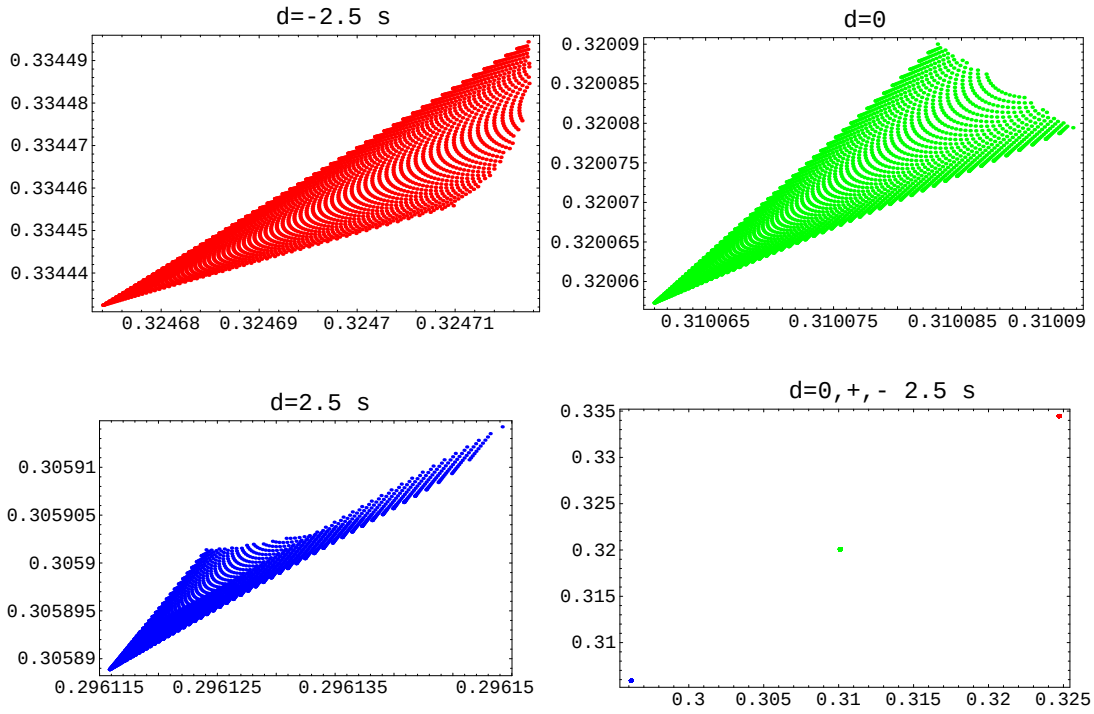

Figure 10.10: Tune footprints for the LHC case 4.

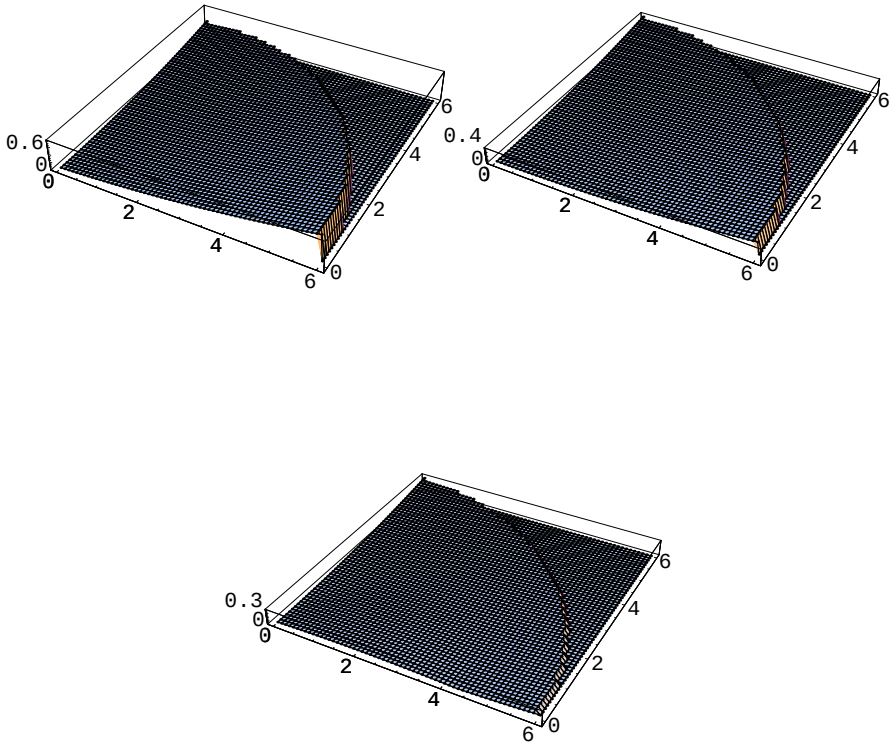

Figure 10.11: Tune shifts for the LHC case 4.

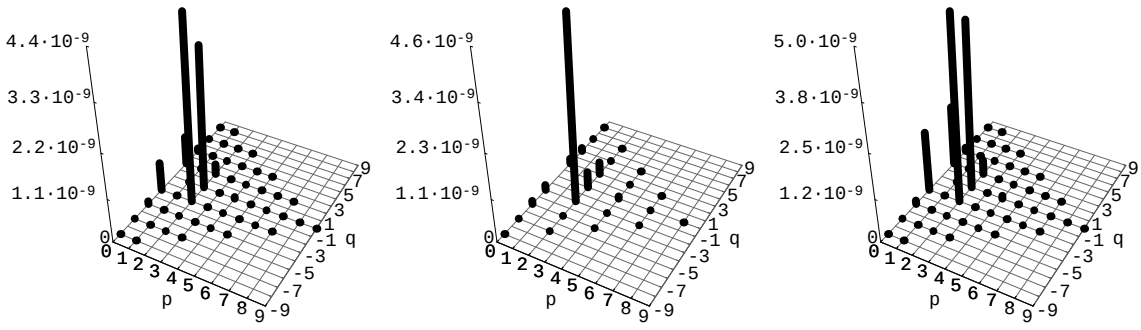

Figure 10.12: Resonance strengths for the LHC case 4.

Figures 10.17, 10.18 and 10.19 show that the tune shifts and footprints of case 6 are almost like adding up the corresponding pictures from cases 2 and 5. The resonance strengths are looking similar to those of case 2. This proves that the dominating fringe field effects are concentrated in the interaction regions, which has been showed to hold for other effects too, which are limiting the dynamic aperture.

The next two cases deal with the body errors. As mentioned in section 10.2, we have two possible signs for the uncertainty part of the errors. We use the same "average" seed for the random part in both cases. Case 7 is the $(-)$ case, and case 8 is the $(+)$ case.

For case 7, Figures 10.20, 10.21 and 10.22 show a little bigger tune shifts and footprints than for case 6, but still inside the safe region. The footprints are elongated and curved, and even overlapping for $\delta = -2.5\sigma_E$ and $\delta = 0$, respectively. On the other hand, the resonance strengths are amplified by 3 orders of magnitude. The new dominating resonance is $(0, 3)$. The resonances that are excited mainly by fringe fields and intrinsic nonlinearities are negligible.

Case 8 is the first situation where the maximum tune shift exceeds the acceptable level of 10^{-3} at 6σ (Figure 10.24). See also Figures 10.23 and 10.25.

Comparison of cases 7 and 8 proves that the systematic errors are important.

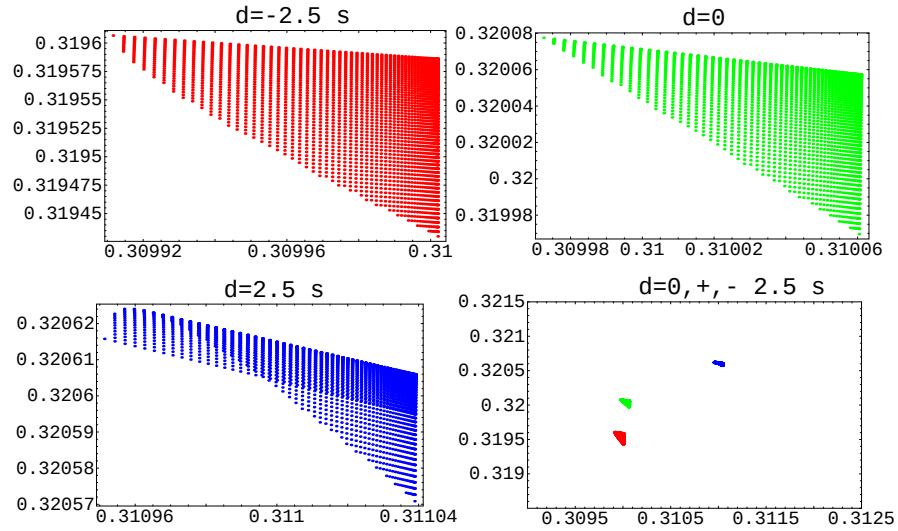

Figure 10.13: Tune footprints for the LHC case 5.

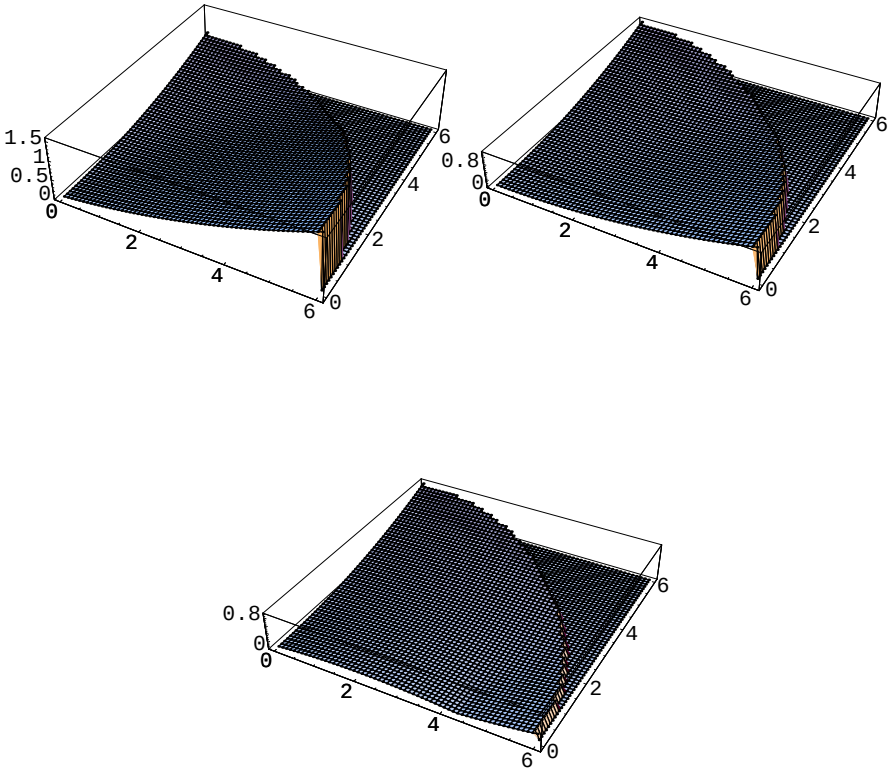

Figure 10.14: Tune shifts for the LHC case 5.

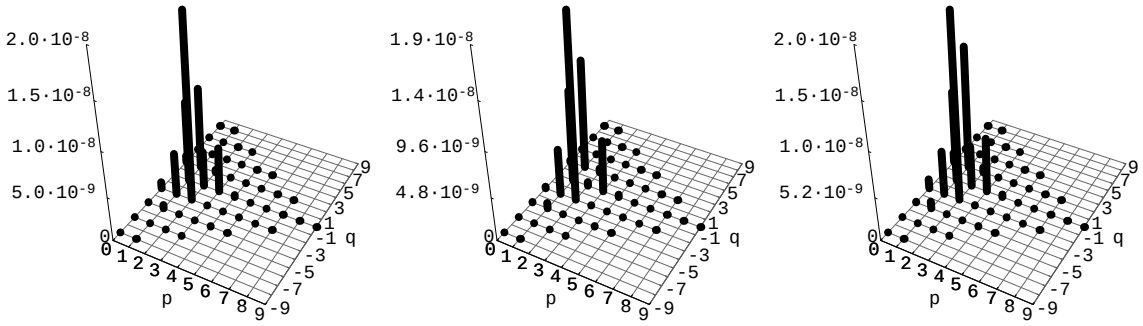

Figure 10.15: Resonance strengths for the LHC case 5.

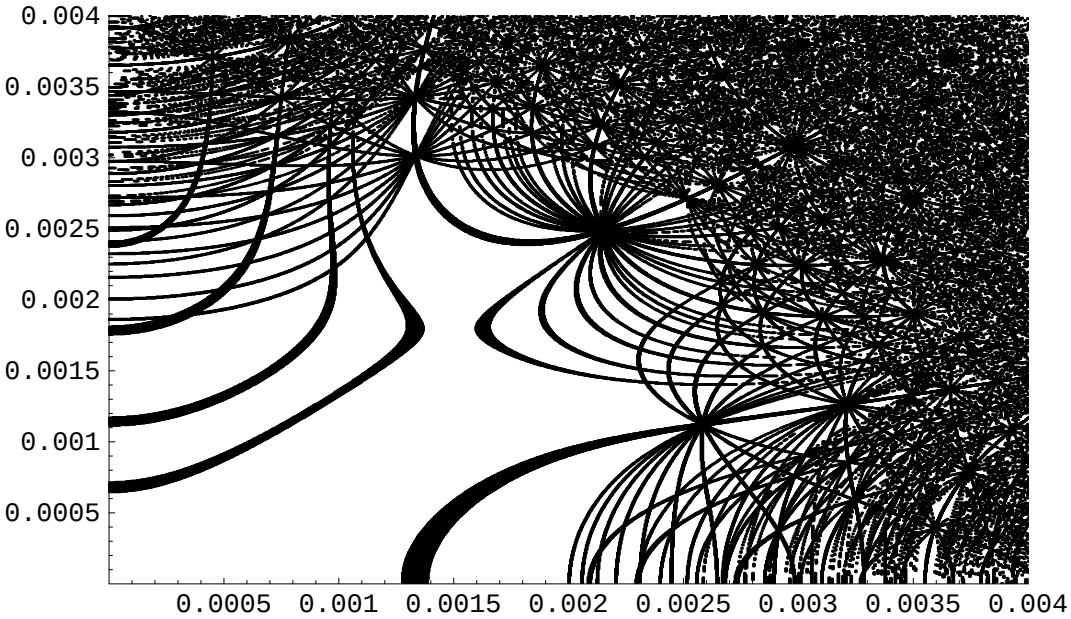

Figure 10.16: Resonance web for the LHC case 5, for $d = 0$.

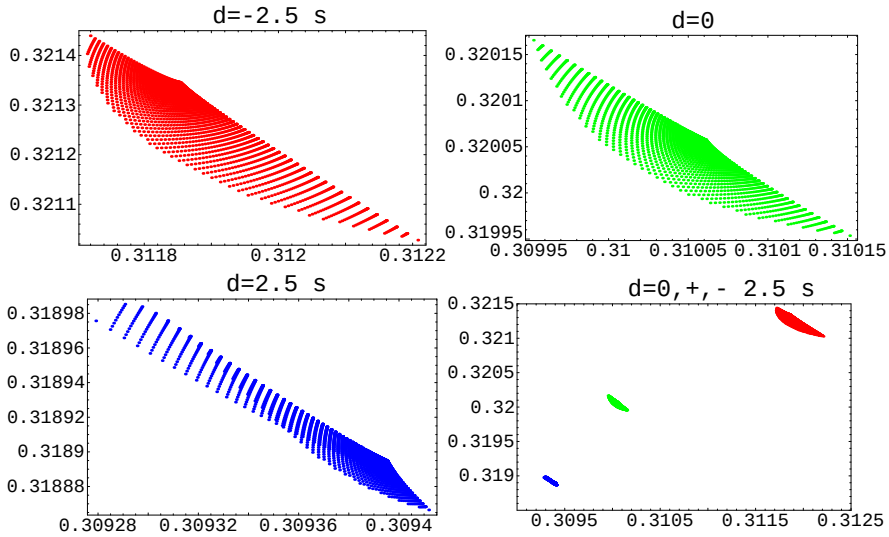

Figure 10.17: Tune footprints for the LHC case 6.

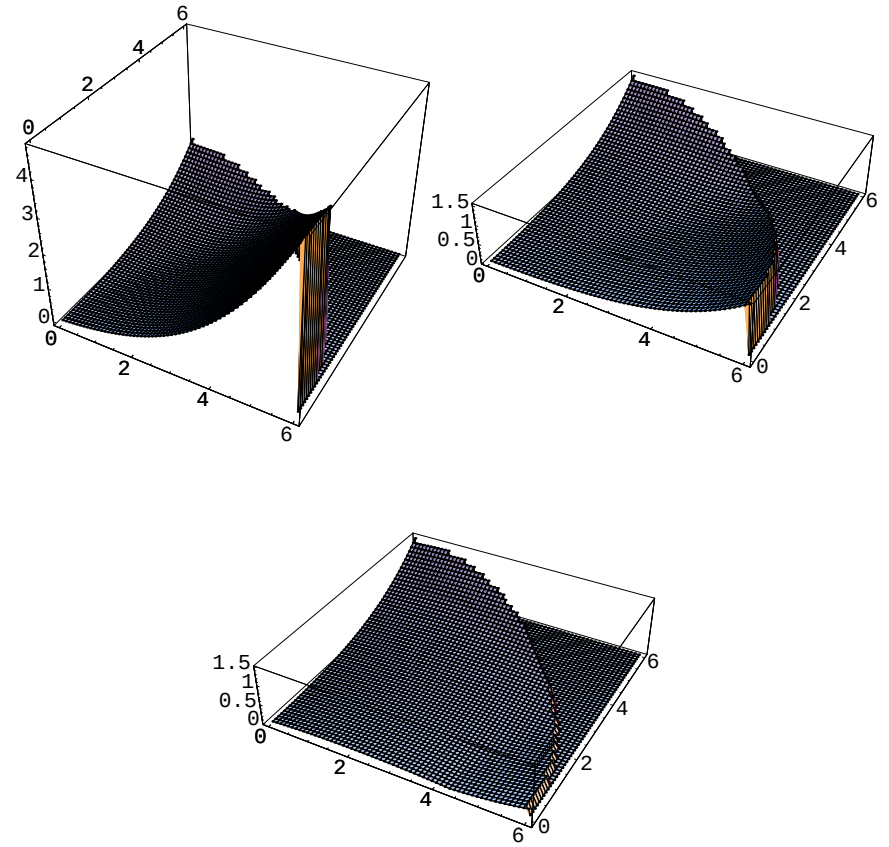

Figure 10.18: Tune shifts for the LHC case 6.

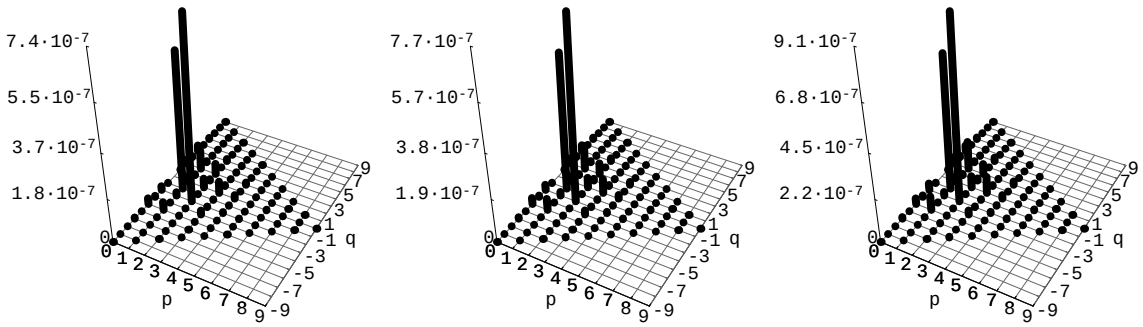

Figure 10.19: Resonance strengths for the LHC case 6.

However, notice that only a small fraction of the total particles, with predominantly horizontal initial amplitude, have tune shifts bigger than 10^{-3}. The other tune shifts are still bigger than in case 7, but within acceptable limits. The tune footprints are regular, triangle shaped, very elongated in one direction. The dominating resonance is still $(0, 3)$, with an important contribution from $(1, 2)$. Despite the fact that the tune shifts are bigger than in case 7, the magnitude of the resonance strengths are slightly smaller in case 8. The resonance structure is invariant with respect to energy.

The last two cases are the closest to reality among all studied cases. We included the whole lattice at order 8, detailed fringe fields of the High Gradient Quadrupoles in the interaction regions and generic fringe fields for the rest of the ring, and body errors for interaction regions with the two possible signs. So, case 9 is actually cases 6 and 7 superimposed, and case 10 is cases 6 and 8 superimposed, respectively.

Figures 10.26 and 10.27 show that the tune footprints are only slightly distorted compared to case 7. The only case when the fringe fields clearly have a considerable effect is for $\delta < 0$ particles, but still inside acceptable limits. From Figure 10.28 it is obvious that the dominating resonances are excited by the body errors. Hence, the body errors dominate the fringe field effects. Note that the fringe fields alter the natural chromaticity (even change its sign). It is interesting to compare Figures

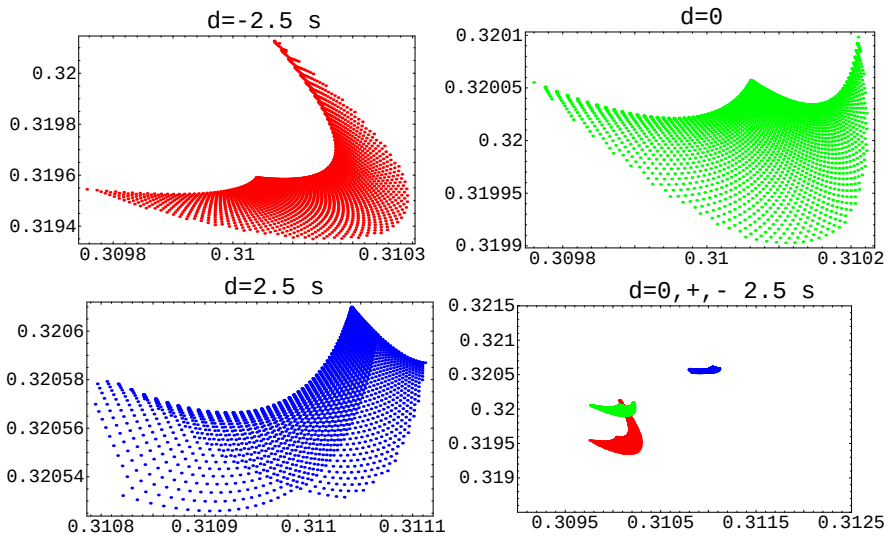

Figure 10.20: Tune footprints for the LHC case 7.

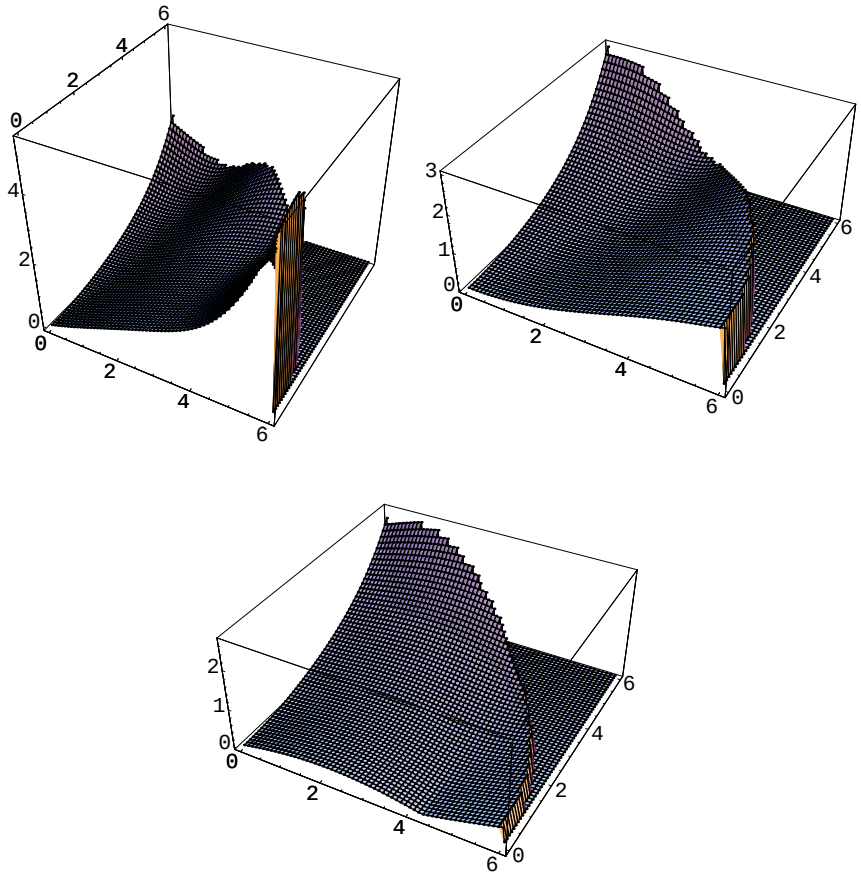

Figure 10.21: Tune shifts for the LHC case 7.

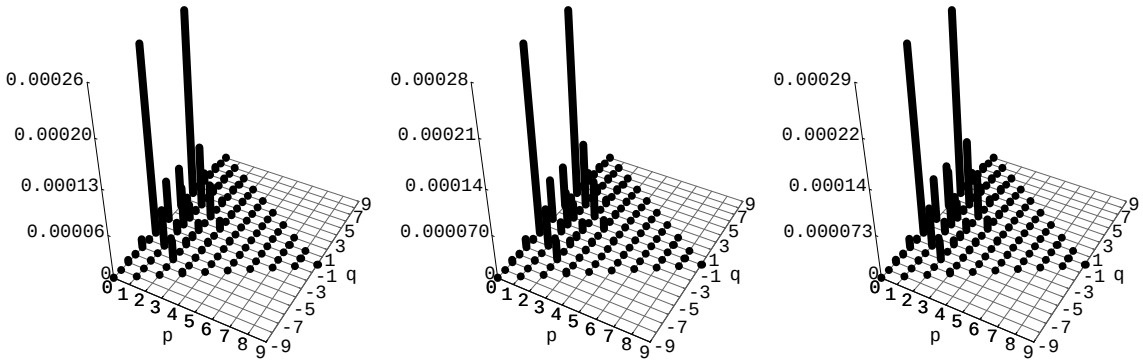

Figure 10.22: Resonance strengths for the LHC case 7.

10.29 and 10.16. The resonance channels in this case move much closer to the origin, inside the region occupied by the beam at target dynamic aperture. The chaotic boundary is around the target dynamic aperture. The thickest resonance channels remain $(1, -1)$, $(2, -2)$, $(3, -3)$, $(4, -4)$, $(0, 3)$ and $(1, 2)$.

Beside the fact that the tune shifts for $\delta < 0$ are much bigger in case 10, Figures 10.30, 10.31 and 10.32 tell the same story as case 9. Again, the situation resembles case 8, only in this case the fringe fields have a little more influence than they had in case 9.

We computed the resonance webs for $\delta = -2.5\sigma_E$ and $\delta = 0$ to show a general conclusion, that the resonance web structure is essentially invariant with respect to energy. This is consistent with the invariance of resonance strengths with energy. From Figure 10.33 results that the closest resonance lines are slightly farther away from the origin than in case 9. Also, in general the magnitudes of the resonance strengths increase with energy, and the resonance strengths of case 10 are smaller than the resonance strengths of case 9. It is exactly the opposite for the tune shifts; the biggest are of case 10.

Finally, for cases 9 and 10 we computed the resonance strengths for $\delta = 0$ on a grid in action space, to identify the dominating resonances at different locations. Due

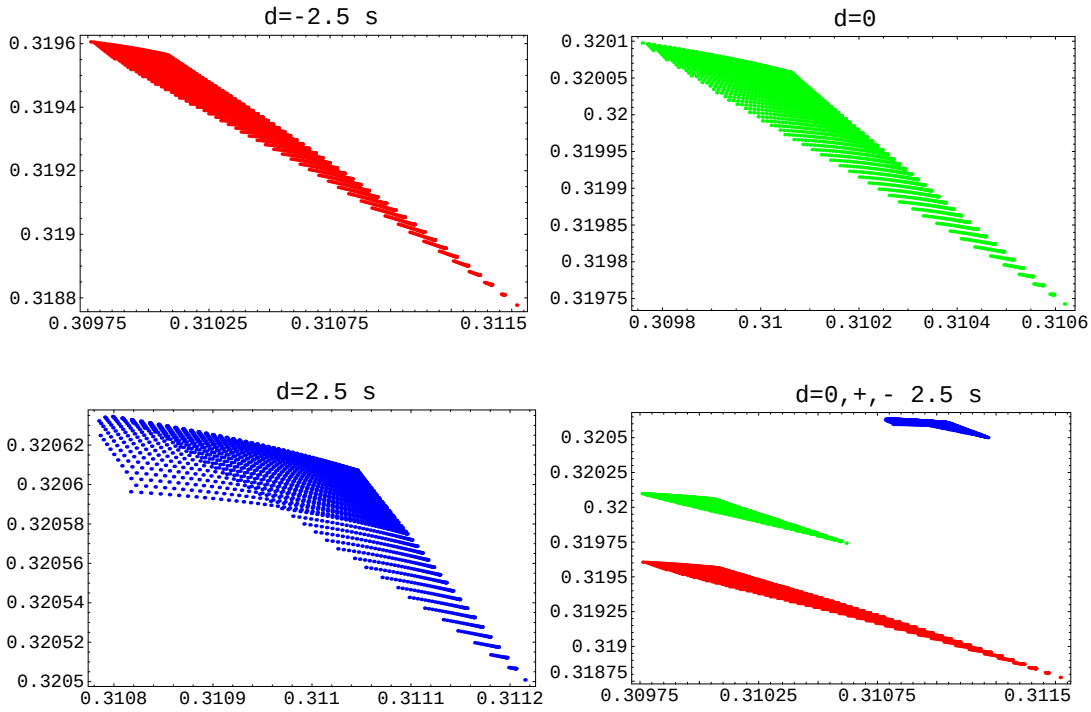

Figure 10.23: Tune footprints for the LHC case 8.

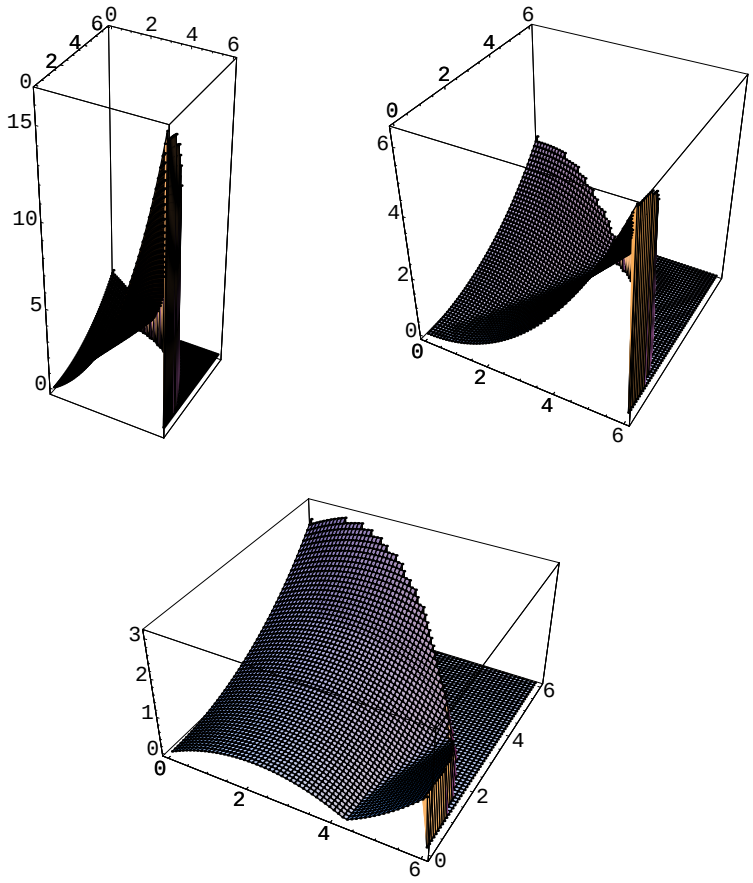

Figure 10.24: Tune shifts for the LHC case 8.

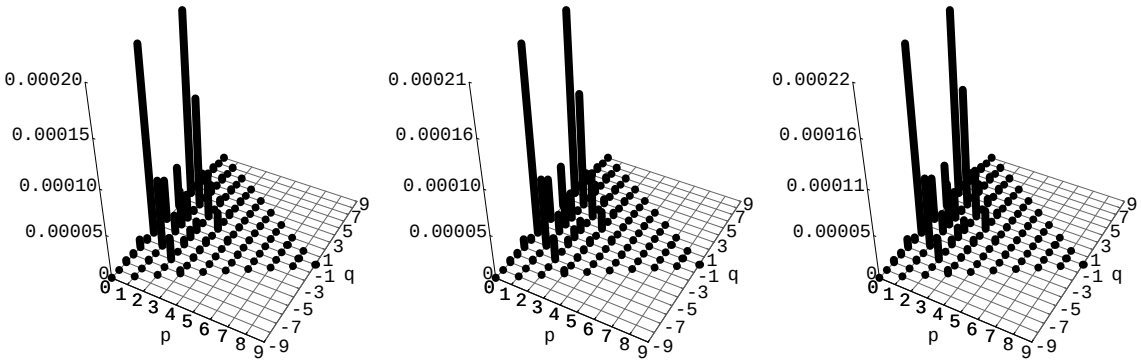

Figure 10.25: Resonance strengths for the LHC case 8.

to lack of space, only the picture that summarizes the conclusions is shown in Figure 10.34.

Obviously, $(0, 3)$ is the dominating resonance in a major part of action space. For exactly horizontal motion $(3, 0)$ is the dominating one, and there is a narrow region of predominantly horizontal motion for which $(1, -1)$ for case 9, and $(1, -1)$ or $(1, 2)$ for case 10 are the dominating resonances, respectively. As we saw, the $(1, -1)$ is excited by the quadrupole component of the fringe fields. Hence, there is a small region where the dominating resonance is given by fringe fields. However, the magnitudes of the respective resonances are very small. Actually, the magnitude of the resonance strengths increase much more quickly in the vertical direction. Also, from the resonance web pictures results that the closest resonance line to the origin is always along the vertical.

In a final paragraph we draw a few general conclusions. While the fringe fields generate important dynamical effects, as far tune shifts, footprints and resonance strengths are concerned, they are dominated by body errors. If there is a correlation between dynamic aperture and these quantities, than also the DA is determined by body errors. The fringe fields do decrease the dynamic aperture of the ideal lattice by a factor of around 6, as was shown in section 4.5. In this sense, they have a

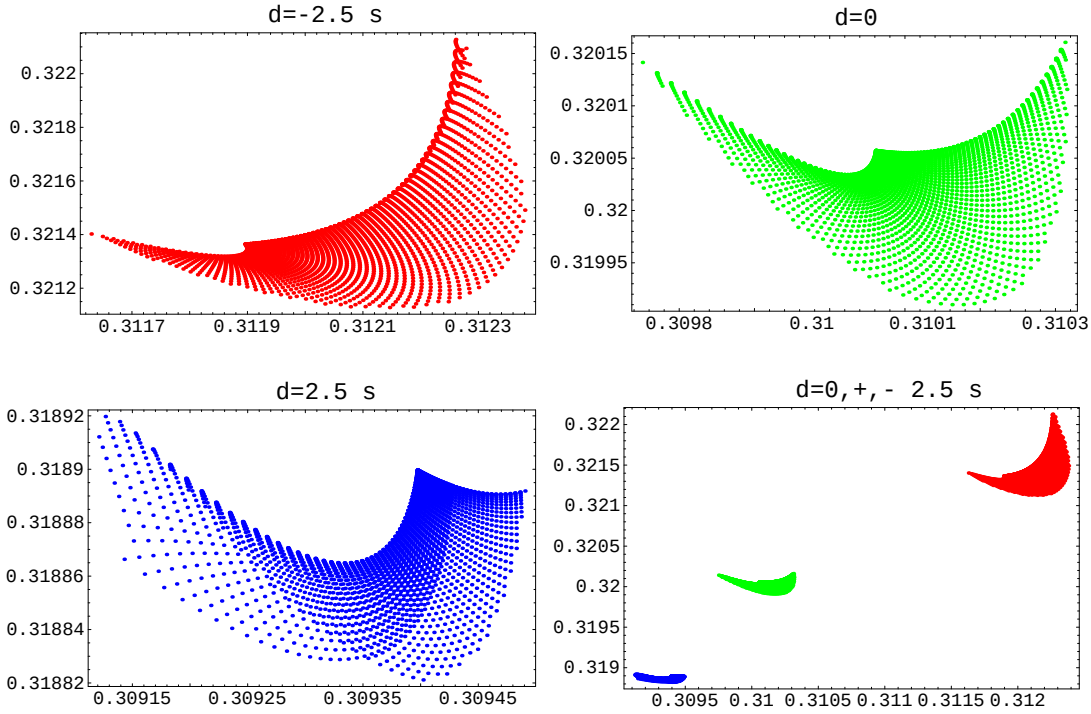

Figure 10.26: Tune footprints for the LHC case 9.

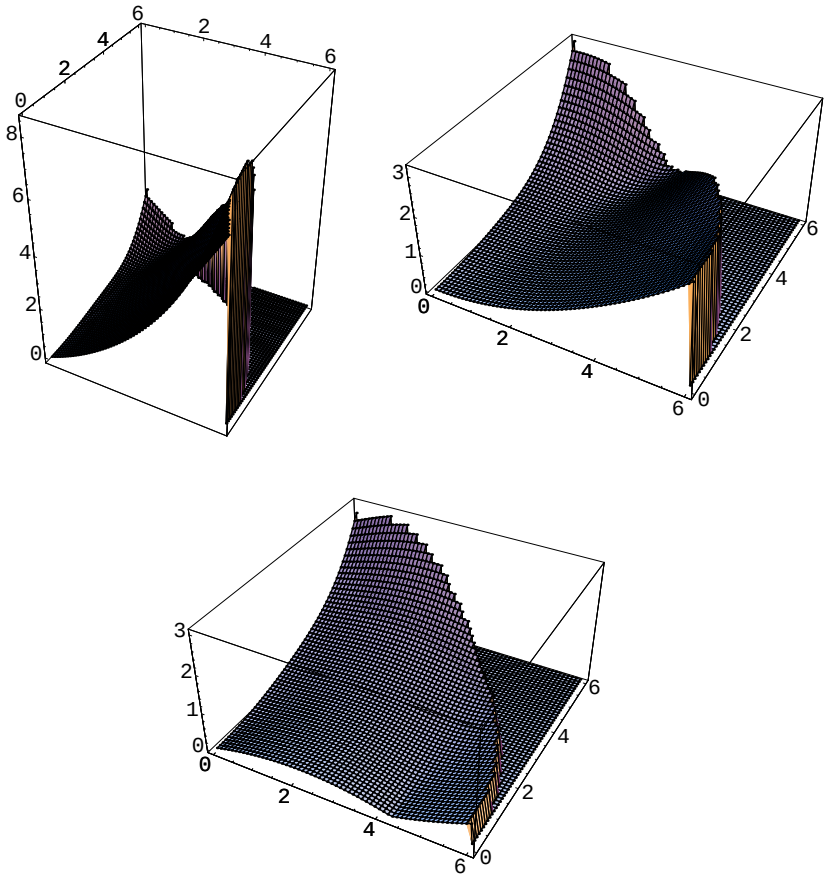

Figure 10.27: Tune shifts for the LHC case 9.

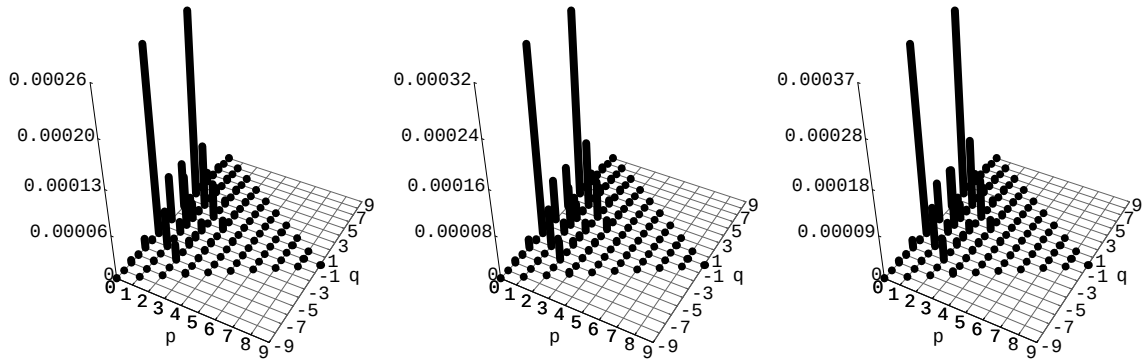

Figure 10.28: Resonance strengths for the LHC case 9.

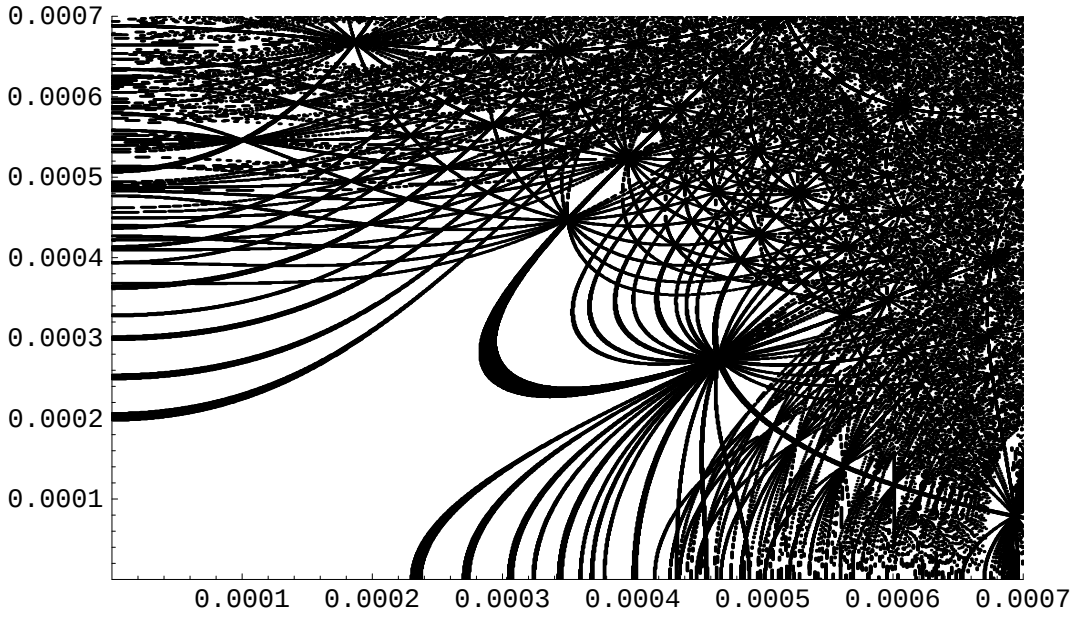

Figure 10.29: Resonance web for the LHC case 9, for $d = 0$.

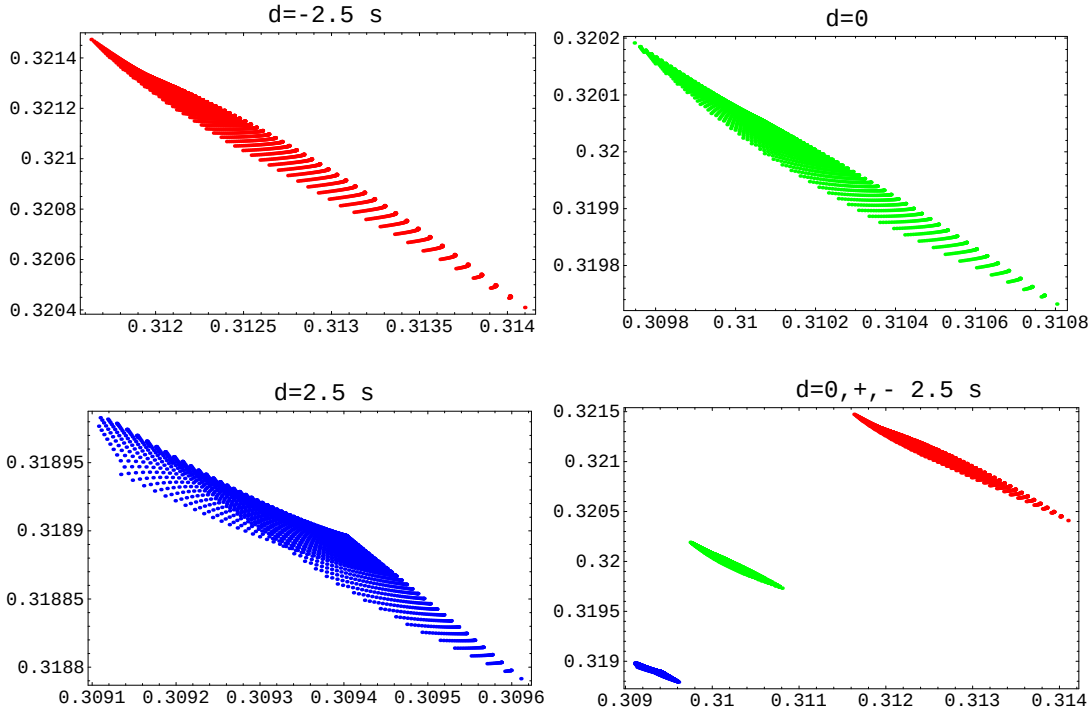

Figure 10.30: Tune footprints for the LHC case 10.

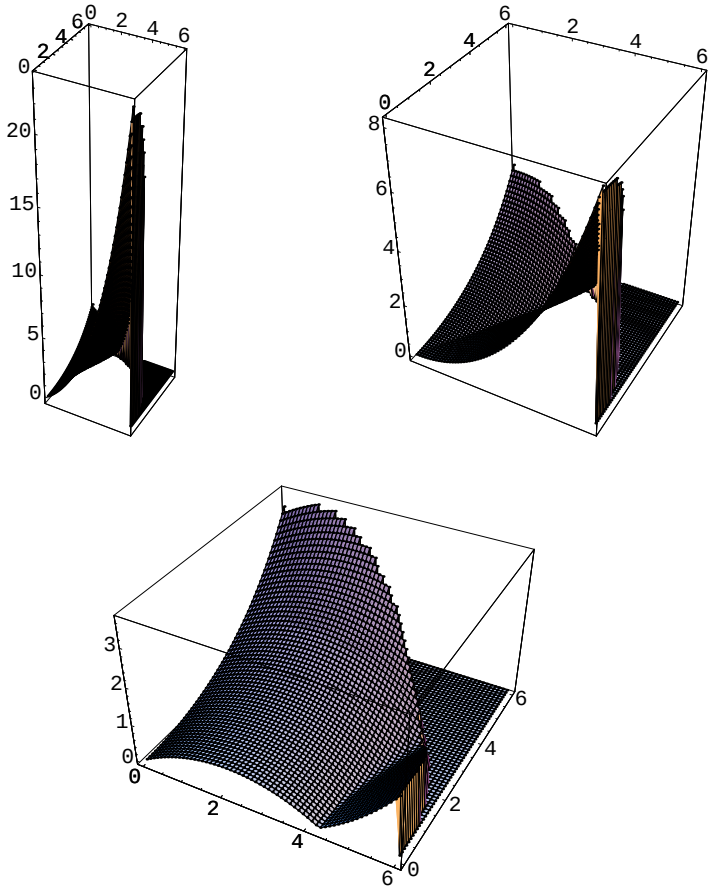

Figure 10.31: Tune shifts for the LHC case 10.

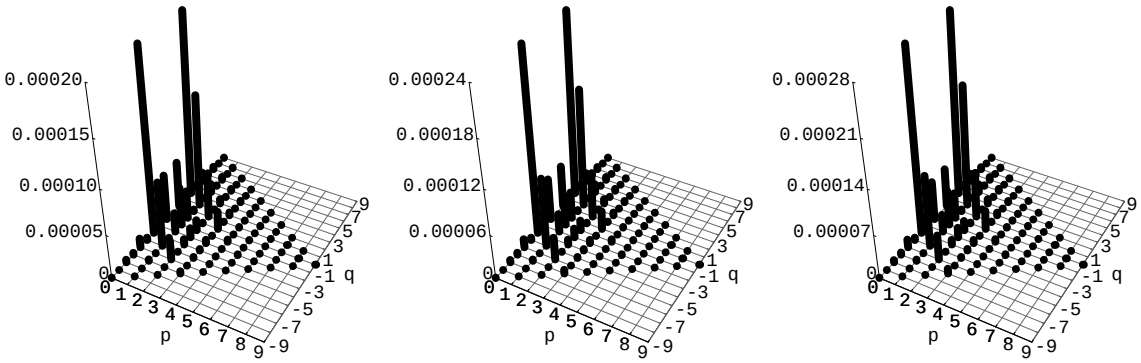

Figure 10.32: Resonance strengths for the LHC case 10.

huge effect. However, this reduced DA is still way above the expected DA; the approximate DA value with fringe fields is around 20σ. However, the body errors alone decrease the DA to the level where is starts to hit a lower acceptable limit, and the fringe fields do not affect it very much anymore. Indeed, this is confirmed by tracking; the loss in DA due to fringe fields is at most $0.5\sigma_{x,y}$. On the other hand, the DA cannot be correlated exactly with both tune shifts and resonance strengths. This can be seen from the fact that we do not get the largest tune footprints for the case with the largest resonance strengths and vice versa. However, roughly it is correlated with both indicators. The resonance strength and resonance web results are consistent in the sense that resonance lines closer to the origin give larger resonance strengths. Regarding the shape of fringe fields, we could conclude that the exact shape does not matter. However, intrinsically the fringe field effects are not very important for the LHC, and for other situations, like the proposed Muon Collider, where the relative importance of the fringe fields are greater, the shape of fringe field is also important. For the LHC, most of fringe field effects are generated by the High Gradient Quadrupoles. The energy dependence of the tunes show that in general tune shifts are maximized for predominantly horizontal motion for $\delta < 0$, and as energy increases, the maximum decreases and shifts towards predominantly vertical motion. For on-energy particles the tune shifts are approximately symmetric with

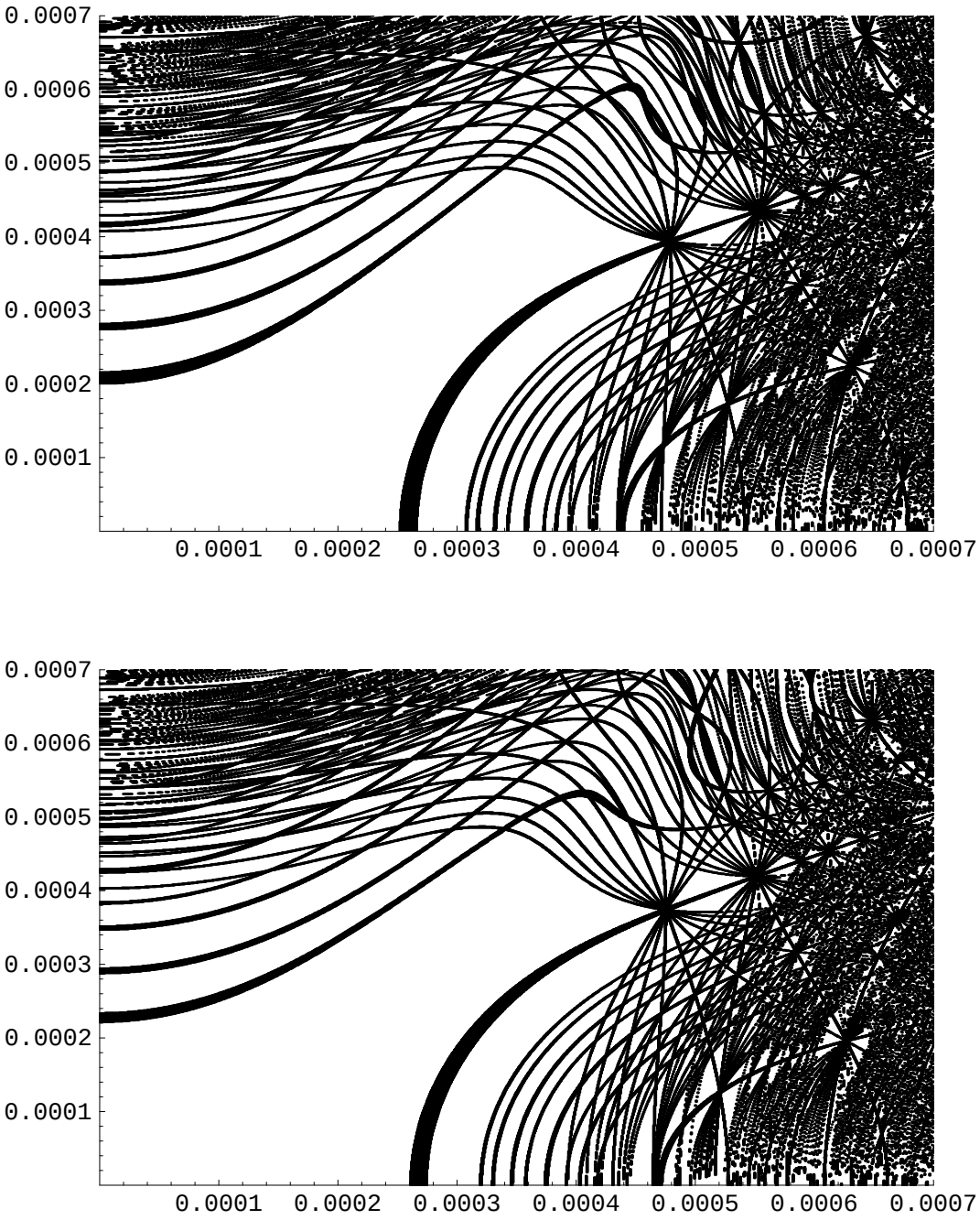

Figure 10.33: Resonance web for the LHC case 10, for $d = -2.5 s_E$ and $d = 0$.

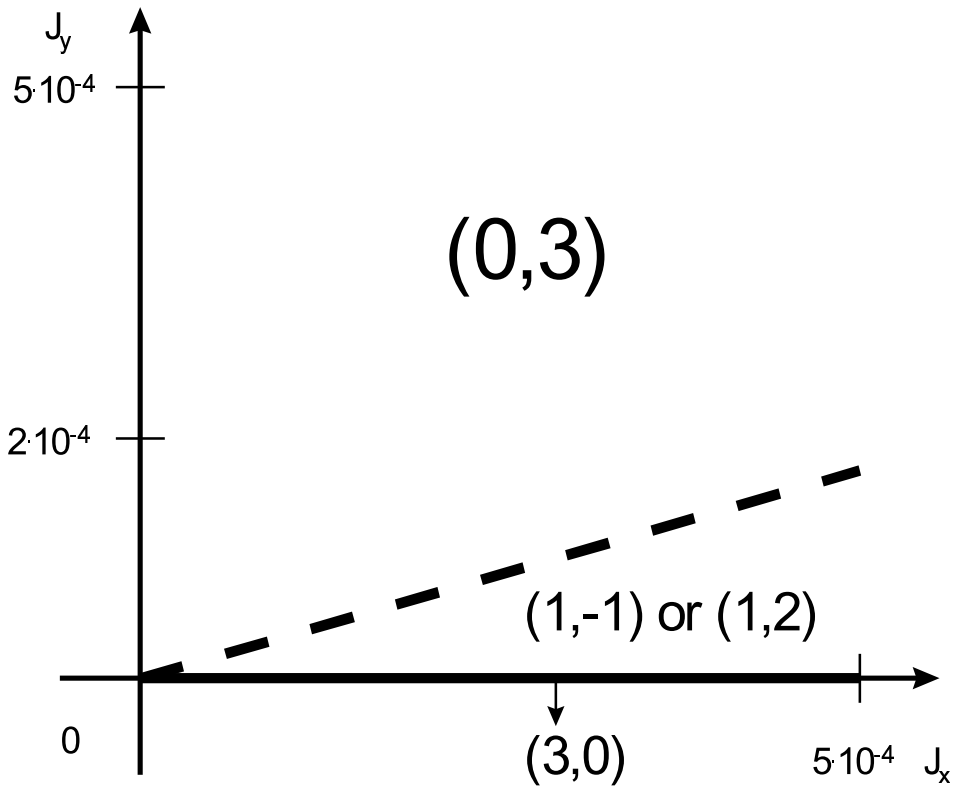

Figure 10.34: Dominating resonances for the LHC cases 9 and 10.

respect to diagonal, with minimums attained around the diagonal. This implies that, if the tune shifts are correlated with the DA, the estimation of the DA using only on-energy particles launched along the diagonal will result in an overestimation of the DA. Resonance strengths and resonance webs are roughly invariant with respect to energy. However, a marginal increase of the resonance strengths with energy is usually observed. The trend for the tune shifts is exactly opposite. In some cases, a substantial decrease of the footprints is observed as energy increases. Over a large portion of action space the dominant resonance is $(0, 3)$. The resonance strengths increase in magnitude faster in the vertical direction. The magnitudes of the dominating resonances in the strip of predominantly horizontal motion are much smaller than in the rest of action space. The biggest jump in the magnitudes is observed at around $2 \cdot 10^{-4}$ along the vertical, which, by coincidence or not, is the location of the closest resonance line to the origin in the resonance web pictures.

10.4 Map Transformations Under Orientation Flips

Sometimes, orientation changes of particle optical elements in an accelerator lattice are used as a mean to compensate or correct nonlinearities, improving the characteristics of the accelerator. One specific case is the LHC HGQs in the interaction regions [103]. The question arises what are the proper symmetry operations on certain maps that give the correct answer for maps of systems that differ by some symmetry transformation. That is, knowing the map of an element in a "default" orientation, what kind of transformations are necessary in order to obtain the maps of the "flipped" elements? Specifically, we need 3 different (similarity) transformations on the map, corresponding to mirroring the "default", or "forward" element with respect to a plane. Here we use W. Wan's nomenclature [104]. Mirroring the forward element with respect to the $x-y$ plane gives the "reversed" element, with respect to the $y-z$

plane gives the "switched" element, and with respect to the $x-z$ plane gives the "upside-down" element. In [104] it is explained how to obtain the map of mirrored elements knowing the map of the forward element.

The map of the reversed element in the (x, a, y, b, l, δ) symplectic basis is given by

$$\mathcal{M}_R = \mathcal{R} \circ \mathcal{M}^{-1} \circ \mathcal{R}, \tag{10.6}$$

where

$$\mathcal{R} = \begin{pmatrix} 1 & 0 & 0 & 0 & 0 & 0 \\ 0 & -1 & 0 & 0 & 0 & 0 \\ 0 & 0 & 1 & 0 & 0 & 0 \\ 0 & 0 & 0 & -1 & 0 & 0 \\ 0 & 0 & 0 & 0 & 1 & 0 \\ 0 & 0 & 0 & 0 & 0 & -1 \end{pmatrix} \tag{10.7}$$

is an involution: $\mathcal{R} \circ \mathcal{R} = \mathcal{I}$, $\mathcal{I}$ being the identity. It follows that $\mathcal{R}^{-1} = \mathcal{R}$. The map $\mathcal{M}$ is the map of the forward element.

Analogously, the switched map can be obtain from the forward map as

$$\mathcal{M}_S = \mathcal{S} \circ \mathcal{M} \circ \mathcal{S}, \tag{10.8}$$

with

$$\mathcal{S} = \begin{pmatrix} -1 & 0 & 0 & 0 & 0 & 0 \\ 0 & -1 & 0 & 0 & 0 & 0 \\ 0 & 0 & 1 & 0 & 0 & 0 \\ 0 & 0 & 0 & 1 & 0 & 0 \\ 0 & 0 & 0 & 0 & 1 & 0 \\ 0 & 0 & 0 & 0 & 0 & 1 \end{pmatrix} \tag{10.9}$$

possessing similar properties as $\mathcal{R}$: $\mathcal{S} \circ \mathcal{S} = \mathcal{I}$, and $\mathcal{S}^{-1} = \mathcal{S}$.

The last one is the upside-down transformation

$$\mathcal{M}_U = \mathcal{U} \circ \mathcal{M} \circ \mathcal{U}, \tag{10.10}$$

with

$$\mathcal{U} = \begin{pmatrix} 1 & 0 & 0 & 0 & 0 & 0 \\ 0 & 1 & 0 & 0 & 0 & 0 \\ 0 & 0 & -1 & 0 & 0 & 0 \\ 0 & 0 & 0 & -1 & 0 & 0 \\ 0 & 0 & 0 & 0 & 1 & 0 \\ 0 & 0 & 0 & 0 & 0 & 1 \end{pmatrix}. \tag{10.11}$$

Again, $\mathcal{U} \circ \mathcal{U} = \mathcal{I}$, and $\mathcal{U}^{-1} = \mathcal{U}$. It is well known that an element satisfying midplane symmetry is invariant under the upside-down transformation.

Next, we show under what conditions an element is invariant with respect to reversion. The conditions can be deduced from Hamilton's equations. In the case of planar reference orbit, no electric fields, and s-independent magnetic fields (in which case the fields are derivable from the vector potential component A_s, and $A_x = A_y = 0$), the most general Hamiltonian [105] is invariant under the transformation $\mathcal{R}$. Moreover, the canonical equations of motion, and hence the map of a such an element, are invariant under the transformation $\mathcal{R}_\alpha$, where α means that it inverts the sign of the independent variable s, when acting on a map:

$$\mathcal{R}_\alpha \circ \mathcal{M} = \mathcal{M} \circ \mathcal{R}_\alpha. \tag{10.12}$$

In the Lie Algebraic notation, the map can be written in the form

$$\mathcal{M} = e^{-\Delta s : H :}, \tag{10.13}$$

where $: H :$ is the Poisson bracket operator attached to the Hamiltonian of the system. Hence, $\alpha(\mathcal{M}) = \mathcal{M}^{-1}$, since $: H :$ commutes with itself. Inserting it in the invariance relation we obtain that

$$\mathcal{R} \circ \mathcal{M}^{-1} = \mathcal{M} \circ \mathcal{R} \tag{10.14}$$

$$\Downarrow$$

$$\mathcal{M} = \mathcal{R} \circ \mathcal{M}^{-1} \circ \mathcal{R}. \tag{10.15}$$

Comparison with the map of the reversed element gives the result

$$\mathcal{M}_R \equiv \mathcal{M}. \tag{10.16}$$

In the specific case of the LHC HGQs, 180 degree rotations of quadrupoles around the y axis are performed. This transformation is equivalent to mirroring the forward element with respect to the $x-y$ plane, and then with respect to the $y-z$ plane. In other words, we obtain a "combined" element as the combination of the reversed and switched element. Finally, we can identify the combined element's map with the map of the "opposite" quadrupole's map. For details, see [103].

Now we can show that the combined element is unique, that is the reversed and switched, and switched and reversed elements have the same map. i.e. the two symmetry operations commute.

1) Reversed and Switched

$$\mathcal{M}_C = \mathcal{S} \circ \left(\mathcal{R} \circ \mathcal{M}^{-1} \circ \mathcal{R}\right) \circ \mathcal{S}. \tag{10.17}$$

2) Switched and Reversed

$$\begin{aligned}
\mathcal{M}_C^{'} &= \mathcal{R} \circ \left(\mathcal{S} \circ \mathcal{M} \circ \mathcal{S}\right)^{-1} \circ \mathcal{R} && (10.18)\\
&= \mathcal{R} \circ \mathcal{S} \circ \mathcal{M}^{-1} \circ \mathcal{S} \circ \mathcal{R} && (10.19)\\
&= \mathcal{S} \circ \mathcal{R} \circ \mathcal{M}^{-1} \circ \mathcal{R} \circ \mathcal{S} && (10.20)\\
&= \mathcal{S} \circ \left(\mathcal{R} \circ \mathcal{M}^{-1} \circ \mathcal{R}\right) \circ \mathcal{S} && (10.21)\\
&= \mathcal{M}_C. && (10.22)
\end{aligned}$$

We used the fact that $S^{-1} = S$, and being diagonal matrices $[R, S] = R \circ S - S \circ R = 0$. Actually, all the individual transformations commute due to the fact that they are generated by diagonal matrices.

So we have an easy procedure to compute the maps of arbitrary "opposite" elements from the "default" ones. Moreover, the map approach is valid for arbitrary field configurations, including detailed fringe fields and compositions of several maps. In the case of s-independent elements, we obtain simplifications due to invariance under reversion. This property is relevant for the implementation of the body errors in section 10.3, in which case we can get the map of the opposite quadrupole by switching the default map. Of course, in the case of detailed fringe field maps, one needs to perform the reversion too.

To compare the above results with the rules for multipole sign changes due to orientation changes [103], we derive the results based on field multipole expansion. Suppose that (10.23) gives the multipole expansion in the default reference frame.

$$B_y + iB_x = \sum_n \left(b_n + ia_n\right)\left(x + iy\right)^n . \tag{10.23}$$

As a contrast with the map methods, this formula, and hence the derivation, is valid only for s-independent elements, or the integrated strengths in the end regions. In the same way, we assume that the expansion in the opposite frame is

$$B_{y'} + iB_{x'} = \sum_n \left(b_n^{'} + ia_n^{'}\right)\left(x^{'} + iy^{'}\right)^n . \tag{10.24}$$

First, the reversion consists of the following transformations:

$$x' \rightarrow x \qquad y' \rightarrow y \qquad z' \rightarrow -z, \tag{10.25}$$

$$B_{x'} \rightarrow -B_x \qquad B_{y'} \rightarrow -B_{y'} . \tag{10.26}$$

Inserting them in the expansion gives

$$B_y + iB_x = \sum_n -\left(b_n^{'} + ia_n^{'}\right)\left(x + iy\right)^n . \tag{10.27}$$

Comparing coefficients with (10.23) we obtain that

$$b_n^{'} \equiv -b_n, \tag{10.28}$$

$$a_n^{'} \equiv -a_n . \tag{10.29}$$

The switching can be cast in a similar way to correspond to the following transformations

$$x' \rightarrow -x \qquad y' \rightarrow y \qquad z' \rightarrow z, \tag{10.30}$$

$$B_{x'} \rightarrow B_x \qquad B_{y'} \rightarrow -B_{y'}, \tag{10.31}$$

$$-B_y + iB_x = \sum_n \left(b_n^{'} + ia_n^{'}\right)(-x+iy)^n\,. \tag{10.32}$$

Taking the complex conjugate of the above expression we arrive to

$$-B_y - iB_x = \sum_n \left(b_n^{'} - ia_n^{'}\right)(-x-iy)^n \tag{10.33}$$

$$B_y + iB_x = \sum_n (-1)^n \left(-b_n^{'} + ia_n^{'}\right)(x+iy)^n\,. \tag{10.34}$$

Comparing coefficients with (10.23) we obtain

$$b_n^{'} \equiv (-1)^{n+1} b_n, \tag{10.35}$$

$$a_n^{'} \equiv (-1)^n a_n \tag{10.36}$$

The upside-down transformation can be expressed as

$$x' \rightarrow x \qquad y' \rightarrow -y \qquad z' \rightarrow z, \tag{10.37}$$

$$B_{x'} \rightarrow -B_x \qquad B_{y'} \rightarrow B_{y'}, \tag{10.38}$$

$$B_y - iB_x = \sum_n \left(b_n^{'} + ia_n^{'}\right)(x-iy)^n\,. \tag{10.39}$$

Taking the complex conjugate expression we arrive to

$$B_y + iB_x = \sum_n \left(b_n^{'} - ia_n^{'}\right)(x+iy)^n\,, \tag{10.40}$$

which gives the relation between multipole coefficients,

$$b_n^{'} \equiv b_n, \tag{10.41}$$

$$a_n^{'} \equiv -a_n. \tag{10.42}$$

Finally, we get the rule for the combined (opposite) element as the commutable product of the reversion and switching transformation

$$b_n^{'} \equiv (-1)^n b_n, \tag{10.43}$$

$$a_n^{'} \equiv (-1)^{n+1} a_n. \tag{10.44}$$

in agreement with [103]. Direct calculation shows that the above results are in complete agreement with [103] for every case, after, in case it is necessary, the polarity is changed following the transformation such that the fundamental term remains positive.

As a conclusion, the above map manipulations based on the matrices R, S, and U form a complete set of commutable transformations to perform any flip scenario, including arbitrary s-dependent fields, and maps of composed elements. All the necessary map computations, compositions and inversions are easily performed in the Differential Algebra based code COSY INFINITY.

Chapter 11

Summary of Part II

Accurate simulation of fringe field effects requires more effort than the traditional piecewise arclength independent fields. While some approximations and simplifications work in some cases, there is the danger that one always relies on them, and as a consequence, yield inaccurate or misleading results in situations were fringe fields cannot be safely neglected anymore. It was shown that, in general, fringe fields affect the motion at all orders, starting with the linear part of the transfer map, and induce modifications in every indicator used to asses the single particle dynamics: center tunes, chromaticities, tune shifts, resonance strengths, and dynamic apertures. Moreover, it is not straightforward to asses a priori the importance of fringe fields, and it is recommended to deal with fringe fields on a case-by-case basis. It was shown that fringe fields are important "in absolute value" for the LHC, but not a limiting factor, are a limiting factor for the dynamic aperture of the Neutrino Factory, and induce only a very slow diffusion for the Proton Driver, which does not alter the short term dynamic aperture. Further work identified that only a few matching section quadrupole fringe fields are responsible for the drastic reduction of the DA of the Neutrino Factory, and increasing their length, with the simultaneous reduction of the strength, restored the DA above the target value [12]. More detailed fringe field and other nonlinear effects simulations of the Muon Accelerators can be found in [56].

In the end, careful consideration of fringe field effects amounts to integration of the correct ordinary differential equations of the motion, in which the nonlinear effects are accounted for, including the electromagnetic fields in accordance to Maxwell's equations. Besides fringe fields, the so-called kinematic effect can also lead to inaccurate results [56]. It was shown that the sharp cutoff approximation leads to divergences in the map, truncation of high order pseudo-multipoles can also give inaccurate results, and not even symplectification can undo the errors made in modeling the systems, as, for example, neglect of details of the fringe field shapes.

It was shown that it is possible to obtain very accurate fringe field maps for current dominated superconducting magnets, using Differential Algebraic methods. The procedure includes field computation of current wires in the Differential Algebra framework, employing a novel form of the Biot-Savart formula for rectilinear currents. The method was illustrated by the multipole decomposition and map computation of the LHC's HGQ ends. Clearly, the method can be used unaltered for any element with large enough radius of curvature, and can be adapted for bending elements by using different coordinate systems. Moreover, it is also possible to obtain multipole information from measured field data, for example from data on the surface of a cylinder, or in one or several planes. All is needed is some good interpolation method, that interpolates both the field values and the derivatives accurately. Although more research is needed in this direction, the Gaussian interpolation is promising [106].

The need to satisfy Maxwell's equations in the ODEs resulted in the development of two methods to enforce them. It was shown that, in the Differential Algebraic framework, it is trivial to check and enforce Maxwell's equations locally as well as globally. These methods are useful to correct small computational errors or occasional magnet design flaws.

Finally, a detailed study of fringe field effects on the LHC single particle dynamics revealed that the fringe fields introduce large nonlinear effects, and decrease the dynamic aperture typically by a factor of six, but the resulting DA is still well above the target. The fringe field effects are concentrated in the interaction regions. It was shown that the fringe field effects are dominated by the HGQ body errors. However, we mention that for the body errors the worst case scenario was utilized for the systematic parts of the errors, and the fringe field errors were neglected.

In conclusion, fringe fields can be important for any accelerator, and there are methods that allow a careful and accurate representation and simulation of their effects on the dynamics. Once the fringe field maps have been computed, the effort pays off by noticing that the subsequent dynamical studies require the same effort with fringe fields as without, including normal form based quantities such as tunes and tune shifts, chromaticities, resonance strengths and webs, and symplectic tracking for fast, efficient, and reliable dynamic aperture estimation.

Bibliography

[1] J.M. Sanz-Serna and M.P. Calvo. *Numerical Hamiltonian problems*. Chapman and Hall, London, 1994.

[2] Z. Shang. KAM theorem of symplectic algorithms for Hamiltonian systems. *Numer. Math.*, 83:477–496, 1999.

[3] Z. Ge and J. Marsden. Lie-Poisson Hamilton-Jacobbi theory and Lie-Poisson integrators. *Phys. Lett. A*, 133:134–139, 1988.

[4] G. Benettin and A. Giorgilli. On the Hamiltonian interpolation of near-to-the-identity symplectic mappings with application to symplectic integration algorithms. *J. Stat. Phys.*, 74, 5-6:1117–1143, 1994.

[5] B. Leimkuhler, S. Reich, and R. D. Skeel. Integration methods for molecular dynamics. In *IMA Summer Program: Molecular Biology, K. Schulten and J. Mesirov, Eds.*, New York, 1994. Springer-Verlag.

[6] J. Wisdom, M. Holman, and J. Touma. Symplectic correctors. *Fields Institute Communications*, 10:217–244, 1996.

[7] G. Benettin and F. Fasso. From Hamiltonian perturbation theory to symplectic integrators and back. *Appl. Numer. Math.*, 29, 1:73–87, 1999.

[8] M. Suzuki. Quantum Monte Carlo methods and general decomposition of exponential operators and symplectic integrators. *Physica A*, 205:65–79, 1994.

[9] M. Berz. Differential algebraic description of beam dynamics to very high orders. *Particle Accelerators*, 24:109, 1989.

[10] M. Berz. *Modern Map Methods in Particle Beam Physics*. Academic Press, San Diego, 1999, also available at http://bt.nscl.msu.edu/paperscgi/display.pl?name=AIEP108book.

[11] M. Berz, K. Makino, and B. Erdelyi. Fringe field effects in Muon Rings. In *Proceedings of HEMC'99, Workshop on Muon Colliders at Highest Energies*, Long Island, 1999. Montauk.

[12] F. Zimmermann, C. Johnstone, M. Berz, B. Erdelyi, K. Makino, and W. Wan. Fringe fields and dynamic aperture in the FNAL Muon Strorage Ring. Technical Report SL-2000-011 AP and NUFACT-NOTE 21, CERN, 2000.

[13] M. Berz, B. Erdelyi, and K. Makino. Fringe field effects in small rings of large acceptance. *Phys. Rev. ST-Accel. Beams,*, 3:124001, 2000.

[14] D. Abell. *Analytic properties and approximation of transfer maps for Hamiltonian systems*. PhD thesis, University of Maryland, 1995.

[15] J. Shi and P. Suwannakoon. Single-particle dynamics in particle storage rings with integrable polynomial factorization maps. *Phys. Rev. E*, 58, 6:7868–7873, 1998.

[16] I. Gjaja, A.J. Dragt, and D.T. Abell. A comparison of methods for long-term tracking using symplectic maps. *IOP Conf. Ser.*, 131:173–184, 1993.

[17] M. Berz. Symplectic tracking in circular accelerators with high order maps. In *Nonlinear Problems in Future Particle Accelerators*, page 288, Singapore, 1991. World Scientific.

[18] H. Hofer. On the topological properties of symplectic maps. *Proc. Royal Soc. Edinburgh, Sect. A*, 115:25–38, 1990.

[19] R. deVogelaere. Methods of integration which preserve the contact transformation property of the Hamiltonian equations. Technical Report 4, Department of Mathematics, Univ. Notre Dame, 1956.

[20] P.J. Channell. Symplectic integration algorithms. Technical Report Internal Report AT-6, ATN-83-9, Los Alamos National Laboratory, 1983.

[21] P.J. Channell and J.C. Scovel. Symplectic integration of Hamiltonian systems. *Nonlinearity*, 3:231–259, 1990.

[22] A.J. Dragt and D.T. Abell. Symplectic maps and computation of orbits in particle accelerators. *Fields Institute Communications*, 10:59–85, 1996.

[23] A. J. Dragt, L. M. Healy, F. Neri, and R. Ryne. MARYLIE 3.0 - a program for nonlinear analysis of accelerators and beamlines. *IEEE Transactions on Nuclear Science*, NS-3,5:2311, 1985.

[24] K. Makino and M. Berz. COSY INFINITY version 8. *Nuclear Instruments and Methods*, A427:338–343, 1999.

[25] Y.T. Yan, P.J. Channell, and M. Syphers. Performance of an algorithm for symplectic implicit one-turn map tracking. Technical report, SSC Laboratory Report SSCL-157, 1993.

[26] R. Warnock and J. Ellison. From symplectic integrator to Poincare map: spline expansion of a map generator in Cartesian coordinates. *Appl. Numer. Math.*, 29:89–98, 1999.

[27] H. Goldstein. *Classical Mechanics*. Addison-Wesley, Reading, MA, 1980.

[28] K. Feng, H.M. Wu, M.Z. Quin, and D.L. Wang. Construction of canonical difference schemes for Hamiltonian formalism via generating functions. *J. Comp. Math.*, 7, 1:71–96, 1989.

[29] K. Feng. The calculus of generating functions and the formal energy for Hamiltonian algorithms. *J. Comp. Math.*, 16, 6:481–498, 1998.

[30] C.K. Siegel. Symplectic geometry. *Amer. J. Math.*, 65:1–86, 1943.

[31] A. Weinstein. Symplectic manifolds and their Lagrangian submanifolds. *Advances in Math.*, 6:329–346, 1971.

[32] A. Weinstein. Lagrangian submanifolds and Hamiltonian systems. *Ann. of Math.*, 98, 2:377–410, 1973.

[33] A. Weinstein. Normal modes for non-linear Hamiltonian systems. *Invent. Math.*, 20:47–57, 1973.

[34] A. Weinstein. *Lectures on symplectic manifolds.* CBMS Reg. Conf. Series in Math. 29, AMS, Providence, RI, 1977.

[35] R. Abraham and J.E. Marsden. *Foundations of Mechanics.* Addison-Wesley, Reading, Second edition, 1978.

[36] J.P. Amiet and P. Huguenin. Generating functions of canonical maps. *Helv. Phys. Acta*, 53:377–397, 1980.

[37] A.M. Ozorio de Almeida. On the symplectically invariant variational principle and generating functions. *Proc. R. Soc. Lond. A*, 431:403–417, 1990.

[38] M.J. Sewell and I. Roulstone. Anatomy of the canonical transformation. *Phil. Trans. R. Soc. Lond. A*, 345:577–598, 1993.

[39] Henri Poincare. *New Methods of Celestial Mechanics*, volume 3, chap. XXVIII. American Institute of Physics, New York, 1893/1993.

[40] A. Weinstein. The invariance of Poincare's generating function for canonical transformations. *Invent. Math.*, 16:203–213, 1972.

[41] A. Banyaga. *The structure of classical diffeomorphism groups.* Dordrecht, Boston, Kluwer Academic, 1997.

[42] A. J. Dragt. Lectures on nonlinear orbit dynamics. In *1981 Fermilab Summer School*, New York, 1982. AIP Conference Proceedings Vol. 87.

[43] R. Abraham, J. E. Marsden, and Tudor Ratiu. *Manifolds, Tensor Analysis, and Applications.* Springer-Verlag, New York, 1988.

[44] B. Erdelyi, J. Hoefkens, and M. Berz. Rigorous lower bounds for the domains of definition of extended generating functions. in preparation, 2001.

[45] D. McDuff and D. Salamon. *Introduction to symplectic topology.* Oxford University Press, New York, 1995.

[46] H. Hofer and E. Zehnder. *Symplectic invariants and Hamiltonian dynamics.* Birkhauser, Basel, 1994.

[47] J. E. Marsden and T. S. Ratiu. *Introduction to Mechanics and Symmetry.* Springer-Verlag, New York, 1994.

[48] P. Libermann and C.M. Marle. *Symplectic geometry and analytical mechanics.* Dordrecht, Boston, Kluwer Academic, 1987.

[49] I. Vaisman. *Symplectic geometry and secondary characteristic classes.* Prog. in Math., Birkhauser, Boston, 1987.

[50] M. Gromov. Pseudo-holomorphic curves in symplectic manifolds. *Invent. Math.*, 82:307–347, 1985.

[51] G. Rangarajan and M. Sachidanand. Symplectic integration using solvable maps. *J. Phys. A*, 33:131–142, 2000.

[52] C. Johnstone. Collider ring lattices. In *Proceedings of HEMC'99, Workshop on Muon Colliders at Highest Energies*, Long Island, 1999. Montauk.

[53] C. Johnstone. Large acceptance, transitionless lattice for FNAL Proton Driver. In *Proceedings of the NuFact'00 Workshop*, Monterey, 2000. MC Collaboration.

[54] C.M. Ankenbrandt et al. Status of muon collider research and development and future plans. *Phys. Rev. ST-AB*, 2:081001, 1999.

[55] R.B. Plamer, A. Sessler, and A. Tollestrup. Feasability study of muon colliders. In *Proceedings of Snowmass '96, DPF/DPB Summer Study on High-Energy Physics*, Menlo Park, CA, 1997. SLAC.

[56] M. Berz, K. Makino, and B. Erdelyi. Nonlinear effects in muon accelerators. *Phys. Rev. ST-Accel. Beams*, submitted, 2000.

[57] B. Erdelyi and M. Berz. Theory of extended generating functions for symplectification of truncated Taylor maps. *Phys. Rev. ST-Accel. Beams*, submitted, 2000, preliminary version available at http://130.83.124.174/frames/index.htm.

[58] B. Erdelyi and M. Berz. Optimal symplectic approximation of Hamiltonian flows. *Phys. Rev. Lett.*, in print, 2001.

[59] G. Rangarajan, A. Dragt, and F. Neri. Invariant metrics for Hamiltonian systems. In *Proceedings 1991 Particle Accelerator Conference*, San Francisco, CA, 1991. IEEE.

[60] C. Altafini, The De Casteljau algorithm on $SE(3)$. *A. Isidori, F. Lamnabhi-Lagarrigue, and W. Respondek (eds.), Nonlinear Control in Year 2000.* Springer-Verlag, Berlin, 2000.

[61] Y. Eliashberg and L. Polterovich. Bi-invariant metrics on the group of Hamiltonian diffeomorphisms. *Int. J. Math.*, 4:727–738, 1993.

[62] A.J. Dragt. Lectures on nonlinear dynamics and Lie methods with applications to Accelerator Physics. *Univ. of Maryland preprint*, 1998.

[63] M. Bialy and L. Polterovich. Geodesics of Hofer's metric on the group of Hamiltonian diffeomorphisms. *Duke Math. J.*, 76:273–292, 1994.

[64] F. Lalonde and D. McDuff. Hofer's L^∞ geometry: energy and stability of Hamiltonian flows. Parts I, II. *Invent. Math.*, 122:1–33, 35–69, 1995.

[65] K.F. Siburg. New minimal geodesics on the group of symplectic diffeomorphisms. *Calc. Var. and PDEs*, 3:299–309, 1995.

[66] C. Viterbo. Symplectic topology as the geometry of generating functions. *Math. Ann.*, 292:685–710, 1992.

[67] Dusa McDuff and Jennifer Slimowitz. Hofer-Zehnder capacity and length minimizing Hamiltonian paths. arXiv:math.SG/0101085.

[68] Y. Long. Geodesics in the compactly supported Hamiltonian diffeomorphism group. *Math. Z.*, 220:279–294, 1995.

[69] J.C. Sikorav. Systemes Hamiltoniens et topologie symplectique. *ETS, Editrice Pisa*, 1990.

[70] Z.J. Shang. *On KAM theorem for symplectic algorithms for Hamiltonian systems.* PhD thesis, CAS Computing Center, Beijing, 1991.

[71] G. Lee-Whiting. *Nuclear Instruments and Methods*, 83:232, 1970.

[72] H. Matsuda and H. Wollnik. The influence of an inhomogeneous magnetic fringing field on the trajectories of charged particles in a third order approximation. *Nuclear Instruments and Methods*, 77:40, 1970.

[73] H. Matsuda and H. Wollnik. Third order transfer matrices of the fringing field of an inhomogeneous magnet. *Nuclear Instruments and Methods*, 77:283, 1970.

[74] H. Matsuda and H. Wollnik. Third order transfer matrices for the fringing field of magnetic and electrostatic quadrupole lenses. *Nucl. Instr. Meth.*, 103:117–124, 1972.

[75] B. Hartmann, H. Irnich, and H. Wollnik. Analytical determination of 5th-order transfer matrices of magnetic quadrupole fringing fields. In M. Berz, S. Martin, and K. Ziegler, editors, *Nonlinear Problems in Accelerator Physics*, pages 87–96, Bristol, 1993. Institute of Physics Publishing.

[76] M. Venturini. Scaling of third-order quadrupole aberrations with fringe field extension. In *Proceedings of the 1999 Particle Accelerator Conference*, New York, 1999. IEEE.

[77] E. Forest and J. Milutinovic. Leading order hard edge fringe fields effects exact in $(1+\delta)$ and consistent with Maxwell's equations for rectilinear magnets. *Nucl. Instr. Meth. A*, A269:474–482, 1988.

[78] E. Forest, D. Robin, A. Zholents, M. Donald, R. Helm, J. Irwin, and H. Moshammer. Sources of amplitude-dependent tune shifts in the PEP-II design and their compensation with octupoles. In *Proceedings of the Fourth European Particle Accelerator Conference*, London, 1994. World Scientific.

[79] H. Wollnik. *Optics of Charged Particles.* Academic Press, Orlando, Florida, 1987.

[80] J. D. Jackson. *Classical Electrodynamics*. Wiley, New York, 1975.

[81] W. Wan, C. Johnstone, J. Holt, M. Berz, K. Makino, M. Lindemann, and B. Erdelyi. The influence of fringe fields on particle dynamics in the Large Hadron Collider. *Nucl. Instr. Meth. A*, 427:74–78, 1999.

[82] M. Berz. Arbitrary order description of arbitrary particle optical systems. *Nuclear Instruments and Methods*, A298:426, 1990.

[83] M. Berz. COSY INFINITY, an arbitrary order general purpose optics code. *Computer Codes and the Linear Accelerator Community*, Los Alamos LA-11857-C:137, 1990.

[84] M. Berz. Computational aspects of design and simulation: COSY INFINITY. *Nuclear Instruments and Methods*, A298:473, 1990.

[85] M. Berz. COSY INFINITY Version 8 reference manual. Technical Report MSUCL-1088, National Superconducting Cyclotron Laboratory, Michigan State University, East Lansing, MI 48824, 1997. see also http://www.beamtheory.nscl.msu.edu/cosy.

[86] K. L. Brown and J. E. Spencer. Non-linear optics for the final focus of the single-pass-collider. *IEEE Transactions on Nuclear Science*, NS-28,3:2568, 1981.

[87] D. Bazin. personal communication, 2000.

[88] F. Meot. personal communication, 2000.

[89] Ingrid Daubechies. *Ten Lectures on Wavelets*. SIAM, Philadelphia, 1992.

[90] L. Sagalovsky. Beam transport optics of dipole fringe-field in the framework of 3rd order matrix theory. *Nucl. Instr. Meth. A*, 298, 1-3:205–222, 1990.

[91] F. Zimmermann. Tune shift with amplitude induced by quadrupole fringe fields. Technical Report SL-2000-009 AP and NUFACT-NOTE 18, 2000.

[92] G. Sabbi. Magnetic field analysis of HGQ coil ends. Technical Report TD-97-040, Fermilab, 1997.

[93] F. Méot. The ray-tracing code Zgoubi. *Nucl. Instr. Meth.*, A 427:353–356, 1999.

[94] The LHC Study Group, The Large Hadron Collider, Conceptual Design. The Large Hadron Collider, Conceptual Design. Technical Report AC/95-05, CERN, 1995.

[95] F. Pilat et al. US-LHC IR magnet error analysis and compensation. In *Proceedings of the EPAC*, Stockholm, Sweden, 1998. IOP.

[96] S. Russenschuck. A computer program for the design of superconducting accelerator magnets. Technical Report CERN AT/95-39, CERN, 1995.

[97] S. Caspi et al. An approach to 3D magnetic field calculation using numerical and differential algebra methods. Technical Report LBL-32624, L. Berkeley Laboratory, 1992.

[98] M. Berz. *Differential Algebraic Techniques, Entry in 'Handbook of Accelerator Physics and Engineering', M. Tigner and A. Chao (Eds.).* World Scientific, New York, 1999.

[99] K. Makino and M. Berz. Arbitrary order aberrations for elements characterized by measured fields. In *Optical Science, Engineering and Instrumentation '97*, SPIE, 1997. IEEE.

[100] J.-P. Koutchouk. The LHC dynamic aperture. In *Proceedings PAC '99*, New York, 1999. AIP.

[101] M. Berz. Differential algebraic formulation of normal form theory. In *M. Berz, S. Martin and K. Ziegler (Eds.), Proc. Nonlinear Effects in Accelerators*, page 77, London, 1992. IOP Publishing.

[102] R. Bartolini and F. Schmidt. Normal form via tracking of beam data. Technical Report LHC Project Report 132, CERN, 1998.

[103] L. Bottura, A. Jain, D. McChesney, F. Pilat, G. Sabbi, and J. Wei. Summary of US-LHC magnet database workshop. Technical Report RHIC/AP/160, BNL, Long Island, New York, 1998.

[104] W. Wan. *Theory and Applications of Arbitrary-Order Achromats.* PhD thesis, Michigan State University, East Lansing, Michigan, USA, 1995. also MSUCL-976.

[105] K. Makino. *Rigorous Analysis of Nonlinear Motion in Particle Accelerators.* PhD thesis, Michigan State University, East Lansing, Michigan, USA, 1998. also MSUCL-1093.

[106] K. Makino and M. Berz. Arbitrary order aberrations for elements characterized by measured fields. In *Optical Science, Engineering and Instrumentation '97.* SPIE, 1997.